School of Physics and Astronomy

Measurement of thickness and phase transitions in supported lipid bilayers using quantitative differential interference contrast microscopy

David Regan

PhD Thesis
School of Physics and Astronomy
Cardiff University

2019

Contents

List of Figures

List of Tables

List of Acronyms

AOM acousto-optic modulator

AFM atomic force microscopy

CCD charge-coupled device

Chol ovine wool cholesterol

CMOS complementary metal-oxide-semiconductor

DIC differential interference contrast

DW distilled water

DHM digital holographic microscopy

$DC_{15}PC$ 1,2-dipentadecanoyl-*sn*-glycero-3-phosphocholine

DMPC 1,2-dimyristoyl-*sn*-glycero-3-phosphocholine

DOPC 1,2-dioleoyl-*sn*-glycero-3-phosphocholine

DOPE 1,2-dioleoyl-*sn*-glycero-3-phosphoethanolamine

DPPC 1,2-dipalmitoyl-*sn*-glycero-3-phosphocholine

ESM chicken egg sphingomyelin

FMM Fluid-Mosaic Model

GIF green interference filter

GUV giant unilamellar vesicle

HPLC high performance liquid chromatography

IUPAC International Union of Pure and Applied Chemistry

LUV large unilamellar vesicles

OWLS optical waveguide lightmode spectroscopy

PBS phosphate buffered saline

PC phosphocholine

PSF point spread function

PTFE polytetrafluoroethylene

SLB supported lipid bilayer

SANS small-angle neutron scattering

SNR signal-to-noise ratio

SPR surface plasmon resonance

SUV small unilamellar vesicles

TopFluorPC 1-palmitoyl-2-(dipyrromethene boron difluoride)undecanoyl-*sn*-glycero-3-phosphocholine

$T_{\mathbf{m}}$ main phase transition temperature

QCM-D quartz crystal microbalance with dissipation monitoring

qDIC quantitative differential interference contrast

$\mathbf{V_{pp}}$ peak-to-peak voltage

Abstract

Supported lipid bilayers are one of the most commonly used model membrane systems, studied with a wide variety of different techniques. One family of microscopy techniques is quantitative phase imaging, which measures the phase shift of light passing through a sample. This phase shift is determined by a sample's thickness and refractive index, and so the phase information provides meaningful structural information about the sample. Here, we seek to investigate how a relatively new form of quantitative phase imaging, quantitative differential interference contrast (qDIC), can be used to further the study of supported lipid bilayers.

Of particular interest is the thickness of the supported bilayer, since this is an important parameter which can affect protein-membrane interactions. Given a known refractive index of the bilayer, the thickness can be extracted from the phase information. Using literature values for the refractive index of lipids we obtain thickness values which are in good agreement with those in the literature obtained using other techniques. We show that qDIC can detect differences in the thicknesses of supported bilayers of less than one nanometre, revealing that the hydrophilicity of the glass support causes significant reductions in the thickness of the supported bilayer in closest contact with it, and that this effect is modulated by the choice of fluorophore and the degree of coverage at the surface.

Another application of qDIC is in the study of the supported bilayer phase behaviour. We use qDIC to study the main phase transition during cooling from the solid-ordered to liquid-disordered phase, and measure thickness changes which take place during the transition. We also show that qDIC can be used to image liquid-liquid phase coexistence, with the liquid-ordered phase distinguished from the liquid-disordered by its greater optical thickness, and we measure the difference in thickness between these phases.

Acknowledgements

To begin with, I want to express my sincere gratitude to my lead supervisor, Prof. Wolfgang Langbein, for giving me the opportunity to work within his group, and for his invaluable support over the past four years. I have been continually amazed by his passion for science, his ability to solve problems, and his capacity to look at data in new ways to discover more information than I would have thought possible. The rigorous meetings we have had throughout my time here have challenged me to become a better scientist. I would also like to thank my second supervisor, Prof. Paola Borri, whose guidance and insightful contributions throughout have helped keep the work focussed and on track.

I would like to thank other current and former members of the Quantum Optoelectronics and Biophotonics Group. Firstly, I am indebted to both Dr. Iestyn Pope and Dr. Lukas Payne, for the training they have provided in the operation of the Ettore and Galileo microscope setups, and for being dependable sources of advice throughout my PhD. Their patient help saved many otherwise doomed measurement sessions.

I want also to acknowledge the work of Dr. George Zoriniants, in developing the first versions of the qDIC software that made all the work shown in this thesis possible, and Dr. Francesco Masia for his contributions to the qDIC energy minimisation. Likewise, I would like to recognise the work of Dr. Craig McPhee in laying the groundwork for the spin-coating protocol I have used throughout, and thank him for training me in the piranha etching and electroformation procedures. Additionally, I am thankful to Dr. Yisu Wang for his help in the wet lab, and in measuring the filter spectra. I would also like to thank my viva examiners, Prof. J. Emyr Macdonald and Prof. Stephen Evans for their feedback regarding the thesis.

Finally, I also want to give particular thanks to Alexander Nahmad-Rohen, with whom I collaborated on the interferometric reflectometry experiments, and Joseph Bleddyn Williams, who has been responsible for making countless improvements to the qDIC software, which have helped my work immensely. The long discussions we have had over the years have helped me overcome the difficulties I have faced, given me a better understanding of the science underpinning my work, and most importantly, have been fun.

This work was funded by the EPSRC, grant code EP/M507842/1.

Chapter 1

Background

This chapter will provide the theoretical background necessary to understand and contextualise the results that will be presented in later chapters. First, the functions and biological significance of the cell membrane will be discussed in Sec. 1.1, and a short history of the study of the cell membrane will be given. Next, in Sec. 1.2, the model membrane systems that are used to investigate the properties of the cell membrane will be introduced, and the different phase states that are observed in model membranes will be explained. Particular emphasis will be given to supported lipid bilayers, since these are the focus of the experimental chapters of this thesis.

Once the applications, advantages and limitations of supported lipid bilayers have been explained, several of the techniques commonly used in the literature for studying supported bilayers will be compared in Sec. 1.3. This leads to the introduction of the quantitative differential interference contrast technique in Sec. 1.4. This section will first discuss the theory behind normal DIC imaging, and then move on to explain how ordinary DIC images can be used to create reconstructed phase maps by Wiener filtering.

1.1 The Lipid Bilayer

One of the defining features of every living cell is the cell membrane, which forms the boundary between the cell and its exterior. The cell membrane is a roughly 5 nm thick, semi-permeable barrier which partitions the machinery of the cell from its surroundings, providing protection against the external environment and allowing the cell to optimise its internal conditions and maintain homoeostasis. The importance of cellular membranes is underscored by the fact that the most basic division of living organisms - into eukaryotes and prokaryotes - is based on the presence or absence of membranes internal to the cell. Eukaryotes use membranes for a wide assortment of different purposes, including subdividing the cell interior into additional subcompartments such as the nucleus, mitochondria or chloroplasts, acting as sites for protein synthesis or modification as in the endoplasmic reticulum or the Golgi apparatus, and for the transport of material into or out of the cell in enclosed membrane sacks called vesicles.

To effectively perform all these functions, there are a wide variety of different physical requirements that cell membranes must meet; they must be flexible enough that they can assume whatever shape is required by the cell; they must be strong enough that they do not rupture under the mechanical forces experienced during typical cell processes such as movement, mitosis and spreading; and they must be

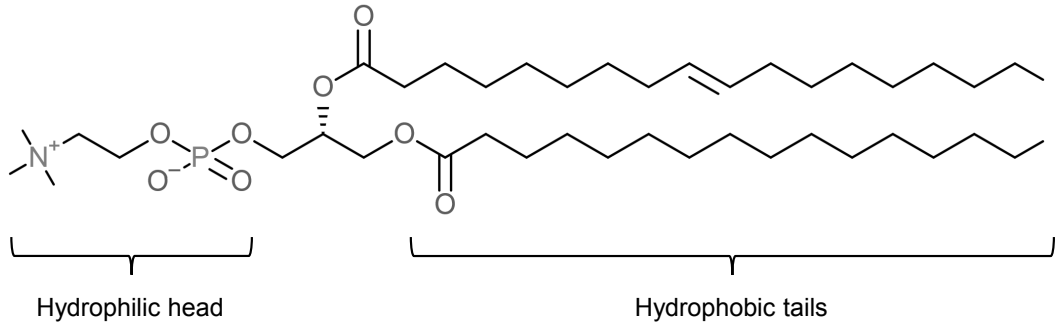

Figure 1.1: An example phospholipid molecule, POPC (see Appendix A for an explanation of lipid nomenclature), which has one saturated and one unsaturated hydrocarbon chain, making it typical of the phosphocholine molecules that are found in the cell membrane [6].

stable against the various different environmental conditions in which the cell might find itself. These physical requirements come in addition to a range of biochemical requirements, such as impermeability to ions and large molecules, and the ability to host proteins used for cell signalling or other processes.

The only biological material with all the required properties is the lipid bilayer. Lipid bilayers are formed from two antisymmetric sheets (referred to as 'leaflets') of special lipid molecules which are described as being *amphiphilic*. Amphiphilic molecules are those which have both hydrophilic groups (polar regions which can interact via hydrogen bonding or electrostatic interactions with other polar regions) and hydrophobic groups (non-polar regions which incur a strong entropic penalty when surrounded by polar molecules [1]). While there are many different amphiphilic lipids in the cell, the most common such lipids in the lipid bilayer are those made up of a large hydrophilic 'head' group attached to two hydrophobic long-chain fatty acid 'tail' groups. When in water, hydrophobic and hydrophilic interactions [1] drive such lipids to spontaneously self-assemble into a bilayer arrangement [2]. The hydrophilic headgroups orient themselves outwards, facing the aqueous environment, while the hydrophobic fatty acid tails are expelled from the aqueous medium, resulting in them being oriented facing towards each other in the bilayer interior.

These simple hydration interactions give the bilayer its vital biological properties. For instance, the energetic penalty associated with exposing the hydrophobic bilayer interior to water serves to prevent rupture and quickly reseals any small pores should they occur, helping to maintain cell integrity. Further, the lipid bilayer is permeable to small, uncharged molecules such as oxygen [3] and carbon dioxide [4], enabling these molecules to diffuse in and out of the cell unhindered, while the hydrophobic core also renders the lipid bilayer impermeable to ions [5] due to their charge and hydration shell in water. This is particularly important, since it not only helps the cell maintain the required internal conditions, but it also allows the flow of ions across cell membranes to be controlled, which is essential for many cellular processes such as neural signal propagation, muscle contraction and relaxation, and ATP synthesis.

Cell membranes contain a large variety of different lipid species, and the major constituents can be grouped into a few basic categories. The majority component of the lipid bilayer are phospholipids [6], to the extent that cell membranes are also referred to as phospholipid bilayers[1]. Phospholipids consist of a hydrophilic phos-

[1]Since there are a wide variety of other lipids which are important to cell membrane function,

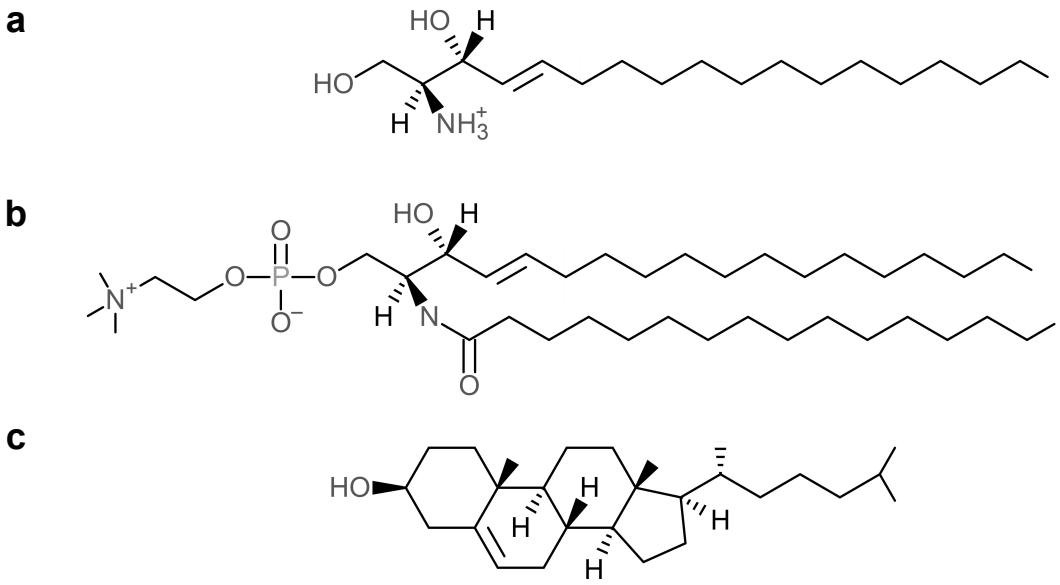

Figure 1.2: An illustration showing a) the chemical structure of a sphingosine molecule, to which fatty acids are attached at the amine group to form ceramides, and b) palmitoyl sphingomyelin. Sphingomyelins are similar to ceramides, but with a phosphocholine headgroup attached at the end hydroxyl group. Cholesterol, the most common sterol in mammalian cells is shown in c).

phate head attached to two fatty acid tails by a glycerol backbone. Several different phosphate heads exist (phosphocholine, phosphoethanolamine, and phosphoserine for example), each with different molecular sizes and charge distributions, leading to phospholipids with distinct physicochemical properties. These heads may be coupled with any two of a multitude of different possible fatty acid tails, giving rise to the huge number of different possible phospholipids which are present in nature. Analysis of human plasma revealed the presence of 160 separate phospholipid species [7]. An example of one possible phospholipid molecule is shown in Fig. 1.1.

Sphingolipids are another major component of cellular membranes, and are similar to phospholipids in that they have both a relatively large hydrophilic head and long hydrophobic hydrocarbon tails. The key difference is that rather than glycerol, sphingolipids have a sphingosine backbone (shown in Fig. 1.2a). Various different fatty acids may be attached to the amine group, though unlike phospholipids which tend to have one saturated and one unsaturated chain, in sphingolipids the amine group tends to be linked to long all-saturated chains, 16 to 32 carbons in length [6]. While they make up a smaller proportion of total membrane lipid content, biological sphingolipids are even more diverse than phospholipids, with human plasma containing over 200 different sphingolipids. Sterols, such as cholesterol shown in Fig. 1.2c, are another major component of cell membranes [6, 8]. Sterols differ considerably from sphingolipids and phospholipids, in that they are only weakly hydrophilic, with a singe hydroxy group being the only polar region in their otherwise hydrophobic structure.

Even though science now has a reasonable understanding of membrane composition and structure, much of this knowledge was not acquired until relatively recently. For example, while the existence of the cell has been known since 1665, the idea that

the more general term 'lipid bilayer' will be used here.

there existed a barrier at the periphery of animal cells was not universally accepted until the 1920's [9]. This was largely due to technological limitations; although the thick protein cell wall around plant cells and bacteria was easily visible using early microscopes [9], the technology to detect the nanometre scale cell membrane was not available until the 20^{th} century. Even after experimental evidence that the cell membrane was a lipid bilayer was obtained in 1925 by Gorter and Grendel (when they observed that the area of cell membrane lipids spread over an air-water interface was double the surface area of the original cells [10]), doubts persisted, and the lipid bilayer has only been fully accepted as the fundamental unit of the cell membrane since the late 1960's [11].

The full significance of lipid bilayers was not appreciated for some time after this, as historically membranes were viewed as inert structural components of the cell, which acted simply as barriers, or as scaffolds for the proteins which were responsible for the true biological functionality of the cell. Gradually, this view has been changing, and the full biological significance of the lipid bilayer appreciated more. It is now known that different cellular organelles have different, precisely controlled lipid compositions [5, 6], suggesting that the specific lipid composition of organelle membranes is important to their function. Examples of membrane lipids with specific biological functions include certain membrane phospholipids with the phosphatidylinositol headgroup which are known to regulate the dynamics of the actin cytoskeleton [12], and ceramides which have been shown to have roles in signalling pathways relating to cell death and autophagy [13]. In addition to these biological roles, it has been established that the physical and chemical properties of cellular membranes are themselves extremely important, and their disruption can have extremely damaging effects on cells [5].

The importance of the lipid membrane is underscored by an increasing awareness of the interplay between the lipid composition of the cell membrane (the so-called lipidome) and a wide array of different diseases [5, 7]. For example, in patients infected with the Ebola virus, numerous differences in the proportions of membrane lipids circulating in blood plasma were observed between patients that survived infection and patients that died [14]. Changes in the lipid composition of the cell membrane are associated with the progression of many cancers, as lipids modulate signalling events resulting in increased tumour proliferation and metastasis [15]. Additionally the lipidome of the prefrontal cortex of the brain changes with age, and is different in individuals with schizophrenia, autism and Down syndrome, with the latter two appearing similar to a young brain lipidome, while the former appears closer to an 'old age' lipidome [16], suggesting an important connection between the physical and chemical properties of cellular membranes and brain function. A complete understanding of these diseases therefore requires an understanding of the cell membrane.

In the context of the wide range of biological processes to which the physicochemical properties of the cell membrane are connected, the need to understand the properties of the lipid bilayer is clear. However, the study of lipid membranes is relatively recent, and views have changed considerably over time. One of the most important steps in understanding the properties of the cell membrane was the development of the Fluid-Mosaic Model (FMM), first presented by Singer and Nicholson in 1972 [17]. In this model, shown in Fig. 1.3, the membrane is formed from a fluid matrix, consisting primarily of a phospholipid bilayer in which membrane proteins may be on either side of the membrane, and span either the full width of the bi-

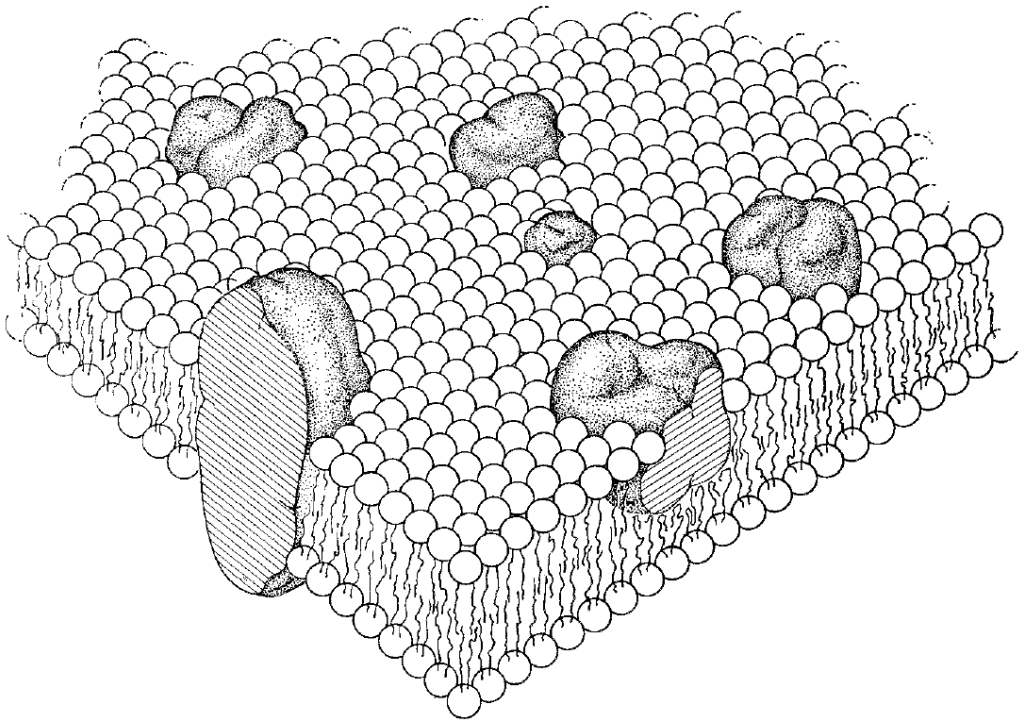

Figure 1.3: Figure showing the Fluid-Mosaic model of the cell membrane, as presented in 1972 by Singer and Nicholson [17].

layer (transmembrane proteins), or only part of the bilayer (peripheral membrane proteins). The bilayer itself behaves as a two-dimensional fluid, with membrane components free to diffuse within the plane of the membrane, and is laterally homogeneous, with all the different lipid components evenly distributed across the area of the cell membrane.

While the FMM remains highly influential, the limitations of this simplistic picture soon began to emerge. Within a decade after the FMM was published, new experimental evidence suggested that there were regions with distinct levels of molecular order within the cell membrane [18]. This led to the development of the theory that the membrane is laterally segregated into different domains with distinct properties, in sharp contrast to the FMM's image of the cell membrane as essentially homogeneous. In the cell membrane these domains are enriched in cholesterol and sphingolipids, as well as other lipids with saturated hydrocarbon chains, and are believed to be more rigidly ordered and solid-like than their surroundings. A popular analogy is that these solid-like regions are 'floating' on the 'sea' of surrounding fluid phase lipids, and for this reason they are therefore commonly referred to as lipid rafts[2].

These lipid rafts have attracted considerable attention, as they are thought to be a key mechanism by which the lipid bilayer can influence biological processes. Lipid rafts are believed to have a significant role in signalling across the cell membrane [19]; in the immune response for example, ordered domains form around activation sites of the T-cell receptor [23] during T-cell activation. Additionally, many proteins

[2]Strictly speaking, the original term 'lipid rafts' has been officially deprecated in favour of the term 'membrane rafts' [19]. However, since the term lipid rafts remains in widespread use in the literature [20, 21, 22], that is the term that shall be used here.

involved in cancer have been found to be associated with lipid rafts [21]. Beyond cell signalling, the phase boundaries between lipid rafts and the surrounding disordered phase have been implicated as sites of attack by viral proteins [22].

While considerable progress has been made regarding possible functions of lipid rafts, studying rafts still presents considerable challenges, as they are far too small to be imaged directly within the cell membrane. A typical cell membrane domain has a lateral size of approximately 10 - 200 nm [19, 24], and lifetimes often in the millisecond range [24]. Conventional optical microscopy, the oldest and most well established tool for the study of cellular biology, tends to have a maximum lateral resolution on the order of hundreds of nanometres, and requires many milliseconds for high quality images to be taken, which renders it incapable of imaging lipid domains [2]. Even with super-resolution techniques, the reliable measurement of cell membrane rafts is extremely challenging [25]. Other high-resolution techniques such as electron microscopy have the required resolution [26], but require cells to be fixed, which will cause changes to bilayer organisation [25].

Because of these difficulties, early experiments identified putative lipid raft components indirectly, based on their solubility in Triton X-100 detergent at 4°C [2, 27]. Membrane material is exposed to the detergent, and then centrifuged to separate detergent-soluble and detergent-insoluble fractions [2, 27]. Non-raft components of the membrane were believed to be soluble in non-ionic detergents, while the lipid and protein components of the rafts were insoluble due to the tight packing of the lipid acyl chains in rafts [28]. Eventually however, this was determined to be an unreliable means of identifying raft components [19], and the very existence of rafts came under question [27]. This episode underscores the importance of alternative, more direct methods of studying the biophysical properties of lipid rafts.

1.2 Model Membranes

Efforts to study biological membranes *in situ* are faced with considerable obstacles. In living cells, protein and lipid material is continually being trafficked to and from the membrane in response to external stimuli, making it difficult to disentangle the inherent biophysical properties of the lipid bilayer from the dynamic biological responses of the cell to its environment. Cell membranes can also have complex topographies that can frustrate the interpretation of images [25]. Additionally, the cell membrane is not an isolated system, it is coupled to the extracellular matrix [25] and an underlying protein meshwork called the cytoskeleton [12, 25] which can significantly influence the behaviour of lipids in the cell membrane [21], for example by promoting the formation of ordered regions of the cell membrane [23].

An alternative to studying biological membranes directly is to use model membrane systems that recreate many of their key properties. In the previous section we discussed the wide variety of different phospholipids that are present in cell membranes, along with different sphingolipids and sterols. In spite of this plethora of different membrane lipids found in each cell, such compositional diversity is not necessary for lipid bilayers to form. It is actually possible, and in many cases more informative, to create bilayers from as little as one appropriately chosen lipid species. This is done purely artificially, without needing to start from biological membranes at all, by exploiting the inherent self-assembly property of the amphiphilic lipids [2, 25].

These model membranes have long been a major asset in the effort to better

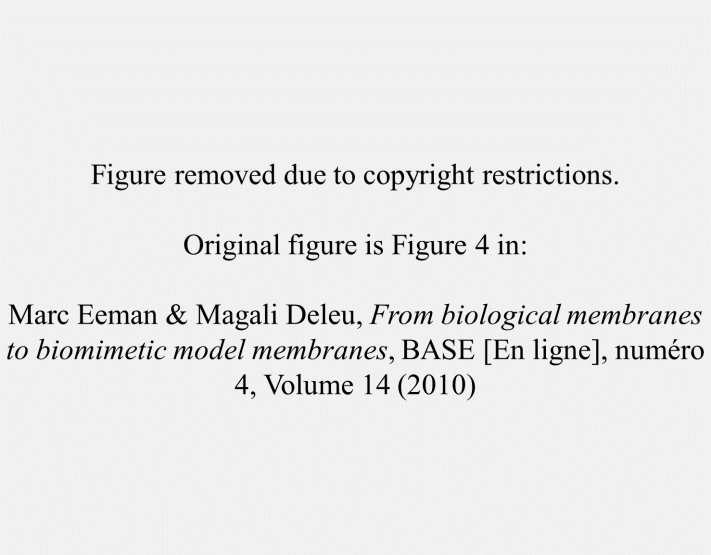

Figure 1.4: An illustration showing the arrangement of lipids in the L_d, S_o, and L_o phases, taken from Eeman and Deleu [2].

understand the properties of the cell membrane. Indeed, artificial lipid bilayers were first created before the structure of the cell membrane was fully understood, and ultimately helped inform the creation of the FMM [9]. Later, it was comparisons of the behaviour of cell membranes with model membranes that led to the development of the lipid raft hypothesis [18]. By carefully choosing the lipid composition, artificial membranes have been designed with well-defined properties, chosen to facilitate explorations into specific aspects of membrane behaviour.

For example, as previously mentioned, many particular lipid species have been identified as having specific biological roles, which depend on both the headgroup and the fatty acid chains [14]. Model membranes with controlled compositions provide excellent tools for exploring these roles, by enabling the functions of each of these lipids to be individually explored. This is done, for instance, in studies into how phosphoinositides help regulate actin binding proteins at the cell membrane [12], how sphingomyelin affects membrane associated aggregation of Alzheimer's disease proteins [29], or experiments into how specific sterols influence membrane bending rigidity [8].

In addition to helping further the understanding of the cell membrane, the versatility of artificial membranes means they are increasingly being touted for other potential uses. One example is for biosensors, which look for the presence of an analyte (such as a protein, toxin or sugar) by detecting at changes in membrane properties in response to the analyte interaction with the bilayer [30, 31]. Bilayers have also been used as sensors for non-biological material, such as for the measurement of the temperature profile around photothermally heated gold nanoparticles [32]. Synthetic membranes are also being investigated as possible vectors for drug delivery that are intrinsically biocompatible [30], with the additional benefit that control over the chemical composition of the membranes enables a wide array of different release mechanisms [33].

One area for which the development of model membrane systems has been a considerable advantage is in the understanding of membrane phase behaviour. In a lipid

bilayer formed from only a few lipid components, the phase behaviour is relatively straightforward. When only a single phospholipid species is present, the bilayer will undergo transitions between states with characteristic molecular arrangements at known temperatures. The states that lipid molecules can form depend on the properties of the headgroup and the tails, as well as the external conditions such as hydration, temperature and pressure; the phospholipid DOPE for example can form five distinct lipid phases under different conditions [34].

While different species of phospholipids can arrange themselves into wide variety of different configurations [33, 35], the most biologically relevant phospholipid phases are the lamellar phases, in which the lipids are arranged in the bilayer structure described in Sec. 1.1. At normal temperature and pressure, model lipid bilayers formed from a single lipid component tend to exist in one of two such phases, either a fluid phase (henceforth referred to as a 'liquid-disordered' or L_d phase), or a gel phase (also known as the 'solid-ordered' or S_o phase). Bilayers will transition from the S_o phase to the L_d phase when the temperature is raised above a species-specific transition temperature (T_m). The importance of these two states is such that the transition between the S_o phase and the L_d phase is often referred to as the *main* phase transition [36].

There are considerable structural differences between these two phases, as shown in Fig. 1.4. In the L_d phase there is no long-range order in the bilayer. The hydrocarbon chains are not aligned, and the lipids are free to move within the plane of the membrane. The phase state of the cell membrane as described in the Fluid Mosaic Model is a homogeneous L_d phase. In the S_o phase, the lipids in the bilayer are more closely packed (by up to 25% relative to the L_d phase [37]), with a corresponding increase in bilayer thickness. The individual lipids are arranged in a tight triangular lattice arrangement, with their hydrocarbon chains elongated and oriented in parallel with each other, so the S_o phase has long range order. This increase in packing density causes a corresponding reduction in the mobility of lipids in the S_o phase, with in-plane diffusion constants several orders of magnitude lower than in the L_d phase [2], as well as a reduction in bilayer elasticity [38].

The exact main phase transition temperature of a particular lipid is dependent on both the length and degree of unsaturation of the hydrocarbon tails. More unsaturated lipids have a lower phase transition temperature [37] because the carbon-carbon double bonds create 'kinks' in the hydrocarbon chain, making it harder to achieve the tight chain alignment characteristic of the S_o phase [5]. Conversely, longer chains are associated with increasing phase transition temperature [36]. Longer chains also lead to the creation of subtransitions within the S_o phase, in which the angle of the aligned S_o phase hydrocarbon chains changes (from about 35° [39]) to become parallel to the bilayer plane [36] when heated. Phospholipid headgroups can also effect transition temperature; in some cases, the main phase transition can be up to 20 °C apart for lipids with identical hydrocarbon chains [37].

Before the advent of the lipid raft hypothesis in the 1980's, the cell membrane was considered to be exclusively in the L_d phase, and this is still considered to be the natural state of most of the membrane. However, biological membranes are not composed exclusively from one phospholipid species like the models discussed above, and so their phase behaviour is somewhat more complex. A major component of the cell membrane is cholesterol, which comprises up to 50% of the total lipid fraction of the mammalian plasma membrane [2, 25]. Cholesterol, as shown in Fig. 1.2c, is structurally distinct from phospholipids, and is comprised of four hydrocarbon

rings with a short acyl chain on one end and a small hydrophilic hydroxyl group on the other. While cholesterol does not form bilayers on its own, it can insert into phospholipid bilayers, and can strongly modify their phase behaviour.

Much of the knowledge about the effect of cholesterol on membrane phase behaviour is derived from experiments on model systems. When in artificial bilayers containing lipids with saturated hydrocarbon chains, unsaturated chains and cholesterol, cholesterol preferentially interacts with the saturated chain lipids, and causes them to separate from the rest of the lipid mixture. Cholesterol induces a local ordering of the saturated hydrocarbon tails reminiscent of the S_o phase, even as the ability of lipids (and proteins) to diffuse laterally remains close to that of the L_d phase [27]. This intermediate phase is therefore called the 'liquid-ordered' (L_o) phase, and is shown in Fig. 1.4. Because the lipid rafts in biological membranes discussed in Sec. 1.1 are enriched in cholesterol and saturated chain lipids such as sphingomyelins, the L_o phase is generally considered to be the phase of the raft domains, though this is not yet universally accepted [19].

The strong interaction between cholesterol and saturated chain lipids is the result of cholesterol's small hydrophilic region. The large hydrophobic rings of cholesterol make it insoluble in water, but its amphiphilic nature allows it to insert into the membrane, with its hydrophilic region aligned with the heads of the surrounding lipids, and its hydrophobic rings positioned next to the hydrocarbon tails. However, with only the small hydroxyl group to shield it from the aqueous medium, it experiences a higher energetic penalty associated with contact with water than the surrounding phospholipids do. It is for this reason that cholesterol cannot form bilayer structures on its own [40].

To overcome this penalty, contact between cholesterol and the aqueous medium is minimised by a condensation of the neighbouring phospholipid or sphingolipid molecules around cholesterol, such that their larger hydrophilic heads reduce cholesterol's contact with water [40]. This picture is therefore sometimes described as the 'umbrella' model. Saturated chains make association with cholesterol easier because the straightness of the chains allows for a closer lipid packing than is possible with unsaturated chains (which have kinks along the length of the chain [40]); this is due to the fact that the chains themselves take up a smaller volume, analogous to the spacing of the trunks of trees in a stone pine forest compared to those in a mangrove forest.

Cholesterol has particularly strong interactions with sphingolipids (shown in Fig. 1.2) due to hydrogen bonding with the sphingosine backbone [41]. Therefore, in mixtures containing cholesterol, a sphingolipid and a phospholipid, the cholesterol will preferentially associate with the sphingolipids, even if the phospholipid has saturated chains [41]. This results in ordered domains enriched in cholesterol and sphingolipids, separate from the surrounding phospholipid rich L_d phase, and so is highly reminiscent of the lipid rafts observed in biological membranes. Model membranes therefore offer the opportunity for direct investigation of the properties of lipid rafts, and so have been an essential part of efforts to understand lipids rafts since the very beginning of the raft hypothesis. Indeed, the discovery of the L_o phase in model membranes actually predates the raft hypothesis, and was highly influential in its development [27].

In particular, the ability to precisely control bilayer composition in model membranes has proven to be an enormous benefit to the study of lipid rafts. As discussed earlier, the nanometre scale of the lipid rafts [19] and their extremely short lifetimes

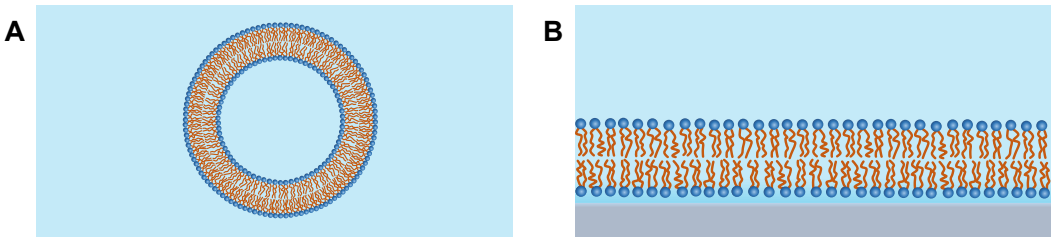

Figure 1.5: A cross section illustration showing the arrangement of lipids in A) a unilamellar vesicle, and B) a supported lipid bilayer. Illustrations are not to scale.

[25], make direct imaging of these rafts in cellular membranes almost impossible. In contrast, in model membranes, specific lipid compositions can be chosen which produce micron scale L_o domains which are stable over timescales of hours or longer, making them easily visible using traditional forms of microscopy, while at the same time having compositions extremely similar to those of biological rafts. Furthermore, control over bilayer composition also enables precise control over the physical and chemical properties of these domains, such as their thickness relative to the surrounding L_d phase [22, 42], allowing the physiologically important properties of rafts to be identified.

We have now described how the chemical composition of model membranes can be controlled to suit the needs of the experiment, and how the phase behaviour of model membranes is simplified compared to the case of the cellular membranes. However, we have not yet discussed the precise nature of the model membranes themselves. In fact, there are many different types of model membranes that have been developed over the last 60 years, all with particular advantages and disadvantages. One of the oldest model lipid bilayer systems is the black lipid membrane, developed in the early 1960's [26]. The black lipid membrane consists of a free standing bilayer formed over an aperture which may be millimetres in diameter [43]. Use of this model system has declined over time, largely due to fragility of membranes prepared in this way [43, 44], but also due to other limitations such as retention of solvents within the bilayer structure [26, 44].

Unilamellar vesicles are a common model system[3], shown in cross section in Fig. 1.5A. In unilamellar vesicles, the lipid bilayer is curved into a spherical arrangement, which can range in size from small (SUVs, below 100 nm in diameter), large (LUVs, 0.1 - 1 µm in diameter) and giant (GUVs, 1 - 100 µm in diameter) [30, 44]. The most widely used of these are the GUVs. They have the advantages of having a level of curvature comparable to biological cells, and have enclosed internal environments which may be distinct from the outside. High yields of vesicles can be formed easily from thin films of randomly arranged lipid molecules in aqueous solution by the application of an electric field [44, 45] (for LUVs and GUVs) or by either sonication [46] or extrusion [32] (for SUVs).

Probably the only other model system that shares the ubiquity of unilamellar vesicles is the supported lipid bilayer (SLB). In SLBs, the lipid bilayer is formed over a solid substrate, separated by a hydration layer around 1 -2 nm thick [20, 47], as shown in Fig. 1.5B. Typically SLBs are formed on glass [48, 49] or mica [37,

[3]Some have objected to the use of the term 'vesicles' to describe spherical artificial membranes, believing that this term should be reserved for biological structures only. However, the term vesicle is dominant in the literature over alternatives such as 'liposome' and so will be used here.

50], however a wide variety of different substrates can be used for preparing SLBs, including quartz [48, 49], thermally oxidised silicon wafers [48, 50, 51], titanium dioxide [51], and gold [52], among others [50]. The widespread adoption of SLBs is in large part due to the fact that they are straightforward to produce using an assortment of different techniques, large in size, and stable over long time scales (SLBs in the S_o phase are stable for several months after preparation).

While GUVs might appear to be the more biologically relevant case due to the fact that they are free floating and have curvature, SLBs do have a number of advantages over GUVs. Firstly, the fact that the membrane is adhered to the surface eliminates problems with lateral movement of membranes inherent to imaging GUVs in solution [45]. Furthermore, greater freedom over the surrounding aqueous solution is possible with SLBs, as SLBs can be easily prepared in media with high ionic strength that approximates that found around cells. In contrast, this is extremely difficult with GUVs due to the interference of ions with the electroformation technique generally used for GUV preparation [44]. When curvature is required, SLBs can even be formed on special curved substrates to provide curvature comparable to that of vesicles [53, 54].

Since their development over thirty years ago by Tamm and McConnell [48], SLBs have proven to be an immensely powerful tool for studying the biophysical properties of lipid membranes, and have been used for a wide range of different bilayer studies. To give just a few examples, SLBs formed on deformable substrates have been used to show the shape transformations bilayers undergo in response to mechanical stress [46], and patterned substrates have been used to explore how curvature influences domain formation [54]. Experiments on SLB stacks have been used to measure structural changes in the bilayer in different phases [39], while single SLBs showing liquid-liquid phase coexistence have been used to explore the interaction of viral proteins with L_o phase domains [22].

Over the years, multiple different techniques have been developed for the preparation of SLBs, but the most common is vesicle fusion. In this technique, a hydrophilic surface is immersed in a solution containing SUVs. The SUVs rupture following contact with the hydrophilic substrate, forming a large, continuous unilamellar film by one of two mechanisms. In the first, individual SUVs deform to maximise contact with the hydrophilic support, eventually causing them to rupture leaving small patches of lipids [49], which, due to the large number of individual rupture events, soon results in the entire surface being covered with a single supported bilayer. GUVs can also be used in this manner, though this is usually done with the intention of producing isolated bilayer patches rather than a continuous SLB. In the second mechanism, the vesicles adhere to the hydrophilic surface, but do not rupture until the entire surface is covered with SUVs, whereupon they fuse to form a unilamellar film [49].

The oldest techniques for SLB preparation are Langmuir-Blodgett and Langmuir-Schäfer deposition, both of which involve depositing individual monolayers onto a surface, one at a time, in order to form the bilayer [48]. While these are much more technically complex than vesicle fusion, these methods have the unique advantage of enabling the creation of asymmetric SLBs, where the lipid composition of the lower (support facing) leaflet and the upper (facing away from the support) leaflet are different. These SLB therefore more closely reflect the biological case where the cytoplasmic and extracellular faces of the bilayer have differing lipid compositions [2, 6].

A much more recent technique for forming supported bilayers is by spin coating [55], in which a solution of lipids is deposited on a rotating hydrophilic surface to spread the lipids evenly across the surface. The hydrophilic surface causes the lipids closest to the surface to orient with their polar headgroups pointing towards the support and their hydrophobic tails pointing away, forming a lipid monolayer. A layer of lipids above this then orient themselves with their tails facing the tails of the first monolayer, with additional monolayers then forming one on top of the other in an alternating orientation [56], with heads facing heads and tails facing tails to produce a stack of dry monolayers. Upon hydration of the surface in aqueous solution, any exposed hydrocarbon tails become energetically unfavourable, causing the stack of monolayers to rearrange into a stack of bilayers.

This method has the advantage of being fast, and enables the easy production of stacks of multiple lipid bilayers, with the number of bilayers in the stack being controllable simply by adjusting the concentration of the lipid solution. Although multilamellar bilayer stacks can be produced using unilamellar vesicle rupture techniques [54], this is a far more complex process than spin coating, and would not be practical for very large numbers of stacked bilayers. The ease with which multilamellar SLBs can be produced with spin coating represents another advantage of SLBs over vesicle-based model systems. While multilamellar vesicles can be produced [44], the number of bilayers within each vesicle is difficult to control and not always immediately clear by inspection [45]. Such multilamellar vesicles are generally produced as an unwanted by-product of the vesicle preparation.

A major difference between the SLBs produced by spin coating and those of other techniques is the number of defects (holes) in the bilayer. While Langmuir deposition and vesicle rupture tend to produce SLBs with very few defects, large holes of tens or even hundreds of microns are often present in spin coated bilayers [55]. Although some spin-coating protocols can form defect-free bilayers [56], such defects may in fact be an advantage in some contexts. For instance when obtaining topographic maps of the bilayer, defects allow a measurement of the separation between the upper surface of the bilayer and the glass support [20].

A complication in the use of SLBs is the strong influence of the preparation procedure on the properties of the bilayer. It is known for instance that the specific preparation technique can change the bilayer phase behaviour, as bilayers prepared one leaflet at a time as in the Langmuir-Blodgett or Langmuir-Schäfer methods can produce separate, non-overlapping ordered domains in the upper and lower leaflet, while SLBs formed using vesicle fusion techniques always form domains which are symmetric in both leaflets [47]. However, even within the same technique the bilayer can be sensitive to a wide array of different factors. For the case of SLBs formed by vesicle rupture for example, solution pH, ionic strength, temperature and the substrate material [56] all influence the outcome.

However, the main difference between SLBs and biological membranes is their proximity to the support. While once it was assumed that the hydration layer insulated the bilayer from the influence of the support, it is now accepted that interactions between the bilayer and the substrate can perturb bilayer properties in a number of ways. One of the clearest examples of a lipid-substrate interaction is the reduced lipid mobility in SLBs. The diffusion constant of lipid molecules in SLBs is reduced to between one third and one half of that of free standing bilayers by the support [49]. Additionally, not only can the diffusion constant in SLBs be different to free standing bilayers, but it can actually be different between the upper

and lower leaflets of the SLB. Due to its closer proximity to the substrate, the lower leaflet has a significantly reduced diffusion constant compared to the upper leaflet [50]. The influence of this lipid-substrate interaction can be clearly seen on patterned substrates, where individual lipid molecules can actually become confined in compartments which reflect the patterning of the support [51]. Such patterning can also affect the localisation of L_o domains within the SLB [49].

While SLBs continue to be a popular model system with which to study bilayer phase behaviour [22, 37], it is now known that this too can be strongly influenced by the support. For example, it is now understood that the support suppresses the main S_o to L_d phase transition temperature [47], and on mica substrates, the strength of the interaction is high enough to cause the phase behaviour of the two bilayer leaflets to become decoupled. In decoupled bilayers, the phase transition temperature of the two leaflets is separated by approximately 14 K [20], though this splitting is itself affected by the temperature at which the bilayer was formed. For SLBs prepared by vesicle rupture, the difference in transition temperature of the two leaflets was reduced when the formation temperature was increased [20]. This decoupling is a substrate dependent effect, and has not been observed on surfaces such as glass for example. It has been suggested that the atomically flat nature of mica enables greater interactions between the support and the bilayer [50], which leads to the observed effects.

As the extent to which this interaction can influence the bilayer has become better understood, some have argued that this limitation could in fact be interpreted as a benefit. It is argued that since biological membranes might be considered to be 'supported' on the cytoskeleton, the supported bilayer model system could in some respects be considered a more accurate representation of biological membranes [20]. However, while there are some similarities, such as how solid substrates [57] stabilise L_o domains reminiscent of the cytoskeleton [23], this assumes that the low density meshwork of the cytoskeleton is comparable in its influence on the bilayer to a solid sheet of glass, mica, or silicon dioxide, for instance, which seems unlikely. Still, a clear understanding of the interaction between bilayer and substrate may allow the development of substrates which more accurately mimic the influence of the cytoskeleton.

To overcome the surface interaction, various alternative SLB arrangements have been developed. One alternative is the polymer cushion, which separates the bilayer from the support by means of a layer of hydrophilic polymer [31, 52, 53]. These hydrophilic layers have been shown to eliminate the shift in phase transition temperature, resulting in transition temperatures identical to those of free floating vesicles [53]. However, these systems do have limitations. Although the difference in transition temperature is eliminated, the width of the phase transition is still three times greater than in free-floating membranes. Additionally, while their diffusion constants are the same in both leaflets, lipid diffusion may still be reduced by approximately 30% [53] (though the effect of the polymer cushion on diffusion is dependent on the choice of polymer [52]). These cushions also make preparation of SLBs more difficult, requiring the use of either Langmuir-Blodgett or Langmuir-Schäfer deposition [52].

Another alternative are tethered SLBs. Here, the lipids of the lower leaflet are covalently attached to the substrate via a linker molecule [52]. Gold substrates are common for example, and these use thiol linkers connected to the lipid headgroups [52] to spatially separate the bilayer from the support. These systems also come

with their own disadvantages. The covalent links between the lower leaflet of the bilayer and the substrate naturally lead to a reduction in the diffusion constant in the lower leaflet, which is dependent on the density of the linker molecules [52]. Also, the structure and functionality of these tethered bilayers strongly depend on both the density and chemical structure of the tether molecules [52], meaning that one unwanted influence may simply be traded for another.

So while there exist techniques to minimise the influence of the substrate in SLBs, the effects of the binding the bilayer to a support cannot be eliminated entirely, and, due to their numerous advantages, SLBs are likely to continue to be used as a model system for the foreseeable future. As such, it is essential that the substrate effects are properly understood to ensure the validity of the design and interpretation of experiments performed on SLBs.

1.3 Studying SLBs

As previously mentioned, because lipid bilayers are only around 3 to 6 nm thick, they are virtually invisible using a standard bright-field microscope. Early structural investigations on the cell membrane used electron microscopy [26], but this precludes any investigation into the dynamic behaviours of the bilayer, as both scanning and transmission electron microscopy require fixed samples. These limitations have spurred researchers over the last fifty years to use a wide assortment of different and complimentary techniques to better understand the biophysical properties of the lipid bilayer.

One of the most widely used approaches to studying small structures in biology is fluorescence microscopy. In fluorescence microscopy, structures that would ordinarily be invisible are tagged with a fluorescent probe. These probes absorb photons of a characteristic wavelength (usually in the visible range), resulting in the promotion of electrons within the probe molecules to an excited state [33]. Upon relaxation, these electrons then emit a photon of lower energy to return to the ground state [33]. The lower energy of these emitted photons means that they have a longer wavelength than the excitation. This difference in wavelength between the excitation and emitted photons is called the Stokes shift, and it allows the emitted light to be separated from the excitation light during imaging by means of an appropriate filter. Using multiple probes allows different structures to simultaneously imaged by exploiting the different excitation and emission wavelengths of each probe.

Fluorescence microscopy is widely used for the study of model membranes [58], as the ability to control bilayer composition allows the incorporation of fluorescent probe molecules directly into the bilayer structure. These fluorescent molecules are often tagged to either the head or tail groups of phospholipids similar to those which comprise the bulk of the membrane, or have acyl chains attached to give them a structure closer to that of the phospholipids between which the fluorophore must insert [58]. The inclusion of fluorescent molecules not only renders the approximately 5 nm thick lipid bilayer easily visible to conventional light microscopy, it also allows for measurement of diffusion within the membrane, and, through the use of environment sensitive fluorophores, can also measure bilayer hydration, viscosity and polarity [18, 21, 59].

An inherent advantage of fluorescence microscopy when applied to the study of lipid domains is that most fluorescently labelled molecules will preferentially segregate into one of the two membrane phases. This segregation is driven by the degree

to which the membrane probe disrupts the packing of the ordered phase [58]; fluorescent probes with unsaturated chains, or with their fluorophores close to the lipid headgroup thus tend to partition into the disordered phase, while probes that have small fluorophores or fluorophores at the end of the lipid acyl chains are more likely to prefer the ordered phase [58]. The tight packing of the ordered phase means that the majority of probes enrich in the L_d phase. This segregation then allows the two coexisting membrane phases to be distinguished by their different fluorescence signals [21, 60].

Fluorescence imaging has significant limitations however. The first and most obvious of which is photobleaching. There is an inherent limit to how long fluorophores can be excited before they no longer fluoresce. Fluorophores in their excited states may react with surrounding molecules [33], resulting in structural changes to the fluorophore which prevent it from fluorescing further [61]. While this effect can be utilised to gain information about the sample, for example in fluorescence recovery after photobleaching experiments to measure diffusion within the membrane, generally it simply limits the time over which samples can be usefully imaged.

Of most concern is the possibility that the fluorescent probes themselves might affect the behaviour of the bilayer. It has been shown for example that excited states of fluorescent probes can decay through non-radiative emission to triplet states, which react with surrounding molecular oxygen to form reactive oxygen species [33]. These reactive oxygen species can then react with the bilayer, causing peroxidation of membrane lipids [33], which alters the raft forming capacity of bilayers [57] and disrupts lipid packing due to the addition of hydrophilic hydroperoxide groups [33] to the normally hydrophobic hydrocarbon chains. Additionally, there is concern that the inclusion of the fluorescent labels themselves may disrupt lipid packing [62], or otherwise alter membrane behaviour [25, 32, 63]. These concerns motivate the search for alternatives to fluorescent labelling, and for a more complete understanding of how the inclusion of fluorescent labels can affect the bilayer.

The unique nature of SLBs as a model system fixed on a solid support makes them amenable to study with a wide assortment of surface sensitive techniques that would not be effective on free standing bilayers. This, coupled with the wide variety of different surfaces on which SLBs can be formed has led to their study using a plethora of different methodologies, each providing different information on the properties of SLBs.

One example is quartz crystal microbalance with dissipation monitoring (QCM-D), which measures changes in the acoustic vibrations of a quartz crystal in response to the adhesion of material to the crystal surface. Unlike fluorescence, which is used to image the features of bilayer samples, QCM-D collects data which is an average over the whole crystal surface, to obtain information on the mass and viscoelasticity of adhered material [63]. This is commonly used to study changes in the structure of the SLB. Wang et al. for instance used QCM-D to elucidate the mechanism by which antimicrobial peptides cause lysis of bacterial cell membranes by looking at changes in the resonant frequency of the quartz crystal oscillation and the decay rate of the crystal vibrations as the peptide begins to alter the membrane structure [63]. QCM-D can also be used to study the mechanism of SLB formation by vesicle rupture, as the transition from an adsorbed layer of SUVs to an SLB is detectable by changes in resonant frequency [63].

Another group of surface sensitive methods look at changes in the evanescent field near the substrate caused by the presence of the lipid bilayer, and, like QCM-D, take

data which is an average over the entire surface of the sensor. One example is surface plasmon resonance (SPR) microscopy, which is often used to study the interaction of biological material such as proteins with lipid bilayers [64]. Another example is optical waveguide lightmode spectroscopy (OWLS), in which a lipid bilayer is formed on top of a waveguide, and the bilayer properties are extracted by looking at how the intensity of light passing through the waveguide to a detector changes as a function of in-coupling angle [65]. This technique has been used to simultaneously measure changes in bilayer thickness and refractive index over the main gel-to-fluid phase transition of DMPC bilayers [65]. Plasmon waveguide resonance combines elements of both, using a thin metal layer with a waveguide for better signal-to-noise than SPR, and has similar applications [29, 66].

X-ray and neutron scattering are other techniques which have been used for the study of lipid bilayers. These techniques provide extremely fine detail on the structural arrangement of lipid molecules [35], giving the ensemble averaged relative positions of specific chemical groups within the bilayer structure with a precision well below one nanometre [67], and have been used to observe structural changes in lipid bilayers during phase transitions [34, 68]. They are, however, ensemble techniques, which require stacks of hundreds of bilayers (or large numbers of vesicles [69]), and so cannot be used for measuring the behaviour of a single supported lipid bilayer. This, coupled with the immense technical complexity and associated cost of these techniques, precludes their application to many types of experiment.

All these techniques are limited by the fact that the data they collect is an average over the whole sensor surface, and so provide no information on the lateral structure of the SLB. This means the data may be influenced by small defects in the bilayer, which can be below the resolution of fluorescence microscopy [70] (which is often used for checking the bilayers in these experiments [64]). The presence of such defects would therefore limit the accuracy of these experiments if the data was analysed assuming complete lipid coverage [64].

Another surface sensitive technique widely used for studying SLBs but which does have a high lateral resolution is atomic force microscopy (AFM), which scans a probe tip over a sample and measures the vertical displacement. This allows topographic maps of single lipid bilayers to be created with sub-nanometre axial resolution. AFM therefore makes different membrane domains readily visible, and so has also been used to study the bilayer during the phase transition [37]. Another application of AFM is force spectroscopy, which can provide mechanical information on the bilayer [37, 38, 71]. AFM suffers from the limitation that the SLB heights it measures also contain an unknown contribution from the hydration layer, and tip indentation into the sample may also systematically influence the height measurements [70].

One new possibility for studying SLBs is by quantitative phase imaging, a family of optical microscopy techniques which measure the phase shift of light passing through a sample by interferometry. Simply, light passing through an optically dense object such a lipid bilayer will be slowed relative to light propagating through air (which has a refractive index close to one), according to the equation $v = c/n$, where n is the refractive index of the medium, and v is the phase velocity. The result of this is that the light which passes through the sample acquires a phase shift relative to light that bypasses the sample. The magnitude of this phase shift is dependent on two parameters of the sample; its refractive index (the higher the refractive index, the greater the effect on the light traversing the object), and the

distance light travels through the sample (the greater the distance, the longer the object can influence the light). The product of these is called the optical thickness of the object. By interfering the light passing through the sample with a suitable reference beam, the phase shift of light can be detected.

Exploitation of the phase behaviour of photons for imaging low contrast samples is nothing new [72], with phase contrast microscopy and differential interference contrast (DIC) (also referred to as Nomarski interference contrast) microscopy having long since been used as tools by biologists for label-free imaging of samples that would be invisible or barely visible under normal bright-field microscopy [73]. The distinguishing feature of quantitative phase imaging is that while the aforementioned techniques use the phase information solely as means of generating contrast, quantitative phase methods seek to measure the precise phase shift of the light passing through the region of interest, theoretically allowing quantitative information about the structure of the sample to be obtained.

Several quantitative phase techniques have been applied to the study of lipid bilayers. One such technique is digital holographic microscopy (DHM). In DHM, laser light is split into two beams by a beam splitter; one beam, the sample beam, is passed through the microscope objective and interacts with sample, while the other, the reference beam, travels a distance with an optical path length which is matched to that travelled by the sample beam as closely as possible. The two beams recombine at a camera to generate an interference pattern from which the phase information about the sample can be obtained. A simple application of DHM has been to differentiate between L_o and L_d phases in SLBs [74], by exploiting differences in the thickness and refractive index of the two phases. In addition to studies on SLBs, by using the phase information to reconstruct the position of lipid bilayers in 3D space, DHM has also been used to observe shape transformations in GUVs in response to changes in the surrounding ionicity [75] and thus determine the bending rigidity of GUVs by using surface fluctuations [76].

Other forms of quantitative phase imaging have been used to study biological membranes *in situ*, for instance to measure membrane remodelling events in response to ATP [77] or membrane fluctuations associated with disease [78] in red blood cells, and to measure changes in cell membrane potential [79]. The ability to observe fluctuations in free-standing lipid bilayers allows measurements of membrane tension in both red blood cells and GUVs [80], providing a powerful alternative to conventional methods which rely on direct contact with the membrane.

In practise, the entanglement of thickness and refractive index often complicates the interpretation of phase data from biological samples. Extraction of one of these properties generally requires *a priori* knowledge of a system under investigation, which is frequently not possible. In an object such as a typical eukaryotic cell for instance, the extreme degree of variation in both refractive index and thickness over the cell makes separation of thickness and refractive index information impossible. This is why most quantitative phase studies of biological cells are carried out on erythrocytes [78, 80], which have a more optically consistent internal structure [80]. Despite these difficulties, the in-plane homogeneity of supported lipid bilayers makes them an ideal candidate for study with quantitative phase imaging. A bilayer with a given composition under set conditions will have both a fixed thickness and refractive index, and so, if the refractive index of the bilayer is known, accurate thickness information across the lipid bilayer can be obtained from phase measurements.

This is useful, because bilayer thickness is an important structural parameter.

The hydrophobic thickness of bilayers (the combined thickness of the hydrocarbon tails in the two apposing leaflets) can control the behaviour of membrane proteins, altering their structure to modulate their interactions with other proteins [13]. The size of the hydrophobic transmembrane domains of proteins may also regulate their segregation in lipid bilayers, as the proteins move to regions of the bilayer with hydrophobic thicknesses that best match their transmembrane domains. Significant mismatch between the transmembrane domains of proteins and their lipid surroundings can result in protein aggregation [21]. Also, experiments on SLBs have shown that local differences in bilayer thickness have been shown to act as binding sites for HIV proteins, with the strength of the interaction dependent on the magnitude of the thickness step [22].

1.4 Quantitative Differential Interference Contrast

A limiting factor to the widespread adoption of many quantitative phase techniques is their complexity. Often they require specialist knowledge and training to operate the setups (which are generally custom built), and analyse the data produced. One alternative however is to take an existing, widely used qualitative technique and modify it to obtain quantitative phase information about the sample. This is the basic idea behind quantitative differential interference contrast (qDIC).

Differential interference contrast microscopy (DIC) is a technique developed in the 1950's as a means of generating image contrast from optically transparent samples, primarily used in biological applications for imaging cells without staining [45, 73]. The arrangement of components in our DIC microscope (which is a typical, commercially available setup) is shown in Fig. 1.7. In this DIC setup, light from a monochromatic source is used. For standard DIC imaging, a polychromatic source would be used to minimise speckle; however, since qDIC requires knowledge of the illumination wavelength, we use a filter with a bandwidth of around 50 nm to produce light with a known peak wavelength, and a coherence length of a few microns.

The light is first passed through a combination of a quarter wave plate and a polariser called a de Sénarmont compensator. The angle between the fast axis of the quarter wave plate and the polariser axis[4], ψ, may be adjusted to precisely control the polarisation state of the light that exits the compensator. The polarisation state of the field leaving the de Sénarmont compensator is given by the Jones vector in Eq.(1.1), where $\boldsymbol{E}$ is the electric field vector and E_0 is the field amplitude. When ψ is 0, the light is linearly polarised, however for other angles the light has an elliptical polarisation.

$$\boldsymbol{E} = E_0 \frac{1}{\sqrt{2}} \begin{pmatrix} 1 \\ e^{\mathrm{i}2\psi} \end{pmatrix} \tag{1.1}$$

The polarised light then reaches a Wollaston prism, located in the back focal plane of the condenser. Wollaston prisms are comprised of two wedge shaped birefringent crystals in direct contact with one another, and arranged such that their optic axes are at an angle. The polarised light hits the prism at normal incidence,

[4]While we describe here the axis of the polariser to be aligned with the fast axis of the quarter-wave plate, the polariser axis could be aligned with the slow axis of the quarter-wave plate and the effect on the light exiting the de Sénarmont compensator would be the same.

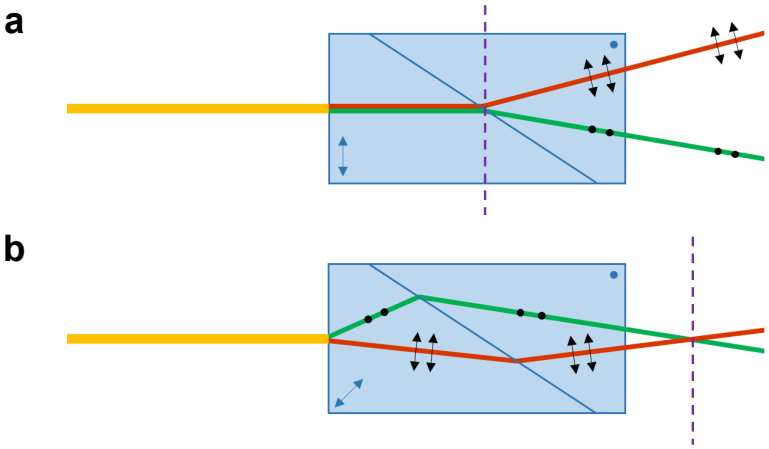

Figure 1.6: An illustration showing the splitting of the orthogonally polarised linear components of elliptically polarised light (yellow) caused by a) a Wollaston prism, and b) a Nomarski prism. The polarisation of the different components (green and red) are indicated by black arrows. The optic axes of the crystals are denoted by blue arrows. Dots represent arrows pointing out of the plane of the page. The purple dashed lines indicate the interference plane of the two polarisations.

and the beam is split into ordinary and extraordinary rays according to their alignment with the optic axis of the crystal. The ordinary and extraordinary beams propagate in parallel through the crystal, until they reach the interface between the two crystals. Because the boundary between the two crystals is not normal to the propagation direction, the two beams are refracted when they hit the interface, as the ordinary ray becomes the extraordinary ray, and vice versa. This ultimately results in the elliptically polarised light entering the prism being split into two spatially separate diverging beams with orthogonal linear polarisations, as shown in Fig. 1.6a.

In some DIC configurations, a Nomarski prism is used in the condenser. A Nomarski prism is a form of Wollaston prism in which the optic axis of the first crystal is at an oblique angle to the propagation direction. Unlike a Wollaston prism where the ordinary and extraordinary components of the light travel in parallel through the first crystal, in a Nomarski prism the two beams diverge immediately upon entering the prism due to the different direction of the group velocity of the extraordinary ray compared to the ordinary ray. At the boundary between the two crystals, the beams are refracted towards each other by the same mechanism as in the Wollaston prism, resulting in their convergence to a point outside the prism, the position of which can be controlled. Because the interference plane is outside the prism, Nomarski prisms can be used when inserting a Wollaston prism into the back focal plane of the objective or condenser is impractical.

The two beams exiting the prism are focussed onto the sample by the condenser lens. They travel through the sample in parallel, separated at the focal plane by a small distance $\boldsymbol{s}$ called the shear, which is typically similar to or slightly below the lateral resolution of the system [73]. Each beam acquires a phase shift equal to the optical thickness ϕ of that particular part of the sample. The two beams imaged at a position $\boldsymbol{r}$ on the sample thus have a relative phase difference, $\Delta(\boldsymbol{r})$, between

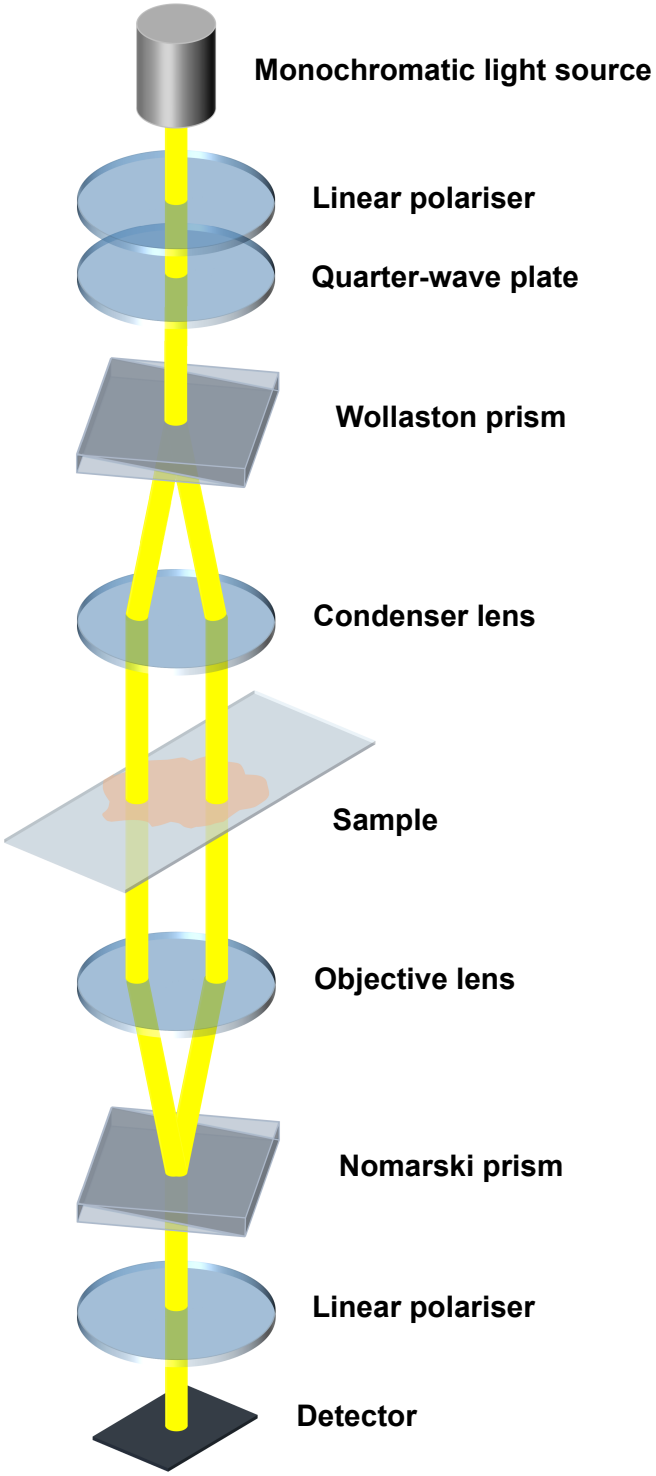

Figure 1.7: Simplified illustration of the arrangement of components in a DIC microscope in de Sénarmont configuration.

them given by Eq.(1.2).

$$\Delta(\boldsymbol{r}) = \phi\left(\boldsymbol{r} + \frac{\boldsymbol{s}}{2}\right) - \phi\left(\boldsymbol{r} - \frac{\boldsymbol{s}}{2}\right) \tag{1.2}$$

Once they have passed through the sample, the two beams then reach the objective lens, which collimates the beams before they reach a Nomarski prism (the back focal plane of the objective in our setup is inside the lens system and so a Wollaston prism cannot be used here) where the two beams are recombined. Any change in the relative phase between the two beams results in a change of the polarisation state of the light compared to when it first left the de Sénarmont compensator. Finally the light is passed through a second polariser (referred to as the analyser) which is aligned orthogonal to the fast axis of the quarter-wave plate, before being sent either to the eyepiece, or a camera.

The resultant output intensity I_{DIC} at each point $\boldsymbol{r}$ on the sample is given by Eq.(1.3). The angle ψ results in an offset in the intensity such that the intensity is non-zero even when there is no structure in the image. The result of this is that the image intensity becomes brighter when $\Delta(\boldsymbol{r})$ is positive and lower when $\Delta(\boldsymbol{r})$ is negative, and so information on the direction of the phase gradient is captured by the DIC image.

$$I_{\mathrm{DIC}}(\boldsymbol{r}, \psi) = \frac{I_{\mathrm{ex}}}{2}[1 - \cos(2\psi - \Delta(\boldsymbol{r}))] \tag{1.3}$$

The angle ψ has to be set to optimise image contrast and detail for a specific sample. If ψ is set very large, for instance to 45°, the variation in the image contrast I_{DIC} with $\Delta(\boldsymbol{r})$ is very low for small phase gradients. Such small variations in the measured intensity might be obscured by the shot noise of the camera, resulting in loss of fine image detail. Therefore in order to obtain the clearest DIC images, 2ψ should be set slightly larger than the strongest phase difference, $\Delta(\boldsymbol{r})$, in the sample so that contrast is maximised. Given that supported lipid bilayers are thin and would thus provide weak phase gradients, optimal DIC imaging of SLBs requires ψ to be set to small angles.

A DIC image with intensity I_{DIC} does not itself provide quantitative phase information about the sample, as it contains the unknown term I_{ex}. However, as the image contrast in DIC is dependent on the optical thickness difference Δ at each point on the sample, a DIC image can be thought of as being akin to the derivative of the original phase profile of the sample, taken along the shear direction $\boldsymbol{s}$. It is this property that many have tried to exploit to reconstruct the sample phase profile $\phi(\boldsymbol{r})$ and thus obtain quantitative sample information from ordinary DIC images. The arrival of digital image processing has led to the development of multiple approaches for the recovery of this phase information from DIC images.

Orientation independent DIC works by taking two DIC images, with the sample rotated to 0° and 90° by means of a rotatable stage [81], which is equivalent to taking images with orthogonal shear vectors. The DIC imaging process is modelled as a convolution of ϕ with the DIC point spread function (PSF), and then, using a gradient descent method, a single reconstructed phase profile is produced from the two independent DIC images [81]. Phase shifted DIC (PS-DIC) also uses a pair of images taken at orthogonal shear directions, with each image generated from individual acquisitions at four different phase angles (ψ) in 90° intervals from 0° to 270° [82]. The images at both shear directions are combined to create a complex image, which is inverse filtered in the Fourier domain to produce a reconstructed quantitative phase map [82].

Other techniques for obtaining quantitative phase information from DIC images abandon the traditional DIC setup altogether. This has been done for instance by using a structured aperture with four holes (one pair separated in the x-direction and another in the y-direction) to produce an interference pattern which contains quantitative information about the phase gradient in both the x and y directions [83]. This technique also relies on moving the sample, in this case raster scanning it such that light from all points in the field of view pass through the aperture [83], and so loses some of the speed of normal DIC imaging.

Another approach to reconstructing the phase maps is based around Wiener filtering, and this is the approach we use. Our quantitative DIC technique works to recover the phase profile by effectively integrating the DIC image in the Fourier domain. The Fourier transform converts a signal into the sum of an infinite series of sinusoidal waveforms, and when applied to an image, produces a representation of that image where the spatial frequencies contained within the original image can be seen directly, as specific points in what is referred to as the Fourier domain. Fourier domain integration is superior to standard numerical methods of integration such as Simpson's rule and the trapezium rule in terms of frequency response and provides a close fit to the original function [84].

To understand how the Wiener filter is used to recover the phase information, first let us consider the DIC imaging process. Ignoring the effect of the point spread function of the objective, the phase gradient in a DIC image can be described as a convolution ($*$) between the phase profile of the sample, $\phi(\boldsymbol{r})$, with two Dirac delta functions, separated by the shear vector, $\boldsymbol{s}$, as shown in Eq.(1.4).

$$\Delta = \left[\delta_{\boldsymbol{r}}\left(\boldsymbol{r} + \frac{\boldsymbol{s}}{2}\right) - \delta_{\boldsymbol{r}}\left(\boldsymbol{r} - \frac{\boldsymbol{s}}{2}\right)\right] * \phi(\boldsymbol{r}) \tag{1.4}$$

We then take the Fourier transform, $\mathcal{F}$, of Eq.(1.4), as shown in Eq.(1.5).

$$\mathcal{F}(\Delta) = \int_{-\infty}^{\infty}\left[\delta_{\boldsymbol{r}}\left(\boldsymbol{r} + \frac{\boldsymbol{s}}{2}\right) - \delta_{\boldsymbol{r}}\left(\boldsymbol{r} - \frac{\boldsymbol{s}}{2}\right)\right] e^{-2\pi \mathrm{i}\boldsymbol{r}\boldsymbol{\nu}} d\boldsymbol{r} \cdot \mathcal{F}(\phi) \tag{1.5}$$

In the Fourier domain, convolutions become multiplications, and due to the linearity of the Fourier transform, the Fourier transform of the sum of the two Dirac delta functions is just the sum of the delta function Fourier transforms. The Fourier transform of a Dirac delta function is given in Eq.(1.6), where $\boldsymbol{\nu}$ is the spatial frequency.

$$\mathcal{F}(\delta(x + a)) = e^{2\mathrm{i}\pi\boldsymbol{\nu}_{\boldsymbol{x}} a} \tag{1.6}$$

This means that the Fourier transform of Eq.(1.4) can be written as shown in Eq.(1.7).

$$\mathcal{F}(\Delta) = [e^{\mathrm{i}\pi\boldsymbol{\nu}\boldsymbol{s}} - e^{-\mathrm{i}\pi\boldsymbol{\nu}\boldsymbol{s}}]\mathcal{F}(\phi) \tag{1.7}$$

By substituting the spatial frequency, $\boldsymbol{\nu}$, with the wave vector $\boldsymbol{k} = 2\pi\boldsymbol{\nu}$, we can express the original DIC transform (the differentiation) of the sample phase map in the Fourier domain as shown in Eq.(1.8), with the Fourier multiplier ξ given by Eq.(1.9).

$$\mathcal{F}(\Delta) = \xi\mathcal{F}(\phi) \tag{1.8}$$

$$\xi = 2\mathrm{i}\sin\left(\frac{\boldsymbol{s}\cdot\boldsymbol{k}}{2}\right) \tag{1.9}$$

The most straightforward way to reverse the DIC process then would be to divide $\mathcal{F}(\Delta)$ by ξ. However, this would result in division by zero when $\boldsymbol{s}\cdot\boldsymbol{k}$ equals an integer multiple of π. Additionally, the intensity of the image captured by the camera is not just I_{DIC}; because of the practical limitations of the microscope system, there is always a noise component added to the image, which makes it impossible to perfectly recover ϕ by dividing $\mathcal{F}(\Delta)$ by ξ due to the amplification of noise this would cause close to the zero points of ξ.

To overcome these limitations the inverse transform (the integration) is instead carried out using Wiener deconvolution. Wiener deconvolution is an approach for image reconstruction developed in the late 1940's by Norbert Wiener which minimises the mean square error between the original image and its reconstruction [85]. It does this by incorporating a signal-to-noise ratio (SNR) term, κ, into the inverse multiplier, which limits the enhancement of image noise in the reconstruction. For our phase reconstructions, the Wiener filter, W, has the form given in Eq.(1.10).

$$W = \frac{1}{\xi + (\kappa\xi^*)^{-1}} \tag{1.10}$$

This is then used to recover the Fourier transform of the phase as shown in Eq.(1.11), which can then be inverse Fourier transformed to show the reconstructed quantitative phase map of the sample.

$$\mathcal{F}(\phi) = W\mathcal{F}(\Delta) \tag{1.11}$$

The effect of Eq.(1.11) on $\mathcal{F}(\Delta)$ can be seen in Fig. 1.8. A simulated circular phase object, with an optical thickness comparable to a lipid bilayer, is shown in Fig. 1.8a, and Fig. 1.8b shows the same object in the Fourier domain. The corresponding phase gradient Δ, is shown in Fig. 1.8c, with the shear direction oriented from the bottom right to top left of the image. The fast Fourier transform of the Δ image is shown in Fig. 1.8d. In this representation, it can clearly be seen that those spatial frequencies perpendicular to the shear direction are weakened in the Δ image relative to the original phase image. The Wiener filter amplifies these weakened frequencies, resulting in a reconstructed phase image shown in Fig. 1.8e, which closely resembles the original. Comparing the images in the Fourier domain, it can clearly be seen how the weaker frequencies have largely been restored.

The shape of the Wiener filter itself in the Fourier domain is shown in Fig. 1.8g and Fig. 1.8h. Varying κ changes the shape and intensity of the 'stripe' controlling the amplification of the spatial frequencies. In Fig. 1.8g, showing W when $\kappa = 20$, the peak amplification is low (the maximum amplification is $\sqrt{\kappa}/2 = 2.2$) and the stripe itself is very broad, so the frequency enhancement is weak, and many of the lowest spatial frequencies are not boosted at all. In contrast, for $\kappa = 100$, shown in Fig. 1.8h, the peak amplification is more than doubled, to a factor of 5, and the central black stripe is much thinner, resulting in a much stronger enhancement of the lower spatial frequencies. For $\kappa = 4\times10^5$, as used in the reconstruction shown in Fig. 1.8e, the peak amplification is 316.2, roughly two orders of magnitude higher, and the central black stripe is so thin it cannot be resolved in Fig. 1.8f.

While it is possible to use different values of κ for each spatial frequency (determined by the estimated SNR at each frequency, which depends on the objects

being imaged), in our Wiener filter, κ is a constant. In our qDIC measurements, the objective is to obtain measurements of the thickness of SLBs using phase steps over the bilayer edge (described in more detail in Sec. 3.1). To this end, the optimal value of κ for measuring the step heights must be determined by systematic investigation of the effect of the SNR on the reconstructed image. The setting of the SNR is a compromise between image artefacts in the form of lines parallel to the shear direction that arise when κ is set too high (these can be seen in Fig. 1.8e), and the loss of low frequency information that occurs when κ is set too low. These artefacts, and the tuning of the SNR parameter, are discussed in more detail in Sec. 3.2.

Using Wiener deconvolution requires the phase gradient, $\Delta(\boldsymbol{r})$. Ideally, the variation in I_{DIC} as a function of $\boldsymbol{r}$ would come solely from $\Delta(\boldsymbol{r})$. However, other factors influence the measured intensity. For example, the illumination intensity I_{ex} may not be uniform across the field of view, and there may be spatial variations in the optical system and at the detector, all of which would appear in the reconstructed phase image. In order to compensate for these factors, a DIC contrast image of the sample is produced. This is done by taking the intensity measurement twice, once with the polariser at $+\psi$ and then again with the angle at $-\psi$. The difference between the two intensities are then divided by their sum, as given in Eq.(1.12). This compensates for background inhomogeneity and the extinction of the sample which might affect the recovery of an accurate value of $\Delta(\boldsymbol{r})$.

$$I_{\mathrm{C}}(\boldsymbol{r}) = \frac{I_{+}(\boldsymbol{r}) - I_{-}(\boldsymbol{r})}{I_{+}(\boldsymbol{r}) + I_{-}(\boldsymbol{r})} \tag{1.12}$$

This can be rewritten in terms of the angle ψ and the phase difference Δ;

$$I_{\mathrm{C}}(\boldsymbol{r}) = \frac{\sin(2\psi)\sin(\Delta)}{1 - \cos(2\psi)\cos(\Delta)} \tag{1.13}$$

This is then rearranged to obtain an exact formula for Δ in terms of the measured contrast image, and the known phase offset, given in Eq.(1.14)[5]. Several techniques for quantitative analysis of DIC images based on Wiener deconvolution have been developed [86, 87], and our technique builds on these in a number of ways. Previous approaches to Wiener deconvolution based phase reconstruction have used a linear approximation of the relationship between the measured intensity and $\Delta(\boldsymbol{r})$ [45]. In contrast, we analytically invert Eq.(1.13) to give a precise value for $\Delta(\boldsymbol{r})$ using the DIC contrast image I_{C}.

$$\sin(\Delta) = -I_{\mathrm{C}} \frac{1 - \cos(2\psi)\sqrt{1 - I_{\mathrm{C}}^2}}{\sin(2\psi)} \frac{1}{1 + I_{\mathrm{C}}^2 \cot^2(2\psi)} \tag{1.14}$$

In addition to this improvement in accuracy, our qDIC technique includes a number of features to reduce artefacts caused by the integration. The fast Fourier transform assumes that the image is periodic in the x and y directions, which is not true for DIC images. This produces discontinuities at the edges of the images which produce artefactual phase gradients around the edge of the phase reconstruction if not addressed. These discontinuities can be minimised to a large extent by fitting a second-order polynomial to the I_{C} image, which is used to subtract background

[5] The images produced from this equation which have the quantitative $\Delta(\boldsymbol{r})$ values will be referred to in text as qDIC contrast images; these should not be confused with the standard DIC contrast images, I_{C}.

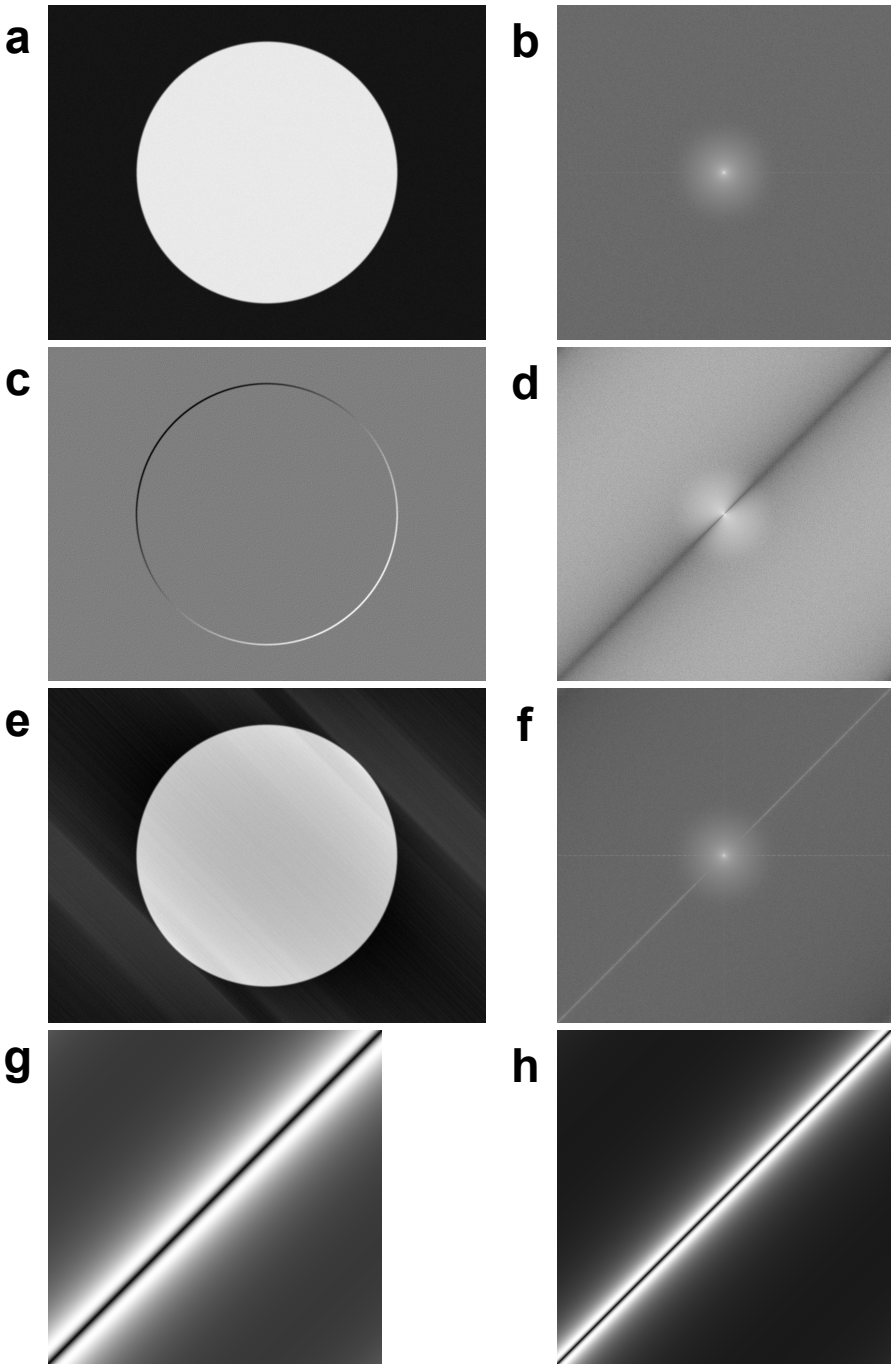

Figure 1.8: A simulated 1344×1024 image of a disc shaped phase object (with added Gaussian noise of amplitude 62.5 µrad) is shown a) in real space (m = -0.5 mrad to M = 5.5 mrad) and b) in the Fourier domain (m = -19.9 to M = 16.2). The corresponding Δ image (the shear direction runs from the bottom right of the image to the top left) is shown c) in real space (m = -1×10^{-3} to M = 1×10^{-3}) and d) in the Fourier domain (m = -21.4 to M = 4.0). The reconstruction of the original phase image using κ = 4×10^{5} is shown e) in real space (m = -2.2 mrad to M = 3.8 mrad) and f) in the Fourier domain (m = -21.0 to M = 18.0). The Fourier domain images b), d) and f) are shown as the logarithm of the power spectrum. The Wiener filter is shown in the Fourier domain for g) κ = 20 (m = 0 to M = 2.3), and h) κ = 100 (m = 0 to M = 5) on a linear scale.

gradients [88]. This effectively suppresses most discontinuities at the edges and so eliminates most of the background phase gradients in the reconstruction.

The assumption of periodicity causes other issues however, as high-contrast objects near the edges of the DIC image can affect the reconstruction of the phase on the opposite edge. To overcome this, apodisation is used. The image is padded with eight equally sized images (forming a 3×3 grid with the real image at the centre) before application of the Fourier transform. The intensity values moving away from the edge of the original image are blurred using a Gaussian function with a width proportional to the distance from the edge of the original image. The intensity values are then taken to zero at the edges of the padded images using a $\cos^2$ function, resulting in a larger image where the intensity and the first derivative at the edges are continuous [88]. After Wiener deconvolution, the padding area is removed, restoring the original field of view in the final phase reconstruction. Most of the remaining artefacts that are incurred due to the image edges are restricted to these padded regions, and so cropped out when the original field of view is restored.

A further approach which can be applied to improve the qDIC phase reconstructions uses a global minimisation method to reduce the line artefacts which run along the shear direction (these can be seen in Fig. 1.8e), which are caused by missing information perpendicular to the shear vector. This minimisation varies the qDIC phase image to minimise not purely the deviation between measured and simulated DIC contrast, but the sum of this deviation, and the magnitude of the gradient, elevated to a power α and multiplied with a weight λ. For powers between zero and one, small gradients carry a higher penalty, resulting in qDIC phase images with flat regions connected by steps, consistent with the structure of an SLB.

This method, inspired by Koos et al. [89], and described in detail in [88], is implemented in MATLAB R2015a. The power and the weight have to be chosen suitably to provide a small minimum step height while still flattening regions dominated by measurement noise. Due to initial concerns over the effect of this minimisation on the quantitative values of the bilayer phase steps, it was not used in the analysis, and minimised images are only shown here when the reconstruction artefacts would be particularly intrusive. A complete list of all images processed using this minimisation technique, as well as the parameters used in the minimisation, is given in Appendix D.

As a method of studying lipid bilayers, DIC has the advantages of being technically straightforward to implement and not requiring the use of chemically modified lipids as labels. In spite of this, DIC on its own has rarely been applied to the of study of lipid bilayers. While DIC has seen some use in observing 3D changes to lipid arrangements [35], it is generally restricted to acting as a substitute for fluorescence when fluorescence is incompatible with the setup [90]. The underlying reason for this is likely that the purely qualitative topographical map produced by the standard DIC process is harder to interpret than a fluorescence image, while at the same time doesn't provide any useful information about the bilayer that isn't already accessible using fluorescence.

This is not the case with qDIC however. Our qDIC technique has the benefit of enabling completely label-free quantitative imaging of lipid bilayers, allowing measurements of the bilayer optical thickness. It has already been applied to the study of lipid bilayers to accurately measure the lamellarity of GUVs in solution, however the high resolution of the phase maps makes it ideal for imaging SLBs. Using qDIC, it should be possible to visualise lipid domains, and (given a known refractive in-

dex) obtain measurements of bilayer thickness with a precision comparable with that obtained with AFM. Another advantage of qDIC is the fact that it is compatible with fluorescence, making it possible to take complimentary information about the sample by incorporating fluorophores, which do not affect the DIC signal.

Chapter 2

Materials & Methods

This chapter will detail the protocols used to take the data shown throughout this work. First, the procedures used when handling the lipids themselves will be described in Sec. 2.1, which will also cover the preparation of the lipid mixtures used for the spin coating process. In Sec. 2.2, the surface treatments applied to the glass substrates will be covered. This will focus mainly on the piranha etch procedure which is used for most samples, but will also cover alternative surface treatments. In the following section, Sec. 2.3, the spin-coating procedure will be explained, along with the handling of the lipid coated glass up to the point where the coverslip is sealed into an enclosed microscope slide. Quantification of the surface hydrophilicity (which we later find to be an important surface property) is described in Sec. 2.4. An alternative method for forming planar lipid supported bilayers by rupturing GUVs is covered in Sec. 2.5.

Subsequent sections will cover the procedures used for image acquisition. In Sec. 2.6, the camera settings used for the acquisition of DIC and fluorescence images will be described, along with the properties of the objectives and filters used. The temperature control system used during imaging will be described in Sec. 2.7 and an explanation of the different temperature readings taken will be given. Finally, a description of another quantitative phase imaging technique used briefly in this work, interferometric reflectometry, will be given in Sec. 2.8.

2.1 Storage and Handling of Lipid Solutions

The majority of the lipids used in sample preparation, namely 1,2-dioleoyl-*sn*-glycero-3-phosphocholine (DOPC), 1,2-dioleoyl-*sn*-glycero-3-phosphoethanolamine (DOPE), 1,2-dipentadecanoyl-*sn*-glycero-3-phosphocholine ($DC_{15}PC$), ovine wool cholesterol (Chol), chicken egg sphingomyelin (ESM), and 1-palmitoyl-2-(dipyrromethene boron difluoride)undecanoyl-*sn*-glycero-3-phosphocholine (TopFluorPC) were purchased in powdered form from Avanti Polar Lipids (Alabaster, US). The fluorescently labelled lipid ATTO488-DOPE was purchased in powdered form from ATTO-TEC (Siegen, Germany).

Lipid powders were dissolved in chloroform and stored at -20 °C. These solutions will be referred to throughout as the stock solutions. To protect lipids against peroxidation, these stock solutions were always handled in a nitrogen cabinet. Glass vials containing lipid solutions had caps with polytetrafluoroethylene (PTFE) linings to prevent the chloroform solvent leaching impurities out of the cap. The vials were sealed with Parafilm to prevent infiltration of oxygen into the vials during storage,

and in cases where the solution contained fluorescent labels, the vials were enclosed in aluminium foil to minimise bleaching of the fluorophore during storage and handling.

The use of these stock solutions for spin coating was impractical for a number of reasons. Firstly, to facilitate storage, the concentrations of these stock solutions (50 mg/ml for DOPC and $DC_{15}PC$, 10 mg/ml for Chol and ESM, and 1 mg/ml for the various fluorophores), was chosen far higher than needed for the spin coating process. Secondly, the SLBs being prepared were generally mixtures of different lipids, not formed from pure lipid like that contained within the stock solutions. Thirdly, different solvents were needed for different mixtures of lipids. As such, before sample preparation, particular lipid mixtures were produced from the stock solutions to suit the needs of the spin-coating process. Since these new lipid mixtures could be used for multiple experiments, this had the added benefit of minimising the use of the stock solutions, and thus reducing the contamination and oxidation of the lipid stocks during handling.

The lipid mixtures were prepared by depositing the appropriate volumes of stock solutions into a glass vial and then redissolving in a new solvent. To ensure complete removal of the original solvent, vials containing the lipid mixture were placed on a hotplate at 50 °C for 30 minutes. To prevent lipid peroxidation and further encourage evaporation of the original solvent, the lipid mixture is kept under nitrogen flow during this process[1]. The nitrogen flow is initially gentle to prevent splashing of the lipid solution, but is then increased once most of the solvent has dried.

After this, the vial is kept under vacuum for one hour to remove the last traces of the original solvent. The vacuum is created by connecting a Vacuubrand (Wertheim, Germany) MZ 2C vacuum pump, which has an ultimate vacuum of 0.7 kPa, to a desiccator for five minutes to establish a vacuum. If the lipid mixture contains fluorophore, the vial is wrapped in aluminium foil during drying on the hot plate, and is stored in the dark while under vacuum to prevent photobleaching of the fluorophore. After an hour under vacuum, a thin film of dried lipid is left at the bottom of the vial, which is then dissolved in the new solvent in a nitrogen cabinet, and then vortexed to ensure full dissolution of the lipid powder.

Mixtures containing lipids that form bilayers entirely in the L_d phase at room temperature, such as DOPC, were dissolved in a mixture of chloroform and acetonitrile at a volumetric ratio of 95:5. These solvents have been chosen as they provided the best results from the spin coating process (see Sec. 2.3). Chloroform is non-polar, so the small proportion of acetonitrile, a polar molecule, is added to improve the solubility of the polar headgroups. For mixtures containing lipids which form bilayers in the S_o phase at room temperature, such as $DC_{15}PC$ or ESM, 2-propanol, a solvent with both polar and non-polar groups, was used. The motivation for using these specific solvents is given in Appendix B.

For samples designed to observe L_o-L_d phase coexistence, a mixture of DOPC, ESM and Chol was used, with a molar ratio of 55/25/20 (DOPC/ESM/Chol). An explanation for the choice of this specific ratio is given in Appendix B. For fluorescence imaging, either ATTO488-DOPE or TopFluorPC was included in the lipid mixtures at a molar concentration of 0.1 % unless otherwise stated. For those samples exhibiting liquid-liquid phase coexistence, for the labelled samples the ratio of the different components was therefore 54.9/25.0/20.0/0.1 (DOPC/ESM/Chol/ATTO488-

[1]While the purity of the nitrogen is limited, and so may still contain some oxygen capable of oxidising the lipids, the purity of the nitrogen is at least 99.998% according to the manufacturer (BOC, Guildford, UK), and so the risk of oxidation is greatly reduced compared to being in air.

DOPE).

To prevent contamination of lipid solutions, the inside of the glass vials were cleaned before use by filling with chloroform and vortexing for several seconds. This was repeated five times. Glass syringes were washed through with at least ten successive washes with chloroform after use to remove any trace amounts of lipid solution left within the syringe and minimise any possibility of cross-contamination between different lipid solutions.

All solvents were HPLC grade purchased from Sigma-Aldrich (St. Louis, US) or Honeywell (Charlotte, US).

2.2 Cleaning of Glass Surfaces

For the sample preparation, $(24 \times 24)\,\mathrm{mm}^2$, thickness #1.5 Menzel Gläser (Braunschweig, Germany) glass coverslips were used as substrates. Coverslips straight from the box were often coated with small amounts of dust and debris, so to ensure the coverslips were clean, they were wiped with acetone soaked cleanroom wipes to remove any inorganic impurities. Each cleanroom wipe was only used for a few wipes, as excessive use of the same individual cleanroom wipe would lead to the deposition of small fibres on the glass. The removal of any remaining organic impurities on the glass was achieved by piranha etching unless otherwise stated.

The piranha etching process consisted of immersing a batch of coverslips in an 80 ml solution of ACS grade sulphuric acid and hydrogen peroxide (30 % in water) at a 3:1 volumetric ratio. The beaker containing the solution was placed in a water bath with a depth of approximately 2 cm, heated to 95 °C. The coverslips were left in the piranha solution for one hour. The coverslips were held in a PTFE rack and care was taken to ensure that the coverslips were not in contact with one another, so that the piranha solution had access to both faces of all the coverslips during entire etching process.

After etching, residual piranha solution was removed from the glass by washing in three successive baths of distilled water, and the coverslips were then dried under nitrogen flow. The piranha etch also serves to render the glass surface hydrophilic, which is a necessary condition for most SLB preparation methods. To ensure the surfaces were still hydrophilic when used, the glass coverslips were stored in nitrogen at 4 °C and used within two weeks of etching.

Issues with the effectiveness of the piranha etch were encountered stemming from the age of the H_2O_2. In several instances, the piranha etch produced only weakly hydrophilic surfaces. This was found to be due to the gradual decay of H_2O_2 into H_2O over time, effectively diluting the H_2O_2. This was monitored by observing the reaction of the sulphuric acid to the addition of H_2O_2. Addition of recently opened H_2O_2 to sulphuric acid resulted in a vigorous reaction, in which many bubbles were produced. In contrast, addition of older H_2O_2 would produce relatively few bubbles. This was used as a qualitative metric to determine whether the H_2O_2 stock needed replacing.

Another cleaning procedure used as an alternative to piranha etching involved immersing the coverslip in successive baths of different solvents. First, the coverslip would be sonicated in a 150 ml bath of toluene for 20 minutes. This would then be immediately followed by sonication in a 150 ml bath of acetone for 20 minutes. Next, the coverslips would then be transferred to a 150 ml bath of distilled water and placed in a microwave at full power until boiling (approximately 30 seconds).

The microwave power would then be reduced to 30 % and left for a further three minutes. Finally the coverslips would then be transferred to a bath of hydrogen peroxide (30 % in water) and sonicated for 20 minutes. The coverslips would be stored in baths of hydrogen peroxide at 4 °C until needed. While this process uses several different solvents, for simplicity it shall be referred to hereinafter as the H_2O_2 cleaning procedure, due the fact that the coverslips were stored in H_2O_2.

2.3 Preparation of Supported Lipid Bilayers

The majority of SLB samples were prepared by spin coating, using a procedure developed starting from the one by Mennicke and Salditt [55]. Coverslips were centred on the chuck of a Laurell WS-650-23 spin coater, and the coverslip surface wetted with a volume of lipid solution sufficient to fully wet the surface. For 2-propanol and chloroform:acetonitrile, 150 µl and 300 µl were needed respectively. The coverslips were then rotated about their centre axis at a speed of 3000 rpm for 30 s, preceded by a 6 s acceleration stage and followed by a 6 s deceleration stage. This resulted in the ejection of the excess lipid solution from the coverslip, leaving the surface apparently dry. In cases where a high lipid concentration was used, a lipid film was visible on the coverslip.

The concentration of the lipid solution could be adjusted to control the average lipid thickness on the surface. Generally, the aim was to produce a mostly unilamellar bilayer film with some empty regions and bilamellar patches. By a parameter dependent study, it was determined that a lipid concentration in the range from 0.8 - 1.0 mg/ml corresponded to an average thickness of a single bilayer as required. As such most DOPC samples were prepared from lipid concentrations of 0.8 mg/ml. While it might be expected that different solvents might have different relationships between concentration and coverage (because of differences in viscosity and volatility between solvents), in practise no such differences were observed, and so the same concentration range was generally used regardless of solvent. However, due to the $DC_{15}PC$ SLBs contracting during imaging above T_m (see Sec. 4.5), slightly higher concentrations of 1.2 mg/ml were used in some cases with this lipid.

Following spin coating of the lipid onto the glass surface, the samples were placed in a humidified nitrogen environment at 37 °C for one hour. This was to allow the bilayers to absorb some water from the environment before submerging them in aqueous medium. This reduces the hydration gradient acting over the bilayer during full hydration, and so prevents the bilayer from peeling away from the surface and results in better quality SLBs with fewer adhered vesicular structures. The pre-hydration process was carried out at temperatures above T_m for all the lipid mixtures used for consistency. The development of this process is described in more detail in Appendix B.

Following the pre-hydration step, the coverslips were sealed into an enclosed chamber using a glass slide (cleaned by wiping with acetone soaked cleanroom wipes before use), and a Grace Bio-Labs (Bend, US) SecureSeal imaging spacer. The chamber was filled with phosphate buffered saline (PBS) solution at 1× concentration from Gibco (Gaithersburg, US) unless otherwise stated to fully hydrate the bilayer. This was used due to the SLBs being more stable in PBS than distilled water; however in some cases distilled water was used to test the effect of the ionicity of the medium. It was found that the hydration medium often contained small air bubbles which were affecting the qDIC phase images, showing up as small white

speckles. In order to remove these air bubbles, 20 ml of the solution to be used as the medium was degassed in vacuum for five minutes before use. This was sufficient to effectively eliminate the presence of air bubbles in virtually all samples.

Bilayers in a single phase were generally imaged on the day of preparation. Pure S_o phase samples were occasionally prepared several days in advance of imaging to allow the quality of the samples to be checked ahead of extended measurements, and stored below the phase transition temperature at 4 °C until needed. These samples tended to have an irregular bilayer appearance immediately after preparation, which was rectified by heating above T_m, followed by gradual cooling below T_m as shown in Appendix B. Samples exhibiting L_o/L_d phase coexistence were left for 5 days at 4 °C for L_o domains to allow large domains to form.

2.4 Quantification of Surface Hydrophilicity

When preparing SLBs by spin coating, the strength of the hydrophilicity of the glass is evident from the volume of solution needed to fully wet the glass surface. Lower surface hydrophilicity results in smaller volumes of the non-polar chloroform:acetonitrile solvent mixtures needed to fully wet the coverslips, while larger volumes of the polar 2-propanol solutions are required. For our experiments however a more quantitative measure of surface hydrophilicity was needed. Surface hydrophilicity is typically measured using a contact angle goniometer, which photographs a water droplet of known volume from the side and measures the contact angle between the water droplet and the surface in the image. Smaller contact angles indicate a greater hydrophilicity.

Initial attempts to measure the contact angle by photographing the droplet from the side using the available camera proved impractical, due to difficulties in focussing, and resolving the very small contact angle of the droplet. An alternative method of measuring the contact angle was therefore necessary. Quantitative phase imaging has itself been used as a method of determining the contact angle by placing microdroplets on a glass slide and measuring the phase shift of light at the edges of the droplets [91]. However, such small droplets show changes in their contact angle as they quickly evaporate, so this might lead to inconsistent results. Larger droplets evaporate more gradually, but cannot be measured in this way.

Ultimately, it was decided to measure the contact angle indirectly using the spherical section assumption described by Chatterjee [92]. This models a water droplet as a section of a larger sphere, and so for a droplet of known volume, V, the contact angle, θ, can be estimated from Eq.(2.1) [92] by measuring the radius, r, of the droplet. A plot of contact angles estimated for a given radius is shown in Fig. 2.1.

$$\frac{3V}{\pi r^3} = \frac{2 - 3\cos\theta + \cos^3\theta}{\sin^3\theta} \tag{2.1}$$

This assumption is only valid when deformations due to gravity are negligible, and so can only be used with droplets with small volumes and contact angles well below 90°. Therefore, a volume of only 2 µl of distilled water was used for measuring the radius. In order to obtain an accurate measurement of the droplet radius, a test pattern was used consisting of a series of concentric rings of known diameter. This is shown in Fig. 2.2. When photographed directly from above, this test pattern enabled a calibration of the image by measuring the known diameter of the central

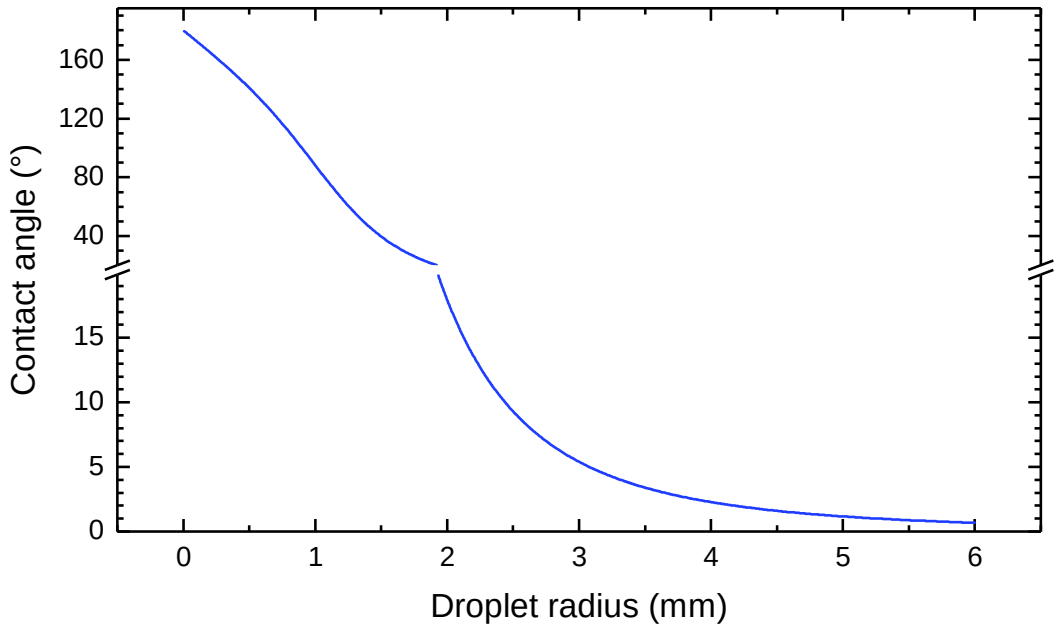

Figure 2.1: Plot showing the relationship between the droplet radius in millimetres and the corresponding contact angle in degrees according to Eq.(2.1).

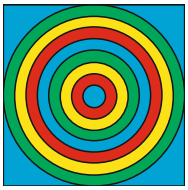

Figure 2.2: The calibration test pattern used for measuring the width of distilled water droplets. Each ring is 3 mm larger in diameter than the previous one.

blue circle. Because the edges of the circle were determined by eye, to minimise errors in the scale calibration, the diameter of the circle was measured eight times from different positions across the circle edge, and an average taken. To measure the radius of the droplet, a circle was drawn around the droplet edge in ImageJ, and the radius calculated from the circumference. The droplet radius measurements had an error of roughly 0.3 mm from uncertainties in the calibration.

The coverslip was placed directly on top of the test pattern before addition of the droplet. Care was taken to ensure that the test pattern was flat on the surface of the workbench to avoid the causing the coverslip to sit at an angle. This would result in the droplet running across the coverslip surface and assuming an aspherical shape, which could not be analysed using Eq.(2.1). In cases when the droplet would be aspherical due to the way it was pipetted for instance rather than the coverslip not being level, another droplet would be placed elsewhere on the coverslip and the measurement repeated. Occasionally, the droplet would be illuminated from the side to enhance its visibility in the image, but this was avoided where possible due to the heat emitted from the light source.

Time (mins)	Voltage (V_{pp})	Frequency (Hz)	Field modulation
60	1.2	10	Square wave
30	1.5	5	Sinusoidal
15	1.5	2	Sinusoidal
15	1.5	1	Sinusoidal

Table 2.1: Table showing the electric field parameters used during the electroformation process.

2.5 Preparation of Lipid Bilayer Patches

Lipid bilayer patches were prepared by rupturing GUVs on a glass coverslip. Suspensions of GUVs were produced using the electroformation technique [45]. First, 10 µl of lipid solution at 1.0 mg/ml concentration was deposited on each of two tantalum electrodes[2]; this was done under extremely gentle nitrogen flow so as to prevent peroxidation while avoiding blowing the droplets of lipid solution off the electrodes. The electrodes were then placed under vacuum for one hour to remove remaining solvent and leave a dry coating of lipid on the electrode surfaces. The electrodes were cleaned by washing with acetone between uses to prevent contamination of the lipid mixture.

The electrodes were then immersed in a 750 µl volume of distilled water. This 750 µl volume was pipetted from a larger 20 ml volume that had been degassed in vacuum for five minutes to avoid the bubbles described in Sec. 2.3. An electric field was then applied over the electrodes for a total of two hours using a function generator (GW Instek, SFG-2010). The output of the function generator was monitored using an oscilloscope (Gould DSO 405). The electric field parameters were sequentially changed during the electroformation process as given in Table 2.1, with the earlier square wave, high frequency settings used to optimise vesicle formation and growth, and the latter low frequency settings used to encourage vesicle detachment from the electrodes [93].

An imaging spacer was then placed on an etched glass coverslip, and 65 µl of the GUV solution was deposited onto the glass surface using a 200 µl pipette (Thermo Scientific Finnpipette F1). To prevent the pipette tip rupturing the GUVs, the end of the pipette tip was cut off, creating a larger aperture (roughly one millimetre in diameter) at the end of the pipette for the GUVs to move through. The GUV solution was left for 30 minutes to allow the vesicles to settle on the coverslip. To prevent evaporation of the GUV solution, the coverslip was placed under a glass dish (without spout) with several pieces of damp tissue to create an enclosed humid environment. Afterwards, 65 µl of PBS was added to the coverslip to induce rupture of the vesicles by osmotic pressure[3]. The medium was then exchanged within several seconds with more PBS solution to remove any remaining free floating vesicles in the solution. The PBS was degassed in vacuum for five minutes prior to use as described in Sec. 2.3.

[2] While most protocols use platinum electrodes for electroformation [93], we use tantalum electrodes as a more cost effective alternative [45].

[3] In response to a higher external osmolarity, the membrane of a vesicle sat on a solid support becomes deformed, causing membrane destabilisation and lowering the energy penalty for vesicle rupture [94]. Rupture is assumed to be virtually instantaneous upon addition of PBS [94].

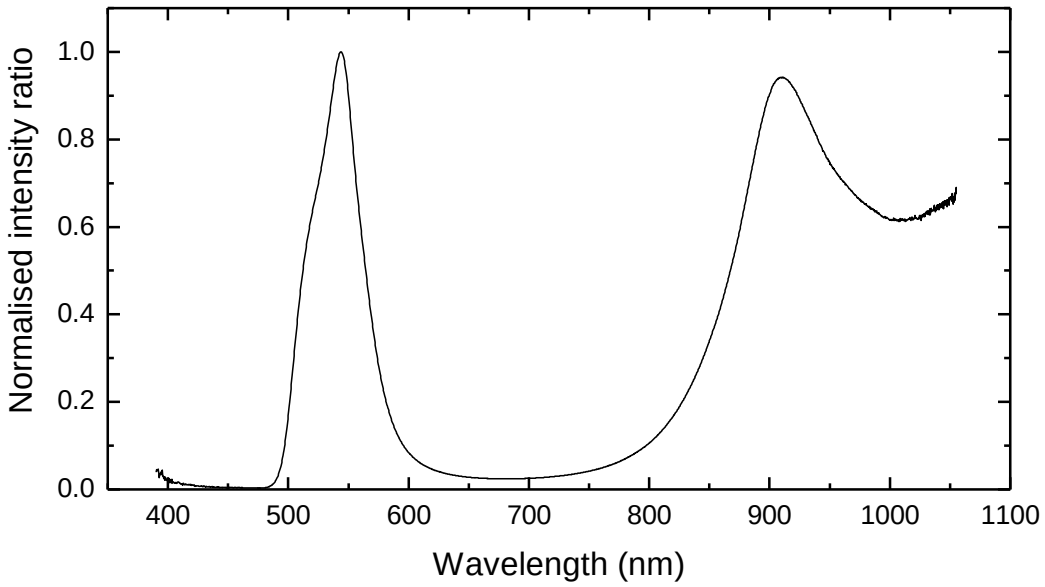

Figure 2.3: Normalised transmission of the GIF used in the qDIC illumination.

2.6 DIC and Fluorescence Imaging

Images were taken using a Nikon Ti-U inverted microscope, with a Hamamatsu Orca 285 CCD camera (having 1344 × 1024 pixels of 6.45 µm size, 18 ke full well capacity, 7 e read noise, and 4.6 electrons per count at zero gain [45, 95]). The lateral position of the sample and its axial position relative to the microscope objective was controlled using a Prior Proscan III, with a stepper motor driven x-y stage (0.04 µm step size, 0.7 µm repeatability) and an objective focus drive (2 nm step size). A 20×, 0.75 NA dry objective (Nikon CFI Plan Apo Lambda MRD00205) was used with a 1.5× tube lens for a magnification of 30× on the camera. For images taken with the 20× objective, a 0.72 NA (Nikon MEL56100) condenser was used.

For transillumination, a 100 W halogen lamp was used. To ensure the lamp output was stable before imaging, the lamp was switched on and adjusted to the optimal intensity 20 minutes before the start of imaging. The lamp output was filtered by a Schott BG40 filter (to remove infrared wavelengths >650 nm outside the operating range of the DIC prisms and polarisers but visible on the camera) and a Nikon green interference filter (GIF), to produce light with a nominal peak emission wavelength of 550 nm, since having a defined peak illumination wavelength is important for qDIC. The transmission spectrum of the GIF was measured using a spectrometer and a white light source separate from the microscope. This is shown in Fig. 2.3. The full width at half maximum of the GIF peak in the visible range was measured to be 52.6 nm.

Epifluorescence imaging used a Prior Lumen 200 lamp with a Semrock GFP-A-BASIC-000 filter cube which produced a power density at the sample of 10.7 W/cm^2. To avoid saturating the camera in samples with strong fluorescence signals, Nikon ND4 and ND8 filters were used to attenuate the lamp intensity (the measured attenuation factors are 0.285 and 0.136 respectively), however unless otherwise stated no filters were used. Fluorescence images were taken with 1 second exposure time, and intensities are given in detected photo-electrons (pe) per pixel. A weak background (typically around 200 pe/s) measured in regions without lipid was subtracted.

Nikon N2 prisms with a measured shear distance of (238 ± 10) nm [45] were used for all DIC images (a Nikon MEH52400 DIC module was used in the condenser and a Nikon MBH76220 DIC slider was used after the objective). The majority of DIC images were captured using 100 ms exposure times (10 Hz frame rate) with around 15 ke detected per pixel, resulting in a root-mean square (RMS) shot noise in the single pixel intensity of about 0.08%. Likely due to limitations of the data transfer rate of the camera, this frame rate setting was found to occasionally produce defective frames when taking continuous DIC acquisitions. Duplicated frames occurred at a rate of 0.171%, and torn frames at 0.026%.

It was eventually determined that a frame rate of 8.3 Hz (corresponding to an exposure time of 120 ms) was sufficient to eliminate these defective frames, and so this increased exposure time is used for the more recently taken data. For data taken at 10 Hz, torn frames were removed from the analysis when they were detected, but the majority of the analysis had already been completed before a reliable method of identifying broken frames was introduced. The exposure times used for all images shown are given in Appendix D.

As explained in Sec. 1.4, in order to account for inhomogeneities in the illumination from the DIC lamp, the camera sensitivity and the microscope optics, two sets of DIC images, $I_{\pm}$, were taken for each region of interest, one with the de-Sénarmont compensator polariser angle set to either $+12.9°$ or $+15°$, and the other with the polariser set to the corresponding negative angle. From each of these image pairs, a DIC contrast image $I_{\mathrm{C}} = (I_+ - I_-)/(I_+ + I_-)$ was generated. The camera dark offset was subtracted from all acquired DIC images before further processing

2.7 Temperature Control

All experiments were conducted at room temperature (21 °C) unless otherwise stated. For experiments where the temperature of the lipid bilayer had to be controlled, temperature regulation was achieved using an enclosed heating chamber built around the microscope encompassing the stage, objectives, and most of the condenser. This heating chamber was connected to a Life Imaging Services (Efringerstrasse, Switzerland) Cube2 heating unit, which cycles air through the chamber. A thermal sensor located behind the stage was connected to the heating unit to provide measurements of the internal temperature, which was regulated by the unit to an adjustable set point. The heating unit was switched on and set to its target temperature at least one hour before mounting the sample. This was to allow the temperature within the heating unit to stabilise, and for the microscope components to reach thermal equilibrium. After mounting the sample, a few minutes were given to allow the sample to also reach thermal equilibrium.

Due to the separation between the built in sensor and the sample position, it may not accurately reflect the temperature at the sample. To account for this, a thermocouple sensor was attached to the side of the sample slide using electrical tape, positioned as close as possible to the coverslip without interfering with imaging. The temperatures measured by the heating unit sensor and the thermocouple typically differed by approximately 2 °C, so during imaging, the target temperature (heating unit set temperature), the heating unit sensor temperature, and the thermocouple temperature were all recorded.

2.8 Interferometric Reflectometry

Interferometric reflectometry is a technique which allows for the amplitude and phase of orthogonally polarised components of reflected light to be quantitatively measured. It works by raster scanning laser light across the sample and interfering the light reflected from the surface (the reflected probe beam) with a reference beam with known parameters, allowing quantitative information about the amplitude and phase of light reflected from the sample at each point to be extracted [96].

The interferometric reflectometry setup utilises a heterodyne detection system to obtain the phase information. The probe and reference beams originate from the same 100 fs pulsed laser source. A simplified diagram showing the arrangement of components in the interferometric reflectometry setup is shown in Fig. 2.4. The beam is passed through an accousto-optic modulator which upshifts the frequency of diffracted orders. The zeroth order diffracted light is unchanged in frequency and becomes the reference beam, while the first order diffracted light is upshifted in frequency and becomes the probe beam.

The probe beam is first passed through a combination of a half wave plate and quarter wave plate to give it circular polarisation at the sample, before being directed into the objective. The rotation angle of these two wave plates can be adjusted to compensate for any birefringence of the microscope optics and ensure that the light arriving at the sample is circularly polarised[4]. When light is reflected back from the sample, it becomes circularly polarised in the opposite direction, and, if the sample has any birefringence, becomes elliptically polarised as two linearly polarised components of the incident light (oriented along and across the birefringence) are reflected differently.

After returning through the two wave plates, the probe beam is made up of two orthogonal linearly polarised components; one which is oriented orthogonal to the original laser light but with altered amplitude and phase from the sample (the co-polarised light), and another originating from the birefringence of the sample (the cross-polarised light). The probe beam is then combined with the reference beam at a non-polarising beamsplitter. The reference beam is linearly polarised, and provides equal intensities in each polarisation direction. The light leaves the beamsplitter as two beams of equal intensity containing both polarisation components of the light, the only difference between the two beams being a difference of the phase shift of π between the probe and the reference, due difference between reflection and transmission at the reflecting layer within the beamsplitter. Finally, a Wollaston prism splits the two beams into four by separating the co- and cross-polarised beams from each other. The four beams are then directed towards separate photodiodes, which measure the intensity.

The photodiodes measure the interference between the reference and probe beam as well as the two DC terms. One pair of photodiodes measures the co-polarised beams and the other measures the cross polarised beams. By subtracting the intensity measured on one of the paired diodes from the other, the DC terms can be removed, leaving only the interference term which contains the desired information on the amplitude and phase of the field. The amplitude and phase are analysed using a lock-in amplifier, as described in Zoriniants et al. [96].

While both interferometric reflectometry and qDIC are quantitative phase tech-

[4]This is done by minimising the co-polarised back reflection from a highly reflective gold film calibration sample.

niques, there are significant differences. Firstly, unlike qDIC, which is a widefield technique, this is a point scanning technique in which a laser is raster scanned across the sample. Secondly, unlike qDIC which uses light transmitted through the sample, interferometric reflectometry uses reflected light, and so is sensitive to axial sample position. This technique also differs from qDIC in that the phase signal carries a contribution from the underlying hydration layer, as the phase signal is generated from the optical thickness travelled by the laser beam, rather than a difference in optical thickness at two nearby regions at the sample.

All interferometric reflectometry data was acquired using a 60× 1.27 NA water-immersion objective (Nikon CFI Plan Apo IR Lambda-S Nano Cystal MRD70650) with a 1.5× tube lens. Corresponding DIC images were taken using a 1.34 NA oil condenser (Nikon MEL41410), matched to the numerical aperture of the objective. As in the case of the images taken with the 20× objective, N2 DIC prisms were used, with a with a Nikon MEH52500 DIC module used in the condenser and a Nikon MBH76264 N2 DIC slider placed after the objective. The sample position was controlled using a piezoelectric sample stage (MadCityLabs NanoLP200, with 0.4 nm resolution and 15 ms response time). Data was taken at two samples per resolution with a pixel dwell time of 200 µs using MultiCARS, a home-built software developed by Wolfgang Langbein. Laser wavelength was 550 nm (bandwidth 5 nm) for all measurements.

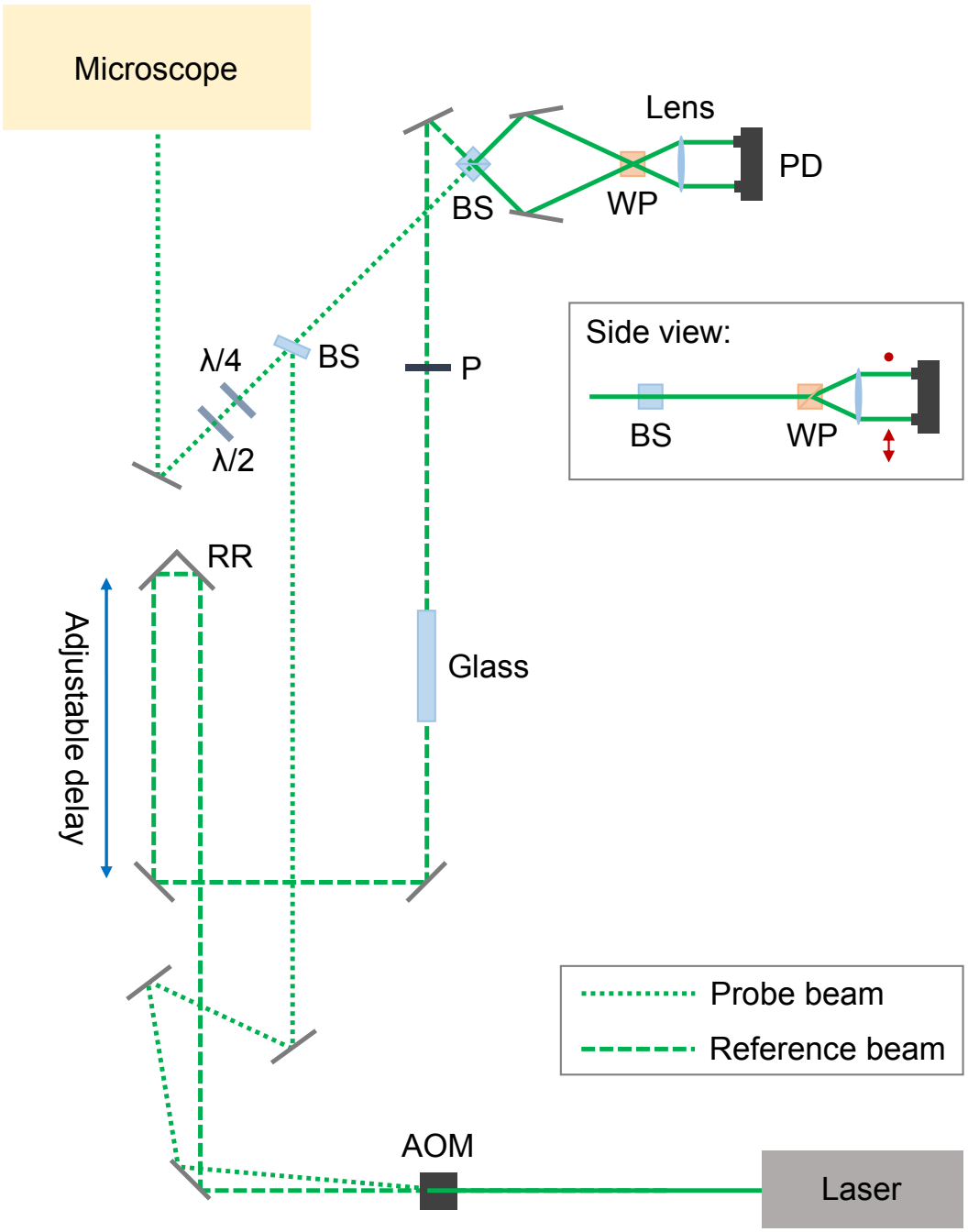

Figure 2.4: Simplified diagram showing the key components of the interferometric reflectometry setup. The laser beam is passed first through an accousto-optic modulator (AOM), which splits the beam into probe and reference beams. The reference beam is passed through a glass block to compensate for the dispersion of the microscope optics, before a polariser (P) changes the polarisation of the beam to have equal parts horizontal and vertical linearly polarised components. The optical path length of the two beams is matched using an adjustable delay stage, with a movable retroreflector (RR) in the probe beam path. The probe and reference beams are reunited at a beam splitter, before being sent through a Wollaston prism (WP) to separate the two linear polarisations, and finally focussed on the four photodiodes (PD) by a lens. The splitting at the Wollaston prism is shown in a side view, with the polarisation of the light indicated with red arrows.

Chapter 3

Liquid Disordered Bilayers

In this chapter, the application of the qDIC technique to L_d phase SLBs will be demonstrated. First, in Sec. 3.1, reconstructed phase images of SLBs will be shown, and the process used to obtain bilayer thickness measurements from phase steps taken over the bilayer edge will be explained. Unusual phase profiles that occur in double bilayer regions will be interpreted by comparing data from interferometric reflectometry experiments. Next, in Sec. 3.2, the process by which an appropriate SNR term (previously discussed in Sec. 1.4) was determined will be explained.

Once this is done, in Sec. 3.3 we will use qDIC to measure the thickness of the bilayers within a multilamellar DOPC supported bilayer stack. We will then identify several factors that influence the thickness of the SLB in Sec. 3.4, and interpret these findings in the context of previous studies in the literature. To further understand the changes that are occurring in the bilayer, in Sec. 3.5 we will attempt to analyse the fluorescence of the bilayers in the stack in the same manner as for the thickness measurements.

Lastly, factors limiting the qDIC technique will be discussed. In Sec. 3.6 we will examine the effect of the number of image averages on the measurement error, and investigate ways of minimising image noise in future qDIC experiments by combining simulated bilayer phase steps with experimentally measured background noise. We will then move on in Sec. 3.7, to explore the reliability of the DIC polariser calibration, and test its effect on the measured data, before finally making an investigation of the effect of image defocus on the bilayer thickness measurements in Sec. 3.8.

3.1 Application of the qDIC Technique

The first SLB system that was studied for this work using qDIC was one formed from DOPC, which is a neutrally charged phosphocholine lipid that readily forms planar bilayers due to its cylindrical shape [5]. Because of its two monounsaturated hydrocarbon chains, the main (S_o to L_d) phase transition temperature of DOPC is relatively low (-16.5 °C for vesicles [97]) compared to lipids with saturated chains of similar length, meaning that DOPC bilayers form a homogeneous fluid phase at room temperature. It is for these reasons that bilayers formed from DOPC are widely used in the literature as a simple model for the cell membrane. The combination of the simplicity of the DOPC SLB system and the high extent to which it has been characterised makes it ideal for testing the application of the qDIC technique to lipid bilayers. For comparison, fluorescence images are taken on bilayers containing 0.1 mol% ATTO488-DOPE fluorophore.

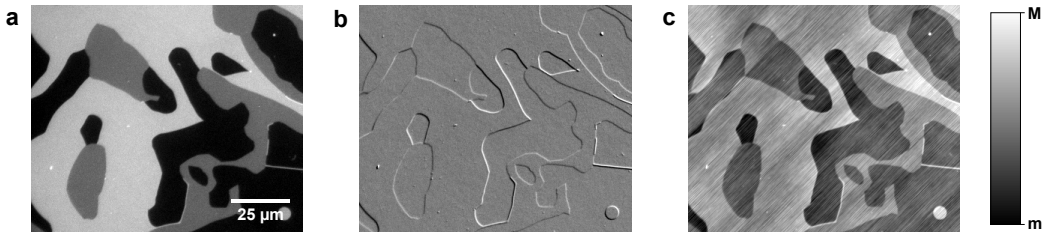

Figure 3.1: Images of the edge of a DOPC lipid film, showing regions of different lamellarities on a grey scale ranging from a minimum intensity, m, to a maximum intensity, M, as given. a) Fluorescence ($M = 600\,\mathrm{pe}$, $m = 0\,\mathrm{pe}$), b) qDIC contrast ($m = -0.004$, $M = 0.004$), and c) qDIC phase ($m = -10\,\mathrm{mrad}$, $M = 9\,\mathrm{mrad}$).

An example of fluorescence and qDIC phase images of a DOPC SLB is given in Fig. 3.1. The parameters used for the image acquisition are as described in Sec. 2.6, with the qDIC images produced from two DIC images taken at $\psi = \pm 12.9°$, while the fluorescence image was taken using a single one second exposure. The region has varying lamellarity, with regions of one or two bilayer coverage, and regions where there is no bilayer. In the fluorescence image, the black regions ($\sim 0\,\mathrm{pe}$) correspond to areas where there is no bilayer present, the dark grey regions ($\sim 290\,\mathrm{pe}$) are areas where there is a single bilayer on the surface, and the light grey regions are areas of two bilayers ($\sim 550\,\mathrm{pe}$). Likewise, in the qDIC phase image, the darker regions correspond to regions of low optical thickness (where there is no bilayer present), while two lighter shades of grey correspond to regions of one or two bilayer thickness.

In some places, the positions of the bilayer edges differ between the qDIC phase and fluorescence images. For the DIC images, 100 frames were taken at each polariser orientation and then averaged to reduce image noise, requiring about 20 seconds for acquisition, during which the bilayer edges can shift slightly. These differences are therefore due to changes in the sample in the time between acquisition of the fluorescence and DIC images. A more comprehensive discussion on the effect of the number of averages, and how the number of averages was chosen, is given in Sec. 3.6.

In order to obtain quantitative information on the bilayer thickness, the phase step over the bilayer edge was measured. This was done by taking a line profile orthogonal to the bilayer edge in ImageJ. The line width was set to eight pixels; ImageJ averages the pixel values along the width of the line, and so this allowed for the effect of noise to be reduced. The value of eight pixels was chosen as a compromise between noise reduction (which increases with the width) and the need to avoid unwanted structures such as small vesicles adhered to the bilayer, or regions where the bilayer edge was not straight.

The phase profile over the bilayer edge generally resembled a step, as expected due to the sharp increase in the sample optical thickness that occurs at the bilayer edge. An example of this step-like phase profile over the bilayer edge is given in Fig. 3.2a. The step was fitted with a hyperbolic tangent function, shown below.

$$y = \frac{a}{2} \tanh\left(\frac{x-b}{c}\right) + dx + e \tag{3.1}$$

In Eq.(3.1), a is the height of the phase step, c is the step width, and $dx + e$ is a background term that accounts for any local phase gradients and the displacement of the phase step from zero. Fitting was carried out using the Curve Fitting Toolbox

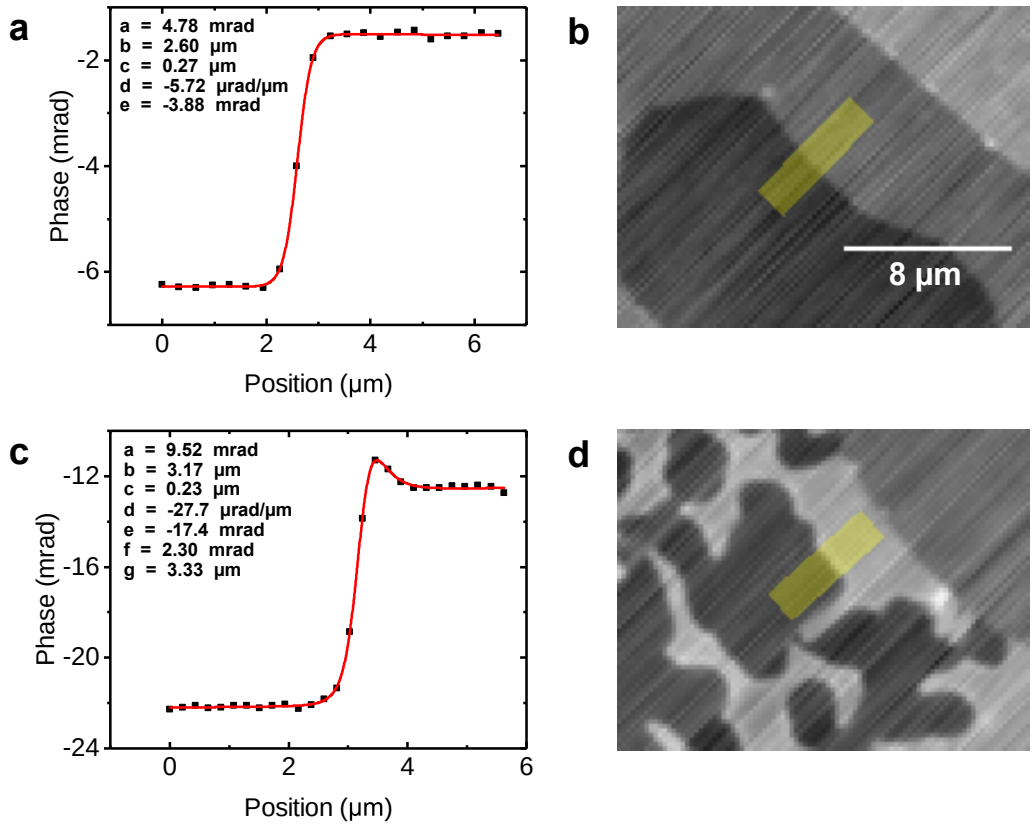

Figure 3.2: Examples of phase profiles taken over bilayer edges. A typical profile over a single bilayer edge fitted with Eq.(3.1) is shown in a), with b) showing the corresponding qDIC phase image, on a grey scale from −12 to +13 mrad. The region from which the profile was extracted is shaded in yellow. Panel c) shows a fit to a double bilayer step, incorporating the sech term to accommodate a hump in the phase profile, with d) showing the corresponding qDIC phase image, on a grey scale from −30 to 0 mrad.

in MATLAB R2015a, which uses the Least Squares method for fitting data.

This equation was fitted to the example data shown in Fig. 3.2a. The function fits the measured data well, and results in a measured phase step for this region of the lipid bilayer of 4.78 ± 0.03 mrad. The error on this value is the estimated standard deviation. This phase step can be converted to an absolute thickness value, h, by using Eq.(3.2), where λ_0 is the illumination wavelength.

$$h = \frac{a\lambda_0}{2\pi(n_\mathrm{l} - n_\mathrm{m})} \tag{3.2}$$

This requires both the refractive indices of the lipid bilayer (n_l) and the surrounding medium (n_m) to be known. Since DOPC is a widely used model lipid, and the PBS solution is a commonly used buffer solution, their refractive indices are available in the literature. For this work, the refractive indices were taken to be 1.445 [29] and 1.3341 [98] for DOPC and PBS respectively at the 550 nm wavelength we use[1]. For the step shown in Fig. 3.2a, these values give an absolute thickness of

[1]The DOPC refractive indices were measured using plasmon waveguide resonance measurements of SLBs at 543.5 nm, while the PBS refractive index was measured at 589 nm using a commercial

3.78 ± 0.02 nm (this error is again derived from the estimated standard deviation of the fit to the phase step).

It is important to note that lipid bilayers are birefringent, and so the effective refractive index will change according to the angle of incidence. Because of the focussing of light at the sample by the condenser lens, there will be a range of different angles of incidence at the sample, with the maximum angle determined by the numerical aperture (NA) according to $\arcsin(\mathrm{NA}/n_\mathrm{l})$. For the 20× objective, this corresponds to a maximum increase in the refractive index of 0.004 compared to normal incidence, which would lead to a decrease in the calculated bilayer thickness of approximately 3.5%. Considering the effect is relatively small, and that most light will be incident at the sample at lower angles (and thus experience an even smaller change in n due to the birefringence), for measurements taken with the 20× objective the influence of the birefringence can be neglected. As such, the ordinary refractive index of the bilayer is used for all thickness calculations.

In some regions, the edges of two bilayers were aligned, resulting in double bilayer steps, many of which can be seen in Fig. 3.1. While most phase profiles over bilayer edges had a shape which was well fitted by Eq.(3.1), occasionally when measuring these double bilayer steps a 'bump' was visible in the phase profile at the edge of the bilayers. This can be seen in the phase profile Fig. 3.2c, though the increase in intensity at the edges of double bilayer regions is sufficiently strong to be visible directly in the qDIC phase image shown in Fig. 3.2d.

One possibility for the origin of this bump in the edge profiles would be the presence of small adhered vesicles present at the bilayer edge. As noted in Sec. 1.2, vesicles can be tens of nanometres in diameter, well below the lateral resolution of the objective, but still optically thick enough to show up in the DIC images. While spin-coated bilayers are not formed from vesicles initially, vesicles with diameters on the order of hundreds of nanometres are visible scattered across the SLB and the glass surface, as round objects of high contrast. These can be seen in Fig. 3.3a. Smaller, sub-resolution, vesicles may be adhering to the double bilayer edges, or they might be forming from the double bilayer edges.

While this can explain the phase profiles at the bilayer edges, this does not account for another feature associated with this phase bump. In extended double bilayer regions where these phase bumps are present, at a small distance away from the edges there is usually an additional phase gradient in the opposite direction to the one at the edge of the bilayer. A typical example is shown in Fig. 3.3a. Unlike the sharp DIC contrast at the double bilayer edges, this second gradient is gradual. In samples formed from both DOPC and L_d phase $DC_{15}PC$, there seems to be a characteristic separation between the edge of the double bilayer region of the bilayer and the gentle gradient, of 2.0 - 3.0 µm.

In order to get better insight into the nature of these structures, the DIC images were compared with corresponding regions imaged using the interferometric reflectometry technique described in Sec. 2.8. The amplitude of the co-polarised beam reflected from the sample is shown in Fig. 3.3b. Stripe patterns across the reflectometry images are motion artefacts resulting from the raster scanning process. All reflectometry images were taken using a 60× 1.27 NA water-immersion objective with a 1.5× tube lens.

Curiously, the signal from the region between the bilayer edge and the shallow gradient is noticeably weaker than the signal in the interior of these patches, resulting

refractometer.

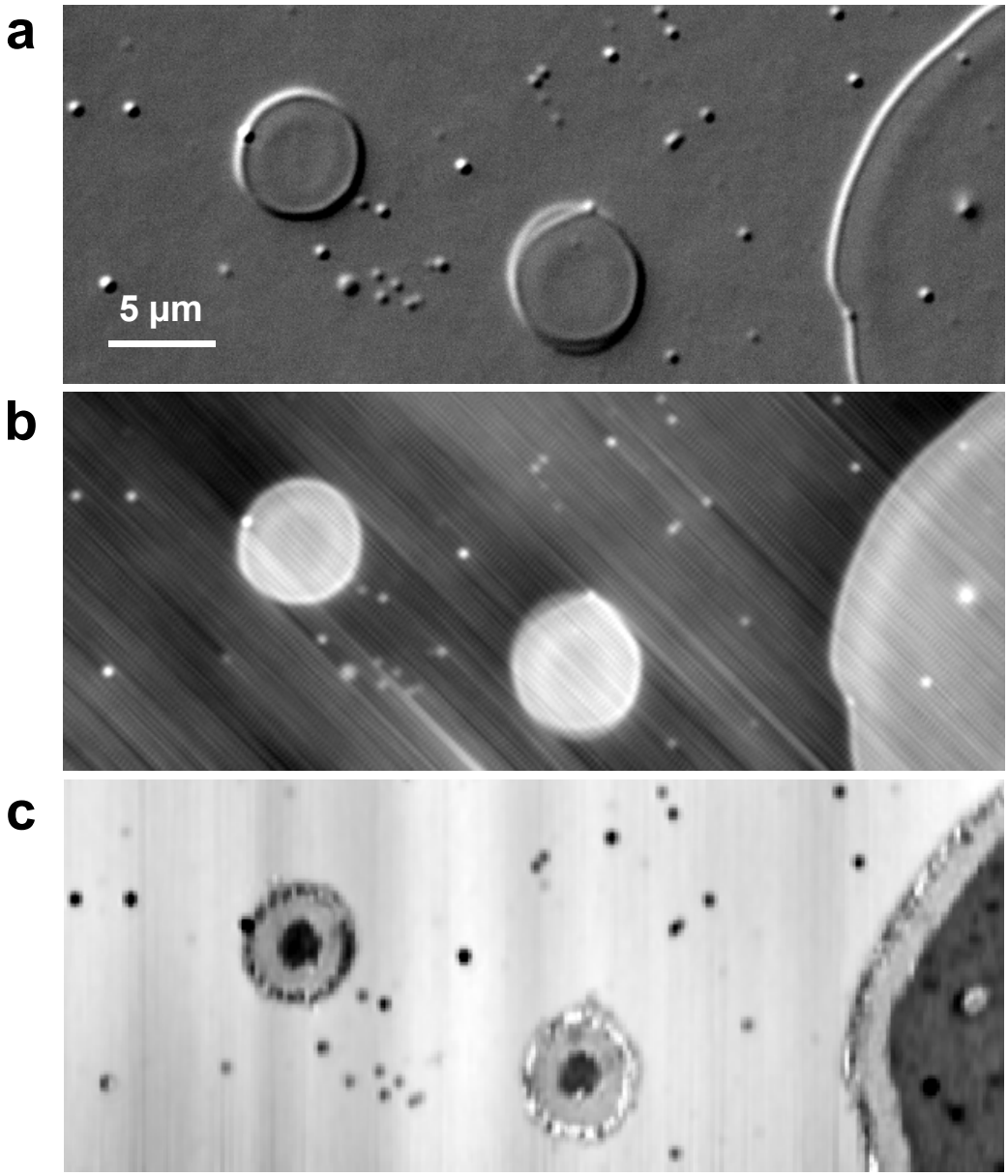

Figure 3.3: Bilamellar lipid bilayer patches, shown in a) a DIC contrast image, b) a qDIC phase image, and c) an interferometric reflectometry co-polarisation amplitude image. The DIC image is scaled from -0.0016 to 0.0035, the qDIC phase image is scaled from - 5 mrad to 5 mrad, while the reflectometry image is scaled from 22.63 mV to 26.26 mV. The upper left edge of the right circular patch has shifted slightly between acquisition of the positive and negative polariser images resulting in the edges appearing duplicated.

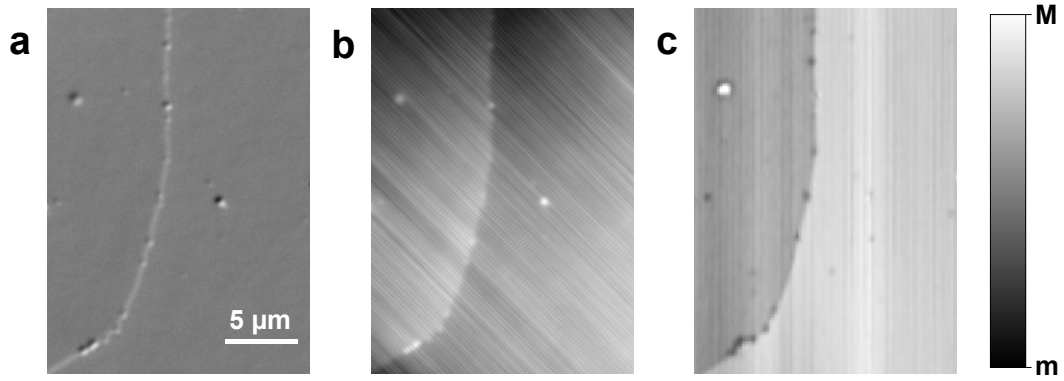

Figure 3.4: A region with the edge of a unilamellar bilayer patch on the left, and an empty region on the right, shown in a) qDIC contrast (m = -0.005 to M = 0.005), b) qDIC phase (m = -15 mrad to M = 1 mrad), and c) interferometric reflectometry co-polarisation amplitude (m = 22.9 mV to M = 27.1 mV).

in a boundary region of weaker signal at the edge of the bilamellar regions. In single bilayer regions, which lack this shallow gradient in the DIC images, this boundary region is not observed, and the reflectometry signal is consistent up to the edge of the bilayer, as shown in Fig. 3.4. Interestingly, when the reflectometry signal is measured in nearby regions of the sample, the signal in this boundary region is (25.4 ± 0.1) mV, closer to that of the single bilayer regions, (25.6 ± 0.1) mV, than the centre of the bilamellar regions, (23.7 ± 0.1) mV [2].

This would seem to be contradictory; the DIC signal suggests that there are two bilayers present at the edges of the bilamellar regions, but the reflectometry signal just one. However, this can be understood when the different focal depths of DIC and reflectometry are taken into account. The reflectometry technique is only sensitive to signal from the sample surface and would only pick up the second bilayer if it was in close proximity to the first[3]. In contrast, the DIC technique is sensitive to structure in a comparatively thick focal volume, and if the first two bilayers were spatially separated, the DIC signal would be the same as for two bilayers in direct contact (so long as the bilayers were parallel to each other) since the phase retardation caused by the sample would be the same in either case.

These edges can be interpreted as a region where the bilayers of the first and second layers in the SLB are joined, as shown in Fig. 3.5, where at the edge of the SLB the first bilayer folds back on itself to form the second bilayer. Such a structure might offer a more energetically favourable conformation of the multilamellar film, as there is an energetic penalty associated with single bilayer edges due to the exposure of the hydrocarbon tails to water, which gives rise to the self-sealing property of biological membranes. Joining the stacked bilayers together would eliminate some of these unfavourable edges in the SLB system.

The rigidity of the bilayers would preclude a sharp fold linking the two bilayers together, as high curvature also creates an energy penalty, so a more gradual bend is needed. This results in a region at the edge of the SLB where the two bilayers are spatially separated, and it is this separation which gives rise to the boundary region in the reflectometry images that have the single-bilayer signal strength. The

[2]The errors are the standard deviation of the amplitude.

[3]Even for two bilayers within the focal volume, any separation between the two bilayers would still result in a change to the reflectometry signal.

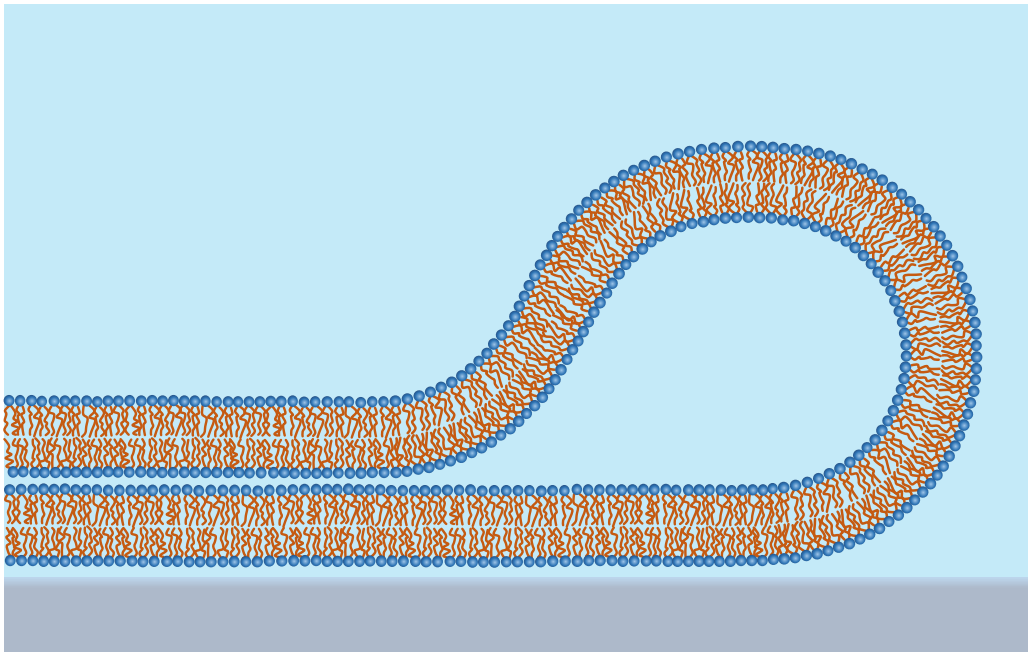

Figure 3.5: Our model for the structure of the SLB at the edge of double bilayer regions in which the first and second bilayers are joined. The illustration is not to scale.

consistent width of the boundary region in the images may be a consequence of the bilayer's fixed rigidity setting the size of the fold. Consistent with this interpretation, gel-phase bilayers, discussed in more detail in Sec. 4.1 and Sec. 4.2, do not have this type of double-bilayer edge, presumably due to their significantly higher resistance to bending [38] making the folds unfavourable. Indeed, when such edges are present in the double bilayer regions of $DC_{15}PC$ bilayers, they disappear after cooling below T_m, suggesting a return to a stack of disconnected planar bilayers.

Another factor that might affect the fold size is the volume of water contained between the first and second bilayers. If the edges of the first and second bilayers are completely joined (such that they form 'deflated vesicle' structures), it might be the case that due to the bilayer's very low permeability to water, the possible arrangements of the bilayer would be limited to those with an internal volume which is equal to the volume of water trapped between the two bilayers.

Away from the edge the distance between the first and second bilayers decreases. Here, the bilayer is oriented at an angle, so the amount of lipid imaged per pixel is larger, thus giving rise to a stronger signal and therefore the gentle phase gradient in DIC. The sharp bump in the phase signal at the very edge of the DIC images is the result of the curvature of the bilayer causing a region where the bilayer is parallel to the direction of light propagation which has an increased optical thickness.

Since the DIC technique isn't sensitive to the separation of the first and second bilayers (assuming they are both within the focal volume), it was decided that edges that showed this folding behaviour would still be suitable for analysis. To accommodate the bump in the phase profile, an additional term was added to the fit function, as shown in Eq.(3.3). This modified version of Eq.(3.1) was applied only to double bilayer edges where the phase profiles had an appearance which suggested that the bilayer at the edge was folded over, such as that shown in Fig. 3.2c. Fitting was always attempted using Eq.(3.1) first, and Eq.(3.3) only tried when the adjusted

R^2 value of the fit was below a threshold value of 0.9970[4].

$$y = \frac{a}{2}\tanh\left(\frac{x-b}{c}\right) + dx + e + f\,\mathrm{sech}\left(\frac{x-g}{c}\right) \tag{3.3}$$

The phase bump was modelled by the addition of a sech term. The width of this bump was set to be the same as the width of the step function, c. This was done due to the fact that the measured width should be a property of the microscope optics, rather than the sample, because the size of the fold is likely to be significantly below our lateral resolution (276 nm for DIC). Thus the apparent width of either structure in the phase images would not be related to the actual size of these structures, but rather a combination optical resolution and degree of focus, which would be the same for both. This function may therefore also be able to fit any other sub-resolution structures that may be present at the bilayer edge, such as small vesicles.

An example of Eq.(3.3) being fitted to phase measurements is shown in Fig. 3.2. It can be seen that the additional sech term models the phase profile well, and results in retrieved step height for the double bilayer edges which is consistent with the measurements of single bilayers. The centre of the sech term is shifted by 0.16 µm relative to the centre of the tanh term. By integrating the sech term, we can determine the length of lipid in the fold, from which we find that the mean radius of curvature is approximately 20 nm. This integration was achieved utilising measurements of bilayer optical thicknesses reported in Sec. 3.4 with a procedure that will be described in more detail in Sec. 4.4[5].

3.2 Signal-to-Noise Optimisation

Before embarking on detailed studies using the phase images, it was necessary to determine how the different integration parameters discussed in Sec. 1.4 affect the reconstruction. While most of the variables needed for the integration (such as illumination wavelength, pixel scaling and shear angle) are known from the acquisition conditions of the original DIC images, an important exception to this is the signal-to-noise ratio (SNR) parameter.

In a DIC image, the spatial frequencies close to orthogonal to the shear direction are weak compared to those parallel to the shear direction. The closer to the shear direction, the weaker the spatial frequencies become, with the frequencies exactly orthogonal to the shear missing altogether. The function given in Eq.(1.10) boosts the amplitude of these weak frequencies, resulting in an image closer to the original phase profile from which the DIC image was generated. This amplification of low spatial frequencies also amplifies the noise, leading to the generation of artefacts in the reconstructed phase image, which appear as streaks running parallel to the shear direction.

[4]This value was determined based on the adjusted R^2 values that were achieved with Eq.(3.1) on phase profiles that showed the expected step-like behaviour, which were typically in the range from 0.9980 to 0.9995.

[5]The radii of curvature were determined by dividing the length of lipid in the fold by π. The exact values for the three lipid bilayers were 18.8 ± 2.8 nm ($n = 6$) for the bilayer formed on a hydrophilic surface ($\theta = 3.4°$) in distilled water, 22.4 ± 2.1 nm ($n = 12$) for a DOPC bilayer formed in PBS on a less hydrophilic surface ($\theta = 11.3°$), and 21.8 ± 2.0 nm ($n = 27$) for a DOPC bilayer in PBS on a fully hydrophilic surface ($\theta = 3.4°$). All data comes from samples prepared using the first lipid stock.

The strength of these artefacts is dependent on the signal-to-noise term in the Wiener filter, κ, which controls the degree of amplification of the spatial frequencies close to the shear direction, as discussed in Sec. 1.4. The effect of this SNR parameter on the phase reconstruction can been seen in Fig. 3.6. As κ is increased, the recovered phase profile becomes gradually closer to the expected step-like shape, as can be seen in Fig. 3.7, which shows an example phase profile over the edge of a single bilayer (taken in a different sample to that shown in Fig. 3.6).

In order to determine the effect of this parameter on the step heights measured using the procedure described in Sec. 3.1, the same step was measured in images integrated using different values of κ, and fitting carried out in the usual manner. The effect of varying κ on the phase step height is shown in Fig. 3.8. It is clear that κ has a strong influence on the relative phase values in the integrated image. At low values of κ, the measured height of the phase step increases sharply with increasing κ, however when κ is more than several thousand, the relationship is much weaker, and the measured thickness remains roughly constant within error. A high value of κ would therefore seem to be needed in order to obtain an accurate recovery of the phase steps.

On the other hand, increasing κ leads to a proliferation of artefacts, which eventually begin to obscure genuine image information and complicate interpretation and analysis. These artefacts tend to appear around high-contrast objects, and have the form of a bright and a dark tail extending in opposite directions from the object, parallel to the shear direction. An example of this can be seen in the example image given in Fig. 3.6, which shows an SLB region with a high contrast object (likely a multilamellar vesicle or vesicle cluster) in the centre. As κ is increased, the image gradually becomes more phase-like and the contrast between the different lamellarities increases consistent with the behaviour shown in Fig. 3.8. However the intensity of the artefacts projecting from the high contrast object also increases, and eventually the artefacts can be seen to extend across the entire section of the field of view at $\kappa = 10000$.

While in an ideal sample, such high-contrast objects would be rare, in practise there is wide variation in the density of such structures between samples. In a field of view with many high-contrast objects, a high κ setting would result in large numbers of artefacts which could overlap bilayer edges and affect nearby phase measurements. This precluded the use of a very high value of κ in the analysis. As such, an intermediate value of 4000 was chosen for all further analysis of images taken with the 20× objective, as a compromise between the need to set κ at a value where the phase was no longer very sensitive to κ and the need to prevent long artefacts. For images taken using the 60× objective, a lower κ value of 1000 was used.

Even when κ is optimised, some artefacts are still present in the phase images. Very strong artefacts, such as those shown in Fig. 3.6 can be avoided, but all the edges in the sample produce some artefacts along the shear direction. The consequence of this is that the background noise in the phase image is directionally dependent. When the phase profile measurements made in ImageJ cross these artefacts running parallel to the shear it appears as a strong background noise. To minimise the effects of these artefacts on the measured phase steps, phase steps were taken as close to parallel to the shear direction as possible, to minimise the crossing of these artefacts by the line profile.

This effect can be seen in Fig. 3.9, which shows example phase profiles taken

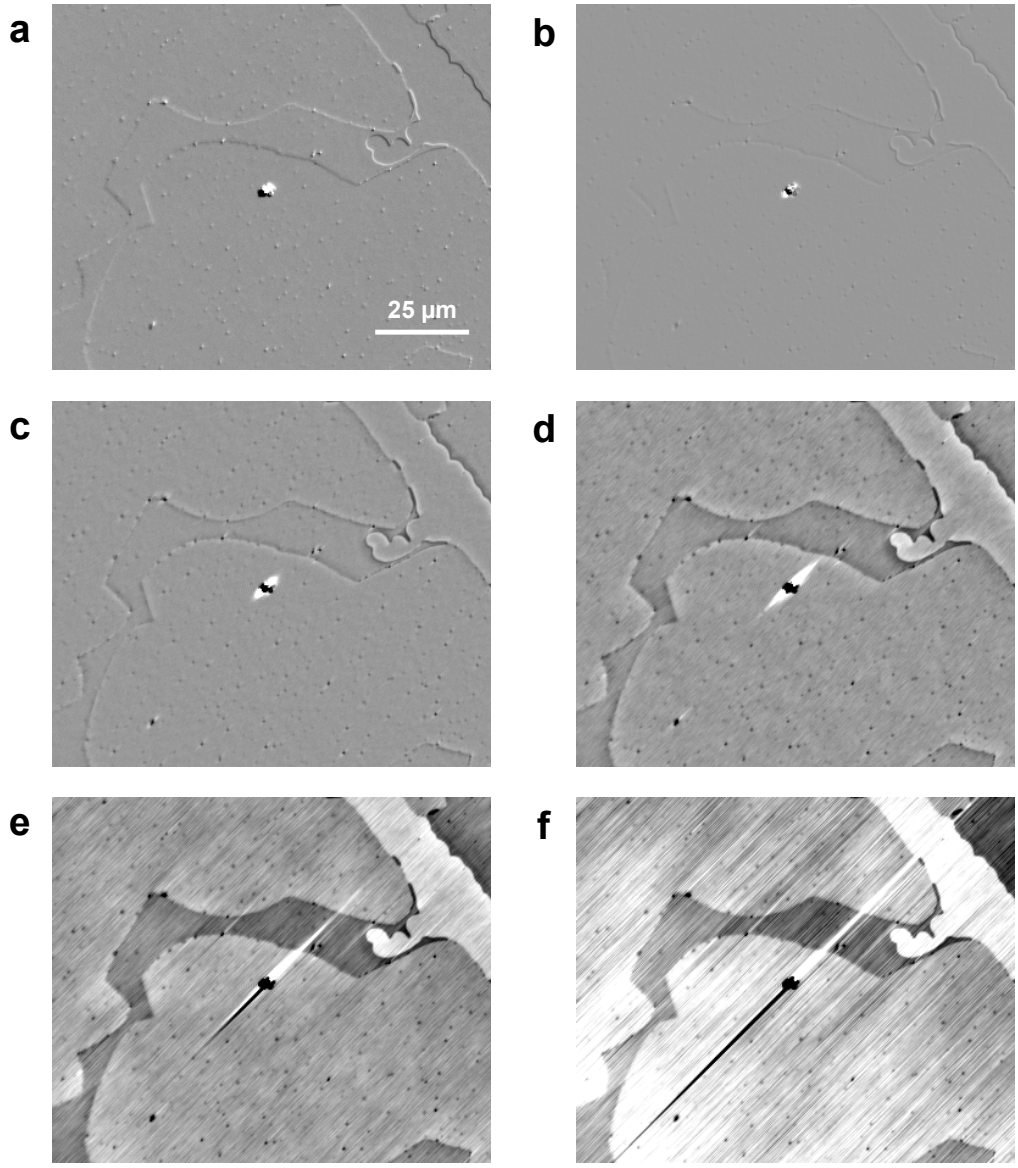

Figure 3.6: A region of a DOPC bilayer shown in a) DIC contrast, and qDIC phase, using κ of b) 1, c) 10, d) 100, e) 1000 and f) 10000. All images are scaled from -0.009 to 0.006. The contrast image is unitless while the scale of the phase image is in radians. Note that the intensity scale on the phase images are inverted compared to those shown in other figures. The 'bumps' present in the image are small vesicles sat on the surface of the bilayers.

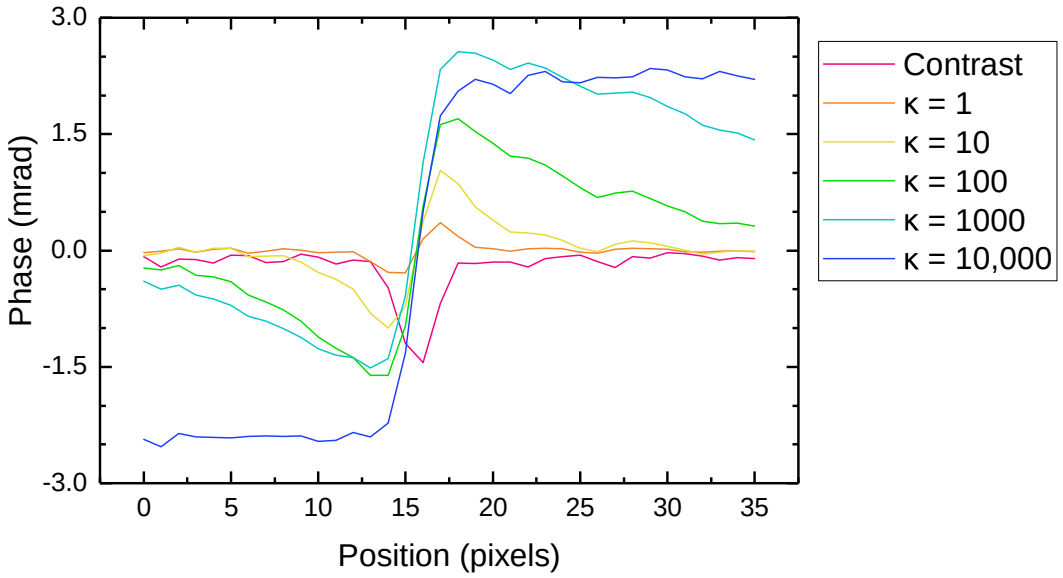

Figure 3.7: Phase profiles taken at the same position over the edge of a single lipid bilayer for different values of κ. The line profile was measured in the same sample as shown in Fig. 3.1.

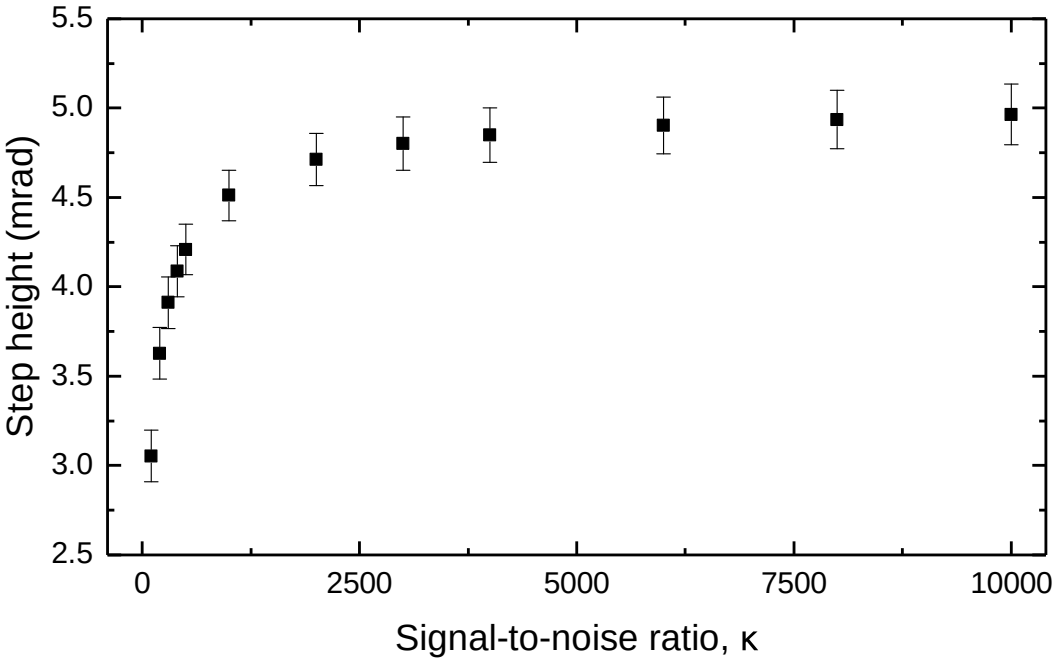

Figure 3.8: The phase step over a lipid bilayer edge, measured on qDIC phase images generated using different values of κ. The length of the line profile used in the fit was 50 pixels (5.37 µm). Errors are the estimated standard deviation of the fit.

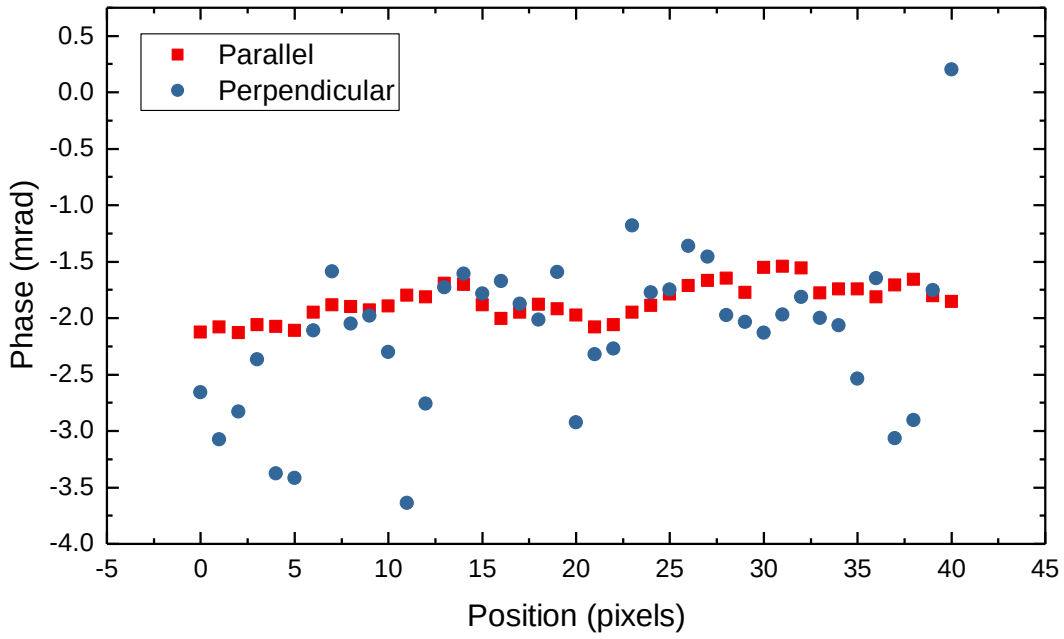

Figure 3.9: A graph showing an example of the background noise in regions where there is no bilayer, when the measurements are made either parallel or perpendicular to the shear direction. The phase profiles are averaged over a width of eight pixels, with $\kappa = 4000$, just as for normal bilayer measurements.

over the same region of glass (regions with no bilayer) at angles either parallel or perpendicular to the shear direction. It can clearly be seen that the variation in the phase taken perpendicular to the shear is much stronger than for the line taken parallel to the shear, with a range of 3.8 mrad, almost comparable to a single bilayer optical thickness. The effect of this background noise on measurements of bilayer thicknesses is discussed further in Sec. 3.6.

3.3 Measurement of Bilayer Thickness

Having demonstrated that the qDIC technique can convert phase steps to thickness values in Sec. 3.1, the DOPC/ATTO488-DOPE (99.9/0.1) lipid bilayer in PBS[6] system was studied in more detail. Due to the uncertainty in the thickness value for the individual single bilayer step described in Sec. 3.1, large numbers of individual bilayer thickness steps were measured across several fields of view in each sample, and an average was taken to reduce the error. The images were taken using the 20× objective with a 1.5× tube lens, and κ was set to 4000 as discussed in the previous section. An example of an analysed image with the positions of the individual line profiles shown is given in Appendix C.

Since the spin-coated lipid films contain regions with different numbers of stacked bilayers, the thicknesses of the first bilayer (the bilayer formed on the glass surface) and the second bilayer (the bilayer formed on top of the first) were measured separately. Additionally, where the edges of the first and second bilayers overlap, the combined first and second bilayer thickness was measured. Third bilayer measure-

[6]This is the lipid composition and medium used for all lipid bilayers in this chapter unless otherwise stated.

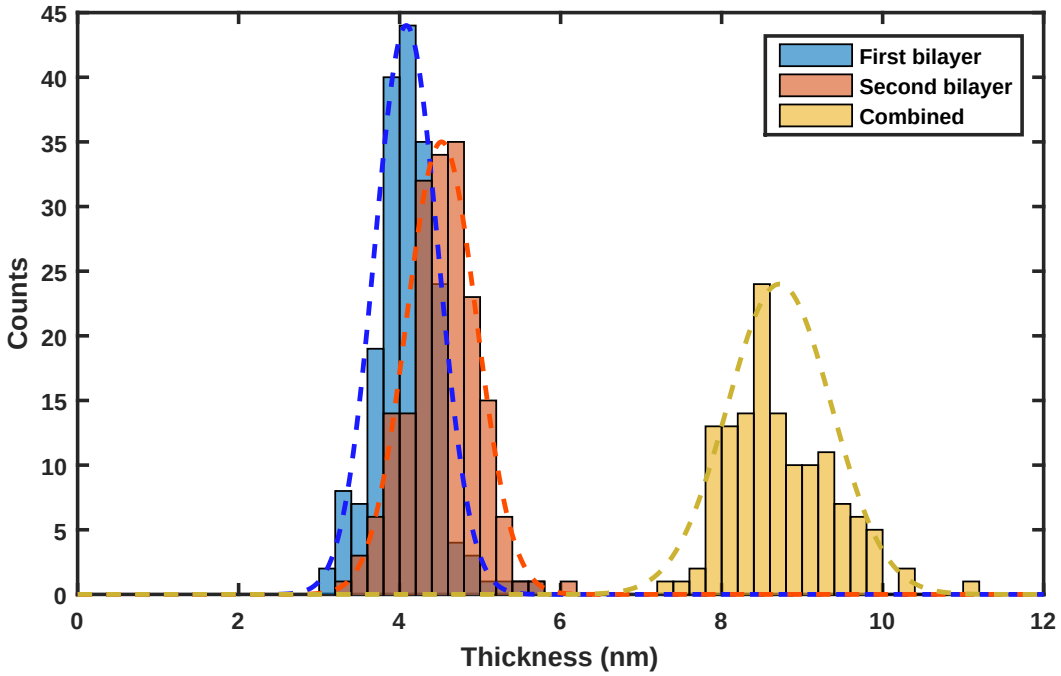

Figure 3.10: Histogram showing the distribution of measured thickness values for the first bilayer (blue, $n = 190$) and second bilayers (orange, $n = 186$) in the DOPC SLB, as well as the combined first and second bilayer measurements (yellow, $n = 134$). Gaussian fits to each of the three data sets are overlaid.

ments were taken when possible, but there were comparatively few third bilayer regions extended enough to measure in the samples.

The distribution of measured values is shown in Fig. 3.10. The mean first bilayer thickness was 4.08 ± 0.03 nm (averaged over $n = 190$ individual steps), while the second bilayer thickness was significantly larger at 4.52 ± 0.03 nm ($n = 186$). The errors given are the standard error of the mean taken over n individual line profiles. The thickness of the first and second bilayers together, as measured at points where the edges align, was 8.72 ± 0.06 nm ($n = 134$), in good agreement with the thickness expected from the sum of the individually measured thicknesses (8.60 ± 0.04 nm). The limiting factors for the error in these values is explored in Sec. 3.6.

A wide assortment of DOPC bilayer thicknesses have been reported in the literature, taken under a variety of different conditions. The second bilayer thickness measurements are in good agreement with the thicknesses of DOPC membranes reported for bilayer systems where the lipid bilayer is not in contact with the support, or the influence of the bilayer in proximity to the support is negligible. This includes the 4.57 ± 0.05 nm obtained from X-ray scattering experiments taken on multilamellar stacks in distilled water at 15°C [99], as well as the 4.62 ± 0.15 nm thickness measured in small-angle neutron scattering (SANS) experiments on unilamellar vesicle suspensions at 25°C [100]. In contrast, our first bilayer thickness value is close to the 3.98 ± 0.60 nm obtained for an SLB on a piranha etched silicon surface by spectroscopic ellipsometry [101].

Comparing our measurements with those in the literature would therefore seem to indicate that the second bilayer thickness in our system is the same as that of a 'free' DOPC bilayer, while the first bilayer thickness is being somehow reduced. However since the number of third bilayer (the bilayer formed on top of the second

bilayer) measurements from this data set is very small (4.11 ± 0.22 nm, $n = 8$), it was not possible from this data set to definitively establish whether the observed effect was due to a reduction in the optical thickness of the first bilayer, or an increase in the optical thickness of the second.

This question was addressed using data taken from earlier measurements taken on an SLB prepared using a previous lipid stock[7], where there were more third bilayer regions that could be measured. When comparing this data to the more recent data, it is important to note that measurements on samples prepared using this first stock showed consistently lower bilayer thickness values than measurements taken using the second stock. We attribute this to peroxidation of the lipids, as this is known to result in reduced bilayer thickness values [102]. Aside from the lipid stock however, the sample was identical in terms of the nominal lipid composition and surface treatment, and also used PBS as a hydration medium.

In this sample, the first bilayer thickness was 3.80 ± 0.02 nm ($n = 186$), the second bilayer thickness was 4.13 ± 0.02 nm ($n = 186$), and the third bilayer thickness was 4.06 ± 0.10 nm ($n = 27$). This sample shows the same reduction in the first bilayer thickness compared to the second. While the absolute thickness difference is smaller here (0.33 ± 0.03 nm for the first stock sample compared to 0.44 ± 0.03 nm for the sample prepared using the second stock), the relative difference is similar, at $(8.1 \pm 0.7)\%$ for the first stock compared to $(9.7 \pm 0.9)\%$ for the second stock.

In this data set, the third bilayer thickness is equal, within error, to the second bilayer thickness. Additionally, the combined second and third bilayer thickness (again, measured at joint edges) was 8.28 ± 0.20 ($n = 20$) is the same within error as double the second bilayer thickness (8.27 ± 0.49 nm). These data confirm that the observed thickness difference between the first and second bilayers is the result of a thickness reduction in the first bilayer, and that the second bilayer (and other bilayers not in direct contact with the support) has a thickness similar to that of free-standing bilayers.

One possible explanation for this thickness difference relates to the sample preparation conditions. Before having lipids spin coated over their surface, the glass coverslips are treated using piranha solution (as described in Sec. 2.2), which has the dual purpose of cleaning the glass surface of organic debris, and rendering the glass hydrophilic, the latter serving to facilitate SLB formation. Given that sulphur is a strong oxidising agent, one possible explanation for the reduced thickness in the first bilayer is that residual piranha solution on the glass coverslips is reacting with the first bilayer. Indeed, both lipid components of the bilayer, DOPC and ATTO488-DOPE, are particularly susceptible to oxidation, because of the double bond within each of their oleic acid chains.

It is known from molecular dynamics simulations that oxidised bilayers show reductions in thickness [102], and this thickness reduction might be caused by a number of different mechanisms. Firstly, the oxidised forms of DOPC may have significantly shortened hydrocarbon chains. This can be seen in Fig. 3.11, where an example of a oxidised form of DOPC is compared with the normal structure of a DOPC molecule. Additionally, many of these oxidised hydrocarbon tails are partially hydrophilic at the site of oxidation due to the incorporation of a polar oxygen group,

[7]This previous stock will henceforth be referred to as the first lipid stock. Preliminary measurements with the first stock gave thickness values comparable to the second stock (first bilayer 3.99 ± 0.05 ($n = 65$), second bilayer 4.50 ± 0.09 ($n = 45$)), while the measurements discussed in the text, which were taken approximately one year later showed reduced thickness.

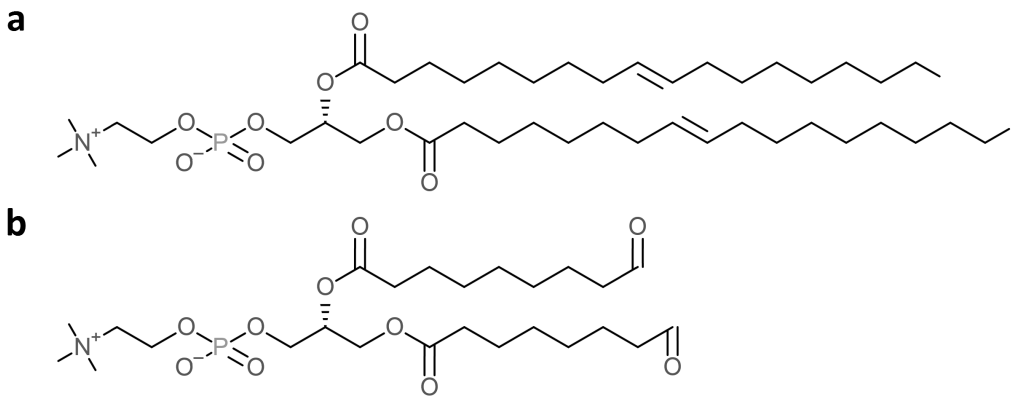

Figure 3.11: A figure showing a) the chemical structure of DOPC, and b) an example of one of many possible oxidised forms of DOPC [102].

such as in the aldehyde group at the end of the lipid tails in Fig. 3.11b. This can result in the chains 'looping up', back towards the aqueous medium [102], disrupting the bilayer structure and reducing thickness.

To investigate this possibility, an alternative surface treatment was tested, that rendered the surface hydrophilic without needing sulphur. This treatment involved sonicating the coverslip in successive baths of different solvents before ultimately being stored in a bath of H_2O_2. This H_2O_2 cleaning procedure is described in more detail in Sec. 2.2. To verify that the H_2O_2 surface treatment was equivalent in terms of its chemical effect on the surface (aside from the use of sulphur) the hydrophilicities of piranha etched and H_2O_2 cleaned surfaces were quantified by measuring the contact angle as described in Sec. 2.4. While the piranha etched surface had a contact angle, θ, of $(3.4 \pm 0.1)°$, the H_2O_2 cleaned surface had a slightly lower contact angle, $\theta = (4.9 \pm 0.3)°$, indicating a slightly lower hydrophilicity[8].

The measurements of a bilayer formed from the second lipid stock on the H_2O_2 cleaned surface gave a mean first bilayer thickness of 4.23 ± 0.02 nm ($n = 454$), a mean second bilayer thickness of 4.68 ± 0.03 nm ($n = 342$), and a mean third bilayer thickness of 4.58 ± 0.12 nm ($n = 10$). Again, the first bilayer showed a markedly reduced thickness compared to the second and third, which were the same within error. The relative difference was $(9.7 \pm 0.6)\%$, the same within error as for the second lipid stock sample on the piranha etched surface. This indicates that the observed effect is not the result of contaminants left over from the piranha etching procedure.

Given that the mechanism of bilayer formation in spin-coating is different to that of other techniques such as SUV rupture, in that it involves the hydration of a dry lipid film, it was decided to test whether bilayers formed using a different technique would show a similar thickness reduction. This was done by using bilayer patches, which were produced by using osmotic pressure to induce the rupture of GUVs adhered to the coverslip surface, as described in Sec. 2.5. This process is similar to the SUV rupture procedure which is most commonly used for SLB preparation; however GUV rupture doesn't form a continuous bilayer, but separate patches created from individual GUV rupture events, from which thickness measurements can be made at the edges. An example of such a patch is shown in Fig. 3.12.

[8]Errors given are the standard deviation derived from the eight different pixel calibrations.

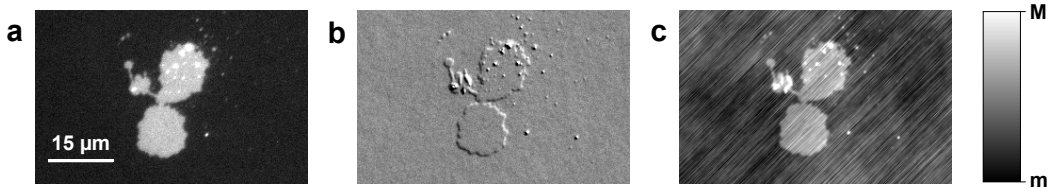

Figure 3.12: Images of a lipid bilayer patch, scaled from m to M. a) fluorescence (m = 0 pe to M = 150 pe), b) qDIC contrast (m = -0.00250 to M = 0.00206), and c) qDIC phase (m = -8.79 mrad to M = 3.40 mrad).

The GUVs were formed from the second lipid stock in distilled water (DW). The GUVs were allowed to associate with the piranha etched glass surface of the coverslip before being induced to rupture by the addition of PBS, which created the necessary osmotic gradient across the bilayer. The thickness of these patches measured using qDIC was 4.13 ± 0.05 nm (n = 56). While there were no second bilayer regions where the thickness difference in this sample could be measured directly, the first bilayer thickness of the patches was very close to that measured for the spin-coated samples formed using the second lipid stock, indicating that preparation technique is not a factor which influences the first bilayer thickness.

3.4 Factors Affecting Supported Bilayer Thickness

In an effort to understand the origin of the thickness reduction in the first bilayer, a number of different factors which influenced the magnitude of this thickness reduction were identified. The two most important of these were the total bilayer coverage, and the hydrophilicity of the glass coverslip. Because these two effects must be disentangled from each other to be properly understood, the effect of bilayer coverage will be addressed first.

While spin coating can produce extremely consistent bilayers with few gaps [55], we have adjusted the parameters such that there are many edges over which the bilayer thickness can be measured. This results in a sample where the coverage can vary greatly in different regions, from areas having almost total coverage aside from a few very small gaps, to regions in which there is effectively no contiguous bilayer at all, only independent bilayer patches a few microns in size, reminiscent of the bilayer patches fabricated from GUVs. Thus far, we have neglected the influence of this parameter, and the data presented in Sec. 3.3 is averaged over data from regions where the coverage ranges from 24.5% to 99.8%.

To understand the effect of coverage, the local bilayer thickness difference was investigated. We define the local thickness difference as the difference between the mean first bilayer thickness measured within a given field of view, and the mean second bilayer thickness averaged over the whole sample, under the assumption that since the second bilayer behaves as a free floating bilayer, it shouldn't be affected by the first bilayer coverage and the second bilayer thickness should be the same everywhere. This was done to allow for sufficient statistics for the second bilayer thickness. The local thickness difference was plotted against the the area fraction of the glass covered with lipid bilayer within the field of view for all the measurements taken with the first lipid stock, as shown in Fig. 3.13.

While the measurements use a variety of different experimental parameters (the effect of which on the thickness difference will be discussed later), the thickness

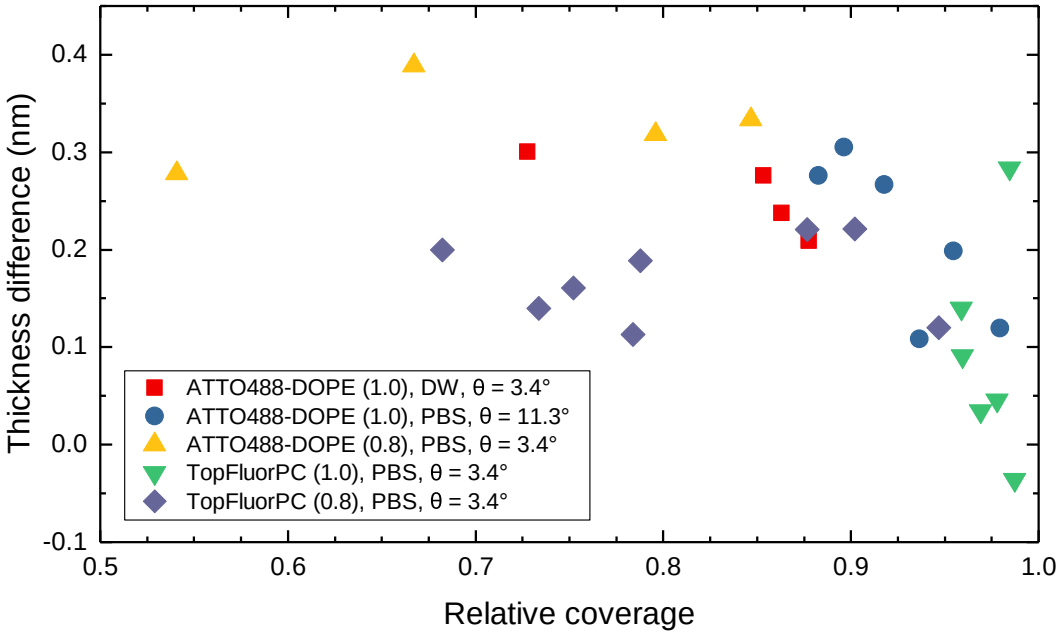

Figure 3.13: Local bilayer thickness differences against local bilayer coverage for experiments carried out using the first lipid stock. The legend describes the fluorophore (total lipid concentration in mg/ml), hydration medium and contact angle.

difference exhibits a clear behaviour as the coverage is varied. In the coverage range from 90% to 100%, the thickness difference gradually reduces with increasing coverage, reaching close to zero near the point of 100% coverage. In contrast, below 90%, there seems to be no clear effect of coverage on the thickness difference. This seems to suggest that the thickness difference increases as coverage is reduced from 100% down to 90%, below which the first bilayer thickness is not dependent on coverage.

While the effect of surface coverage on the first lipid stock was immediately evident, measurements taken using the second lipid stock showed a far less convincing relationship. A scatter plot for the samples prepared using the second lipid stock is shown in Fig. 3.14. In this plot, the clear dependence on coverage above 90% is absent, and the thickness difference seems to be insensitive to the coverage for all parameters tested. The absence of a clear relationship may be a result of the high level of noise in the data (the error on each point is typically around 0.1 nm).

In spite of the lack of a clear relationship in the data for the second lipid stock, in order to eliminate possible effects of coverage on the thickness difference, all first bilayer thickness measurements taken in regions with above 90% bilayer coverage were removed from the analysis, including for measurements taken on bilayers prepared with the second stock. For the measurements on the samples discussed in Sec. 3.3, the first bilayer thickness becomes 4.08 ± 0.03 nm (n = 179) and 4.20 ± 0.02 nm (n = 234) for the bilayers formed from the second lipid stock on piranha etched and H_2O_2 cleaned surfaces respectively, and 3.81 ± 0.02 nm (n = 184) for bilayers formed on piranha etched surface from the first stock. All mean first bilayer thickness values presented for the remainder of this section are taken from regions where the coverage is below 90%.

The other key parameter that was found to affect the thickness difference was

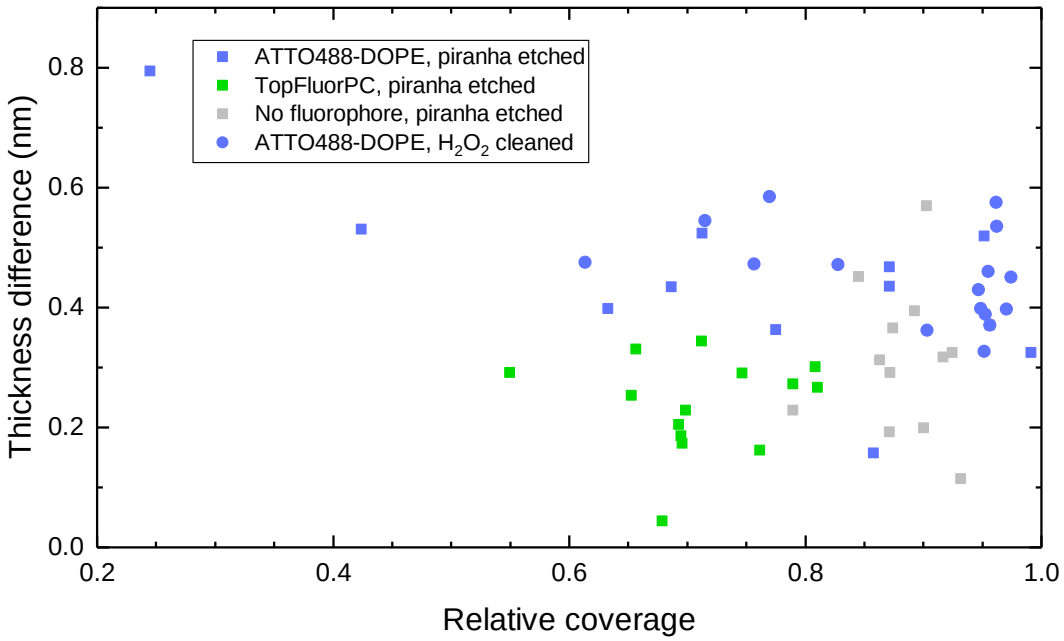

Figure 3.14: Local bilayer thickness differences against local bilayer coverage for experiments carried out using the second lipid stock. The legend describes the fluorophore and surface treatment. All samples formed in PBS.

hydrophilicity. The hydrophilicity of the SLB substrate is known to affect lipid diffusion rates and domain formation within the bilayer [103], as well as the degree to which bilayers can slide over the support [104]. In order to test whether it was having any effect on bilayer thickness, two new samples were prepared. In one, an SLB was formed on an etched coverslip that was left in air and stored at room temperature for six days in order to reduce its hydrophilicity, while another SLB was formed on a coverslip that was only cleaned by wiping with acetone, and was not piranha etched.

The results of this are shown on Fig. 3.15. For comparison, the results from the freshly piranha etched surface are shown for both the first and second lipid stock. It can be seen that as the surface hydrophilicity decreases (increasing contact angle), the thickness of the first bilayer relative to the second increases until for the non-etched surface the first bilayer thickness has a value approximately equal to that of the second. This suggests that the surface hydrophilicity is causing the observed thickness difference.

Strictly speaking, the piranha solution has two effects on the glass surface; not only rendering it hydrophilic, but also increasing its nanoscopic roughness [105][9]. This effect complicates our interpretation of the contact angle measurements as such nanoscale surface roughness can itself affect wettability [106], and thus contact angle. Still, it is unlikely that this is responsible for the observed thickness reduction however, given that surface roughness reduces substrate-bilayer interactions [37]. Furthermore, since the same thickness difference was observed on the H_2O_2 cleaned glass discussed in the previous section, we can be reasonably certain that the observed effects are the result of hydrophilicity, not roughness.

[9]Such an increase in nanoscale roughness does not affect light scattering at the coverslip surface and so does not influence the image quality.

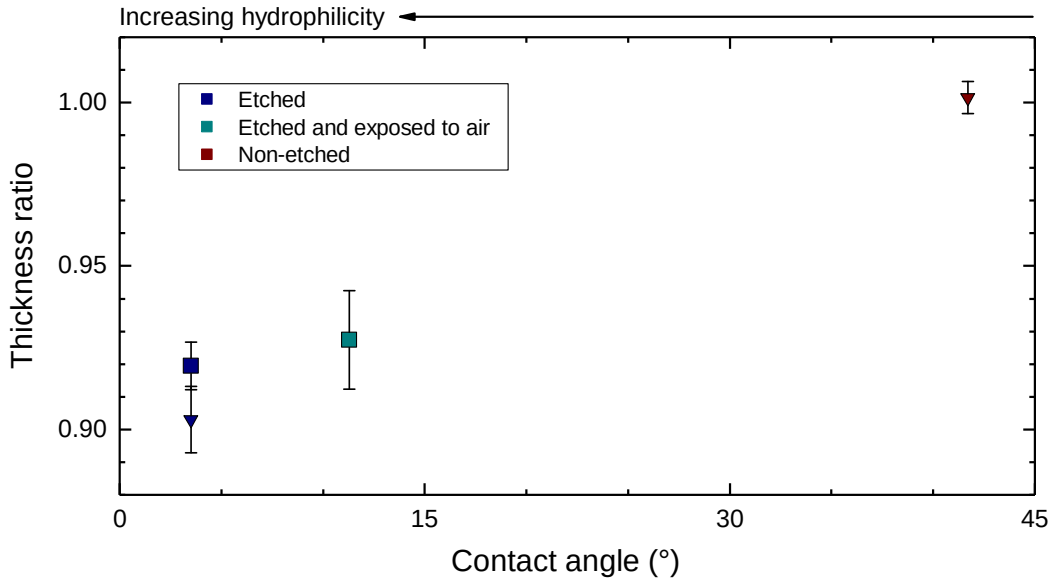

Figure 3.15: Variation of the ratio of the thickness of the first bilayer to the second, plotted against the hydrophilicity of the surface. Measurements taken using the second stock are denoted by inverted triangles, while data taken with the first stock are denoted using squares.

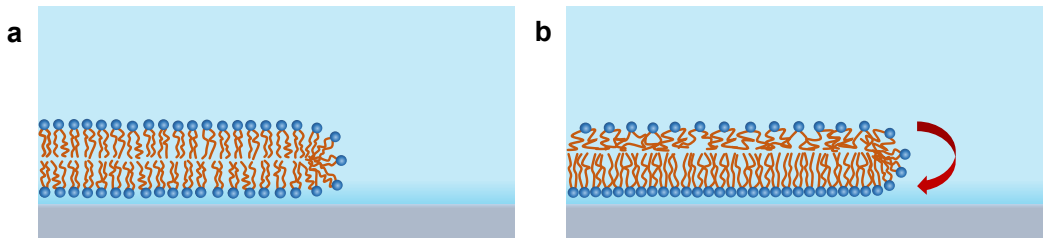

Figure 3.16: An illustration showing how movement of lipids between leaflets of the lipid bilayer could cause the thickness difference. Panel a) shows the unperturbed state of the bilayer, while panel b) shows the interleaflet movement of lipids due to the attraction of the lipids to the hydrophilic substrate, which causes the density difference between apposing leaflets.

This observation that surface hydrophilicity affects the lipid bilayer is consistent with computational studies that have investigated the bilayer-substrate interaction. These studies have suggested that close proximity to the hydrophilic support induces a movement of lipid molecules from the upper (facing away from the support) leaflet to the lower (support facing) leaflet of the bilayer, driven by the attractive interaction between the lipid headgroups and the support [107]. It is this effect, illustrated in Fig. 3.16, that we hypothesise to be the cause of the reduction in the first bilayer thickness.

The lipid movement would create two competing effects on the measured bilayer thickness; a loss of lipid density from the upper leaflet which reduces the optical thickness, and an increase in lipid density in the lower leaflet which increases the optical thickness. Our data suggest that the depletion of lipids from the upper leaflet is the dominant effect, consistent with these computational studies. Coarse-grained molecular dynamics simulations [107] have indicated that the resistance of the lower leaflet to compression should result in the bilayer undergoing an overall

area expansion with increasing interaction energy, which by volume conservation would lead naturally to the reduction in thickness that we measure experimentally.

In order to explain the observed 10% thickness reduction, the upper leaflet would have to undergo an areal expansion of approximately 20%. This may seem high given that the typical rupture strain of supported lipid bilayers is around 2% [46], but ruptures require regions of low hydrophobic density in both leaflets in order to form [108], and the tight lipid packing in the lower leaflet would prevent this. The stress in the upper leaflet counterbalances the difference in surface energy between upper and lower leaflet, leading to an equilibrium. The lower leaflet is under a corresponding compressive stress; however, under compression the leaflet shows a hard-core repulsion [109], making the strain in the lower leaflet much less than in the upper leaflet, thus not compensating the change in surface density.

As we measure optical thickness, which is dependent not only on sample thickness but refractive index as well, the thickness difference we observe in our data might be at least partially caused by a change in refractive index of the bilayer. Assuming that the refractive index undergoes its maximum possible change, from the ordinary index 1.445, to the extraordinary index 1.460 [29], the first bilayer thickness would appear to be 3.98 nm thick (assuming the true thickness is equal to that of the second bilayer). This is close to our first bilayer thickness of measurement 4.08 $\pm$ 0.03 nm. Despite this, a change in refractive index is unlikely to be the sole cause of our measurements. It is improbable that the bilayer could rearrange itself so dramatically as to assume the extraordinary refractive index at normal incidence. Furthermore, the 9.7% reduction in thickness we find is in good agreement with computational studies which predict that the thickness of bilayers in close proximity to the support should be reduced by approximately 10% [110].

The previously discussed effect of local coverage on the thickness difference can also be understood in the context of this hypothesis. In regions of low coverage, every position within the bilayer is close to an exposed bilayer edge where the two leaflets are linked, as shown in Fig. 3.16. At these edges, lipids can move between the two leaflets, enabling the attraction of lipids to the lower leaflet that our interpretation suggests is the driving force for the thickness difference. In contrast, where there is high bilayer coverage, such edges are rare, and the only way for lipids to move between leaflets is by moving through the bilayer interior (so-called 'flip-flop'); this is an extremely slow process due to the high penalty associated with moving the hydrophilic lipid headgroup through the hydrophobic bilayer interior, taking place over a period of hours or even days, much longer than the timescale of the experiments [2]. As such the lack of edges would be expected to suppress the thickness difference.

The apparent lack of this coverage effect in the data with the second lipid stock is puzzling however, as the need for edges as sites of lipid movement between leaflets shouldn't be affected by the use of a different lipid stock. In contrast, it would be more intuitive for the first stock to show a weaker coverage effect. After all, we have attributed the lower thickness of the lipids in the first stock to lipid oxidation, and such oxidation should enhance the flip-flop rate within the bilayer [102], reducing the need for edges to establish a density difference in the bilayers formed from the first stock. No significant differences in the appearances of the DOPC bilayers was observed between the first and the second stock.

A possible explanation might arise from the changes to the intrinsic curvature of the lipids upon oxidation. The movement of lipids over the bilayer edges should

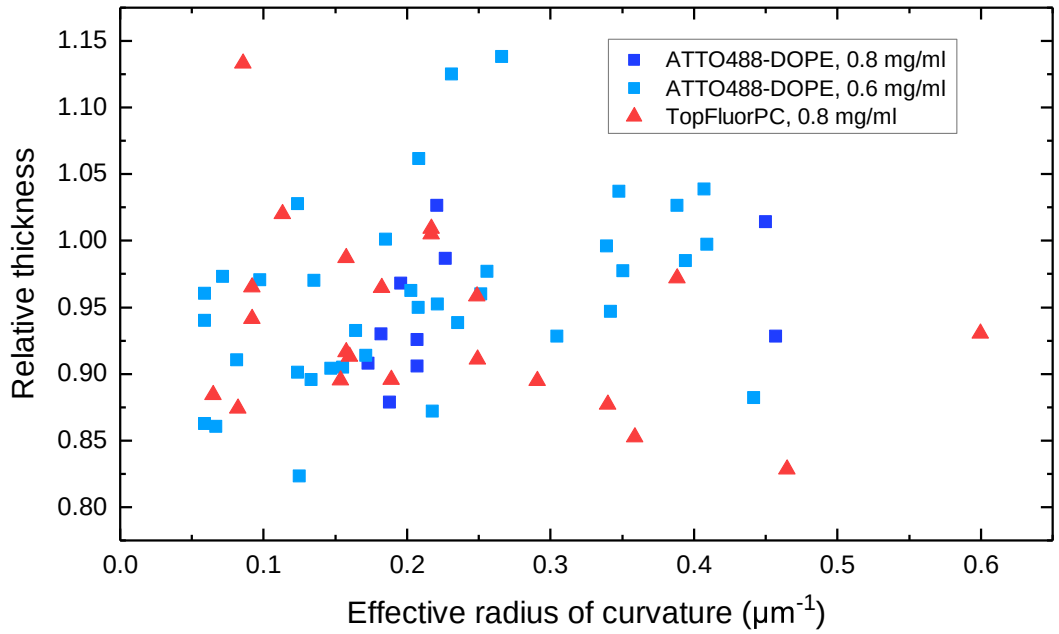

Figure 3.17: Thickness of individual first bilayer patches relative to the sample average second bilayer thickness plotted against the effective patch radius of curvature ($\sqrt{\pi/A}$). The fluorophore used and the spin coating concentration are given in the legend.

be dependent not only on the total length of available edges, but also the ease with which lipids can move across those edges. Oxidation alters the relative head-to-tail area, resulting in lipids which prefer regions of strong positive curvature, such as the bilayer edges [35]. This is in contrast to the neutral curvature of normal DOPC. In the partially oxidised sample, in order for a normal DOPC molecule to move between leaflets, it would have to displace an oxidised lipid from the edges, incurring an energetic penalty due to the shape mismatch. Therefore, in the samples made using the peroxidised stock, the increased barrier to movement between leaflets makes the total length of edges more important for the establishment of the thickness difference than in the non-oxidised DOPC stock, where the lipids are much freer to move.

This explanation for the discrepancy is highly speculative however, and we have no direct evidence to support it. This might be tested by deliberately oxidising some of the second stock to see if the same behaviour is replicated. Another possibility would be labelling the oxidised lipids to measure their localisation, to determine whether they are preferentially distributed at the edge regions. The latter approach would be problematic however, as fluorescent labelling would also alter the lipid intrinsic curvature, and may not have the required sensitivity.

Another aspect of the coverage that might affect the thickness difference is the size of the individual bilayer patches. For patches not connected to the larger SLB, line tension at the bilayer edge should favour minimising the perimeter-to-area ratio of each patch, which might therefore lead to more compressed patches. This in turn should lead to an increased thickness of the first bilayer relative to the sample average second bilayer thickness. Since the thickness should therefore be inversely proportional to the size of the patches, to investigate this the relative thickness of individual bilayer patches was plotted against their radius of curvature estimated

from the measured patch area A ($1/R = \sqrt{\pi/A}$), as shown in Fig. 3.17. It should be noted that since the patches were frequently not circular, this estimated radius of curvature does not actually describe the degree of curvature at the patch edges. It can be seen in Fig. 3.17 that there is no relationship between the two parameters. As such, it seems that if the patch size does affect the thickness difference, the effect is smaller than our ability to measure.

In spite of the aforementioned theoretical studies [107, 110] predicting substrate-induced thickness reductions, there have been very few experimental reports of thickness changes in the first supported bilayer in the literature. This is likely due to a combination of factors. Firstly, most SLB systems are deliberately designed to be unilamellar, so there would be no other bilayers for comparison. Another issue is that highly sensitive techniques such as X-ray and neutron scattering are not sensitive to changes in individual bilayers, for the reasons outlined in Sec. 1.3, and so any reduction in the first bilayer thickness is lost under the influence of the many other bilayers which are not affected by the support. Spin coated bilayers have been studied using AFM [55, 56], without any thickness difference being reported, but any discrepancy between the first and second bilayer thicknesses observed might have been dismissed as the result of the uncertain hydration layer thickness.

Interestingly, a previous study using imaging ellipsometry (which, like qDIC is a spatially resolved technique) on spin-coated POPC bilayers found that the apparent first bilayer thickness was actually increased relative to the second and third bilayers in the stack, by approximately 1.2 nm [111], the reverse of what we observe. While the authors attribute this to the presence of a 1.2 nm thick ordered water layer with a refractive index of 1.50 [111], this might however be another example of the substrate (in their case a plasma oxidised silicon wafer [111]) affecting bilayer thickness.

Direct comparison of their results with ours is difficult because they do not state the hydrophilicity of their surface. The fact they observe an increase rather than a thickness decrease as we observe might be the result of any of several factors. Firstly, the lipid species they use, POPC, might have a different response to the movement of lipids between leaflets. While DOPC and POPC have the same headgroup (and therefore their interaction with the surface would be expected to be the same), their tails are different and so the equilibrium forces that govern the balance between lipid loss in the upper leaflet and lipid gain in the lower leaflet might be different. Secondly, this work assumes that both the ordinary and extraordinary refractive indices are the same for all bilayers in the film [111]. It may be that movement of lipids between leaflets alters the birefringence of the bilayer, making their calculated thickness value erroneously large.

While reductions in the thickness of the first bilayer have not been reported in the literature, the movement of lipids between leaflets in response to the presence of the substrate that we believe to be the driving force behind the thickness difference has been. In one interesting set of experiments, it was found that in SLBs formed on plasma etched surfaces from binary mixtures of different lipids (DOPC/DPPC, DLPC/DPPC, and DMPC/DPPC), the DPPC was enriched in the lower leaflet, while the other components were enriched in the upper leaflet [112]. At 25 °C, the asymmetry was strongest in the DLPC/DPPC system, then the DMPC/DPPC system, and weakest in the DOPC/DPPC system. In contrast, at 55°C, the order of asymmetry was reversed, with the bilayer containing DOPC being more asymmetric than that of the DLPC containing bilayer [112].

While the authors (having excluded lipid phase state and intrinsic curvature) didn't speculate on a mechanism beyond lipid-substrate interactions [112], this result can be understood in terms of our model. Due to the surface hydrophilicity, the most energetically favourable state of the SLB is one that maximises PC headgroup proximity to the substrate, while minimising penalties incurred by stretching the upper leaflet. At 25 °C, the DPPC is in the gel phase, and so has the highest equilibrium density, favouring its partition into the lower leaflet. Because of the high density of lipids in this phase, the upper leaflet would experience minimal stretching, so it would be most favourable for the system to enrich the upper leaflet with lipids with low area per lipid (from greatest to smallest L_d phase area per lipid DOPC > DPPC > DMPC > DLPC), in order that the total area of each leaflet matched. This results in the strongest upper leaflet enrichment for lipids with areas closest to S_o phase DPPC like DLPC. On the other hand, at 55 °C, DPPC is in the L_d phase and so is more spread out laterally. The upper leaflet would therefore have the strongest preference for a lipid which has the lowest penalty for stretching, which would be DOPC.

Thus our observations help in the interpretation of previous studies in the literature, where substrate effects have either gone unexplained or been ignored. It is important to consider that the mechanism by which we show this thickness difference is established (specifically by lipid movement over bilayer edges) is not unique to the spin coated SLB system. Indeed, during the formation of SLBs by vesicle rupture, there are many exposed edges over which lipids can move [112]. Many experiments are carried out on SLBs where the total coverage is low enough that lack of edges cannot limit the hydrophilicity effect [71, 112]. This hydrophilicity induced thickness difference may therefore be present in a wide variety of SLB systems used in the literature.

Other factors affecting the bilayer thickness were investigated. One of particular interest was the choice of fluorophore. All experiments described so far had been carried out using the ATTO488-DOPE fluorophore, which has a chemical structure as shown in Fig. 3.18a. The ATTO488 fluorophore is attached to the DOPE lipid at the headgroup, and so since the headgroup of the lipids is oriented towards the hydrophilic support, it was plausible that changing the lipid headgroup might alter the lipid interaction with the support in a way which affected the bilayer thickness.

To test this, SLBs were prepared from two alternative lipid mixtures. In one, an SLB was prepared using DOPC with a different fluorophore, TopFluorPC (included at the same 0.1 mol% concentration as used for ATTO488-DOPE), which has a fluorescent tag attached at the end of one of its tails and a phosphocholine headgroup identical to that of the surrounding DOPC molecules. It would be expected then that TopFluorPC would not affect the interaction between the headgroup and the support. In the other, the bilayer was formed from pure DOPC, with no fluorescent label at all.

For the bilayers formed from DOPC only, the first bilayer thickness was 4.06 ± 0.03 nm ($n = 152$), the second bilayer thickness was 4.38 ± 0.03 nm ($n = 181$), and a third bilayer thickness of 4.26 ± 0.05 nm ($n = 38$). The bilayers that were labelled with TopFluor has similar thickness values, 4.13 ± 0.02 nm ($n = 408$) for the first bilayer, and 4.37 ± 0.03 nm ($n = 238$) for the second.

The thickness difference between the first and second bilayers is significantly larger in the ATTO488-DOPE labelled samples (0.44 ± 0.04 nm) than in either the unlabelled (0.32 ± 0.04 nm) or TopFluorPC labelled (0.24 ± 0.03 nm). The second

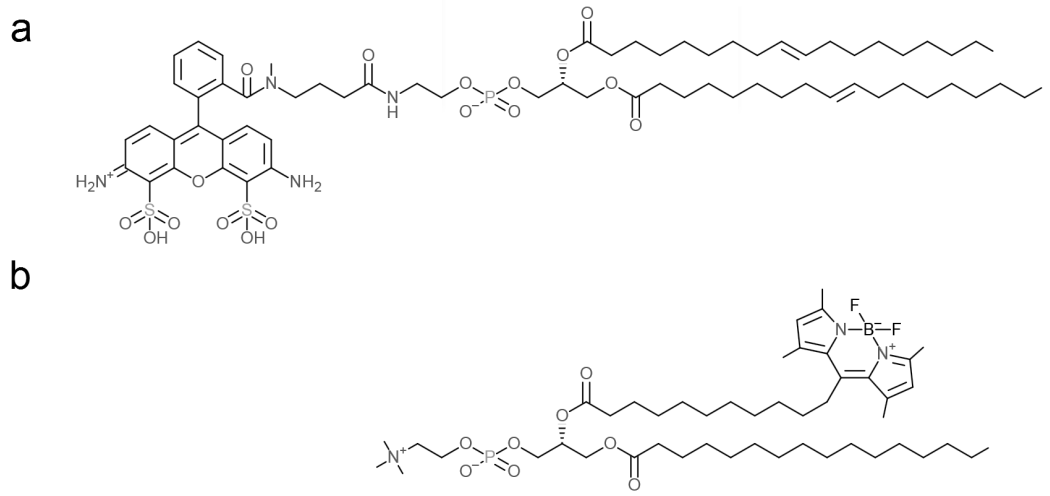

Figure 3.18: The chemical structure of two different fluorophores, a) ATTO488-DOPE and b) TopFluorPC.

bilayer thickness is also lower for the unlabelled and TopFluorPC labelled samples by approximately 0.2 nm, which may indicate that the choice of fluorophore affects the equilibrium thickness of the lipid bilayer also. Age related peroxidation of the lipid stock can be excluded, as later second bilayer thickness measurements carried out with ATTO488-DOPE using the same stock had approximately the same second bilayer thickness as for the previous measurements with ATTO488-DOPE.

Why the choice of fluorophore should affect the thickness difference is unclear. Previous experiments have shown that PC lipids with the fluorophore BODIPY attached at the hydrocarbon tail group (BODIPY is the fluorescent group of TopFluorPC) have a negligible effect on the overall thickness (within $\pm$ 0.1 nm) and refractive index (within $\pm$ 0.0005) of the first bilayer of an SLB up to concentrations 40 times higher than used here [113], in stark contrast to our results which show that just 0.1 mol% TopFluorPC reduces the hydrophilicity-induced thickness difference. The ATTO488 fluorophore is unlikely to be interacting with the support itself, given previous experiments have shown that fluorophores with large hydrophilic headgroups seem to be excluded from the lower leaflet of the bilayer [50].

It may be that the large ATTO488 fluorophore increases the effective size of the lipid headgroup to an extent which allows it act as an 'umbrella', shielding the hydrophobic tails in the upper leaflet from water as the upper leaflet is stretched, in a manner analogous to how cholesterol is shielded from the medium by lipids with larger headgroups. This would reduce the energetic penalty of stretching, and shift the equilibrium point towards more lipid movement. Alternatively, the presence of ATTO488-DOPE might increase the bilayer refractive index, making it appear thicker.

A final factor which appears to affect bilayer thickness is the hydration medium. Previous experiments in the literature have shown that media with high ionic strength can shield the lipid bilayer from the influence of the support [114]. The PBS medium of the previous experiments has a high ionic strength (the manufacturer gives the osmolality of its PBS solution as between 280 and 315 mOsm/kg), so it would be expected that the effect of the support should be greater in a medium with low ionic strength such as DW.

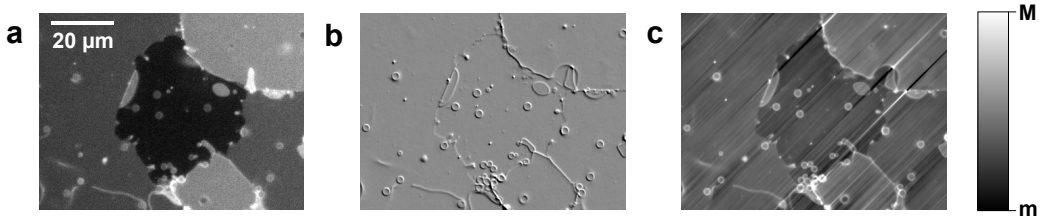

Figure 3.19: A representative region of an SLB formed in distilled water, on a greyscale scaled from m to M, shown in a) fluorescence (m = 0 pe, M = 125 pe), b) qDIC contrast (m = -0.0012, M = 0.0010), and c) qDIC phase (m = -3.7 mrad, M = 2.1 mrad).

The SLB sample formed in DW has significantly more adhered vesicles and other lipid debris, as can be seen in Fig. 3.19. These other structures frustrated the analysis by creating integration artefacts and obscuring bilayer edges, resulting in fewer line profiles being obtained from the fields of view. Despite this, enough measurements were taken to establish that the thickness of the lipid bilayer in DW was significantly thicker than in PBS. The first bilayer thickness was 4.83 ± 0.06 nm (n =79) and the second bilayer thickness was 5.41 ± 0.16 nm (n = 27). The relative thickness difference is 10.6%, which is similar to that measured for SLBs formed in PBS.

Our observation that bilayers are thicker in distilled water than the relatively high ionic strength PBS solution is surprising given previous literature showing that high ionic strength increases bilayer lateral compression [114, 115], and for sufficiently high ionic strengths increases bilayer thickness [116, 117]. For example, dual polarisation interferometry experiments assuming a fixed, isotropic bilayer refractive index have shown that addition of 2 mM Ca^{2+} increases the thickness of a DOPC bilayer by almost half a nanometre [118].

It is known that the nature of the interaction between ions and the lipid bilayer varies greatly depending on the charge, size, valency and concentration of the ions used [116], as well as bilayer composition and phase [117, 118], and bilayer thickness has also been found to decrease with increasing osmolarity within certain ionic strength ranges [117]. However, AFM measurements of gel phase bilayers in PBS solutions with the same ionic strength as used in our experiment have shown an overall increase in lateral bilayer compression [115], which would be expected to produce an overall increase in bilayer thickness from volume conservation arguments.

One possibility is that the refractive index of distilled water is incorrect. However, in order to obtain a thickness value equal to that measured in PBS (4.08 ± 0.03 nm), the refractive index of the distilled water would have to be 1.314, which is much lower than would be expected for water at room temperature at 550 nm. This can therefore be discounted as a possibility.

Also counter-intuitive is the observation that the change in bilayer thickness is unaffected by the presence or absence of ions, given that multiple experiments have previously demonstrated that the presence of ions can block bilayer-substrate interactions [114], resulting in the bilayer properties becoming closer to those of a free floating membrane; for bilayers formed on mica for example, sufficiently high ionic strengths can prevent decoupling of the main (gel-to-fluid) phase transition on different leaflets of the bilayer [114]. A more comprehensive investigation of the relationship between the ionic strength of the hydration medium and bilayer thickness could be conducted with qDIC in the future.

Parameters					Thickness (nm)		
Fluorophore	Stock	Surface treatment	Medium	θ (°)	1st bilayer	2nd bilayer	3rd bilayer
ATTO488-DOPE	Second	Piranha etch	PBS	3.4 ± 0.1	4.08 ± 0.03 (n = 178)	4.52 ± 0.03 (n = 186)	4.11 ± 0.22 (n = 8)
ATTO488-DOPE	Second	H_2O_2 clean	PBS	4.9 ± 0.3	4.20 ± 0.02 (n = 234)	4.68 ± 0.03 (n = 342)	4.58 ± 0.12 (n = 10)
ATTO488-DOPE	Second	Acetone clean	PBS	41.7 ± 2.3	4.65 ± 0.01 (n = 778)	4.64 ± 0.02 (n = 518)	4.52 ± 0.06 (n = 56)
TopFluorPC	Second	Piranha etch	PBS	3.4 ± 0.1	4.13 ± 0.02 (n = 408)	4.37 ± 0.03 (n = 238)	N/A
N/A	Second	Piranha etch	PBS	3.4 ± 0.1	4.06 ± 0.03 (n = 152)	4.38 ± 0.03 (n = 181)	4.26 ± 0.05 (n = 38)
ATTO488-DOPE	First	Piranha etch	PBS	3.4 ± 0.1	3.81 ± 0.02 (n = 184)	4.13 ± 0.02 (n = 186)	4.06 ± 0.10 (n = 27)
ATTO488-DOPE	First	Piranha etch	PBS	11.3 ± 0.7	3.71 ± 0.05 (n = 44)	4.00 ± 0.03 (n = 106)	4.04 ± 0.06 (n = 35)
ATTO488-DOPE	First	Piranha etch	DW	3.4 ± 0.1	4.83 ± 0.06 (n =79)	5.41 ± 0.16 (n = 27)	7.36 ± 0.78 (n = 2)

Table 3.1: Measurements of the non-normalised lipid bilayer thicknesses recorded for the different spin-coated SLB systems tested. First bilayer measurements exclude measurements taken in regions with above 90% coverage.

Parameters					Relative thickness		
Fluorophore	Stock	Surface treatment	Medium	θ (°)	1st bilayer	2nd bilayer	3rd bilayer
ATTO488-DOPE	Second	Piranha etch	PBS	3.4 ± 0.1	0.90 ± 0.01 (n = 178)	1.00 (n = 186)	0.91 ± 0.05 (n = 8)
ATTO488-DOPE	Second	H_2O_2 clean	PBS	4.9 ± 0.3	0.90 ± 0.01 (n = 234)	1.00 (n = 342)	0.98 ± 0.03 (n = 10)
ATTO488-DOPE	Second	Acetone clean	PBS	41.7 ± 2.3	1.00 ± 0.01 (n = 778)	1.00 (n = 518)	0.97 ± 0.01 (n = 56)
TopFluorPC	Second	Piranha etch	PBS	3.4 ± 0.1	0.95 ± 0.01 (n = 408)	1.00 (n = 238)	N/A
N/A	Second	Piranha etch	PBS	3.4 ± 0.1	0.93 ± 0.01 (n = 152)	1.00 (n = 181)	0.97 ± 0.01 (n = 38)
ATTO488-DOPE	First	Piranha etch	PBS	3.4 ± 0.1	0.92 ± 0.01 (n = 184)	1.00 (n = 186)	0.98 ± 0.03 (n = 27)
ATTO488-DOPE	First	Piranha etch	PBS	11.3 ± 0.7	0.93 ± 0.02 (n = 44)	1.00 (n = 106)	1.01 ± 0.02 (n = 35)
ATTO488-DOPE	First	Piranha etch	DW	3.4 ± 0.1	0.89 ± 0.03 (n =79)	1.00 (n = 27)	1.36 ± 0.15 (n = 2)

Table 3.2: Measurements of the lipid bilayer thicknesses recorded for the different spin-coated SLB systems tested normalised to the second bilayer thickness in each case. First bilayer measurements exclude measurements taken in regions with above 90% coverage.

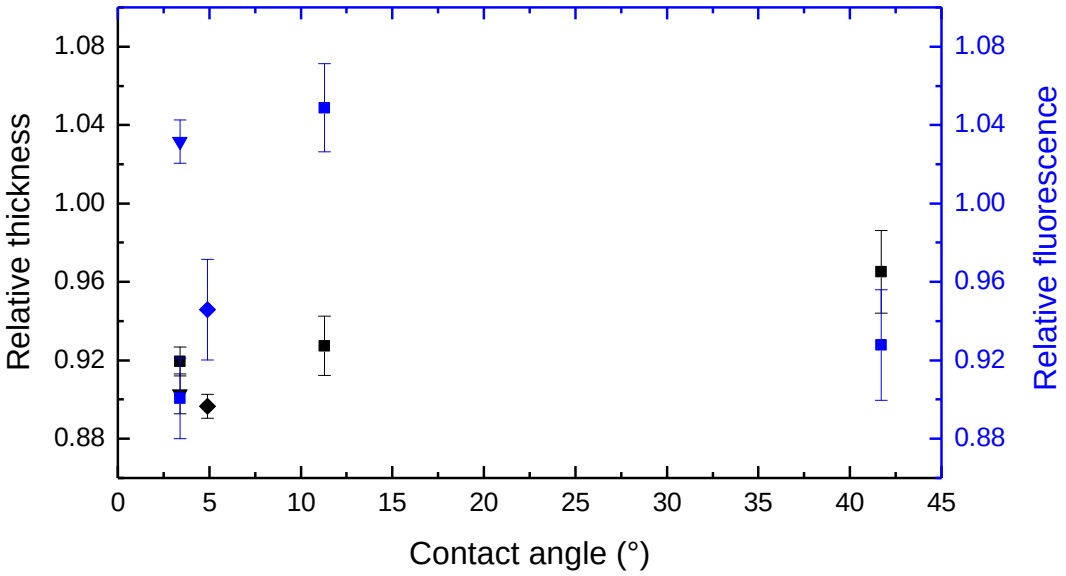

Figure 3.20: A scatter plot showing the relative changes in bilayer thickness (black) and fluorescence intensity (blue) as a function of surface hydrophilicity. Measurements made using first stock are shown as squares, second stock on piranha etched surfaces are denoted by inverted triangles, while second stock SLBs on H_2O_2 cleaned surfaces are denoted by diamonds.

3.5 Measurement of Bilayer Fluorescence Steps

In order to gain further insight into the structural changes in lipid bilayers induced by proximity to the support, the fluorescence signal from the bilayers were examined. Differences in the fluorescence intensity between bilayers might suggest differences in lipid density between bilayers, or differences in fluorophore distribution between bilayers. The same step measuring procedure for extracting the optical thickness of lipid bilayers can be used to measure the fluorescence intensity of the individual bilayers also. Steps were taken in the fluorescence images at as close to the same positions as the phase steps as was achievable.

In our interpretation of the thickness data shown in Fig. 3.16, the overall density of lipids should be lower in the first bilayer than the second (and higher) bilayers due to the stretching of the upper leaflet and the resultant net area increase of the first bilayer. As such, we would expect to see a reduction in the first bilayer fluorescence of a similar percentage to the reduction in thickness, as volume conservation would require that any reduction in thickness be accompanied by an equal increase in area. This would result in a lower fluorophore density in the first bilayer, and make the height of the step in fluorescence intensity from the glass background to the single bilayer region smaller.

In order to investigate whether the hydrophilicity induced thickness difference is accompanied by a concomitant change in the fluorescence, the mean fluorescence intensities obtained by averaging steps taken from over the whole sample ($\bar{F}_1/\bar{F}_2$) were measured, and plotted in Fig. 3.20. To allow easy comparison with the relative thickness changes, these were plotted on the same figure. Using relative fluorescence intensities has the additional benefit of excluding any possible intensity variation between samples due to differences in photobleaching during handling of the sample, exposure time and illumination intensity.

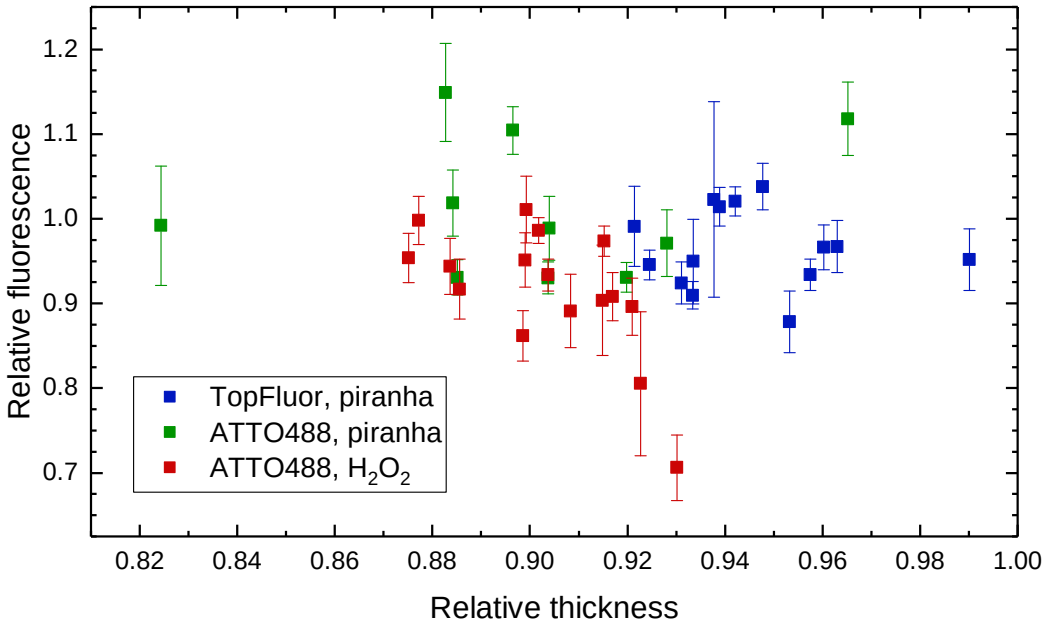

Figure 3.21: The distributions of relative bilayer fluorescence intensity measurements plotted against the relative thickness in each region of interest for the three data sets prepared using the second lipid stock.

Unlike for the bilayer thicknesses, Fig. 3.20 shows that there was not a clear relationship between surface hydrophilicity and the relative first bilayer fluorescence when ATTO488-DOPE was used as the fluorophore. The relative fluorescence differs significantly to the relative thickness in all cases. Since the ATTO488-DOPE has a large hydrophilic headgroup, it might be possible that the fluorophore itself is affecting the partitioning between leaflets in an unanticipated way. The data were therefore compared with measurements taken of the fluorescent intensity of samples labelled with TopFluorPC. However, when using TopFluorPC, the relative first bilayer intensity is 0.98 ± 0.01, which is again substantially different to the corresponding relative thickness given in Table 3.2.

This is curious, considering that the error on the fluorescence measurements is sufficiently low that it should be possible to see the effect of changes in density. The most obvious explanation for the observed lack of correlation is different levels of photobleaching between different fields of view in the same sample. Given that the contributions from each image to the mean values for the first and second bilayer measurements are different (since the number of measurements taken in each field of view are different) the effects of regional bleaching would not cancel out in the ratio $\bar{F}_1/\bar{F}_2$, and so may cause the apparent discrepancy between the first and second bilayer fluorescence data. To address this, the relative local fluorescence (F_1/F_2) was taken in each field of view, and plotted against the relative local thickness difference. The fluorescence measurements were taken relative to the local second bilayer fluorescence step, so the effect of photobleaching should be the same for F_1 and F_2 and thereby cancel out. Thicknesses were taken relative to the second bilayer thickness measured across the whole sample as before.

The results were plotted in Fig. 3.21. Again, no relationship between the thickness difference and the fluorescence step can be discerned. A weak trend seems to be present in the H_2O_2 data, of increasing fluorescence for greater thickness differ-

ence, but this apparent relationship is likely the result of the two low fluorescence outliers. This indicates that differences in fluorescence intensity between samples and regions of interest are not responsible for the absence of the expected behaviour. Inhomogeneous lateral distribution of the fluorophore within the bilayer is unlikely to be the explanation, as the sample appears homogeneous on the scales in which the fluorescence step measurements are taken. While the local environment around the fluorophore can modulate the emission intensity of certain fluorophores, this would be expected to have a consistent effect on each individual sample, while the measured fluorescence in Fig. 3.21 seems random.

It may be that the overall proportion of fluorophore is not constant between bilayers. Experiments on SLBs formed using vesicles found that the overall composition of the bilayer was enriched in components which had the strongest affinity for the support compared to the vesicles used for the SLB preparation [112]. It may be that the same is true in the spin-coating process, with the bilayer closest to the support enriched in the lipids that interact most strongly with the support. If this was true and there were indeed different proportions of fluorophore in each bilayer, the relative intensity between first and second leaflets would no longer reflect the density change.

This explanation has issues however. It would, for example, require that TopFluorPC also has its partitioning between different bilayers in the stack affected by the support during spin coating, even though it has a headgroup identical to the surrounding DOPC lipids. The variation in the relative fluorescence signal is also poorly accounted for by this interpretation. If this were correct, why should the fluorescence of the first bilayer be higher than the second in some samples, and lower in others? If the support caused exclusion of the fluorophore, or attracted the fluorophore, the observed effect should be a constant shift to higher or lower relative fluorescence compared to the expected values.

If there is not a systematic effect, but rather the spin-coating process results in the exact composition of the bilayers being somehow randomised, that raises important questions about the suitability of the spin-coating technique for applications where the composition of the lipid bilayers must be well defined. A prominent example is the study of L_o domains (discussed further in Sec. 4.3), where small changes in the bilayer composition can substantially affect the biophysical properties of these domains [119].

3.6 Effect of Background Noise on qDIC Measurements

Due to the nanometre scale thickness of lipid bilayers, the optical contrast they generate in DIC is very low. To improve the signal-to-noise ratio of the qDIC contrast images, multiple frames were averaged at each polariser angle, as mentioned in Sec. 3.1. It was important that the number of averages be properly optimised, as taking larger numbers of averages would lead to a larger delay between the acquisition of the positive and negative polariser images (as well as the corresponding fluorescence image if one was taken). Such a delay could allow visible changes in the sample to occur between images, possibly resulting in artefactual half-thickness steps where bilayer edges had shifted by large amounts, such as can be seen in Fig. 3.3a, or a blurring of the bilayer edges caused by small shifts in the edge position. On the other hand, a too small number of averages results in increased shot noise, which could make it more difficult to obtain good, clear measurements of phase steps at

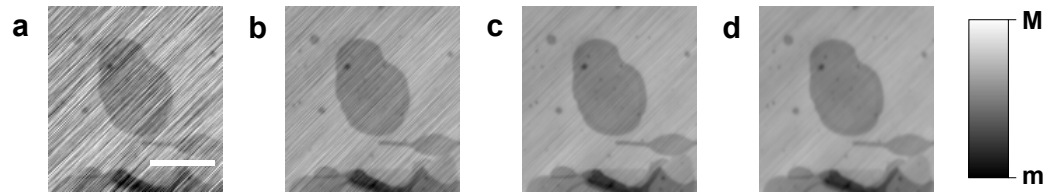

Figure 3.22: The qDIC phase images generated from a) 1, b) 10, c) 100 or d) 1000 averaged frames. The scale bar has a width of 10 µm, and the intensity scale ranges from m = -30 mrad to M = 40 mrad.

the bilayer edges.

To investigate the effect of image noise a single region of interest of a $DC_{15}PC$ SLB was imaged with individual 1000 acquisitions taken at each polariser angle[10]. Each acquisition had an exposure time of 100 ms, meaning at each polariser angle it took 100 s to take the full set of images. The $DC_{15}PC$ bilayer was imaged at room temperature, at which the SLB was in the rigid S_o phase, so there were fewer bilayer edge fluctuations compared to those that would be seen in an L_d phase DOPC bilayer under the same conditions. The behaviour of the S_o phase will be discussed in more detail in the next chapter.

From this large set of 1000 acquisitions at each angle, images averaged from 1, 10, 100 or 1000 image subsets of the full set were generated. The effect of the number of averages on image noise can be seen in Fig. 3.22, which shows a section of a qDIC phase image of a bilayer patch. Increasing the number of averages clearly reduces fine noise in the image, but features such as the bilayer edges and small vesicles appear slightly less sharply defined in the heavily averaged images, possibly due to small fluctuations at the bilayer edge, or sample drift.

For a quantitative measure of the effects of the number of image averages on the mean bilayer thickness measurement, 40 phase steps were measured across four different fields of view for each of the four different numbers of averages tested. For consistency, the phase steps measured were in the exact same positions for each number of averages. Importantly, there was no relationship between the number of DIC image averages and the mean bilayer thickness value within statistical significance, as shown in Table 3.3, as all the values were the same within error.

The effect of the number of averages on the standard error of these mean thickness values can be seen in Fig. 3.23. The expected relationship between the number of averages, N, and the standard error is given by Eq.(3.4), where σ_S is the shot noise in a single frame, and σ_G is the contribution to the noise from the roughness of the glass substrate.

$$\sigma = \sqrt{\sigma_S^2/N + \sigma_G^2} \tag{3.4}$$

This was fitted to the data using the Non-Linear Curve Fit tool in Origin 2017. This gives $\sigma_S = 0.11 \pm 0.03$ nm and $\sigma_G = 0.10 \pm 0.01$ nm. We note that the fit does not describe the data well, possibly due to the influence of lateral drift during the measurement period. Based on these data, it was decided that 100 averages provided the best compromise between acquisition speed, image sharpness and SNR. Using the 100 ms exposure time with 100 averages, only 20 seconds would be needed to

[10]In this section, qDIC images will be described as being averaged over n frames; this is n frames at each polariser angle.

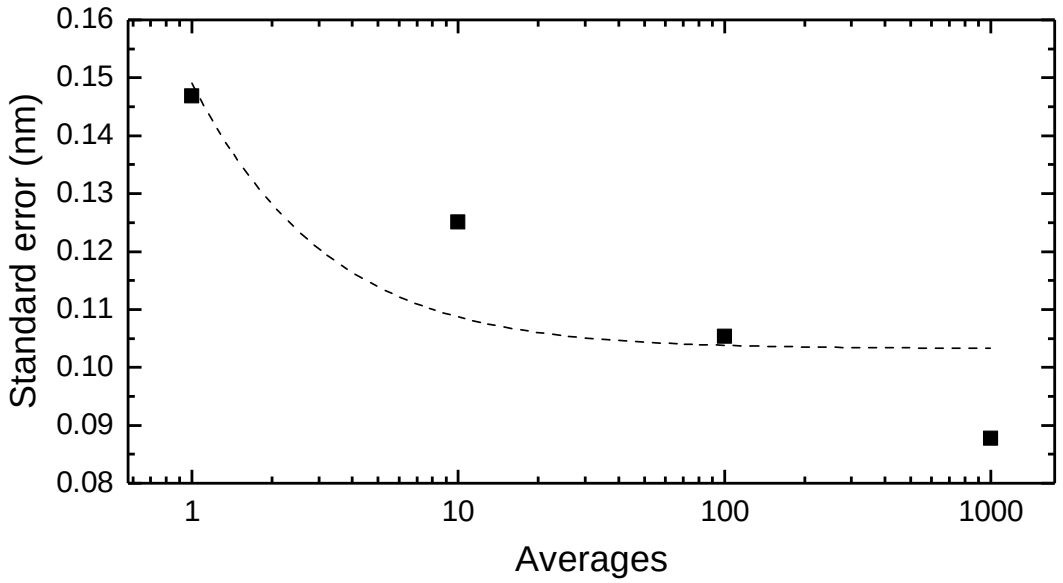

Figure 3.23: A graph showing the effect of changing the number of averages used to generate the qDIC phase image on the standard error of the average bilayer thickness measurement. The expected dependence of the standard error on the number of measurements is fitted to the data (black dashed line).

Number of averages	Mean thickness (nm)
1	4.19 ± 0.15
10	4.07 ± 0.13
100	4.19 ± 0.11
1000	4.07 ± 0.09

Table 3.3: Table showing how the mean value of bilayer thickness changes when the number of averages used to generate the qDIC images is changed. The errors given are the standard error of the mean.

image both polariser orientations. While some background noise remained, it was reduced to a level that was considered acceptable.

Despite this optimisation of the number of averages, for all the bilayer thickness measurements given in Sec. 3.3 and Sec. 3.4, there was a broad distribution of thickness measurements about the mean value, an example of which can be seen in Fig. 3.10. The natural question that arises then is whether this variation is due to remaining noise in the images (from shot noise or the glass roughness), or is reflective of real local variation in the bilayer thickness at the sample. Although literature measurements with AFM have shown that L_d phase SLBs have a roughness on the sub-nanometre scale [101], within our axial sensitivity, much of this variation is below the lateral optical resolution of our setup and so should average out, resulting in bilayers with a smooth appearance.

To test this, many different phase profiles were taken of the glass surface, in regions where there was no bilayer and so should be no meaningful phase variation. To each of these different glass noise measurements was added a mock bilayer phase step, using Eq.(3.1), with values for the five parameters chosen to be representative of the values expected of an L_d phase lipid bilayer, based on those obtained when fitting to real bilayer step measurements (these set parameters are given in Table 3.4). This

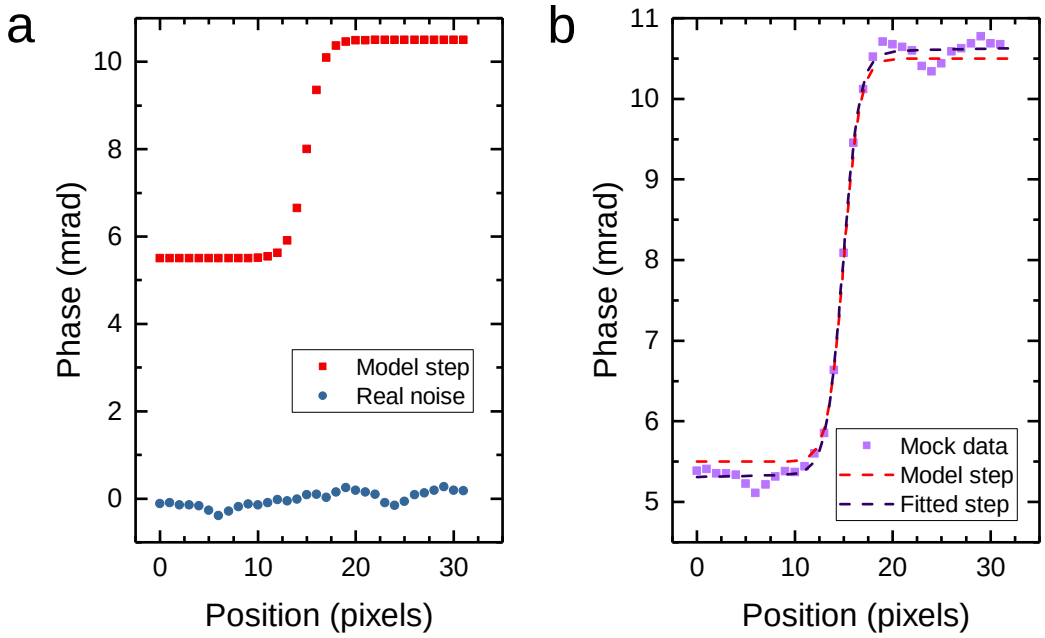

Figure 3.24: Graphs showing a) the model step function (red squares) and an example of a region of noise measured at the glass surface (blue circles), and b) the simulated data (purple squares) generated by combining the model step function with the measured noise. The fits in b) show the model step function (red dashed line) and the step fitted to the simulated data by MATLAB (purple dashed line).

generated a large number of unique simulated bilayer edge measurements, to which Eq.(3.1) was then fitted in the same manner as for real bilayer step measurements.

To ensure the noise obtained from the glass was as close to that which would be present in real data as possible, line profiles were taken averaging over a width of eight pixels. The lines were drawn close to parallel to the shear direction; this was done by eye, rather than by precisely measuring the angles. This approach was taken to reflect the fact that in real data the main aim is getting a phase profile perpendicular to the bilayer edge with the expected step-like shape, which may require deviations from the exact shear angle.

An example of this is shown in Fig. 3.24. In Fig. 3.24a, the 'perfect' noise-free bilayer step generated from the parameters in Table 3.4 can be compared with one of the measurements of the phase noise over the glass surface. These two are added together to generate the simulated noisy data set shown in Fig. 3.24b, which is shown with both the original noise-free step and the best MATLAB fit overlaid. It can immediately be seen in this example that the addition of the noise has resulted in the recovered step height being increased significantly compared to the true value.

The final data set consisted of 100 simulated steps. As a control, when there was no noise added to the step, MATLAB was able to perfectly recover each of the five parameters as expected. However with noise, the mean recovered values deviated slightly from the 'true' values. The main parameter of interest, the step height, has an average value of 5.02 mrad. The sample standard deviation of the distribution is 0.614 mrad, which is very close to widths of the distributions observed in real data. For example, the standard deviation of the second bilayer DOPC bilayer measurements on the etched surface was 0.553 mrad. This indicates that most of

Parameter	Set value	Measured (100 averages)	Measured (1000 averages)
a (mrad)	5.00	5.02 ± 0.61	5.07 ± 0.63
b (pixels)	15.00	14.98 ± 0.24	14.98 ± 0.20
c (pixels)	1.65	1.72 ± 0.32	1.73 ± 0.36
d (mrad/pixels)	0.000	0.028 ± 0.025	0.027 ± 0.024
e (mrad)	80.00	79.31 ± 2.18	79.37 ± 2.23

Table 3.4: Comparison of parameters used to generate the mock step function compared to the mean values obtained by MATLAB fitting to the sum of the mock step function and background noise measured for different numbers of averages during image acquisition. Errors given are the standard deviations on the distributions.

the variation that is present in the single bilayer thickness measurements is the result of the image noise, rather than real variation in the bilayer optical thickness. The effect of noise on the mean thickness values should be negligible, since taking measurements at different positions with different image noise should average out its effects.

While this explains much of the variation in the measured single bilayer steps, it is interesting to note that the distribution of thickness measurements for the double bilayer steps (as can be seen in Fig. 3.10) was significantly broader than for single bilayer steps. It is unclear why this should be the case. Possibly at double bilayer edges, interactions between the two edges introduce fluctuations in the bilayers which affect the qDIC phase measurements. This may merit future investigations, either with qDIC or interferometric reflectometry.

Nevertheless, having determined that the variation in the single bilayer measurements was not intrinsic to the bilayers themselves, it was decided to test whether camera noise was responsible by observing how the variation in the mock data changes when the number of DIC image averages is increased to 1000. Similar to before, 100 line profiles were drawn in regions of images where there was no bilayer present, and a mock step function with the parameters given in Table 3.4 was added to the data. The 100 line profiles were in the same positions for images generated from 100 and 1000 averages. If random camera noise is responsible for the variation in the data, then increasing the number of averages should result in a significantly narrower distribution. The effect of the number of averages on the recovery of the mock step parameters is shown in Table 3.4.

It can be seen that increasing the number of averages used in the generation of the qDIC image has very little effect on either the accuracy of the parameters recovered by MATLAB's fitting, or on the distribution of the data, which remains of a similar scale to the real data. This is consistent with the results shown in Fig. 3.23. This would seem to suggest that the random variation is intrinsic to the sample itself, likely a result of the surface roughness of the glass causing small variations in the optical path of light across the sample. As such, it is unlikely that significant improvements could be made to the data by taking more than 100 DIC averages, since this would not reduce the glass noise. However, taking more line profiles would still reduce the effect of noise on the mean thickness values, as each position would have different glass roughness, the effects of which on the mean would cancel each other out.

To quantify the roughness of the glass, the spatial standard deviation of the glass surface measurements was taken, without the addition of the mock step function.

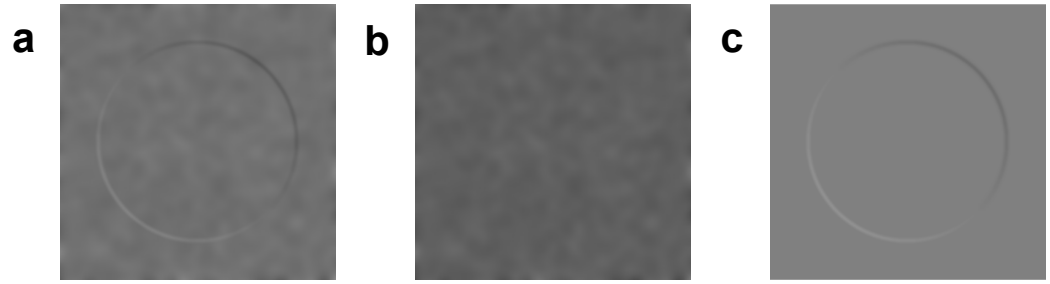

Figure 3.25: Panel a) shows an illustration of a DIC image of a lipid bilayer patch, and b) shows an illustration of the same region, after ablation of the bilayer. Panel c) shows the result of subtracting b) from a), removing the background from the glass and leaving a noise-free DIC image of the bilayer.

To exclude the effects of local gradients which are accounted for in our fit function (and thus wouldn't affect our measurements), a linear fit was made to each line profile which was subtracted before taking the standard deviation. The standard deviation of all our glass phase measurements (a total of 21424 points) was 0.204 ± 0.002 mrad. This is equivalent to a thickness variation of 0.161 ± 0.002 nm using the DOPC refractive index of 1.445, or 0.097 ± 0.001 nm using the glass refractive index of 1.5171.

Knowing that this variation comes from the glass opens up a potential avenue for refinement of the qDIC technique. Given that at high temperatures bilayers begin to detach from the glass surface (see Sec. 4.5), a possible way to eliminate the influence of glass noise from the data would be to image the same region twice, once with the bilayer intact, and then again with the bilayer absent. The latter image would effectively be an image of just the background noise, and could in principle serve as a 'reference' image, and be subtracted from the former 'signal' image to provide virtually noise-free DIC images of the lipid bilayer for analysis. This is illustrated in Fig. 3.25.

This was again tested by adding real noise to the mock step function. Two pairs of DIC images were taken of the glass surface, the pair first to act as a signal image, and the second pair to act as the reference image. In a real measurement, the sample might drift slightly between acquisition of the reference and signal images, due to the time required to detach the bilayer from the surface. To simulate the effect of this sample drift in the test data, the position of the reference image on the microscope stage was shifted by a small (approximately 5 µm) distance relative to the signal image.

The signal image was used to produce a qDIC phase image as normal, from which measurements of the noise were taken to produce 120 unique simulated steps. The reference image was registered to the first using the Registration Estimator in MATLAB R2018a, and the difference taken between the signal and reference; this image should therefore be free of noise. This 'differential' DIC image was then integrated as normal to produce a qDIC phase image from which measurements were taken of the noise and added to the mock step to generate simulated data.

The mean recovered values from the simulated data are shown in Table 3.5. The recovered step parameters in the differential DIC image are slightly closer to the set values for four out of the five parameters. As expected, there is a reduction in the error in the mean values, indicating less spread in the data, however, the reduction in error in the data generated from the differential DIC images compared to the normal

DIC images is marginal. A possible explanation is that imperfections in the image registration process resulted the noise not being fully cancelled out of the differential DIC image, however static lipid bilayer structures appear to be perfectly removed, which suggests that the registration is working as expected. Another explanation is that over the course of the image acquisition, free-floating lipid debris is moving into and out of the focal volume, which is creating an additional noise component.

Another factor that was investigated was the effect of image drift between the acquisition of the positive and negative image sets. At the highest number of averages tested so far (1000 frames per polariser angle) the time delay would be 100 seconds between images, during which time the sample might drift and add a significant additional background noise component. To test this, a different approach to taking the positive and negative images was tested. In this approach, the polariser angle was alternated between positive and negative orientation during imaging of a continuous acquisition of 2000 frames, with the polariser angle switched every 100 frames. To exclude the frames where the polariser angle was changing, only the middle 80 frames of each 100 were taken, so ultimately the positive and negative polariser images were each averaged over 10 blocks of 80 frames. To compare this alternating mode of polariser operation to the normal sequential mode, two pairs positive and negative polariser images were also taken in two separate 800-frame blocks.

The two different modes of operation for the polariser were tested using the same procedure, adding the model step function to 120 measurements of glass noise to create simulated data. The results of this are shown in Table 3.6. No improvement was noted in the error in the recovered parameters between sequential and alternating polariser operation, indicating that over timescales of over a minute, the microscope drift is negligible. Each of the mean values of the parameters are further from the set value in the fits generated from the noise in the alternating polariser images than the sequential polariser images.

A possible explanation for this lies in the limited accuracy of the motorised polariser used for the fast switching needed for this alternating polariser procedure. In theory, the position of the polariser should be the same each time for a given set angle, and the measured intensity at $\pm\psi$ should always be the same in a given region. However, in practise the polariser does not move to the same position every time. This can be seen in Fig. 3.26, which shows the mean intensities at two different fields of view as the polariser position is alternated. For manual operation, the intensities in positive and negative polariser images are typically the same within less than 0.1%, but in Fig. 3.26 it can be seen that the intensities can differ by roughly 10% between switches. Each time the motorised polariser is set to a particular angle, the mean intensity is different to its previous value at the same nominal position due slight variations in the servo movement. This variation would serve to increase the image noise, and so may be the reason why the alternating polariser data is less effective at recovering the 'true' step parameters.

Having established that image drift over short timescales was negligible, and in order to determine the limit to the level of noise reduction that could be achieved, it was decided to use the first and last 400 frames from the data from the 2000-frame block to serve as the signal and reference images respectively for the differential DIC. The time difference between the start of the acquisition of the first 400 images and the end of the last 400 was only 80 seconds, so drift between the two images should be negligible. This was compared with analysis of the noise of a phase image

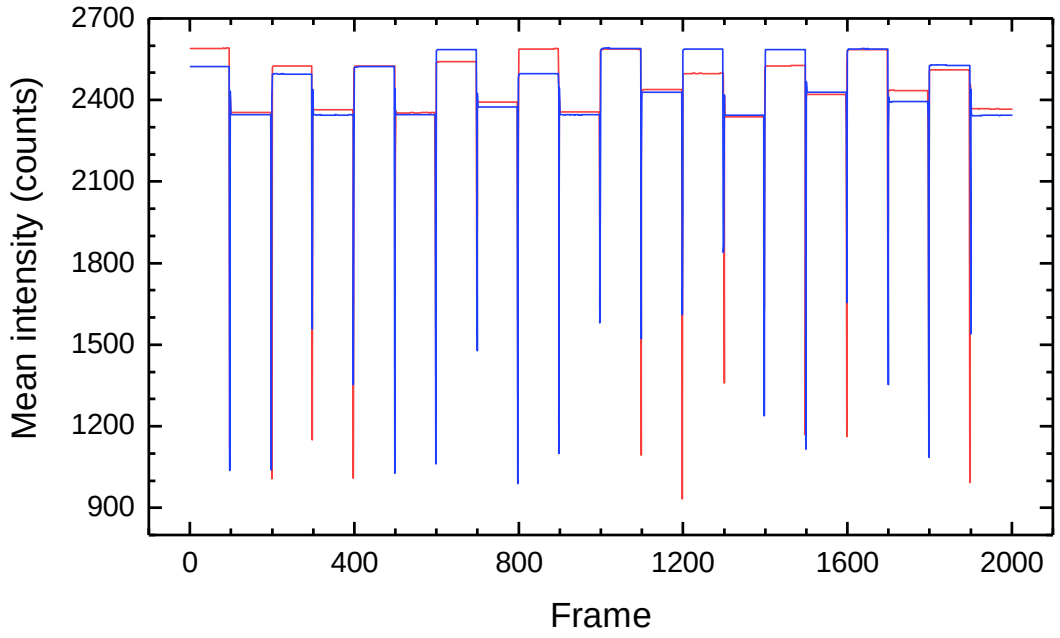

Figure 3.26: Mean image intensity for two different the fields of view (denoted by red and blue lines) when the polariser was alternated between nominal angles of +15° and -15°. The positions where the polariser angle was changed appear as sharp drops in the average intensity.

Parameter	Set value	Normal DIC	Differential DIC
a (mrad)	5.00	5.06 ± 0.55	4.96 ± 0.42
b (pixels)	15.00	15.00 ± 0.19	15.02 ± 0.14
c (pixels)	1.65	1.69 ± 0.26	1.65 ± 0.19
d (mrad/pixels)	0.000	0.026 ± 0.021	0.024 ± 0.020
e (mrad)	80.00	80.17 ± 1.47	80.01 ± 1.29

Table 3.5: Table comparing fit parameters from steps with noise added from phase images generated from differential DIC images with phase images generated from normal DIC images. The DIC images were averaged over 1000 frames. Measured values are averaged over 120 line profiles. Errors given are the standard deviation.

Parameter	Set value	Sequential polariser	Alternating polariser
a (mrad)	5.00	5.06 ± 0.56	5.11 ± 0.56
b (pixels)	15.00	14.99 ± 0.19	14.99 ± 0.19
c (pixels)	1.65	1.69 ± 0.26	1.72 ± 0.22
d (mrad/pixels)	0.000	0.026 ± 0.021	0.027 ± 0.020
e (mrad)	80.00	80.17 ± 1.48	80.40 ± 1.55

Table 3.6: Table comparing fit parameters from steps with noise added from phase images generated from DIC images taken when the polariser was operated in sequence or was alternated during acquisition. The DIC images were averaged over 800 frames. Measured values are averaged over 120 line profiles. Errors given are the standard deviation.

Parameter	Set value	Sequential polariser Normal DIC	Alternating polariser Differential DIC
a (mrad)	5.00	5.07 ± 0.58	5.02 ± 0.19
b (pixels)	15.00	15.00 ± 0.20	15.01 ± 0.07
c (pixels)	1.65	1.70 ± 0.26	1.65 ± 0.09
d (mrad/pixels)	0.000	0.026 ± 0.022	0.007 ± 0.011
e (mrad)	80.00	80.16 ± 1.51	79.98 ± 0.30

Table 3.7: Table comparing fit parameters from steps with noise added from phase images generated from normal DIC images taken when the polariser was operated in sequence or from differential DIC images taken when the polariser was alternated during acquisition. The DIC images were averaged over 400 frames. Measured values are averaged over 120 line profiles. Errors given are the standard deviation.

generated from a normal DIC image under sequential polariser operation, also with 400-frame averaging.

Under these conditions, a substantial improvement in the noise was achieved, as shown in Table 3.7. A modest improvement in the accuracy of most parameters was also achieved. In contrast to the previous observation that the images are apparently well registered after the 5 µm lateral shift, this seems to suggest that the accuracy of the registration process is the limiting factor for the differential DIC process. Taking differential images using a very short temporal separation with no artificial shift produces significantly reduced errors, while even a relatively small positional shift of 5 µm results in a significantly smaller improvement, as shown in Table 3.5.

It should be noted that the low errors achieved here for bilayer thickness measurements represent a purely theoretical limit to what can be achieved with the available equipment, and could not be achieved in practise for real SLB measurements with the existing procedures. The fact that the differential DIC process currently does not produce any worthwhile improvement unless there is absolutely no drift renders it unsuitable for improving bilayer measurements, as the heat-induced ablation of the bilayer is a gradual process, and drift over the timescales in which it occurs is unavoidable.

Improved image registration might offer a means to compensate for this drift, however given that the goal is to remove the most prominent objects within the field of view (i.e. the bilayer) it is unclear whether such registration would have the necessary precision without consistent points of reference between images. Faster removal of the bilayer might be possible by building the sample into a flow chamber and running a solvent over the coverslip, however this might itself cause displacement of the sample which would result in differences between the two images that would prevent full cancellation of the noise. Further development is necessary to determine what improvements are realistically achievable.

3.7 Effect of Polariser Calibration on qDIC Measurements

As mentioned in Sec. 2.6, the DIC polariser angle ψ was set to either $\pm 12.9°$ or $\pm 15°$ for taking measurements. The reason for the different angles used is due to the way in which the polariser angle was set. While later measurements were taken

with a motorised polariser, which allowed for fast switching between preset positive and negative angles (available in five degree intervals), for most measurements, the polariser had to be set manually. This enabled high precision when setting the polariser angle, but was time consuming, and added to the delay between acquisition of the positive and negative angle images.

Assuming no structure in the field of view, the relationship between the polariser angle and the image intensity is given in Eq.(3.5).

$$I = (I_{\max} - I_{\mathrm{bg}}) \sin^2 \psi + I_{\mathrm{bg}} \tag{3.5}$$

For manual alignment, it was first necessary to measure the background counts, I_{bg}. This was done by measuring the mean number of counts read by the camera, when the beam was directed away from the camera. There is an additional background component from non-polarised light coming through the polarisers which is not accounted for here; however, this is negligible compared to the camera background I_{bg}. The maximum intensity, $I_{\max}$ was measured by setting the polariser to the fully open position ($\psi = 90°$). With these values, the expected intensity could be calculated from Eq.(3.5), and the angle of the polariser adjusted until the intensity detected by the camera matched the expected value.

Carrying out this calibration every time the polariser angle was changed would be impractical, since a lengthy calibration time would preclude the possibility of imaging fast events using the qDIC technique, and increase the likelihood of the sample changing between acquisition of the positive and negative contrast image. As such, the polariser angle was switched from positive to negative by recording the image intensity at a given angle, then adjusting the polariser to the opposite position which gives as close to this value as achievable. To avoid drift in the polariser angle over the course of many changes, the polariser angle would be periodically recalibrated when it would not interfere with the measurements being taken.

Due to the limitations of manual precision, it is possible that there may be slight differences between each calibration of the polariser. Because the field of view and lamp power would often be different between separate calibrations, the different calibrations would not be directly comparable using the image intensities, making determining the relative error between calibrations difficult. This uncertainty in the true polariser angle might lead to inconsistencies between data sets taken in different sessions, or within the same session if the polariser angle was readjusted mid-session. It was therefore necessary to establish what effects the normal variation in the manual polariser calibrations might have on the data.

To measure this, a similar approach was taken as for the measurement of the effect of the number of averages discussed in Sec. 3.6. The same field of view was imaged three times, using independent polariser calibrations each time. Within this field of view, 42 measurements of bilayer thickness were taken. For consistency, the measurements of bilayer thickness were taken in the same regions for each calibration.

The results of the calibrations are given in Table 3.8. It can be seen that the three average values agree very well, and are the same within the experimental precision. This indicates that any small variations in the polariser angle are unlikely to cause a detectable error in the mean bilayer thickness values.

Polariser calibration	Mean thickness (nm)
A	3.75 ± 0.04
B	3.72 ± 0.05
C	3.77 ± 0.05

Table 3.8: Table showing the consistency in mean bilayer thickness measured for three independent polariser calibrations, A, B and C.

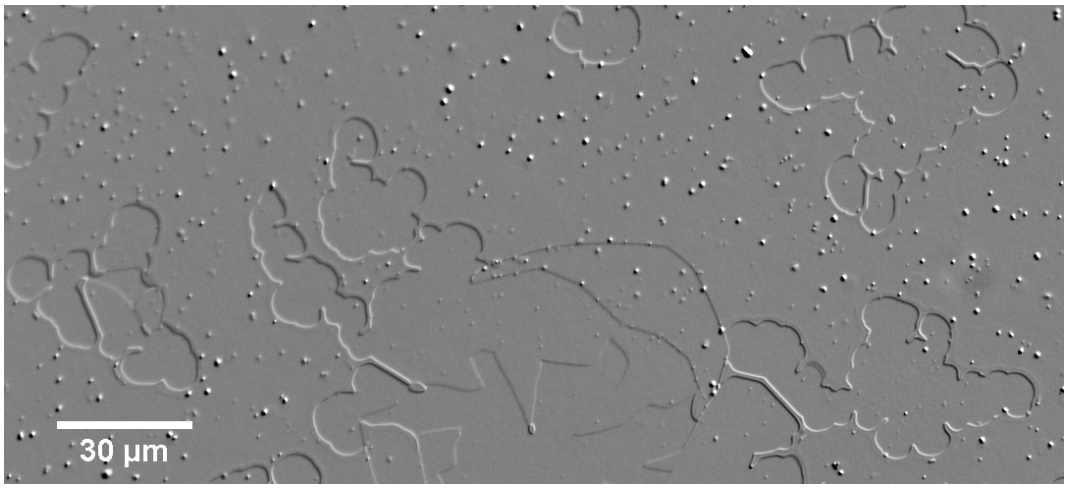

Figure 3.27: A qDIC contrast image showing how the focus can vary within a single field of view. The region on the right is noticeably better focussed than the region on the left. The image intensity is scaled from 0.0004 to 0.0164.

3.8 Effect of Defocus on qDIC Measurements

Another factor which might have an influence on the recovery of the step height is the degree of defocus (deviation from the focal plane) within an image. In many cases, the focus was not constant over a field of view. An example of the variation in focus across an image is given in Fig. 3.27, which shows a gradient in the focus from left to right in one section of the field of view. Gradients such as this likely originate from the way the sample was prepared; if the sticking of the coverslip to the gasket was uneven, this would result in the coverslip being not parallel to the slide and so not being parallel to the focal plane of the objective.

Since such variations are reasonably common (though usually not as extreme as in Fig. 3.27), it was necessary to understand their influence on the data. To accomplish this, a sample was imaged with the objective position relative to the sample adjusted to different positions around the ideal focal plane, in intervals of approximately 0.5 µm. This ideal focal position was determined 'by eye', in the same manner as would be used during normal imaging. The field of view was then cropped down to a region in which the focus was consistent, and 10 line profiles were drawn on the phase image over different points along the edges of single-bilayer patches. As in Sec. 3.6 and Sec. 3.7, the 10 line profiles were in the same positions for each focal position. The degree to which the objective position affects the sharpness of the image can be seen in Fig. 3.28. The degree of defocus in some of these images is considerable, and in practise images with such an extreme degree of defocus as can be seen in Fig. 3.28f would not be taken.

The effect of defocus on the mean bilayer thickness and the standard error can be

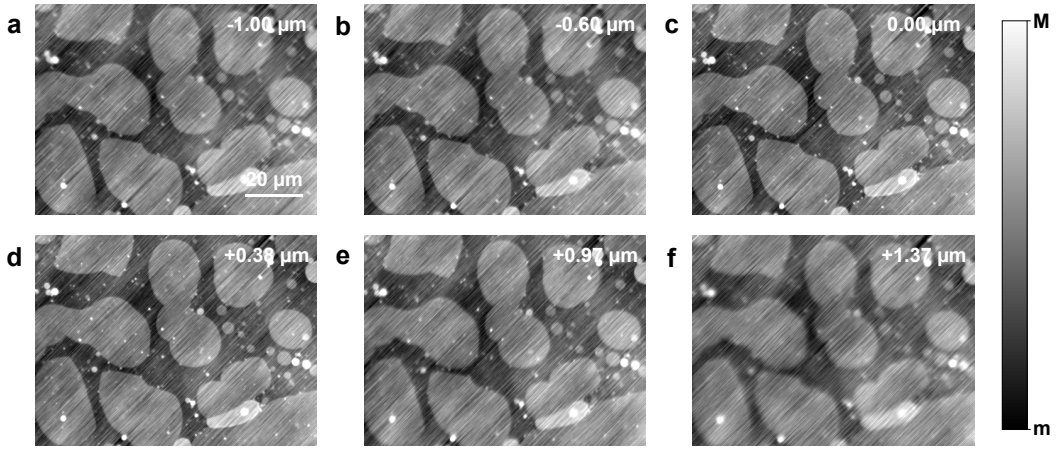

Figure 3.28: A section of a larger field of view of a $DC_{15}PC$ bilayer, within which measurements of bilayer thickness were taken with objective position set at different heights relative to the position of optimal focus. The displacement of the objective from the ideal focal position is given in the images. Images are scaled from m = -12 mrad to M = 4 mrad.

seen in Fig. 3.29 for data taken on a $DC_{15}PC$ bilayer. The changes in the mean value as the objective is moved through the ideal focus position appear effectively random, indicating that slight defocussing of the objective doesn't bias the data. Within the measurement uncertainty, the mean thickness values are effectively equivalent. This indicates that the degree of defocus experienced during normal imaging is acceptable for good qDIC measurements. As expected, moving away from the focal plane increases the width of the step function (parameter c in Eq.(3.1) and Eq.(3.3)) due to the step being less sharply defined in the defocussed images.

The effect of displacement from the position of best focus is shown in Fig. 3.30. Increasing displacement generally results in increasing error, thus there is a meaningful benefit to maintaining good focus when taking qDIC measurements beyond the qualitative improvement in image resolution. Interestingly, the point of lowest error is not the nominal best focus position, but rather a nearby point. This is likely due to statistical variation in the data due to the small sample size.

3.9 Chapter Summary

In this chapter, we have shown that by fitting a tanh function to line profiles taken over the bilayer edge in qDIC phase images, we can obtain measurements of the phase step, from which, given a known refractive index, we can determine the bilayer thickness. To ensure that the integration parameters are not influencing the recovered thickness, we have systematically investigated the SNR setting used in the Wiener filter, and found an optimal value which is a compromise between recovery of the expected phase profile and suppression of artefacts in the reconstructed image. The effects of other parameters, such as the number of averages used to produce the DIC image, the accuracy of the polariser calibration, and variation in the focal plane have also been investigated and found not to significantly affect the results.

In the case of the DOPC bilayers discussed in this section, we have shown that the thickness of the second bilayer in a multilamellar stack is 4.52 ± 0.03 nm, in good agreement with measurements in the literature of free-standing lipid bilayers.

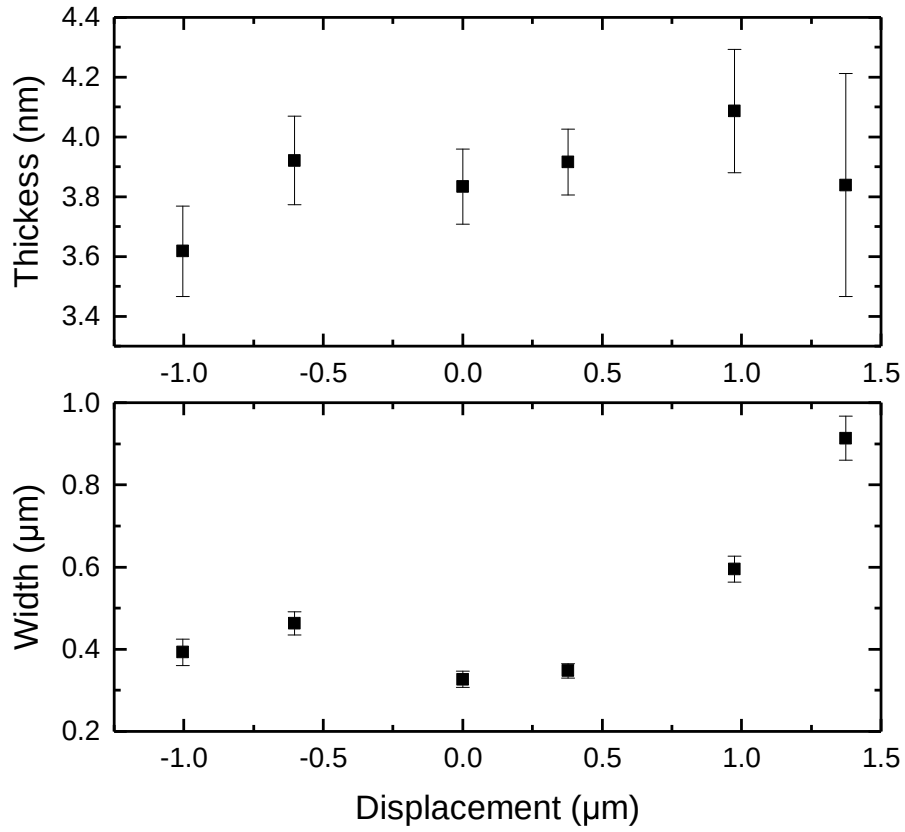

Figure 3.29: The effect of deviation from the position of ideal focus on the height of the bilayer, and the width, c, of the step function fitted to the data.

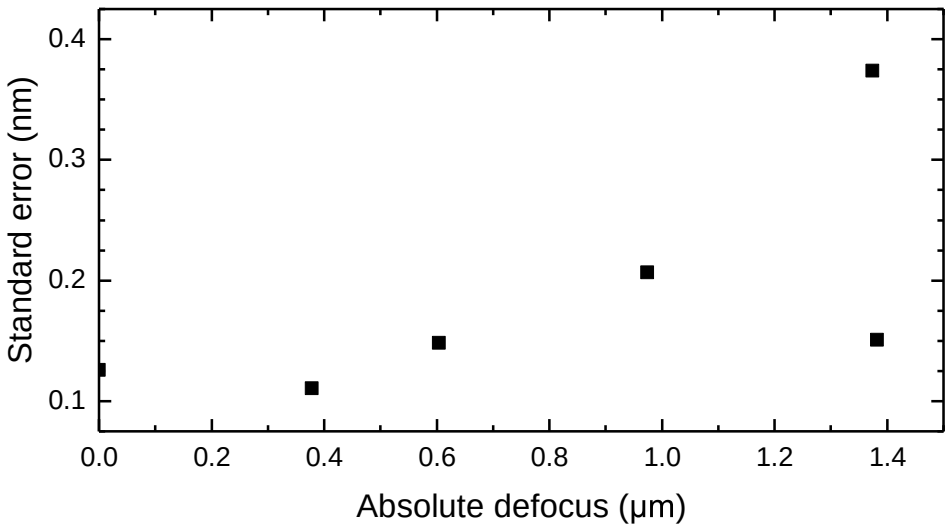

Figure 3.30: The standard error of the measurements plotted against the magnitude of the displacement from the position of ideal focus.

The thickness of the first bilayer has been found to be dependent on a number of factors, most notably the hydrophilicity of the surface. On a hydrophilic surface (θ = 3.4), we found the thickness of the first bilayer to be reduced by (9.7 $\pm$ 0.9)% compared to the second bilayer, while on non-etched surfaces, the thicknesses of the first and second bilayers were the same within error. The second and third bilayer thicknesses were the same within statistical significance for all samples tested.

We interpreted this result in the context of theoretical experiments in the literature, which modelled the interaction of lipid bilayers with solid supports, and had found that the attractive interaction between the substrate and the bilayer causes a movement of lipids from the upper to the lower leaflet. We believe that the resultant depletion of lipids from the upper leaflet, and overall bilayer expansion, is the cause of the thickness difference we observe. We attempted to further test this interpretation by comparing the bilayer thickness changes with the corresponding fluorescence data, however the fluorescence data did not produce consistent results.

We found the scale of this substrate effect to be dependent on several factors. In experiments on the first lipid stock, we found that in regions of sufficiently high bilayer coverage, the hydrophilicity-induced thickness reduction of the first bilayer was suppressed. While this effect was not apparent from later data taken with the second lipid stock, for all subsequent measurements we still excluded data taken in regions of interest where the bilayer coverage was above 90% to ensure that coverage effects are removed when investigating other possible influences on the bilayer thickness. Another factor we found to modulate the hydrophilicity-induced thickness reduction was the choice of fluorophore. For example, at 0.1 mol% the ATTO488-DOPE fluorophore seemed to increase the thickness reduction of the first bilayer by 0.2 nm compared to the case of an unlabelled DOPC bilayer.

Lastly, we explored the limits of the qDIC technique, and found that it was limited by the roughness of the glass substrate. We tested various approaches of eliminating the influence of this roughness from the data; these involved subtracting qDIC images with images of the same region showing only the glass background, but found that this generally did not remove the background noise component well, possibly due to limitations of the image registration.

Chapter 4

Bilayer Phase Behaviour

Building on the work done in the previous chapter, here the phase behaviour of bilayers will be investigated using qDIC. First, the L_d to S_o phase transition will be studied. In Sec. 4.1, the changes in bilayer thickness over the phase transition will be measured, and the effect of the bilayer phase on the hydrophilicity-induced thickness difference found in the previous chapter will be examined. We will use qDIC to try to image coexisting L_d and S_o domains during the phase transition, then, in Sec. 4.2, we will explore how incorporation of different concentrations of fluorophore affects the phase transition.

Next, in Sec. 4.3, the L_o phase will be investigated. Using qDIC we will image coexisting liquid phases, and measure the thickness of both L_d and L_o domains within the bilayer. The influences of the substrate hydrophilicity on the thickness of the different phases will be measured, and the effect of incorporation of the ATTO488-DOPE fluorophore (which partitions into the L_d phase) on the thickness of the two bilayer phases will also be tested.

Finally, we will use qDIC to look at the tubular structures that form in some supported bilayer samples. In Sec. 4.4 we will use qDIC to measure the radius of these tubes, determine the phase state of the lipids in tubes that formed in the L_d-L_o phase coexistence sample, and investigate the influence of the birefringence of the bilayer on the tube phase measurements. Then, in Sec. 4.5, we will observe tube formation in $DC_{15}PC$ samples during cooling, and measure changes in tube radius as the sample transitions from the L_d to the S_o phase.

4.1 The Liquid-to-Solid Phase Transition

In the case of homogeneous lipid bilayers, the bilayer undergoes a transition from the liquid disordered (L_d) phase to the solid ordered (S_o) phase around a well defined phase transition[1] temperature, T_m. This transition is associated with an increase in both the absolute thickness and refractive index of the lipid bilayer [65] caused by the reduced spacing between lipid molecules and increased molecular order in the S_o phase. The resultant increase in optical thickness means the changes in the lipid bilayer over the phase transition should be observable using qDIC.

Since the transition temperature of DOPC is below the freezing point of water, studying the phase transition with DOPC bilayers like those used in the previous

[1] While there are multiple possible phase transitions the lipid bilayer can undergo, throughout Sec. 4.1, Sec. 4.2 and Sec. 4.5, 'phase transition' will only refer to the main phase transition between L_d and S_o phases unless otherwise stated.

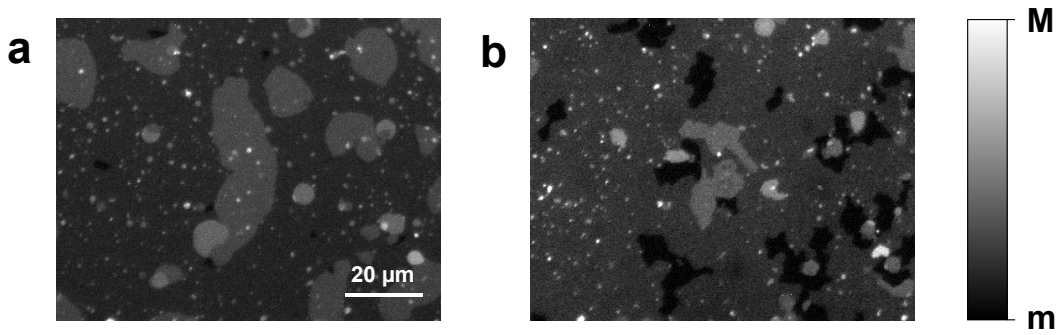

Figure 4.1: Fluorescence images showing a representative region of a $DC_{15}PC$/ATTO488-DOPE(99.99/0.01) bilayer at temperatures a) 40.1 °C (above T_m) and b) 31.9 °C (below T_m). The intensity is scaled from m = 0 pe to M = 110 pe. The intensity of image b) has been adjusted to correct for photobleaching.

chapter would be impractical. Instead, SLBs formed from the saturated-chain lipid $DC_{15}PC$ were used. The nominal phase transition temperature of $DC_{15}PC$ is 33.7 °C [36] (though T_m can vary significantly according the preparation conditions and the model system tested [36]) and so forms an S_o phase at room temperature. The transition temperature of $DC_{15}PC$ is within the safe temperature range of our microscope setup, and so the phase transition can be studied by heating the sample above T_m.

Unfortunately, because $DC_{15}PC$ is less widely used than similar saturated chain lipids like DMPC and DPPC, we could find in the literature no measurements of its refractive index, which is needed for the determination of bilayer thickness. For our analysis then, the refractive index of $DC_{15}PC$ was estimated from literature values for DMPC (1.443 [65]) and DPPC (1.438 [120]), since these are the two lipids which are the closest to $DC_{15}PC$ in terms of molecular structure (see Appendix A). Based on this information we estimated the $DC_{15}PC$ refractive index to be 1.44.

While the refractive index of the bilayer changes with temperature, and particularly over the phase transition, the scale of this effect is relatively small [65]. Experiments using OWLS have shown that the scale of the change in the refractive index of DMPC over a 14 °C temperature range around T_m, is less than 0.002 [65], which is below the two significant figures we use for our refractive index estimate. As such this effect is neglected and the same refractive index is used for the analysis of $DC_{15}PC$ bilayers in both S_o and L_d phases.

Qualitatively, the $DC_{15}PC$ SLB sample in the L_d phase looks almost indistinguishable from a sample composed of DOPC, formed from patches of different lamellarity with rounded edges where the bilayers meet the surrounding medium. Gradual cooling to below T_m results in considerable changes to the arrangement of the sample, as shown in Fig. 4.1. In Fig. 4.1b, it can be seen that more holes in the first bilayer have formed due to contraction of the bilayer over the phase transition, and many of the bilamellar patches seem to have disappeared from the sample altogether. Additionally, the bilayer edges tend to be more angular, in contrast to the rounded appearance of the same edges in the L_d phase.

One area of interest is whether the thickness difference between first and second bilayers induced by surface hydrophilicity discussed in Sec. 3.4 is also present in the $DC_{15}PC$ samples, and if so whether it is affected by the phase transition. For an unlabelled $DC_{15}PC$ SLB formed on a hydrophilic coverslip ($\theta = 3.4°$), when the

bilayer was in the L_d phase at 40.9 °C, a thickness value of 3.02 ± 0.04 nm ($n = 10$) was measured for the first bilayer, and a value of 3.40 ± 0.04 ($n = 10$) was measured for the second bilayer[2]. The thickness difference between the two bilayers is 0.38 ± 0.06 nm, which corresponds to a reduction in thickness of (11.3 ± 1.6) %. This is the same within error as that measured for DOPC bilayers on surfaces with the same hydrophilicity.

When the bilayer was cooled to 28.0 °C, well below T_m, the thicknesses of both the first and second bilayers increased, consistent with expectations. The first bilayer thickness increased to 3.95 ± 0.04 nm ($n = 10$), while the mean second bilayer thickness increased to 4.14 ± 0.05 nm ($n = 10$). The thickness difference between the two bilayers is significantly smaller at this temperature, at 0.19 ± 0.06 nm, approximately half that measured in the L_d phase. Proportionally, the thickness difference between the first and second bilayers in the S_o phase is (4.6 ± 0.1)%.

As we previously described in Sec. 3.3, we propose that the reduction in the first bilayer thickness is the result of stretching of the upper leaflet caused by lipid depletion. This is the result of a net movement of lipids from the upper to the lower leaflet, which continues until the energetic benefit of bringing more lipids into the lower leaflet is counterbalanced by the penalty of stretching the upper leaflet. The fact that the thickness difference between first and second bilayers is phase-dependent can be understood as the result of changes in bilayer elasticity over the phase transition.

In the S_o phase, the bilayer's elastic modulus (a measure of the energy penalty associated with bilayer stretching) is significantly higher than in the L_d phase, therefore in the S_o phase the upper leaflet would have less stretching at this equilibrium energy position than in the L_d phase, leading to a consequently smaller reduction in the bilayer thickness. Literature measurements of S_o phase pure DPPC bilayers and mixed DOPC/DPPC L_d phase bilayers taken using AFM suggest the area elasticity modulus is doubled in the S_o phase compared to the L_d phase [38], so our observation that the thickness difference is halved in the S_o phase is consistent with both our interpretation and literature data.

As the sample temperature is changed over T_m, there exists a temperature range where both S_o and L_d phases coexist [121]. As previously discussed in Sec. 1.3, the S_o phase excludes the ATTO488-DOPE fluorophore during the phase transition because of the two unsaturated hydrocarbon chains of DOPE, rendering the two phases visible by their different fluorescent signal. After the phase transition is complete, the fluorophore gradually becomes homogeneously distributed in the S_o phase, having no L_d regions left to partition into. As in Sec. 3.1, fluorescence images provide a convenient way of testing the ability of the qDIC technique to image the coexisting S_o and L_d phases.

Imaging phase coexistence during the L_d to S_o phase transition is more challenging than the liquid-liquid phase coexistence which will be described in Sec. 4.3 because of the dynamic nature of the system. The phase boundaries are constantly moving as the sample cools, meaning that domain edges may be blurred, since their positions change between acquisition of the positive and negative polariser images, or even during the acquisition of the individual images (which takes 10 seconds due to the number of averages taken). This results in images where the phase edges are often either only weakly visible, or show poor agreement with the fluorescence images.

[2]These values are different to those that will be shown in Fig. 4.3. This will be discussed later.

Figure 4.2: An image of a unilamellar region of a $DC_{15}PC$ lipid bilayer at 32.8 °C, during the liquid-to-solid phase transition. Coexistence between L_d and S_o phases can be seen in a) fluorescence, (M = 280 pe, m - 40 pe), b) qDIC contrast (M = 0.0014, m = -0.0007) and c) qDIC phase (M = 1.2 mrad, m = -2.7 mrad). Ordered domains are visible in the phase image by their increased intensity.

The S_o domains that form during cooling have an angular appearance, originating from the triangular lattice structure of the S_o phase. An example of a region showing solid-liquid phase coexistence is shown in Fig. 4.2. The S_o domain is barely visible above the noise level in the qDIC phase image, but particularly in the portion of the domain on the right, many features of the domain in the fluorescence image can be distinguished in the corresponding phase image. Edges in the S_o domain can be used to measure the difference in thickness between the two coexisting domains in the same way as a normal step over the bilayer edge, since we assume the same refractive index in both phases. In a sample labelled with 1.0 mol% ATTO488-DOPE, the difference in thickness between the two phases at 33.4 °C was 1.00 ± 0.30 nm ($n = 16$).

This value is particularly interesting given our hypothesis that our hydrophilic glass substrates are altering the relative lipid density between the two leaflets of the first bilayer. While in free standing membrane systems such as vesicles both leaflets transition between S_o and L_d phases at the same time [20], as mentioned in Sec. 1.2 AFM experiments on SLBs formed on mica substrates have shown that proximity to the mica support results in a so-called 'decoupled' phase transition. This means that the upper and lower leaflets of the bilayer undergo the phase transition at different temperatures, with the phase transition of the lower leaflet occurring at a higher temperature than the upper leaflet, due to the asymmetry between leaflets the substrate induces [37, 121]. While such decoupled transitions have frequently been observed in SLB formed on mica using AFM [37, 121], they have not however been detected on glass or silicon dioxide, which have a weaker effect on the bilayer [37].

A thickness difference between phases of 1.00 ± 0.30 nm is consistent with a coupled phase transition between leaflets. Measurements of coupled phase transitions in DPPC bilayers using AFM have shown that when coupled, the thickness difference between phases is 0.9 ± 0.5 nm [71], which is consistent with our data. Given that the hydrophilicity causes different thickness reductions in the S_o and L_d phases, it is possible that the surface hydrophilicity affects the height difference between the two phases by up to 0.2 nm. However such effects would not be large enough to confuse coupled and uncoupled phase transitions, which should be different in terms of optical thickness by a factor of two, and so it is likely that the phase transition in our samples is taking place simultaneously in both leaflets.

This conclusion is also supported by the fluorescence data, in which only a single transition event is visible in the first bilayer. This indicates that in spite of the

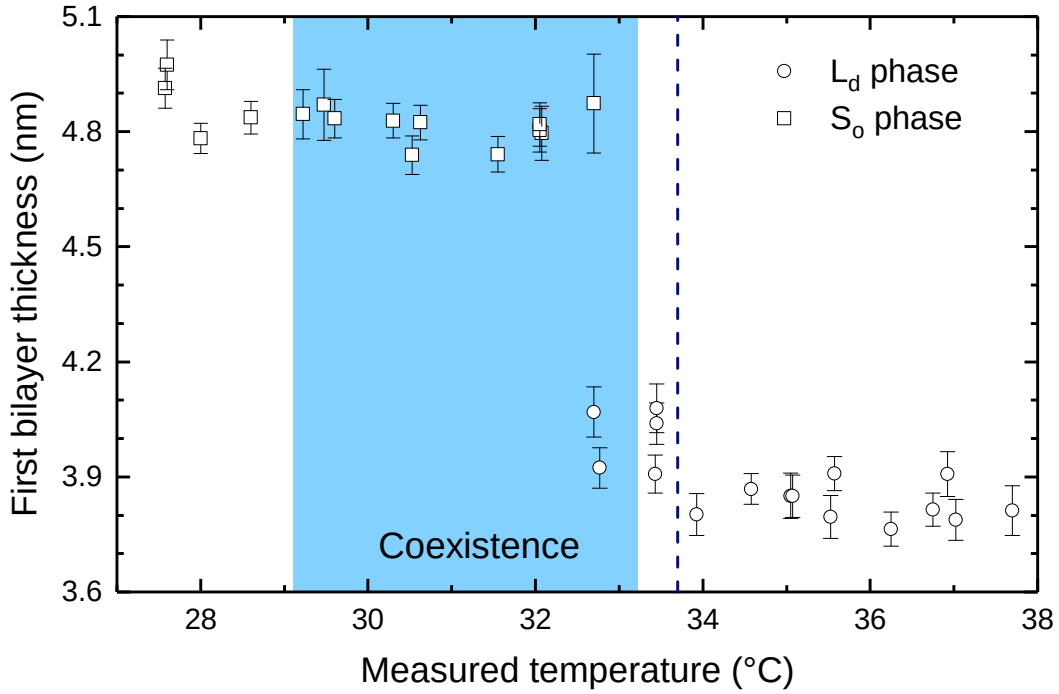

Figure 4.3: A scatter plot of thickness against temperature for a $DC_{15}PC$/ATTO488-DOPE (99.9/0.1) bilayer. The given temperatures are those recorded at the sample. The blue region is the region in which coexisting phases were observed, while the blue dashed line denotes the nominal phase transition temperature.

difference in density in the two leaflets that we believe to be induced by the glass support from our hydrophilicity experiments, the magnitude of this effect is too small to decouple the phase transition. It would therefore be reasonable to speculate therefore that any reduction in first bilayer thickness measured on the mica surfaces commonly used for AFM might be even greater than we have seen on our glass surfaces, due to mica's greater effect on the bilayer phase behaviour.

Next, we applied qDIC to study more closely how the bilayer thickness changes around the phase transition, by taking measurements of the first bilayer thickness in both the S_o and L_d phases at different temperatures either side of T_m. A sample labelled with 0.1 mol% ATTO488-DOPE was cooled in 0.3 °C intervals from a starting set temperature of 37.7 °C (comfortably above T_m) to a set temperature of 27.6 °C, at an average rate of 0.72 °C/hour. During this transition, both the S_o and L_d phase optical thicknesses were measured directly. The results are shown in Fig. 4.3. Experiments on DPPC bilayers using AFM have indicated the presence of additional sub-transitions at temperatures near 60 °C [71] which might also be detectable with qDIC; however since this is above the safe temperature limit for our optical setup, we unfortunately could not investigate this with the equipment available at the time. A device for heating the microscope slide without heating the microscope as a whole has since been developed, which could enable such studies in future.

In Fig. 4.3, the sharp increase in bilayer thickness between the two phases is clearly visible. The phase transition starts slightly below the nominal T_m value of 33.7 °C [36]. Since it is well established that the substrate interaction shifts T_m to higher temperatures [37, 121], it may be the value of 33.7 °C comes from

a sample with a stronger substrate interaction (and consequently a larger increase in T_m) than ours. Alternatively, this apparent discrepancy might simply be the either result of differences in temperature between the thermocouple probe and the sample, or variation from other uncontrolled factors. The latter has been seen to be significant in AFM measurements of phase transitions in DMPC bilayers, where the start of the phase transition was observed to vary by 1.5 °C between nominally identical samples [121].

Interestingly, the phase transition appears to start at slightly different temperatures in the first and second bilayers. While the phase transition appeared for the first time in the same frame for both first and second bilayers, the S_o domains were always larger and more numerous in the second bilayer than the first. This indicates that there is a difference in T_m between the first and second bilayers smaller than the 0.3 °C temperature interval between each frame. This result is surprising; given that the support is supposed to increase T_m, it would be expected that the first bilayer would begin to freeze before the second. It is unclear why our sample should exhibit the reverse behaviour.

The bilayer thickness in the S_o phase remains constant within error as the sample is cooled. In contrast, there does seem to be a slight increase in the thickness of the L_d phase during cooling, particularly as the sample enters the S_o-L_d phase coexistence region. This is consistent with measurements on bilayers formed from other PC lipids with saturated chains (including DLPC, DMPC, and DPPC) using X-ray and neutron scattering [68].

The bilayer thickness values in Fig. 4.3 are conspicuously larger in both S_o and L_d phases than the label-free thickness values that were mentioned earlier. The cause of this is unclear. It is unlikely that the presence of only 0.1 mol% of the ATTO488-DOPE fluorophore would cause a thickness increase of almost 1 nm, especially considering that measurements made on the DOPC bilayers in Sec. 3.4 suggested that the presence of the ATTO488-DOPE fluorophore enhances thickness reductions caused by the substrate. Oxidation of membrane lipids is one possibility, however, different $DC_{15}PC$ stock was used for each set of measurements, and both samples were prepared when the stock was at approximately the same age. Furthermore, the saturated chains of $DC_{15}PC$ should render it more resistant to peroxidation than DOPC.

The label-free measurements were carried out on qDIC phase images produced using an earlier version of the qDIC procedure, which lacked the apodisation step described in Sec. 1.4, resulting in a strong artefactual phase gradient at the edges of the image. It may be that these considerable background artefacts in the phase are affecting the measurements of the phase steps. However this too seems unlikely. In other samples where steps have been measured in the same images integrated both with and without apodisation, it has been found that lack of apodisation lowers the phase steps by only 5%, much smaller than the difference between the two $DC_{15}PC$ data sets. It may therefore be that there was an error in the DIC polariser calibration during one of the sessions. If one of the sets of data is incorrect, the natural question is which one?

It is difficult to compare our values with measurements made in the literature for two reasons. Firstly, as the data in Fig. 4.3 shows, the bilayer thickness is temperature dependent, even within the same phase [68]. Secondly, there are very few direct measurements of the $DC_{15}PC$ bilayer thickness in the literature, and these tend to be AFM measurements which also include an unknown thickness contribution from

the underlying hydration layer, as well as uncertainties relating to the indentation of the AFM tip. For example, in one of the few AFM derived thickness measurements of $DC_{15}PC$, a thickness of 4.9 ± 0.2 nm in the S_o phase was obtained, but the authors believed that the tip indentation might be up to 1 nm [70], making a precise comparison with our data impossible.

Other forms of thickness measurement based around X-ray and neutron scattering might provide more accurate comparisons, but to our knowledge no measurements of $DC_{15}PC$ bilayers have been attempted using these techniques. Using the Gibbs-Luzzati bilayer thickness[3] for the L_d phase of DMPC at 30 °C, a thickness of 3.69 nm is reported, while L_d phase DPPC at 50 °C has a thickness of 3.85 nm [39]. Assuming that the thickness of $DC_{15}PC$ would be at the midpoint between these values, an L_d phase thickness of 3.77 nm would be expected, which is approximately what we see in Fig. 4.3 for the L_d phase away from the phase transition.

Likewise for the S_o phase, the reported thicknesses are 4.78 nm for DPPC at 20 °C [39], and 4.41 nm for DMPC at 10 °C [122]; this leads to a predicted $DC_{15}PC$ S_o phase thickness of 4.60 nm, which is slightly smaller than we observe for the data presented in Fig. 4.3, but much larger than the label-free data. Taken together, the labelled data presented in Fig. 4.3 is probably the more accurate of the two data sets. Small discrepancies between the expected and measured values may be explained as the result the limited accuracy of the estimated refractive index estimate, or the influence of the substrate on the bilayer thickness.

While this means the absolute thickness values for the label-free bilayers that were used to determine the effect of the main phase transition on the thickness difference between the first and second bilayers are subject to a calibration error, the observed reduction in thickness difference between phases should still be valid, since the relative differences between steps are unaffected by errors in the polariser calibration (previously discussed in Sec. 3.7).

4.2 Fluorophore Effects on the Phase Transition

In the experiments described in the previous section, some were carried out on $DC_{15}PC$ bilayers which incorporated various proportions of ATTO488-DOPE fluorophore, while other experiments were carried out on $DC_{15}PC$ lipid bilayers not including fluorescent labels. The fact that the qDIC technique works without the need for exogenous labels enables us to investigate the extent to which the incorporation of this fluorophore into the bilayer affects the phase transition.

To accomplish this, $DC_{15}PC$ SLBs prepared with different concentrations of the ATTO488-DOPE fluorophore were cooled below their phase transition temperature. The four concentrations used were 1.00 mol%, 0.10 mol%, 0.01 mol%, and 0.00 mol%. Each of these samples were cooled in steps of 0.3 °C as before. After each reduction in temperature, the sample was left for 10 minutes to allow the sample to equilibrate to the new temperature. Imaging in fluorescence and DIC then took approximately 3 minutes, after which the target temperature of the heating unit would be reduced again, resulting in an average cooling rate at the sample of 1.4 °C/hour.

An example of one of the samples being cooled is shown in Fig. 4.4. This shows a mixed unilamellar and bilamellar region of a $DC_{15}PC$ bilayer labelled with 1.00 mol%

[3]Thickness can be defined in multiple ways from X-ray scattering data. The Gibbs-Luzzati thickness is defined as $2V_L/A$, where V_L is the lipid molecular volume and A is the interfacial area per lipid [39].

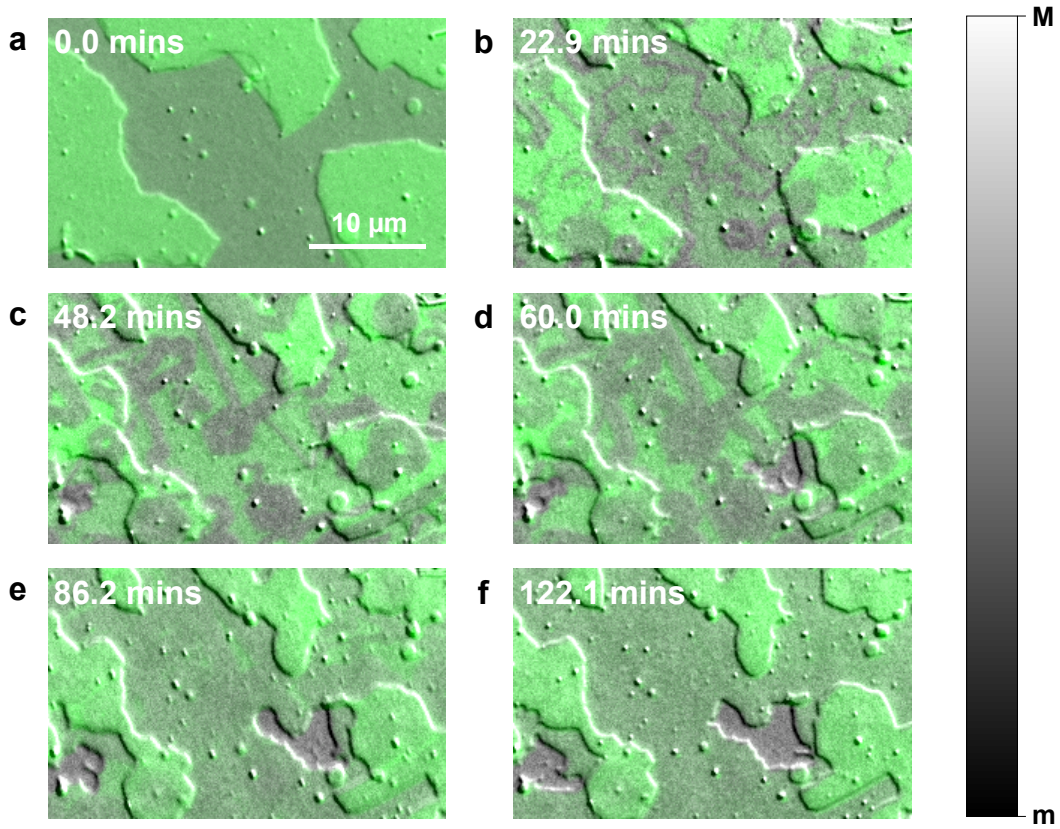

Figure 4.4: qDIC contrast images of a region of a $DC_{15}PC$ bilayer labelled with 1 mol% ATTO488-DOPE undergoing a phase transition during cooling. The green colour channel represents the fluorescence intensity, showing the accumulation of fluorophore in the shrinking L_d phase regions. The images show the region at set temperatures of a) 33.9°C, b) 33.3°C, c) 32.7°C, d) 32.4°C, e) 31.8°C, f) 30.9°C. The time elapsed from the acquisition of image a) is shown in the images. The qDIC contrast is scaled from m = -0.002 to M= 0.001, while the fluorescence is scaled from m = 320 pe to M = 1520 pe.

ATTO488-DOPE. In Fig. 4.4a, the bilayer is entirely in the L_d phase, with phase coexistence becoming visible in Fig. 4.4b, and the sample fully frozen by Fig. 4.4e. Initially, the bilayer covers the field of view shown; however, as the bilayer cools, gaps in the first bilayer begin to appear from Fig. 4.4d due to the areal contraction of the bilayer. The shape of these gaps changes during cooling, from the more rounded shape in Fig. 4.4d, to a more angular shape in Fig. 4.4f; again this is due to the highly ordered arrangement of lipids in the S_o phase as previously discussed.

It is immediately apparent from the fluorescence overlay in Fig. 4.4 that the intensity of the fluorophore in the L_d phase increases during the phase transition. This increase in intensity is especially visible in Fig. 4.4 due to the high (1.00 mol%) proportion of ATTO488-DOPE, but is also visible on other data sets. As the sample cools and the area of the L_d domains decreases, the relative proportion of fluorophore within the L_d phase increases significantly.

The fluorescent intensity gives information on the fluorophore concentration within the L_d phase, however, due to the photobleaching caused by repeated imaging of the same region, the fluorescent intensity cannot simply be measured directly. In order to make quantitative determinations of the fluorophore partitioning, the

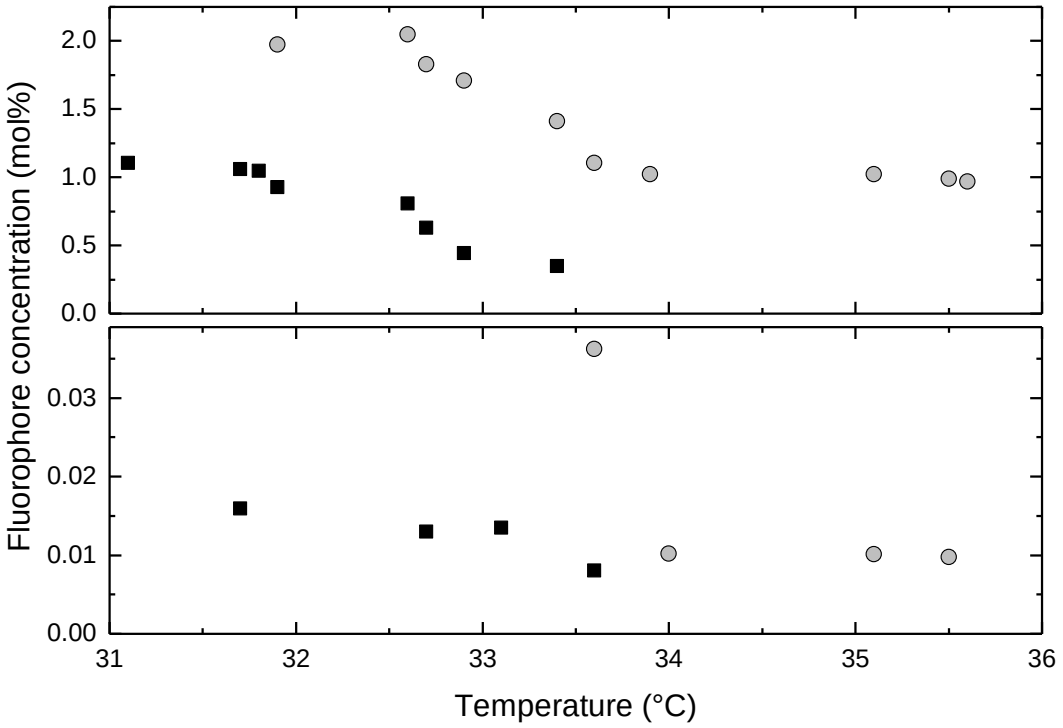

Figure 4.5: Fluorophore concentration (calculated from the bleach corrected fluorescence intensity) in both the fluid (circles) and gel (squares) phases against temperature during the phase transition of the L_d phase of a $DC_{15}PC$ bilayer. The top panel shows data from a bilayer with a nominal overall fluorophore concentration of 1.00 mol%, while the lower panel shows data for a bilayer with a fluorophore concentration of 0.01 mol%.

fluorescence images first have to be normalised to compensate for photobleaching. This was carried out using the 'Simple Ratio' option within the EMBLtools Bleach Correction plug-in for ImageJ, which operates by normalising each image in the sequence to the same mean intensity following subtraction of the background intensity[4]. This should be approximately valid assuming that the total volume of lipid in the in the image area remains constant, and no fluorescent objects such as vesicles enter or leave the field of view during imaging.

The changes in fluorophore concentration in each phase are shown in Fig. 4.5. The fluorophore concentration in the L_d domains increases as their volume fraction decreases while cooling. Assuming the fluorescent intensity scales linearly with the fluorophore concentration, we show the concentration as function of temperature in Fig. 4.5 for bilayers containing either 0.01 or 1.00 mol% ATTO488-DOPE. In the latter sample, the fluorophore concentration in the L_d phase reaches 2 mol% before it finally freezes at a temperature 2.7 °C below the point at which S_o phase domains first appeared. As the S_o domains expand, the concentration of fluorophore within these domains increases gradually over the course of the phase transition, from an initial concentration of 0.35 mol%. Once frozen, the fluorophore diffuses slowly in the solid bilayer, establishing an equilibrium over a timescale of several hours at room temperature.

[4]While the images presented may show smaller regions from within larger fields of view, the photobleaching correction is always carried out on the full field of view captured by the camera.

When the overall proportion of fluorophore is reduced to 0.01 mol%, the range of temperatures over which phase coexistence is visible is reduced to 0.6 °C. The fluorophore concentration in the L_d phase peaks at 3.6 times the starting concentration. However, due to the limited spatial and temporal resolution of our data, we cannot exclude the possibility that smaller L_d domains, with even higher proportions of fluorophore, form before the sample ultimately freezes. The concentration of the fluorophore does not seem to affect the temperature at which the phase transition begins; in the sample with 1.00 mol% ATTO488-DOPE, the first temperature point at which phase coexistence was observed was 33.6 °C (set temperature 33.2 °C), while for the sample with 0.01 mol% ATTO488-DOPE, phase coexistence was first observed at a measured temperature at the sample of 34.0 °C (set temperature 33.2 °C).

In both cases, the fluorophore concentration eventually reaches levels apparently higher that the starting concentration once the bilayer is in a single phase. This can attributed to the lateral contraction of the bilayer when freezing, increasing the areal density of fluorophore. Gravimetric X-ray measurements on DPPC bilayers suggest an increase in lipid density of approximately 40% below T_m [39], which is in between the measured increase in fluorophore density for the nominal 1.00 mol% sample (14% concentration increase in the S_o phase) and the 0.01 mol% sample (66% concentration increase in the S_o phase).

There are a number of possible reasons why our measurements deviate from the expected value. It could be that the behaviour of a multilamellar stack is different to that of a single bilayer. We have already seen that the hydrophilicity of the support can alter the bilayer thickness, so it seems possible that the support could influence the change in lipid density over the phase transition. However, this should produce a consistent result, while we see that the 0.01 mol% fluorophore sample has a higher than expected density change, and the 1.00 mol% fluorophore sample has a lower than expected density change. The fact that our measurements fall either side of the expected value suggests a random error, perhaps due to the error in the fluorescence measurements, or maybe a result of the limited accuracy of the photobleaching correction.

Nevertheless, from this data, we can also estimate the difference in the free energy of the fluorophore between the coexisting L_d and S_o phases. The difference in free energy, ΔF, is given by Eq.(4.1), where R is the ratio of the fluorophore concentration in the S_o phase to that in the L_d phase, T is the temperature of the system in kelvin and k_B is Boltzmann's constant.

$$\Delta F = k_B T \ln(R) \tag{4.1}$$

We measure the free energy for both samples at the start of the phase coexistence region. At 33.4 °C, the difference in free energy between the two phases for the high concentration (1.00 mol%) sample was -37.2 ± 2.7 meV, while at 33.6 °C, the difference in free energy for the low concentration (0.01 mol%) was -39.8 ± 1.9 meV. These values are in good agreement with each other. Literature values of the free energy difference for the fluorophore between phases are somewhat larger than we measure. Simulations of two different fluorescent probes (each with two 18-carbon saturated chains added to improve solubility in the bilayer), found a free energy difference between S_o and L_d phases of approximately -100 meV for one probe, and 200 meV for the other, with the former exhibiting a preference for the L_d phase and the latter the S_o phase [123].

There are several possible explanations for why the magnitude of our measurements are slightly smaller than found in the simulations of the probe molecule which, like ours, segregates into the L_d phase. Firstly, there is the possibility of random error as mentioned earlier, however the close agreement between the two data sets makes this unlikely. Secondly, unlike the ATTO488-DOPE fluorophores used for our experiments, the simulated molecules were not comprised of fluorophores attached to the head group of a phospholipid, but were simply fluorophores with hydrocarbon tails attached. They might therefore be expected to cause greater disruption of lipid packing than ATTO488-DOPE, possibly leading to greater difference in the free energy between phases.

Another possibility is that because in our sample the bilayer was being cooled, the concentration of fluorophore between phases may not have yet reached equilibrium. Evidence for this can be seen in the fact that in the 1.00 mol% fluorophore sample, the calculated free energy decreases continually during the phase transition; the free energy measured at the last temperature where phase coexistence was observed was only -19.9 ± 3.7 meV, almost half that measured at 33.4 °C. To get a better measurement of the free energy, the sample could be held at a temperature in the phase coexistence region for a long period of time to allow the distribution of fluorophore between the two phases to reach equilibrium. Also, the cooling experiment could be repeated with different fluorophores, closer in structure to those in the simulations to allow for a more direct comparison of the data.

Using qDIC, we can also observe the phase transition without the need for fluorophore. When no fluorescent labels are incorporated into the bilayer, phase coexistence was visible in unilamellar regions over a 0.6 °C range (starting from 30.6 °C), with some variation across the field of view. We attribute this observation to the interaction with the substrate, which may vary across the sample. This suggests that when the fluorophore concentration is reduced to 0.01 mol%, the phase transition of the SLB is effectively the same as that of an unlabelled SLB, with a finite coexistence region due to the interaction with the support, or the finite purity of the $DC_{15}PC$ used. The shift in the transition temperature is curious. It seems unlikely that adding just 0.01 mol% of fluorophore to the bilayer should cause a shift in T_m of 3 °C, while increasing the fluorophore concentration 100 fold has no effect. The difference may be an artefact of the faster cooling rate (by approximately 33%) used for the label-free sample compared to the other samples, or variations in T_m from other uncontrolled factors as discussed in the previous section.

To better understand the mechanism by which ATTO488-DOPE alters the phase coexistence region of the sample, the cooling experiment was repeated using a bilayer containing 1.00 mol% DOPE instead of ATTO488-DOPE. In this sample, phase coexistence became visible in the DIC images at 33.4 °C, and was virtually gone by 30.2 °C, a temperature range of 3.2 °C, similar to that observed for the 1.00 mol% ATTO488-DOPE sample. This indicates that the ATTO488 tag itself doesn't affect the phase transition; rather, it is the accumulation in the L_d phase of the DOPE molecule to which ATTO488 is attached that extends the phase transition. The DOPE lipid has a lower phase transition temperature than $DC_{15}PC$, so as the L_d domains shrink and the DOPE within them becomes more concentrated, the transition temperature of the domains is lowered keeping them fluid for longer during cooling. As the L_d domains continue to shrink as the sample is cooled, the concentration of DOPE increases yet further, again lowering the phase transition temperature.

Our results therefore indicate that the incorporation of typical concentrations of other lipids, such as any of the many DOPE-based fluorophores typically used in fluorescence experiments, into the bilayer during the phase transition would lead to significant changes in the bilayer phase behaviour. This is exacerbated by the tendency of these lipids to become more concentrated as the L_d domains contract during the phase transition. It is possible that the use of a fluorophore with chains closely matching the surrounding lipid, such as ATTO488-DC_{15}PE, would allow fluorescence measurements without affecting the phase transition; however, it should be noted that addition of fluorophores to lipid headgroups results in different phase partitioning than would be expected from the tails alone [58], so a labelled DC_{15}PE lipid might still accumulate in the L_d phase.

4.3 Liquid-Ordered Phases

As discussed in Sec. 1.1, the study of lipid rafts is one of the most biologically relevant applications of lipid bilayer model systems. Using qDIC, we have the opportunity to study the liquid-ordered (L_o) phase, which is believed to form the basis of the raft domains, without the need for fluorescent labelling, and with the sub-nanometre axial resolution demonstrated in the previous chapter.

Imaging of ordered domains in qDIC relies on the higher molecular order of the L_o phase of the lipid bilayer, which gives it a higher refractive index [29], and generally also a greater thickness [42], than the L_d phase. Since both of these factors increase the L_o domain optical thickness, L_o domains should be visible in the qDIC phase images as regions of higher brightness. As in Sec. 3.1, corresponding fluorescence images were taken to compare with the qDIC images. We expect the ATTO488-DOPE fluorophore to preferentially partition into the L_d phase, based on the partitioning behaviour of other fluorophores tagged to DOPE described in the literature [124], as well as our observations in Sec. 4.2 of its preference for the L_d phase in the L_d-S_o system. In fluorescence the L_o domains should therefore appear as dark patches in the membrane.

To produce SLBs which show liquid-liquid phase coexistence at room temperature, a mixture of DOPC, ESM, and Chol was used. While there are a wide variety of different possible lipid compositions which can produce ordered domains at room temperature [42, 119], this mixture offers particular advantages. Firstly, using DOPC as the disordered lipid component allows us to make reasonable comparisons between the L_d phase in our ternary samples and the pure L_d phase samples made entirely of DOPC discussed in the previous chapter. Secondly, the use of ESM for the ordered phase makes for a more biologically relevant model system than, for example, DPPC might, as sphingolipids are one of the defining components of lipid rafts [19] in cells.

The phase behaviour of lipid bilayers is highly sensitive to the ratio of these three lipid components [119, 125], and so it is important that this ratio be carefully chosen to suit the requirements of the experiment. For example, the relative proportions of the three lipids determines domain size and domain miscibility temperature. The former is an important factor given that qDIC is an optical technique with a diffraction limited lateral resolution; nanometre-sized domains might be closer to the scale of biological lipid rafts, but are beyond the capacity of qDIC to image. As such, a mixture which produces micron-scale domains is needed. The domain miscibility temperature is equally important. As described in Appendix B, our sample

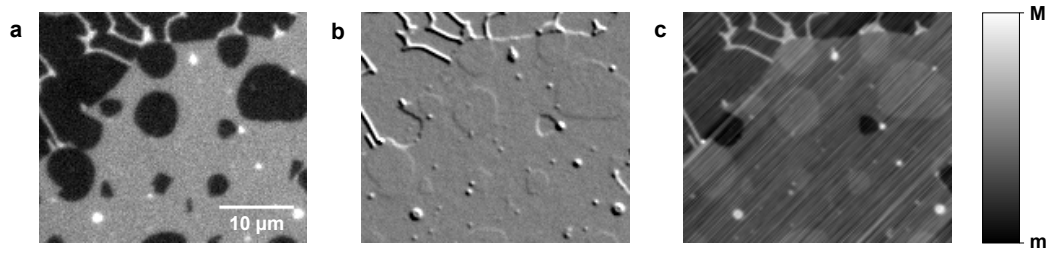

Figure 4.6: Images of a DOPC/SM/Chol/ATTO488-DOPE(54.9/25.0/20.0/0.1). a) Fluorescence ($M = 109\,\mathrm{pe}$, $m = 0\,\mathrm{pe}$), b) qDIC contrast ($m = -0.015$, $M = 0.015$), and c) qDIC phase ($m = -17\,\mathrm{mrad}$, $M = 7\,\mathrm{mrad}$).

preparation procedure requires the sample to be in a homogeneous L_d phase when undergoing pre-hydration at 37 °C; this coupled with the temperature limitations of our setup necessitates a miscibility temperature between room temperature and 37 °C, or no domains will be observed.

Another important consideration is whether the ordered domains are formed from an L_o phase or an S_o phase, since in addition to the L_d-L_o phase coexistence regime, L_d-S_o phase coexistence is also possible when the proportion of cholesterol is sufficiently low. Unlike the L_o phase, the S_o phase is not believed to occur in nature, and so is not representative of the structure of membrane rafts. Differentiating between the L_d-L_o coexistence regime and the L_d-S_o regime in fluorescence is difficult because generally both S_o and L_o domains would appear as dark patches in the membrane, with small differences in domain shape being the only distinguishing factor [125]. Making such a distinction would be extremely difficult even with qDIC due to the small difference expected in optical properties between the S_o and L_o phases. It is therefore necessary to chose a ratio well away from the L_d-S_o coexistence regime.

These considerations motivated the selection of the 55/25/20 (DOPC/ESM/Chol) ratio previously stated in Sec. 2.1. These proportions were selected based on phase coexistence experiments carried out in the literature on GUVs [119]. The lipid composition in these experiments differed from ours in that they used pure palmitoyl sphingomyelin, rather than the chicken egg sphingomyelin we use. However, since egg sphingomyelin is 86% palmitoyl sphingomyelin (according to the manufacturer) this data should still be applicable to our lipid mixture. For fluorescently labelled samples, 0.1 mol% of the overall lipid mixture was changed from DOPC to ATTO488-DOPE, which is expected to have a negligible effect on the phase behaviour.

It was found that this mixture produced micron-scale domains as expected. When the domain stability as a function of increasing temperature was tested using fluorescence microscopy, it was found that a temperature of around 30 °C was sufficient to melt most of the domains, and so this is taken to be the approximate miscibility temperature of the mixture. This is lower than expected based on the GUV data for this particular ratio [119]; however it is still comfortably within the target temperature range, and is sufficiently above room temperature to ensure the domains are stable against melting under normal imaging conditions.

An example of an SLB showing liquid-liquid phase coexistence is shown in Fig. 4.6. The domains are clearly visible in the fluorescence images due to their exclusion of the fluorophore. These domains have a rounded shape, which is ex-

pected of the L_o phase due to the energy penalty associated with the hydrophobic mismatch at the interface between domains. This supports the conclusion that the domains are in the L_o phase rather than the S_o phase, since S_o phase domains would be expected to have a more angular structure, like those seen in Fig. 4.4.

The extent of the fluorophore exclusion is so great that the fluorescence step between phases (measured as described in Sec. 3.5) of 51.2 ± 0.8 pe is the same within error as the step from the L_d phase to glass of 50.1 ± 0.8 pe, indicating that the surface density of fluorophore in the L_o phase is less than 2% of that in the fluid phase. The difference in free energy of the fluorophore between the two phases is therefore below -100 meV, which is similar to simulated values found in the literature [123].

In the qDIC images, the L_o domains are visible in the contrast images as convex regions, and, consistent with expectations, appear in the qDIC phase images as regions of increased intensity. Interestingly, one of the dark patches which appears to be a domain in the fluorescence image Fig. 4.6a is shown in the corresponding qDIC images Fig. 4.6b and Fig. 4.6c to be in fact a small hole in the bilayer. This example highlights the benefit of qDIC for imaging domains, as while in principle this hole could be distinguished from domains in fluorescence by the use of an additional fluorophore which partitions into the L_o phase, the qDIC technique renders this unnecessary.

In order to extract quantitative information about the ordered phase, the optical thickness of the L_o domains must be measured. However, in most regions of the ternary sample it was not possible to measure the optical thickness step from the glass to the L_o regions of the bilayer directly, because of a lack of suitable edges over which to take line profiles. This is likely a result of the greater hydrophobic thickness of the L_o phase than the L_d phase; L_d phase edges exposed to water incur a lower energy penalty than exposed L_o phase edges, causing the SLB to favour a configuration where the L_o domains are surrounded by L_d domains to minimise the exposure of the hydrocarbon tails to water. This tendency of the bilayer to surround L_o domains with L_d regions can be seen clearly in Fig. 4.7a.

Although the phase step between the L_d and L_o phases can be measured in the same manner as described in Sec. 3.1, this on its own cannot be converted to an absolute thickness using Eq.(3.2) because of the differing refractive indices on either side of the phase boundary. The measured optical thickness step between phases $\Delta\phi$ is described by Eq.(4.2), where h_{LO}, n_{LO}, h_{LD} and n_{LD} are the absolute thicknesses and refractive indices of the L_o and L_d phases, respectively.

$$\Delta\phi = \frac{2\pi}{\lambda_0}\Big(h_{\mathrm{LO}}(n_{\mathrm{LO}} - n_{\mathrm{m}}) - h_{\mathrm{LD}}(n_{\mathrm{LD}} - n_{\mathrm{m}})\Big) \tag{4.2}$$

While it was not possible to obtain direct measurements of the L_o phase optical thickness, the optical thickness of the L_d phase (with its larger area and greater localisation towards the edge of the SLB) could be measured directly, allowing the absolute thickness of the L_d phase domains to be measured if the refractive index is known. Though spectroscopic experiments on domain composition have shown that the L_d phase may contain some of the ordered lipid component [126, 127], the small proportions of these ordered lipids coupled with the relatively small difference in refractive index between these ordered lipids and DOPC, should mean that the change in refractive index of the L_d phase compared to pure DOPC bilayers is negligible. The refractive index of the L_d phase was therefore taken to be the same as for pure DOPC bilayers. With the absolute thickness of the L_d phase, h_{LD} known,

the absolute thickness of the L_o phase can be calculated from Eq.(4.3).

$$h_{LO} = \frac{\lambda_0 \Delta\phi}{2\pi(n_{LO} - n_m)} + \frac{h_{LD}(n_{LD} - n_m)}{(n_{LO} - n_m)} \tag{4.3}$$

Using this equation, measurements of both the L_d and L_o phase thickness were taken for the fluorescently labelled sample. All these measurements were taken on the first bilayer using the first lipid stock. This resulted in a bilayer thickness of 3.90 ± 0.05 nm ($n = 48$) in the L_d phase, which is slightly larger than the thickness of the pure DOPC bilayers formed using the first lipid stock presented in Table 3.1. The thickness of the L_o phase was found to be 5.19 ± 0.06 nm ($n = 48$), a thickness difference of 1.29 ± 0.08 nm between the two phases.

As in the DOPC/ATTO488-DOPE samples, double bilayer regions can be seen in SLBs formed from the ternary mixture. Understanding the phase behaviour in these double bilayer regions can be difficult, but the qDIC technique can give more insight into these regions than fluorescence alone. An example of this is shown in Fig. 4.7, which shows a region where double bilayer patches in different phases are linked by thin branch-like membrane structures (the precise nature of which is discussed in more detail in Sec. 4.4).

In Fig. 4.7 the structure of the patches that are connected to the branches is unclear from the fluorescence alone; however when the qDIC phase image is included as an overlay, the different regions can be clearly identified by their colour. Regions that are a single L_d phase bilayer appear dark green, while dark red indicates the single-bilayer L_o phase. Bright red indicates two stacked L_o bilayers (L_o + L_o) and bright green a stack of two L_d bilayers (L_d + L_d), while orange represents a mixed stack of one L_o phase bilayer and one L_d phase bilayer (L_d + L_o, or L_o + L_d). Notably, using only fluorescence it is not possible to distinguish between double L_o phase bilayers surrounded by a double L_d phase border, and regions where the branch structures encircle an empty area. The qDIC technique therefore eliminates the need for a second fluorescent label for the L_o phase that is otherwise required to accurately interpret the data.

Additionally, different combinations of phases can be distinguished by quantitative measurements of their relative fluorescence and optical thickness steps, as can be seen in Fig. 4.8, where the measured step heights are normalised to those of the L_d phase of the first bilayer. The L_d + L_d regions have approximately double the fluorescent intensity of the L_o + L_d regions, while having approximately the same normalised optical thickness. More measurements would likely reveal a shift in the normalised optical thickness between the L_d + L_d regions and the L_o + L_d regions due to the greater optical thickness of the L_o phase.

Measurements of bilayer thickness can also be carried out on samples prepared without fluorescent labels. As in the case of the labelled samples, the thickness of the L_o phase had to be determined indirectly, using Eq.(4.3). For a non-labelled sample, the thickness of the L_d phase was 3.89 ± 0.03 nm ($n = 70$), while the thickness of the L_o phase was 4.96 ± 0.05 nm ($n = 70$). The thickness difference between L_o and L_d phases in the unlabelled sample is 1.06 ± 0.06 nm, markedly lower than the corresponding phase thickness difference measured in the labelled sample.

This result is somewhat counter-intuitive. As has already been established, the fluorophore is almost totally excluded from the L_o phase of the bilayer, yet at first glance, the data appears to indicate that the presence of the fluorophore increases the L_o domain thickness. This is also surprising in the context of experiments on

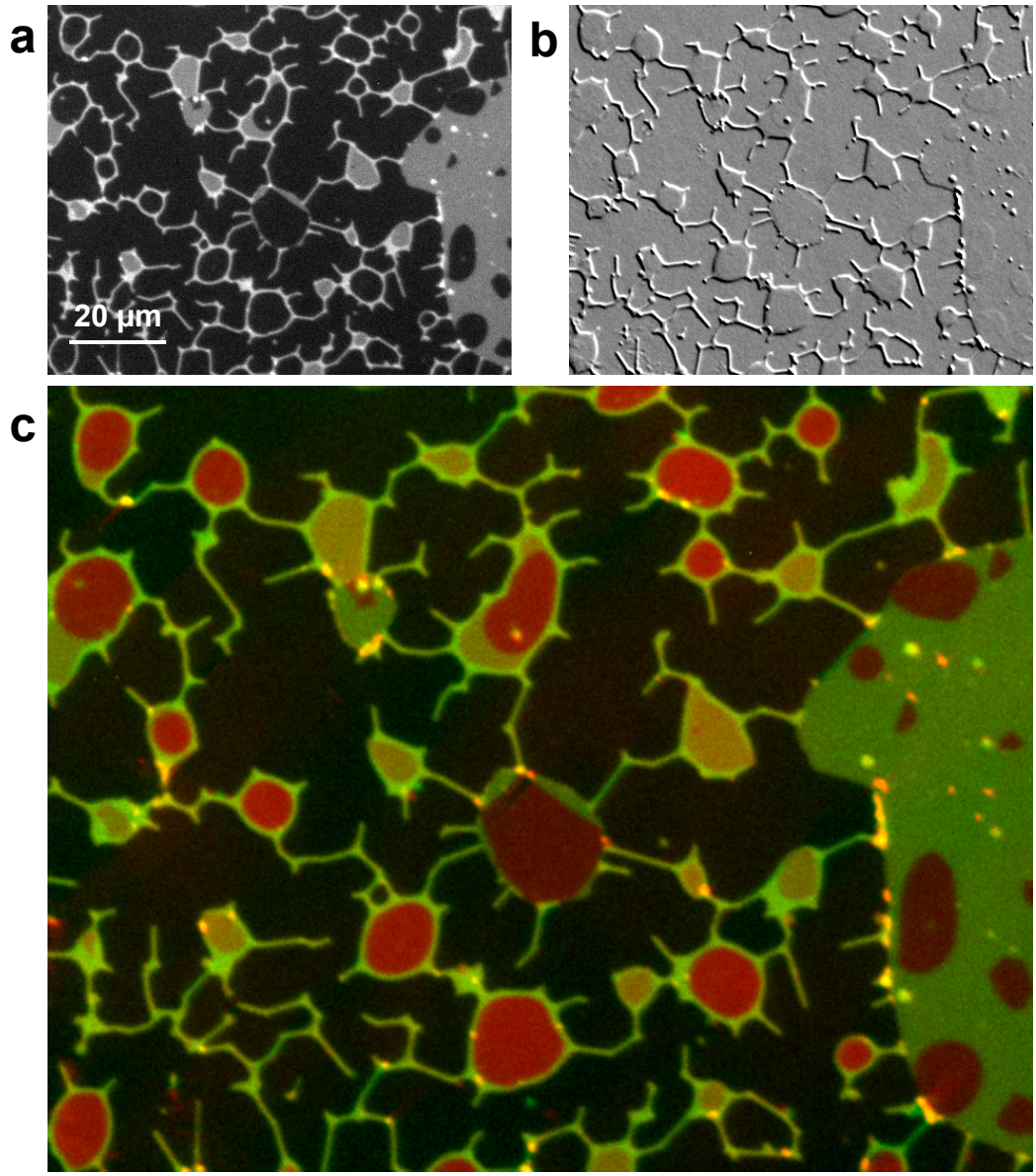

Figure 4.7: Region of a DOPC/ESM/Chol/ATTO488-DOPE (54.9/25.0/20.0/0.1) sample showing a) fluorescence (scaled from 230 to 350 pe), b) qDIC contrast (scaled from -0.00320 to 0.00282), and c) a composite image generated from fluorescence (green) and qDIC phase (red) images.

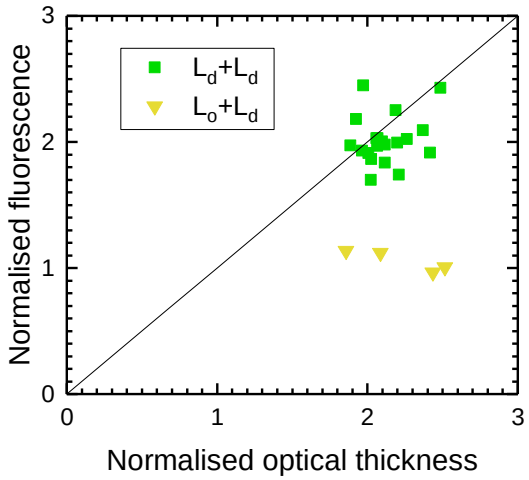

Figure 4.8: Fluorescence versus phase for double bilayers in a ternary sample, normalised to single L_d phase bilayers of the same region. Double L_d bilayers (green squares) are distinguished from L_d+L_o phase bilayers (yellow triangles).

vesicles, which have shown that even relatively large changes to the lipid composition of the L_d phase do not significantly affect the thickness of the L_o domains [128].

To understand this result, it is important to bear in mind how the errors are calculated. The errors presented are based on the distribution of the data, and so most accurately describe the errors between measurements made on the same sample. Variation in factors such as polariser calibration and microscope alignment might cause differences between measurements that would be expected to be otherwise identical. For example, the data presented in Table 3.1, shows that the thickness can vary by 0.1 - 0.2 nm between nominally equivalent bilayers.

This means that while the relative difference in thickness between the L_o and L_d phases for the labelled and unlabelled samples are known with a high confidence, the absolute values are less accurately defined. Given that the sample variation is of a similar magnitude to the measured effect of the fluorophore on the thickness difference between phases, it is reasonable to assume that the L_o domains have the same thickness, as expected from the literature, and the increase in the thickness difference over the phase edge is in fact due to a reduction in the thickness of the L_d phase.

Under this interpretation, the data agrees well with the measurements made on the pure DOPC sample. As described in Sec. 3.4, comparing labelled and unlabelled DOPC bilayers showed that the presence of ATTO488-DOPE causes an additional thickness reduction in the first bilayer of 0.2 nm compared to the label-free bilayers. This is the same magnitude as the discrepancy between domain thickness in labelled and unlabelled samples. The most reasonable interpretation for our data then is that in the fluorescently labelled samples, the L_d phase has an additional 0.2 nm thickness reduction due to the fluorophore-substrate-bilayer effect, while the fluorophore-excluding L_o phase does not, thus increasing the relative thickness difference between the two phases by 0.2 nm compared to the unlabelled sample.

To further test this hypothesis, we looked at the optical thickness step over the domain boundary in the second bilayer of labelled and unlabelled samples. If the effect is, as we believe, due to the interaction between the L_d phase bilayer, the fluorophore and the substrate as discussed in Sec. 3.4, then regardless of the

presence or absence of fluorophore, the difference in optical thickness between L_o and L_d phases should be the same in the second bilayer. This is indeed what the data shows; in second bilayer samples formed from the second lipid stock, $\Delta\phi$ is 1.99 $\pm$ 0.03 mrad (n = 290) for the labelled samples and 1.99 $\pm$ 0.03 (n = 304) for the unlabelled samples. To ensure maximum consistency between these measurements, both samples were imaged in the same session. The data supports the conclusion that the fluorophore does not affect the L_o domains.

To better understand how the surface hydrophilicity affects the different bilayer phases, domains were formed on a piranha etched surface that had its hydrophilicity reduced by exposure to air (as described in Sec. 3.4) using a lipid mixture including the ATTO488-DOPE label. In this experiment, we would expect that the thickness of the L_d phase would be greater based on our previous experiments on pure L_d phase bilayers, however, it is unclear whether the hydrophilicity would affect the L_o phase in the same way. After all, we have established in Sec. 3.4 that the mechanism that causes the first bilayer thickness reduction in pure L_d phase bilayers requires exposed bilayer edges to be effective, but the L_o phase lipids are almost always surrounded by the L_d phase, and so cannot move easily between leaflets. Furthermore, the L_o phase has much greater resistance to stretching, so even if lipids could move between leaflets, the upper leaflet may not be able to stretch enough to measurably change the bilayer thickness. Because of these factors, we might expect then that the L_o domain thickness would be unaffected by substrate hydrophilicity.

In contrast however, both the L_d and L_o phase thickness measurements were larger on the partially hydrophilic surface than on the fully hydrophilic surface. The L_d phase had a thickness of 4.24 $\pm$ 0.04 nm (n = 93), while the L_o phase thickness was 5.56 $\pm$ 0.06 nm (n = 91). The difference in thickness between the two is 1.32 $\pm$ 0.07 nm, which is equal within error to that measured for the labelled sample on the fully hydrophilic surface. While this might seem to contradict our hypothesis that movement of lipids from the upper to lower leaflet over the bilayer edges drives the thickness difference, there are two important considerations to bear in mind.

Firstly, it is important to consider that our observation that bilayer edges are required to establish the thickness difference comes from samples that are imaged within minutes after full hydration of the sample. Therefore, in those samples, thickness differences can only be established where pathways for rapid lipid movement between leaflets, such as edges, are available. Other, slower acting mechanisms for changing the lipid distribution, such as flip-flop, would not be effective on these timescales. However, in the ternary samples, the samples are left for five days to allow domain formation, and so flip-flop might provide an effective means for lipids to move from the upper to the lower leaflet, very gradually establishing the thickness difference in the L_o phase over a prolonged period.

Secondly, domain formation is itself a gradual process, and initially the lipids in the SLB form a single L_d phase before the ordered lipids begin to phase separate. All the lipids in this homogeneous phase would be able to diffuse freely within the bilayer, allowing the ordered phase lipids to move between leaflets over the exposed bilayer edges in the same way as DOPC would. Thus, the density difference of the ordered phase lipid components between leaflets could be established before macroscopic domain formation had even necessarily been completed.

Other factors relating to L_o domain thickness were then investigated. One factor that was looked at was the size of the domains. Small-angle neutron scattering experiments have suggested that, for nanoscale domains at least, the size of domains is

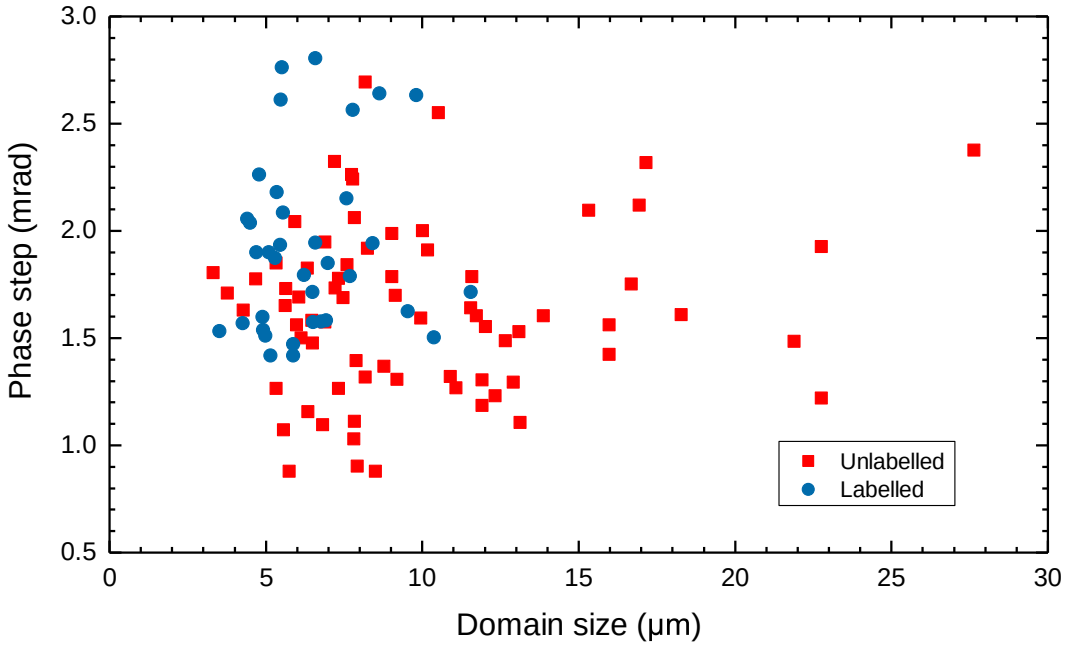

Figure 4.9: Scatter plot showing the optical thickness step over the domain boundary against the size of the domains (defined as the square root of the domain area). Measurements taken in the labelled sample are denoted by blue circles, while measurements taken on the unlabelled same are denoted by red squares.

dependent on the thickness difference between the domains and the surrounding L_d phase [128], with a greater thickness mismatch corresponding to larger domains, due to the increased line tension at the domain boundaries. Given then that the thickness mismatch between the L_o and L_d phases is different in labelled and unlabelled samples, it might be expected that the domains would be larger in labelled samples, where the thickness difference is greater, than in the unlabelled samples. It might also be possible to detect correlation between the thickness and area of individual domains within the same sample originating from variation in lipid composition between domains.

In order to determine whether there was any correlation between the area of the L_o domains and their thickness, the individual thickness measurements for each domain were plotted against the domain size for both the labelled and unlabelled samples. The domain size is defined as the square root of the measured domain area. This is shown in Fig. 4.9. It can be seen that there is no clear relationship between the optical thickness step and domain size visible in the data for either sample, suggesting that for micron-scale domains, the size of the domains is not related to the thickness mismatch. However, given that there is generally only a single thickness measurement for each domain, and the relatively large error in the individual measurements (typically 15% - 20%), we cannot discount the possibility that there is a relationship which is below our capacity to resolve for individual domains. Using energy minimised images might allow lower noise measurements in the future, enabling the optical thickness of individual domains to be accurately measured.

The distribution of optical thickness values was also investigated to try to detect evidence of differences in domain thickness, which might indicate differences in do-

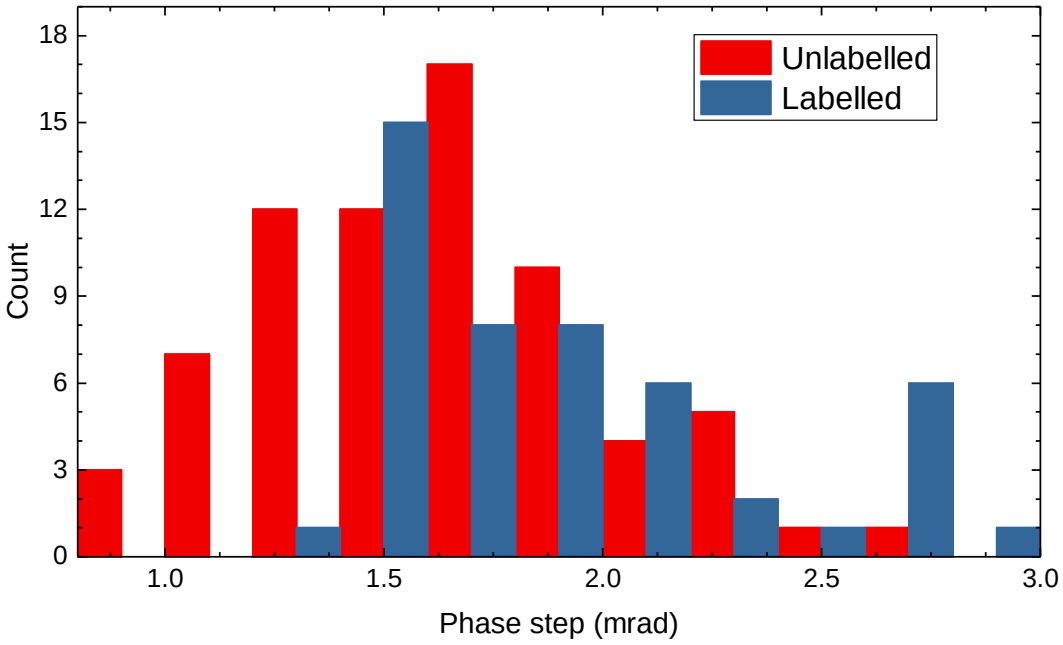

Figure 4.10: Plot of the distribution of the phase steps measured at the boundary between L_o and L_d phases in both labelled and unlabelled samples.

main composition. This distribution is shown in the histogram in Fig. 4.10. There is little evidence in the data to suggest that there are distinct domain populations. Given that the optical thickness step over the domain edges thicknesses are close to the noise level described in the previous chapter, it may be that such differences are not resolvable with qDIC unless a practicable method of reducing the noise from the glass roughness is developed.

4.4 Lipid Bilayer Tubes

As we have shown, the combination of qDIC and fluorescence opens up new possibilities for the investigation of membrane phase behaviour, offering additional insights in cases where the information provided by fluorescence alone might otherwise be ambiguous. One subject of interest were the thin branch-like structures present protruding from the edges of double bilayer regions of certain samples, such as those visible in the upper left region of the L_o-L_d phase coexistence sample shown in Fig. 4.6 and in all but the rightmost region of Fig. 4.7.

While these structures are relatively common, appearing in samples with a range of different lipid compositions, they are not present in all samples, and are not present in every field of view even on those samples where they do appear. Qualitatively, the fluorescence intensity of these structures as seen in Fig. 4.6 appears to be the same as that of a single bilayer, while the corresponding phase signal is comparable to that of a double bilayer region. It was tentatively considered therefore that in the L_o-L_d phase coexistence samples these thin structures might be formed from a stack of one L_d phase bilayer and one L_o phase bilayer.

Due to the small width of these structures, it was not possible to fit them using Eq.(3.1) like the bilayer edges. Instead, the line profile was taken perpendicular to the length of the structures, as shown in Fig. 4.11a. Since they appear in the phase

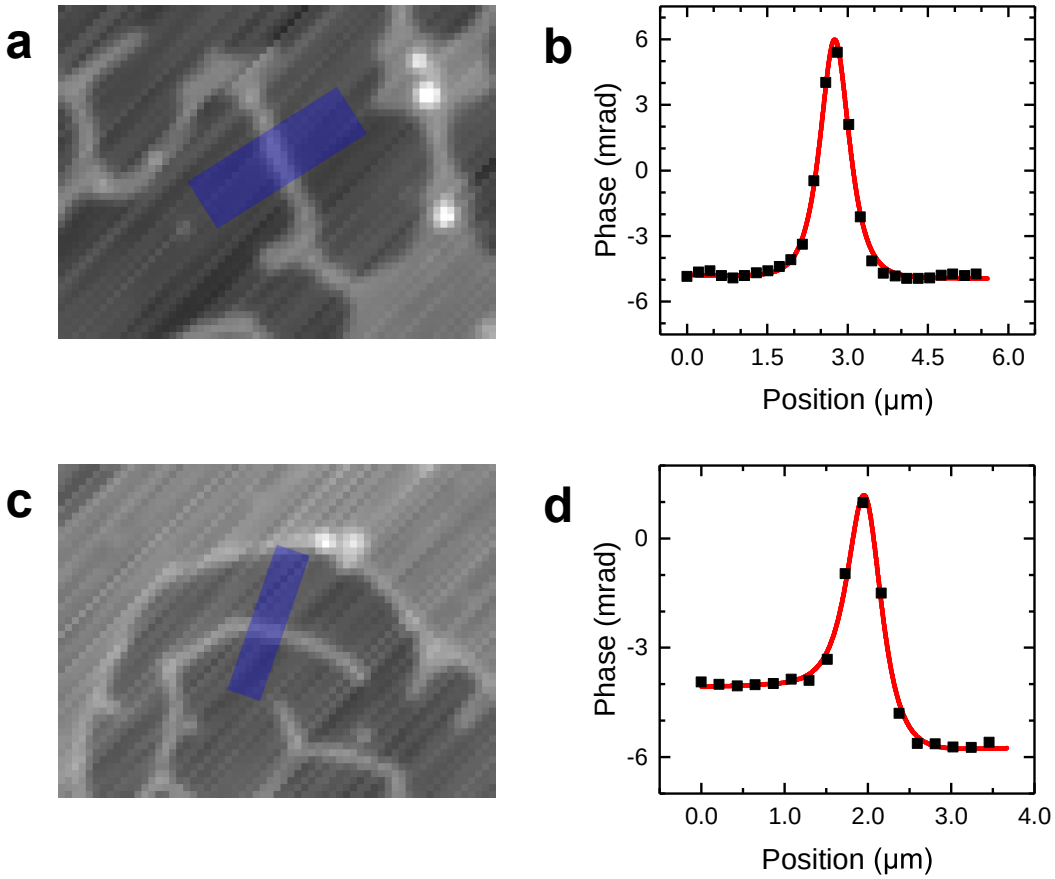

Figure 4.11: qDIC phase images showing line cuts through the branch-like structures. Panel a) shows a 13.6 × 10.5 μm^2 region with a line cut through one such structure (m = -17.8 mrad to M = 27.4 mrad), with an associated phase profile shown in b) which shows the standard peak-like profile. Panel c) shows another 13.6 × 10.5 μm^2 region with a seemingly typical structure (m = -16.0 mrad to M = 16.3 mrad), with a corresponding phase profile shown in d) which is uneven on each side of the peak. Both line profiles (blue) are drawn from the top right down to the bottom left.

and fluorescence line profiles as peaks, a sech function was used as the basis for the fit function, which is given in Eq.(4.4). As for Eq.(3.1), Eq.(4.4) incorporates a linear background term $dx + e$, and the parameters a and c are the magnitude and width of the peak. Fitting was again carried out using the Curve Fitting Toolbox in MATLAB R2015a. An example of this function fitted to a phase peak is shown in Fig. 4.11b.

$$y = a\,\mathrm{sech}\left(\frac{x-b}{c}\right) + dx + e \tag{4.4}$$

Determining the nature of these structures from this data is complicated by the fact that they seem to be below the lateral resolution of the microscope. The average value of the width, c, of the structures was only 1.1 pixels, which indicates that these structures cannot be fully resolved using the 20× objective (the mean width of the single bilayer steps, which are also sub-resolution, is 1.2 pixels). However, that the data suggests that the width of the structures is extremely small (on the order of hundreds of nanometres), is itself reason to doubt the interpreta-

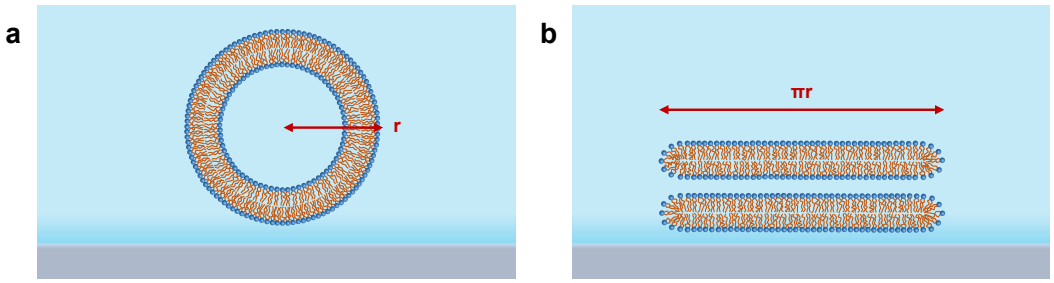

Figure 4.12: The cross section of a) a tube of radius r, and b) two stacked bilayers with the same total cross sectional length as the tube.

tion of the structures as a simple stack of bilayers. Such long, thin double bilayer regions would have very high perimeter-to-area ratios, incurring strong energetic penalties due to exposure of the hydrophobic bilayer interior to water, making it an energetically unfavourable arrangement. While it is conceivable such unfavourable structures might be produced in the sample upon hydration, these samples have had several days to equilibrate, so any highly unfavourable structures generated during the sample preparation should have had ample time to rearrange into lower energy configurations.

An alternative possibility was that these were membrane tubes, regions in which the lipid bilayer had rolled up upon itself to form cylindrical structures. For extremely long, thin bilayer structures, a tubular arrangement might be more favourable than the previously discussed geometry of stacked L_o and L_d domains, since in a tubular geometry the energetically unfavourable exposed bilayer edges are eliminated along the entire length of the tube (except possibly at the ends of the tube). However, unlike planar supported bilayers, tubes would incur other energetic penalties, for bending the membrane, as well as for having a lower area exposed to the hydrophilic substrate. Cross sections of the two configurations are shown in Fig. 4.12.

To test which configuration is most favourable, we can consider the total energy of the system theoretically. The energetic cost of bending a lipid bilayer can be described using the Helfrich Hamiltonian [129] which treats the bilayer as an infinitely thin surface. For a tubular arrangement with a circular cross-section, the bending energy is given by Eq.(4.5), where r is the tube radius, k_b is the bending rigidity and l is the tube length.

$$E_{\text{bend}} = \frac{\pi k_b l}{r} \tag{4.5}$$

Assuming the ends of the tubes aren't closed, there is an additional energy penalty from the line tension, γ, caused by the exposed bilayer edges at the ends of the tube. The energy penalty associated with this is proportional to the exposed length of the bilayer edge, so for each end of the tube this is simply $2\pi r\gamma$. The total energy of the tube is therefore given by Eq.(4.6).

$$E_{\text{tube}} = \frac{\pi k_b l}{r} + 4\pi r\gamma \tag{4.6}$$

For two stacked planar bilayers, there are two energy contributions. The first is the line tension at the edges of both bilayers originating from the association of the hydrophobic lipid tails with water. This acts on both the sides and ends of each bilayer in the stack. The second is a favourable interaction, ϵ, between the first

bilayer and the support. For a stack of two bilayers, which have the same length, l, as the tube described in Eq.(4.5), and combined contain the same total membrane area as this tube of radius r, the width of the stack is πr. We can estimate the total energy using Eq.(4.7), where the first term is the energy penalty from the sides of the stack (two sides for each of the two bilayers with length l), the second is the penalty from the ends of the stack (two ends of two bilayers of width πr) and the last term is the attractive interaction between the first bilayer and the support (first bilayer area $\pi r l$).

$$E_{\text{stack}} = 4\gamma l + 4\pi\gamma r - \epsilon\pi r l \tag{4.7}$$

Because we assume that the length and bilayer area of the stack is the same as for the tubes, the energy cost of the ends, $4\pi\gamma r$, can be neglected as it is the same for both tubular and stacked membrane geometries. The condition for a tubular arrangement being more favourable than a stacked bilayer arrangement is thus given by Eq.(4.8), assuming negligible interaction between the tube and the substrate.

$$\frac{\pi k_{\text{b}}}{r} < 4\gamma - \epsilon\pi r \tag{4.8}$$

The radii at which the most favourable state changes from a stack to a tube (and vice versa) are given by Eq.(4.9).

$$r = \frac{2\gamma \pm \sqrt{4\gamma^2 - \pi^2\epsilon k_{\text{b}}}}{\epsilon\pi} \tag{4.9}$$

We can therefore estimate the range of radii where a tube is the more favourable state by using literature values of the parameters γ (27.7 pN, measured using electroporation on DOPC GUVs [130]), k_{b} (76 zJ for DOPC bilayers in distilled water [99]) and ϵ (-0.5 mN/m for DMPC bilayers on silica substrates in PBS [131]). Using these values, we find that tubes are more favourable than stacks between radii of 0.2 nm to 705.2 nm. Other factors not accounted for in Eq.(4.8), such as the effect of area mismatch between leaflets, and the effect of the ionic strength of the medium on the bending rigidity [132], should lower the cost of bending, and thus raise the maximum radius. Since the structures we observe are not fully resolved, and so must be below 367 nm (the Abbe resolution limit) in diameter, we can say with good confidence that the thin structures we see are membrane tubes.

Such tubular bilayer arrangements are present in a variety of different biological contexts. Microvilli for example are tubular membrane protrusions from the cell membrane with diameters of approximately 100 nm, which are responsible for increasing cell surface area in parts of the body such as the intestines, and may also have roles in producing vesicles [133]. Another example is in the nervous system, where tubular appendages called dendrites, with diameters ranging from a few hundred nanometres to a couple of microns, allow neurones to receive signals from neighbouring cells [134]. Networks of tubular membranes are also present within the cell, and many membranous structures involved in the trafficking of material around the cytoplasm such as the endoplasmic reticulum, the trans-Golgi network, and the endosome, all contain some tubes in their structure [60, 135].

Typically, tubes are produced in model membranes by mechanically forcing shape changes in the membrane, such as by laterally compressing the bilayer [46], by the use of membrane shaping proteins [135], or by pulling the membrane using micropipette aspiration or optical tweezers [60]. These tubes generally retract into the bilayer once

this outside force is removed [46]. Alternatively, tubes can be formed in response to chemically induced density differences between membrane leaflets [136]. In contrast to these systems, the tubes observed in our samples are not being actively moulded by external forces, and once formed are generally stable over timescales of many hours. They may therefore provide an interesting model for investigating 'steady state' bilayer tube behaviour.

Having fitted Eq.(4.4) to the line profiles to obtain the width and peak values of the tubes in both the fluorescence and optical thickness data, the next logical step is to convert this information into meaningful structural information about the tubes. One limitation of attempting to extract information using the peak value a is that the peak of the sech function is reduced by defocus, which would result in a systematic shift towards lower values. Additionally, because the structures are below the resolution, the peak value would not be an accurate measure of the optical thickness.

A more accurate alternative is to integrate the area contained within the sech function and use this as a measure of the phase and fluorescence of the tube, as was briefly described in Sec. 3.1 for measuring the radius of curvature at joined double bilayer edges. This area is less affected by defocus, as any loss of peak intensity due to deviation from the focal plane is accompanied by a corresponding increase in the width of the profile, c. Since only the area of the sech term is of interest, the linear background term can be neglected in the integral of Eq.(4.4). The area of the tubes is therefore simply πac, which gives areas in rad×pixels or pe×pixels for optical thickness or fluorescence respectively.

From these area measurements, the radii of the tubes can be obtained, as shown in Eq.(4.10). The radius is a fundamental structural parameter of the tubes, which in turn is related to fundamental properties of the bilayer such as bending elasticity and tension [60]. The area measurements can be properly calibrated to the scale of the bilayer by multiplying by the pixel calibration, d_{px}, which for these measurements is 0.2161 µm pixel^{-1}. Once this is done, dividing the calibrated fluorescence or optical thickness area by the second bilayer measurements of either the fluorescence, F_2, or optical thickness, ϕ_2, as appropriate, yields the circumference of the tubes from which one obtains the tube radius, r.

$$r_\phi = \frac{a_\phi c_\phi d_{px}}{2\phi_2},\ r_{\mathrm{F}} = \frac{a_F c_F d_{px}}{2F_2} \tag{4.10}$$

The motivation for using the second bilayer optical thickness and fluorescence measurements in Eq.(4.10) rather than the first is to exclude the previously described substrate hydrophilicity effects. Since the majority of the surface of the tube is not in contact with the substrate, the bilayer thickness of the tube should not experience the substrate hydrophilicity induced thickness reduction, and so the second bilayer data is more appropriate for determination of the radius. Also, scattering experiments on LUVs have demonstrated that curvature does not alter the thickness of DOPC bilayers when the radius of curvature is above 31 nm [69], and so the bilayers in the tubes should be equivalent to the second supported bilayer in absolute thickness and fluorescence density so long as the radius of curvature is above this level.

All of the measurements presented here are for bilayers containing fluorescent labels. While we have seen numerous fluorophore related effects on the bilayer (see Sec. 3.4 and Sec. 4.2), previous experiments on POPC bilayers have shown that even

relatively large amounts of fluorophore (up to 2 mol%) do not influence the bending rigidity of the bilayer [137], which we expect to be a key factor influencing the tube radius [60]. So while it would be possible to measure tube radii in unlabelled samples, the negligible influence of the fluorophore found in the literature, suggests that it would unlikely that any significant effects would be detected. Additionally, our tube measurements have shown large variation, which might further obscure small fluorophore effects.

The mean value of the tube radius in the sample with phase coexistence is 180.4 nm as calculated from the optical thickness information. The standard deviation of the tube radius distribution is 24.7 nm. All the individual radius values for the tubes in the sample with L_o-L_d phase coexistence are shown in Fig. 4.13. It is difficult to compare these radius values with those in the literature. The majority of experiments on tubes are carried out using micropipette aspiration of GUVs, in which the resultant tube radius is determined by factors particular to that experimental system, such as the vesicle radius [138], pulling force [60], and the radius of the micropipette [138]. As such, the measured tube radii reported in the literature can vary from seven to hundreds of nanometres [139]; our radius measurements fall comfortably within this range, and so can be considered reasonable.

In order to better understand the phase behaviour in membrane tubes, the measurements of tubes from the L_o-L_d phase separating sample were compared with measurements of tubes from DOPC/ATTO488-DOPE (99.9/0.1) samples, which form a pure L_d phase. As shown in Fig. 4.13, the measurements of the tubes in the sample with L_o-L_d phase coexistence agree well with the measurements of tubes in the pure L_d phase sample. This would seem to confirm that despite the heterogeneous phase distribution in the planar regions, the bilayer tubes in the sample with phase coexistence are formed exclusively from the L_d phase.

This is consistent with experiments in the literature, which have shown that in tubes drawn from GUVs with both L_o and L_d domains, the L_d phase lipids preferentially segregate into the tubes [60]. Even when tubes are formed from the L_o phase, the lipids characteristic of the L_o phase are rapidly replaced [60]. This segregation of lipids between tubular and planar bilayer regions is driven by the higher bending rigidity of the L_o phase, which leads the L_o phase to prefer a low curvature environment. For example, in samples formed from mixtures of DOPC, DPPC and cholesterol, the L_o domains have a bending rigidity almost five times higher than the L_d phase [60].

It can be seen in Fig. 4.7 that the tubes are mostly connected to double bilayer patches. Compared to the tubes, these patches represent a more energetically favourable environment for the lipids because of their lower curvature, and greater contact with the hydrophilic substrate. Because of this, there should be two competing effects on tube radius. First, the bending rigidity of the tubes which favours an increase in tube radius. Second, the preference of the lipids for the planar bilayer regions, which favours a lower proportion of lipids in the tubes, and thus lower tube radius for a fixed length. It may be expected then that these competing forces would eventually counterbalance each other, leading to an equilibrium radius for the tubes.

In contrast to this, the wide range of different tube radii in Fig. 4.13, particularly in the pure L_d phase sample, could be interpreted as evidence that there may be no 'equilibrium' tube radius in the system as a whole. The distribution of the measured tube radii is much larger than the error on the individual tube measurements, which

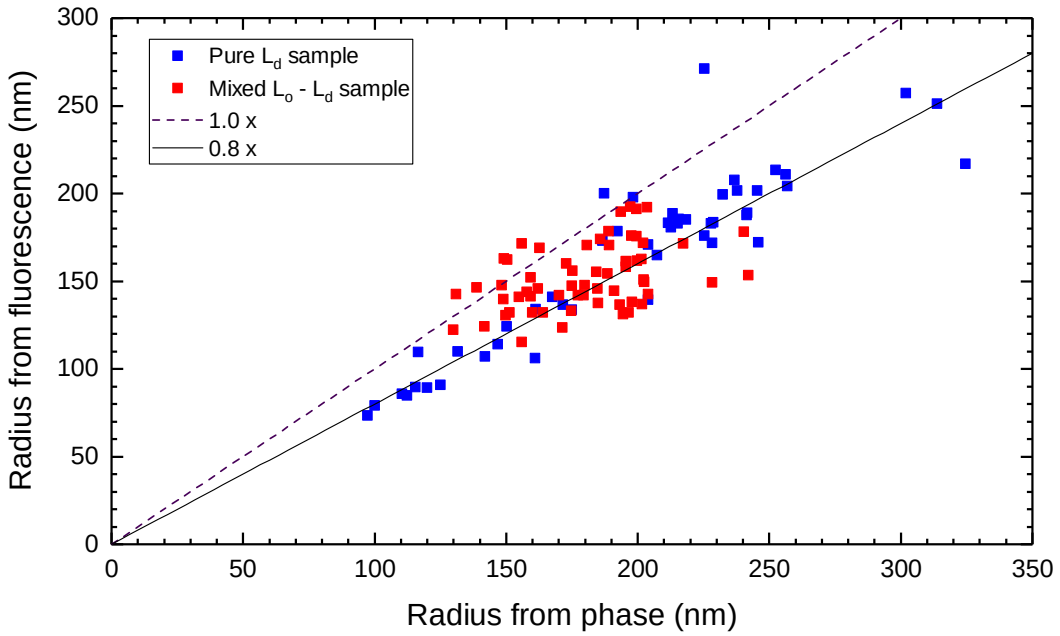

Figure 4.13: Scatter plot showing the relationship between the radius values obtained from the fluorescence measurements against the radius values obtained from the corresponding phase measurements. Lines showing 80% (solid black line) and 100% (dashed black line) of the phase derived radii are included for comparison.

is typically around ±16 nm from the phase and roughly ±12 nm from fluorescence[5], and so seems to represent real variation in the sample. Theoretical models of tube formation from GUVs have shown that the properties of the tube are highly dependent on the geometry of the system from which they formed [140]. It may be then that the broad range of radii observed is a natural result of the differences between the regions from which the tubes formed, such as differences in connected patch size, and number of connections to other tubes and patches.

Alternatively, it may simply take longer for the bilayer to assume the 'equilibrium' radius than the approximately two hour timescale over which the measurements on the pure L_d phase sample were carried out. It is striking that the tubes in the mixed phase sample have a much narrower distribution, considering that such samples were allowed an additional five days to equilibrate at 4 °C in order for domains to form. It also appears that the distribution of radii in the mixed phase sample is positioned at the approximate mid-point of the distribution of the radii in the pure L_d phase sample (ignoring the four large outliers). It would therefore seem reasonable to assume that the initial broad distribution of different radii present in newly prepared samples becomes more sharply defined around this mid-point (which may represent an equilibrium radius) when left for long periods. This possibility could be tested experimentally simply by imaging tubes within a single sample over an extended period of time.

A conspicuous feature of Fig. 4.13 is the disagreement between the radius values calculated from the fluorescence and the phase data, with the average fluorescence-

[5]Assuming the background noise level of 0.204 mrad from the glass is the detection limit for tubes, the smallest resolvable tube should have a radius of 4.2 nm. However, based on the errors on the individual measurements, the true lower limit is likely closer to 15 nm.

based radii values being smaller by approximately 20% than the corresponding phase-based radii estimates. As discussed in the previous section, photobleaching would be expected to cause some reduction in fluorescence, however such photobleaching would equally affect the second bilayer fluorescence measurements used in the radius calculation, and so this should cancel out. Another factor is the potential steric exclusion of the fluorophore from the high curvature bilayer tubes, and there are also considerations relating to how the efficiency of the fluorophore is affected by the relative orientation between the linear dipole of the fluorophore and the fluorescent excitation.

Another possible cause is the birefringence of the lipid bilayer. Previously, the birefringent properties of the bilayer had been ignored because the light passing through the bilayer is at normal incidence and so experiences only the ordinary refractive index, n_o, of the lipid. For DOPC, this is 1.445 [29]. In a tube however, the bilayer curves, and so the extraordinary refractive index, n_e, which for DOPC is 1.460 [29], becomes important. One DIC polarisation will see only the ordinary refractive index of the bilayer n_o, while the other will see the average of the two indices $(n_\mathrm{o} + n_\mathrm{e})/2$ (assuming a perfectly circular cross-section), and so because the overall index is an average of these two, the average refractive index of the tubes will be $(3n_\mathrm{o} + n_\mathrm{e})/4$.

Additional evidence hinting at a possible influence of the tube birefringence on the qDIC phase measurements may be directly visible in some of the individual optical thickness profiles. In several cases, the background phase was different on either side of the tube, as can be seen clearly in the example given in Fig. 4.11d. While the tube shown in Fig. 4.11c looks effectively the same as the one in Fig. 4.11a, the corresponding phase profile in Fig. 4.11d reveals that the background phase is lower before the tube than after. Such a difference in the phase reconstruction could arise from the birefringence, because each of the two DIC polarisations would see a different refractive index, and so the 'step up' over the tube and the 'step down' would not be equal.

Because of the multiple possible ways in which birefringence could be affecting the data, it was decided conduct a more comprehensive investigation. Although those tubes with such irregular phase profiles were ignored for the purposes of the previous analysis (since the tube area is somewhat ambiguous), they can be used here to quantitatively measure the phase difference across the two sides of the tube. This was done using Eq.(4.11), which adds a tanh function to Eq.(4.4), to model the difference in phase, f, on either side of the tube. An example of this function fitted to the experimental data is shown in Fig. 4.11d.

$$y = a\,\mathrm{sech}\left(\frac{x-b}{c}\right) + dx + e + \frac{f}{2}\tanh\left(\frac{x-b}{c}\right) \tag{4.11}$$

The mean difference in the background phase level is 1.07 ± 0.10 mrad (n = 40). No correlation was found between the magnitude of the phase discrepancy and the radius of the tubes (calculated from the phase data) as shown in Fig. 4.14. This is in contrast to the expected linear relationship. However, the noise level in the data limits the accuracy of our measurements of the phase difference, particularly since these are single tube measurements. Additionally, no correlation was found between the phase difference and the fluorescent intensity of the tube, the width of the tube, the angle of the line profile relative to the shear, or the angle of the line profile relative to the tube (this is shown in Appendix C.3). The lack of relationship

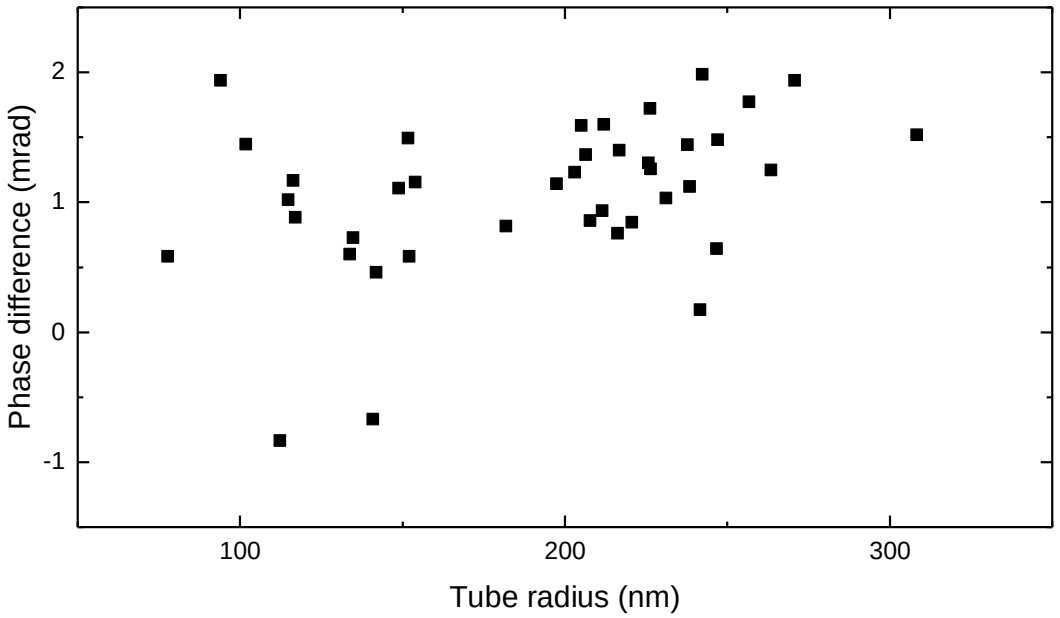

Figure 4.14: Scatter plot showing the phase difference on either side of the tube (in milliradians) against tube radius (in nanometres).

between the angle of the measurement and the shear indicates that artefacts along the shear direction are not contributing significantly to the observed mismatch.

To estimate the expected effect of birefringence on the phase measurements, the refractive index encountered by each of the DIC polarisations must be considered. One DIC polarisation will experience only the ordinary refractive index, while the other will experience the ordinary index in those parts of the tube that are perpendicular to the direction of propagation, and the extraordinary refractive index at the edges of the tube which are oriented parallel to the propagation direction.

The phase gradient Δ for the birefringent tubes can be described as shown in Eq.(4.12), where the $(1+\alpha)$ term describes the change in the phase measured by one polarisation due to the birefringence.

$$\Delta(\boldsymbol{r}) = \phi\left(\boldsymbol{r} + \frac{\boldsymbol{s}}{2}\right)(1+\alpha) - \phi\left(\boldsymbol{r} - \frac{\boldsymbol{s}}{2}\right) \tag{4.12}$$

The effect of the birefringence can therefore be described as an increase relative to the case where there is no birefringence Δ', as shown in Eq.(4.13).

$$\Delta = \Delta' + \phi\left(\mathbf{r} + \frac{\boldsymbol{s}}{2}\right)\alpha \tag{4.13}$$

The phase is given by the integral of Δ, shown in Eq.(4.14), where ϕ' is the phase without birefringence.

$$\phi = \frac{1}{s}\int \Delta d\boldsymbol{r} = \phi' + \frac{1}{s}\int \phi\left(\mathbf{r} + \frac{\boldsymbol{s}}{2}\right)\alpha d\boldsymbol{r} \tag{4.14}$$

The effect of the birefringence of the tube, ϕ_b, is therefore given by Eq.(4.15).

$$\phi_\mathrm{b} = \phi - \phi' = \frac{\alpha}{s}\int \phi d\boldsymbol{r} \tag{4.15}$$

Because the effect of the birefringence is very small, (i.e. $\alpha \ll 1$) we can assume that $\phi \approx \phi'$. Therefore, the effect of the birefringence on the integrated phase of the tube can be estimated from the expected tube optical thickness without birefringence, as shown in Eq.(4.16).

$$\phi_{\mathrm{b}} \approx \frac{\alpha}{s} \int \phi' d\boldsymbol{r} \tag{4.16}$$

Due to the fact that the change in the optical thickness ϕ is dependent not on the change in refractive index but the change in the difference between the lipid index and the refractive index of the PBS medium, the value of $(1 + \alpha)$ is given by Eq.(4.17), where n_{av} is the previously discussed average of the ordinary and extraordinary refractive indices that is encountered by one of the two polarisations, and $n'_{\mathrm{x}} = n_{\mathrm{x}} - n_{\mathrm{PBS}}$.

$$\alpha + 1 = \frac{n_{\mathrm{av}} - n_{\mathrm{PBS}}}{n_{\mathrm{o}} - n_{\mathrm{PBS}}} = \frac{3n'_{\mathrm{o}} + n'_{\mathrm{e}}}{4n'_{\mathrm{o}}} \Longrightarrow \alpha = \frac{n'_{\mathrm{e}}}{4n'_{\mathrm{o}}} - \frac{1}{4} \tag{4.17}$$

For $s = 238$ nm, and assuming a 200 nm radius tube with an integrated optical thickness of 7.20 mrad×nm (estimated from $\phi' = 2\pi r\phi_2$, where ϕ_2 is the second bilayer step), the expected phase mismatch over the tube should be 1.02 mrad, which is in good agreement with the measured mean discrepancy of 1.07 ± 0.10 mrad. It therefore seems to be the case that the tube birefringence is affecting the phase reconstruction around the tubes.

Still, the birefringence remains too small to explain the lower radius values obtained from the fluorescence data. Using $n_{\mathrm{e}} - n_{\mathrm{o}} = 0.015$ [29], there is a 14% increase in optical thickness for the extraordinary index. Assuming a circular geometry, its contribution is half of this for light polarised across the tube, and absent for light polarised along the tube. Averaging the two cases leaves a 3.4% increase in optical thickness, far smaller than the 20% discrepancy seen in Fig. 4.13. The exact cause of this 20% difference therefore remains unclear. It is possible that the effect has no single cause, but rather is the result of a combination of factors which may include birefringence among other fluorescence-based effects.

4.5 Effect of the Main Phase Transition on Tubes

Bilayer tubes are also visible in SLB samples formed from $DC_{15}PC$, at temperatures both above and below T_{m}. The process of cooling a $DC_{15}PC$ bilayer below its phase transition temperature provides an interesting system in which to study bilayer tubes, as it allows shape changes in the tubes as a result of the change from L_{d} to S_{o} phase to be measured. Additionally, unlike the experiments on DOPC based bilayers where the tubes appeared static over the course of imaging, during the cooling process over several hours, the formation of tubes, and shape changes of tubes can be directly observed, even above T_{m}.

Tube formation begins at temperatures well above T_{m}. Tubes form from bilamellar regions of the lipid film, as shown in Fig. 4.15. Initially the bilamellar regions simply contract over time, as can be seen between Fig. 4.15a and Fig. 4.15b, however, eventually during the contraction some points along the bilayer edge seem to become 'pinned' to their current position on the surface and remain so even as the rest of the bilayer edge recedes from that point. It may be then that the formation of tubes is the result of local regions where the substrate-bilayer interaction is so

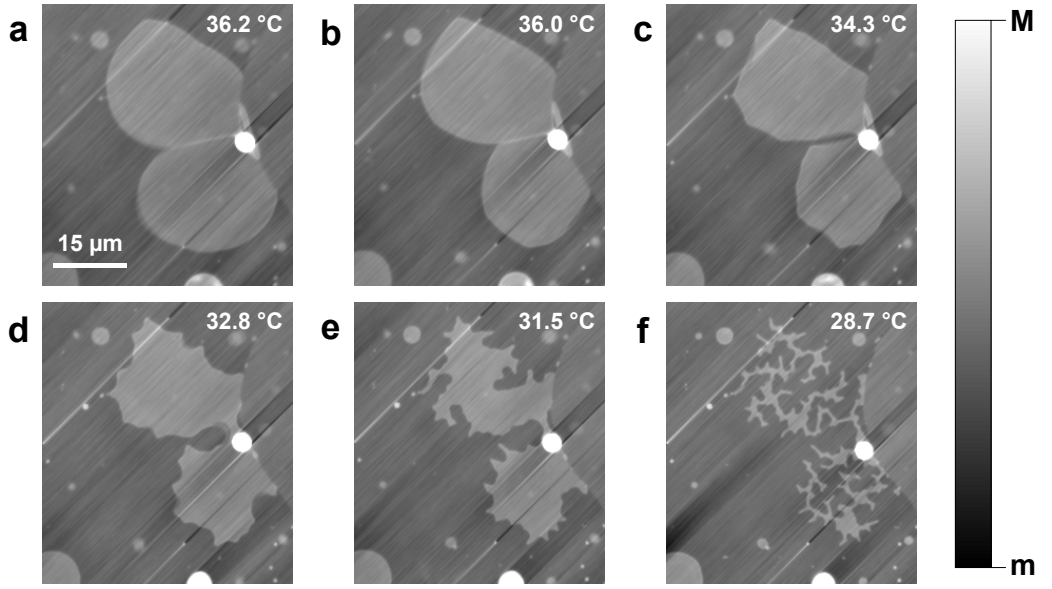

Figure 4.15: qDIC phase images of a double bilayer region of a $DC_{15}PC$/ATTO488-DOPE (99.9/0.1) lipid film undergoing a shape change into a network of lipid tubes during cooling of the sample. A single-bilayer region is present to the right. Temperatures given are the measured temperature at the sample. Images are scaled from m = -3.0 mrad to M = 20.0 mrad.

strong it makes detachment of the bilayer from the surface unfavourable, ultimately leaving the double bilayer as just a network of tubes linking these pinned points.

One interesting aspect of the tube formation process is that tubes seemingly form only from those double bilayer patches that are connected to single bilayer regions; the double bilayer regions that are free standing (i.e. not connected to single bilayer regions) are much more stable over the period of observation. It is important to note that while the lipid is being lost from the double bilayer regions, the single bilayer regions show no corresponding increase in area. In contrast, in single bilayer regions where all the connected double bilayer areas have been converted into tubes, the single bilayer regions begin to contract, with massive loss of lipid from the surface, as can be seen in Fig. 4.16. It may be speculated then, that the double bilayer regions are losing lipid to connected single bilayer regions, to preserve the current boundaries of those single bilayer regions.

In some cases, tubes do begin to form from free double-bilayer regions, as can be seen in the double bilayer patch in the lower right region of Fig. 4.16. This occurs much after all the double bilayer regions connected to the single bilayer areas have been fully converted into tubular networks, and is approximately concomitant with the onset of the main phase transition. This later stage tube formation may therefore be attributed to loss of lipid area due to the higher density of lipid in the S_o phase.

It is important to note however that this areal contraction of the bilayer due to cooling cannot in and of itself account for the extreme loss of bilayer area seen in the data. In DMPC bilayers for instance, the area per lipid in the L_d phase falls by approximately 9% when the temperature is reduced from 60 °C to 30 °C [68]. However, in our samples, much greater area losses can be seen over a much smaller temperature range, even before the onset of the main phase transition. Indeed, in some samples, the loss of area of the first bilayer is so extreme that virtually the

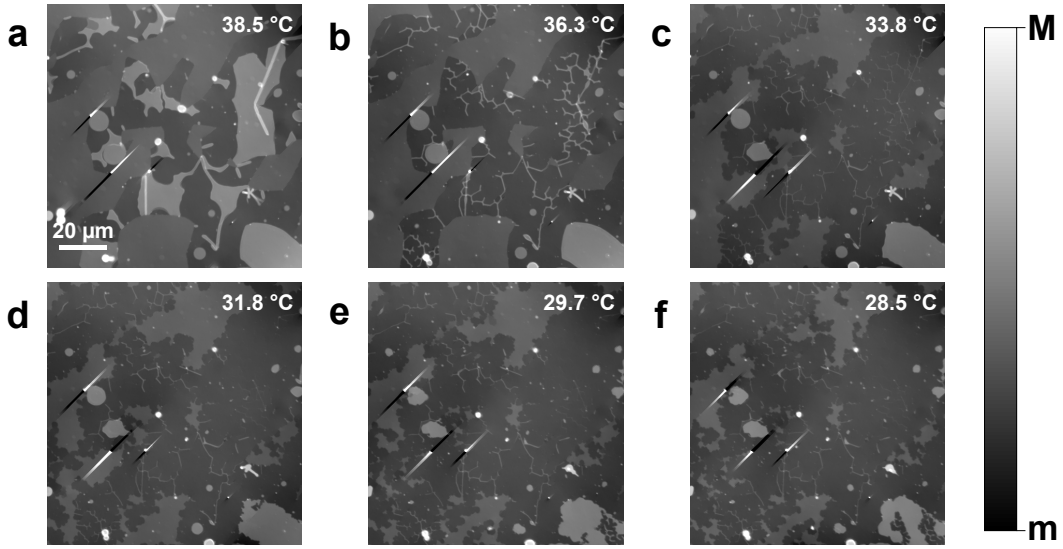

Figure 4.16: qDIC phase images of a mixed lamellarity region of a $DC_{15}PC$/ATTO488-DOPE (99.9/0.1) lipid film during cooling of the sample. After double bilayer regions connected to the single bilayer regions have fully reorganised into tubes, the single bilayer regions and free-standing double bilayer regions begin to lose area. Temperatures given are the measured temperature at the sample. Images are scaled from $m = 19$ mrad to $M = 64$ mrad.

entire field of view shows only exposed glass by the time T_m is reached. It therefore must be the case that membrane material is actually being lost from the surface.

One possible mechanism of lipid loss is through vesicles. There are many vesicles on the surface of the bilayer, which often appear to be connected to the supported bilayer, such as the vesicle in the centre of the bilamellar region in Fig. 4.15. However, while we can clearly see lipid being lost from the bilamellar regions, the size of this vesicle does not seem to change appreciably, showing only a slight reduction in diameter from 3.9 µm at 36.2 °C to 3.6 µm at 28.7 °C. Since the vesicle appears multilamellar, it may be that the lipid from the planar bilayers is becoming part of its multilamellar internal structures rather than contributing to an increase in the outer vesicle diameter. In principle, with qDIC, the total lipid area within the vesicle could be quantified by integrating the phase within the vesicle, thereby allowing an accurate determination as to whether the lipid density within the vesicle was increasing. Unfortunately however, this is not possible for this vesicle, as the complex structures surrounding the vesicle make it impossible to accurately integrate the vesicle area.

However, as a semi-quantitative measure of the amount of material in the vesicle, a qDIC phase cross section through the centre of the vesicle was taken at two different temperature points, one at a high temperature where the double bilayer region is intact, and one at a lower temperature where the double bilayer region has been converted into tubes. This is shown in Fig. 4.17, and it can be seen that the phase profile of the vesicle is approximately the same at both temperatures. Since the shape of the vesicle also remains constant (as can be seen in Fig. 4.15), this indicates that the total lipid volume contained within the vesicle is unchanged.

This suggests that the large adhered vesicles are not the mechanism by which lipid is lost from the supported bilayer. Lipid may then be entering the aqueous medium in the form of micelles or small vesicles detaching from the first bilayer,

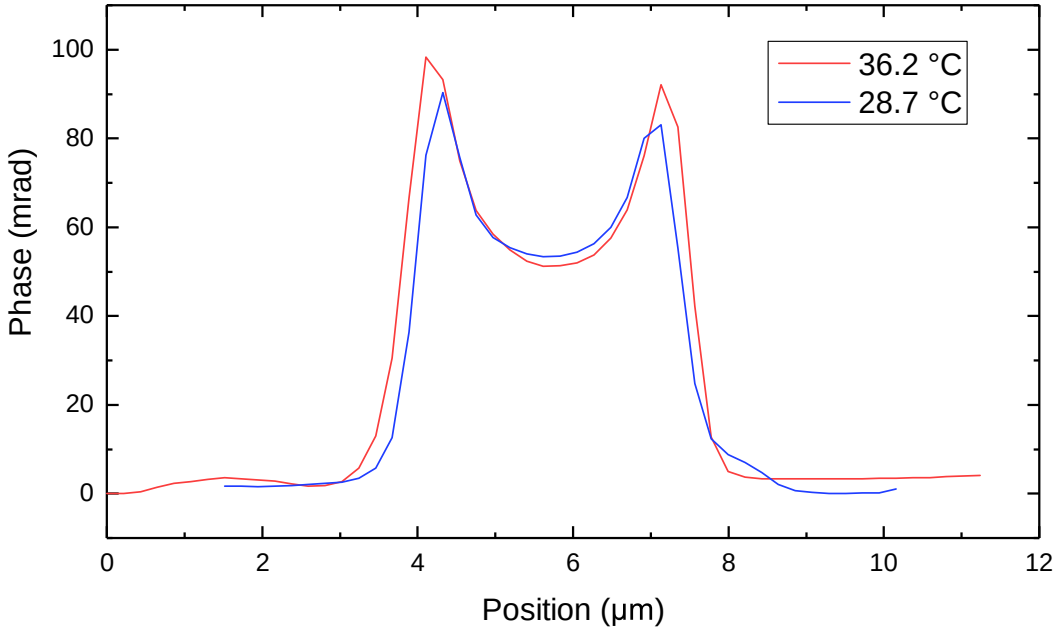

Figure 4.17: The phase profile of the vesicle shown in the centre of the region of interest in Fig. 4.15, averaged over a width of 4 pixels perpendicular to the direction of measurement, and taken at 36.2 °C (red) and 28.7 °C (blue). The vesicle is smaller and has a lower optical thickness at the lower temperature.

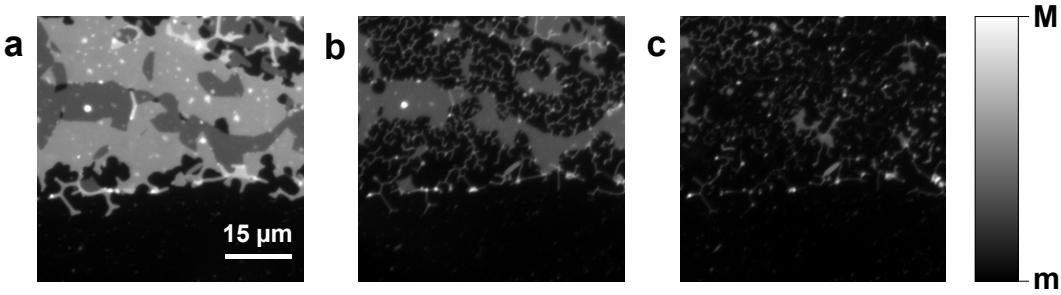

Figure 4.18: A $DC_{15}PC$ bilayer during cooling, shown in fluorescence at a) 37.2 °C, b) 37.0 °C, and c) 36.6 °C. Scaled from $m = 0$ to $M = 3270$.

which are below our lateral resolution. This interpretation is supported by observations from other regions, such as that shown in Fig. 4.18, where after loss of the double bilayer regions, the detachment of the first bilayer from the surface is almost immediate, despite the lack of any large vesicles on the surface.

A possible explanation for these observations is that the adhesion of the first bilayer to the support causes it to resist contraction. As the bilayer cools and the area per lipid reduces, the only way for the first bilayer to maintain its surface coverage is by cannibalising the connected second bilayer regions. Once the second bilayer patches have been completely consumed by the first bilayer, the tension in the first bilayer begins to increase, as the equilibrium area per lipid continues to fall. Eventually, tension exceeds the substrate interaction, causing the bilayer to detach from the surface, leaving only networks of tubes linking regions where the double bilayer was strongly adhered to the glass.

This interpretation would indicate that cooling is essential for tube formation.

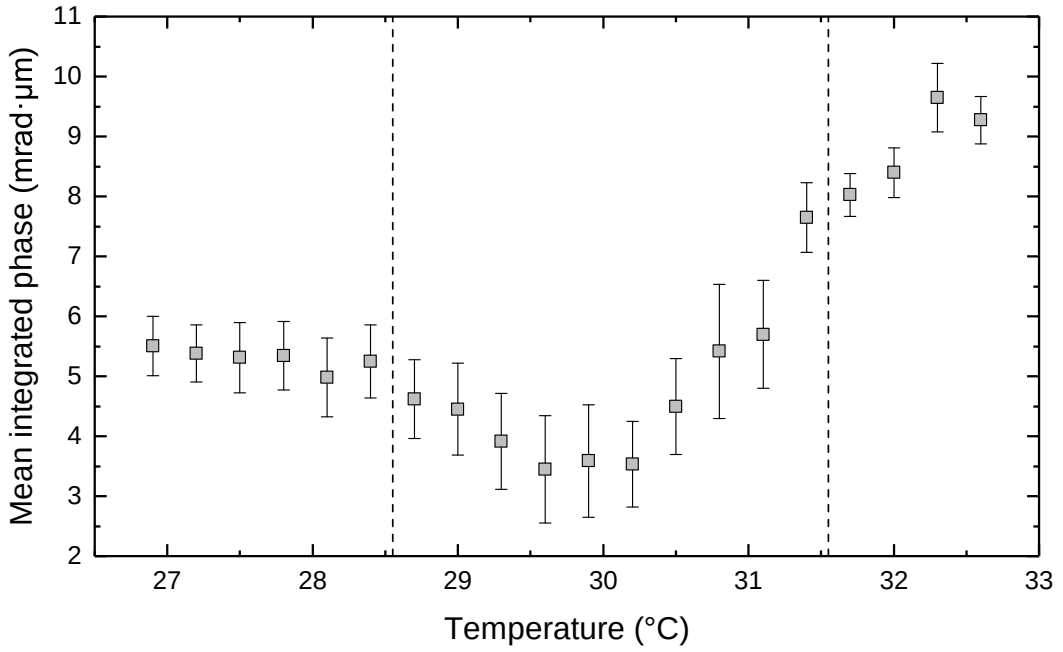

Figure 4.19: The mean of the integrated optical thickness over the twelve tube widths for the $DC_{15}PC$/ATTO488-DOPE (99.9/0.1), plotted against set temperature. The black dashed lines represent the borders of the S_o/L_d phase coexistence region.

Unfortunately however, from the data available, it is difficult to determine this definitively due to the lack of measurements of $DC_{15}PC$ bilayers over similar timescales without cooling. While tubes are relatively rare in the images of DOPC samples compared to $DC_{15}PC$ samples, this may be the result of the generally shorter observational period, rather than the lack of a gradual cooling process. Freshly prepared $DC_{15}PC$ samples appear much the same as fresh DOPC samples, and large tubular networks only are only seen in images taken after several hours of continual observation. Nevertheless, many non-$DC_{15}PC$ samples are cooled following hydration, albeit unobserved, such as those showing liquid-liquid phase coexistence, when they are transferred from the room temperature environment where the samples are prepared, to the fridge at 6 °C for storage. If temperature reduction to below T_m is a driving factor in tube formation, this might provide it for the majority-DOPC samples, such as in Fig. 4.6.

Having qualitatively observed considerable structural changes in the lipid bilayer during cooling, it was decided to attempt to quantitatively measure changes in the radius of the tubes that form during the cooling process. This was done by choosing twelve separate tubes spread evenly over two fields of view, and individually measuring the tube optical thickness as a function of the set temperature of the heating chamber. This is shown in Fig. 4.20a, with examples of the individual tubes being measured shown for different temperatures in Fig. 4.20b. The positions of the line cuts of the example tubes is given in Appendix C.

While the trace of integrated optical thickness against temperature was different for each individual tube, some common features can be observed in Fig. 4.20a. In general, the integrated optical thickness initially reduces as the temperature falls, reaching a minimum around the midpoint of the phase coexistence region, before

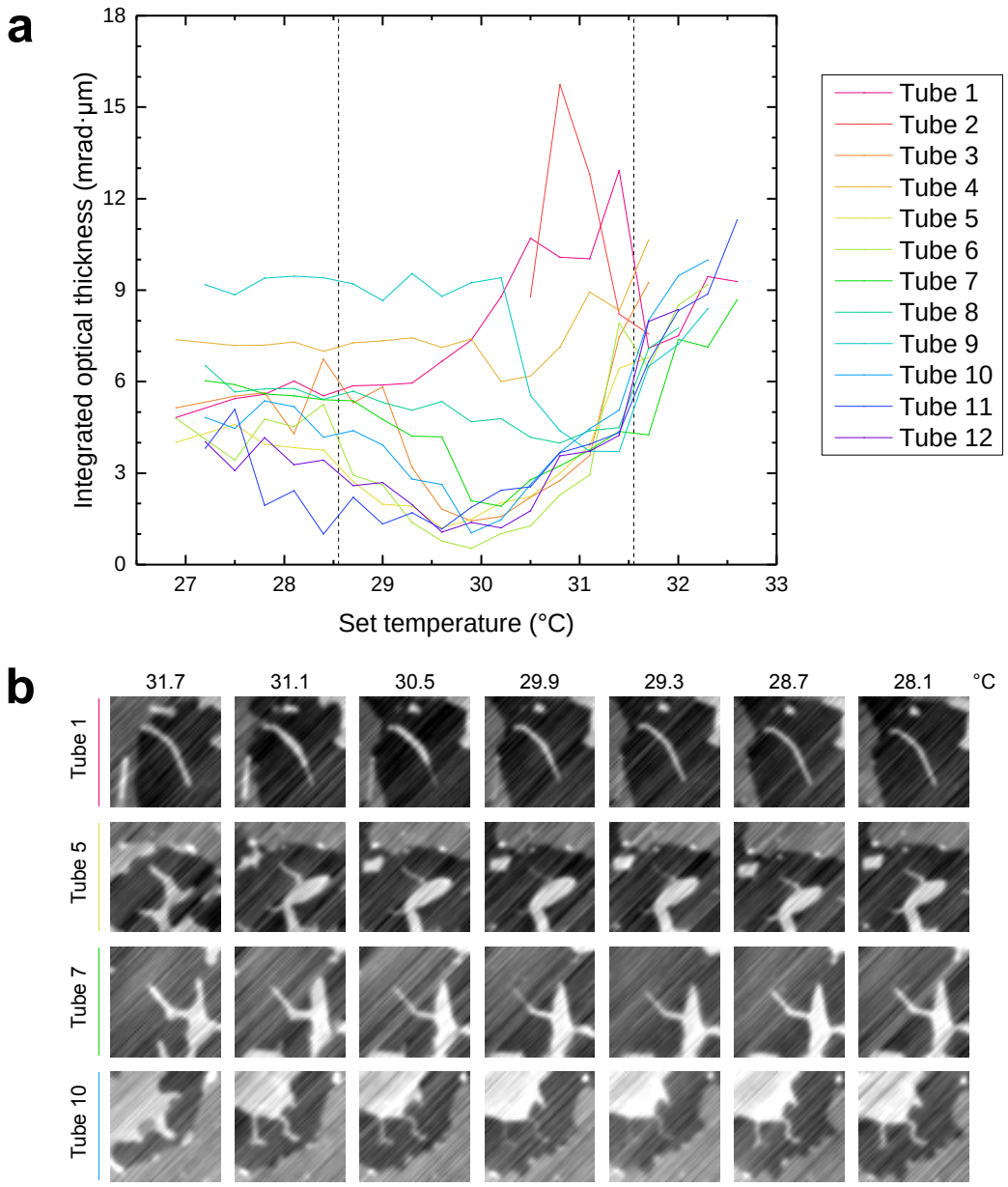

Figure 4.20: Figure showing a) the integrated optical thickness over the tube width for twelve different tubes formed from $DC_{15}PC$/ATTO488-DOPE (99.9/0.1), plotted against set temperature, with black dashed lines representing the borders of the S_o/L_d phase coexistence region, and b) qDIC phase images of four of the twelve tubes at different temperatures during cooling. Images show a 10.8 × 10.8 µm^2 region, with a grey scale from m = -7.7 to M = 9.9 mrad.

beginning to increase again as the sample begins to form a homogeneous S_o phase. This can be clearly seen in the mean of the twelve separate traces shown in Fig. 4.19.

This behaviour can be understood as a result of structural changes in the bilayer as it undergoes the phase transition. When the sample is cooled, and the bilayer begins to freeze, the tubes shrink, due to the greater lipid density in the S_o phase, eventually reaching the minima seen at the mid-point of the phase transition. However, the strong curvature of the tubes at this minimum is highly unfavourable, as the bending rigidity of the bilayer is approximately an order of magnitude higher in the S_o phase than the L_d phase [141]. So, upon completion of the phase transition, the bending rigidity then leads the lipids in the tubes to rearrange themselves to a lower energy configuration, in which the curvature is reduced. Once reached this lowest energy configuration is reached, the tube radius remains approximately constant; this explains the region in which the tube radius appears to approximately level out at temperatures below the phase coexistence range.

Chapter 5

Summary and Conclusions

Model lipid bilayers are a powerful tool for understanding the biophysical properties of the cell membrane, and the supported lipid bilayer system is among the most widespread of these model membranes, used to address a wide variety of different kinds of research questions. Supported lipid bilayers have a set of advantages over other model systems; they are highly stable, and can be created easily on an assortment of different surfaces with a wide variety of different compositions, which can be controlled. This makes them a particularly useful tool for studying the properties of liquid ordered (L_o) domains, regions of increased molecular order used as a model for the raft domains which are believed to exist in the cell membrane. Additionally, the increasing application of supported lipid bilayers for purposes beyond their original function as analogues for the cell membrane, such as their potential use as biosensors for food analysis and environmental monitoring [31], further underscores their continuing importance.

With the diverse array of different questions that can be addressed using supported bilayers comes a large catalogue of different methodologies used to study their biophysical properties. These include a host of surface sensitive techniques such as ellipsometry, various forms of waveguide spectroscopy, X-ray or neutron scattering, and atomic force microscopy, among others. However traditional optical imaging using fluorescence microscopy is still one of the most common approaches for studying SLBs, despite its reliance on the incorporation of fluorescent molecules into the bilayer structure. It is in the context of this multitude of different research tools that we sought to explore how a relatively new type of tool, quantitative phase imaging, could be used to further the study of supported lipid bilayers.

Quantitative differential interference contrast (qDIC) is a quantitative phase microscopy technique which uses Wiener filtering to reconstruct relative phase maps of samples from pairs of images taken using a standard DIC microscope setup. Because it is based on DIC, an existing, widely used microscopy technique, qDIC avoids the technical difficulties associated with taking and analysing data in most forms of quantitative phase imaging. In principle, qDIC enables simple measurements of the optical thickness of supported lipid bilayers, using the phase step at the bilayer edge, from which the absolute thickness of the bilayer can be obtained, given a known refractive index. The thickness is an important property of a lipid bilayer, particularly in the context of lipid rafts, where the thickness difference between the L_o raft phase and the surrounding liquid disordered (L_d) phase controls domain size [128], and the preferential segregation of proteins between domains.

In Chapter 3 we applied qDIC to the simplest SLB system, that of a homogeneous

L_d phase bilayer. For this we used spin coated bilayers prepared from DOPC, a lipid which is widely used in the literature as a basic model for the cell membrane because it forms an L_d phase at room temperature, and so is well characterised. In order to take fluorescence measurements for comparison, the bilayer was labelled with 0.1 mol% ATTO488-DOPE, which is made up of a fluorescent label attached to the head group of a lipid molecule which has hydrocarbon tails identical to those of DOPC. The structure of this fluorophore is similar to those widely used in the literature for fluorescence measurements of bilayers, and is included at a concentration which is generally assumed not to influence bilayer properties.

In Sec. 3.1 we demonstrated that individual lipid bilayers can be clearly resolved using DIC, and, once an appropriate value of the signal-to-noise term, κ, is found, the Wiener filtering produced reconstructed qDIC phase images that have the expected appearance of the original phase profile. Regions of different lamellarity showed distinct differences in the optical thickness, in clear agreement with the different numbers of stacked bilayers that can be seen in the corresponding fluorescence images. Slight differences in the position of the bilayer edges between the fluorescence and qDIC phase images can be attributed to the short delay between the acquisition of each image.

We extracted quantitative information about the SLB from the qDIC phase images by fitting a hyperbolic tangent function to line profiles taken perpendicular to the bilayer edge in order to measure the bilayer phase step. By averaging perpendicular to the direction of the line profile, the noise level was sufficiently low that individual phase steps could be measured with a typical error below 10%. Artefacts running parallel to the shear caused by the Wiener filtering were found to have a negligible influence on the phase steps so long as the line profiles were taken within a few degrees of the original DIC shear direction. We explored how factors such as deviations from the focal plane and routine errors in the polariser calibration might influence the reconstruction, and find that these parameters are sufficiently controlled that they do not produce statistically significant changes to the average bilayer thickness.

By using literature values for the ordinary refractive index of DOPC to convert these measurements of phase steps over bilayer edges to absolute thicknesses, we could determine the thickness of individual lipid bilayers within the multilamellar stack, using positions where the edges of the stacked bilayers were not aligned. By averaging many different steps taken over the edge of a given bilayer, the error in the mean thickness could be reduced significantly. In the case of a stack of DOPC bilayers hydrated in PBS, we found the average thickness of the second bilayer in the stack to be 4.52 $\pm$ 0.03 nm, using 186 individual measurements, n, with the thickness of the third bilayer the same within statistical significance.

This second bilayer thickness value is in good agreement with measurements of the thicknesses of DOPC bilayers in the literature, taken in cases where the bilayer is not in close proximity the support, such as suspensions of SUVs measured using small-angle neutron scattering (4.62 ± 0.15 nm), or the where contribution of the bilayer close to the support is negligible, such as in multilamellar supported bilayer stacks measured using X-ray scattering (4.57 ± 0.05 nm). These data indicate that qDIC is an accurate method of determining the bilayer thickness, assuming an appropriately chosen value for the refractive index.

Interestingly, it was found that the thickness of the first bilayer was only 4.08 $\pm$ 0.03 (n = 178), significantly smaller than that of the second and third bilayers.

Our investigation of this apparent thickness reduction revealed that the difference between the first and second bilayer thicknesses was dependent on a number of factors. One such factor was the degree of bilayer coverage of the surface. Although this effect was different between different lipid stocks, in the first stock there was a clear relationship between coverage and thickness difference. Below 90% relative surface coverage, the thickness difference remained approximately constant as the thickness was changed, however when the coverage was increased above 90%, the thickness difference began to reduce, effectively disappearing close to 100% surface coverage.

The second bilayer thickness always remained approximately the same regardless of the degree of local coverage, indicating that the variation in the thickness difference with the local surface coverage was purely caused by changes in the first bilayer thickness. While the newer second stock seemed to show a constant thickness difference that was unaffected by the surface coverage, in order to definitively exclude this effect from explorations of other possible influences on the first bilayer thickness, all measurements taken in regions above 90% coverage were removed from future calculations of the average thicknesses, regardless of the lipid stock used.

The most relevant factor influencing the thickness of the first bilayer was the hydrophilicity of the surface. On the most hydrophilic surfaces tested, which had a very low contact angle, θ, of $(3.4 \pm 0.1)^\circ$, the first bilayer thickness was $(90 \pm 1)\%$ that of the second bilayer. However, on less hydrophilic surfaces, where $\theta = (11.3 \pm 1.0)^\circ$, the relative thickness was increased to $(93 \pm 2)\%$ of the second bilayer, and on non-hydrophilic surfaces, where $\theta = (47.1 \pm 3.5)^\circ$, the thickness difference between the first and second bilayers was zero within error, as the mean thickness of the first bilayer was $(100 \pm 1)\%$ of the second. Other potential influences, such as contamination from the sulphur used in the piranha etching applied to the glass to render it hydrophilic, and the method used to form the supported bilayer, were excluded, thus establishing that the hydrophilicity is the mechanism by which the thickness of the first bilayer was being changed.

Since qDIC measures the bilayer phase step, we cannot definitively exclude the possibility that some or all of this apparent change in bilayer phase steps is actually caused by changes to the first bilayer refractive index rather than thickness. However, changes in bilayer thickness due to interactions with a solid substrate have been shown in computational studies of SLBs [107, 110], and these studies predict a thickness reduction on a similar scale to that we measure [110], which supports our interpretation that the changes to the bilayer optical thickness are caused by changes in absolute thickness as opposed to the refractive index.

These computational studies suggest that the thickness reduction in the first bilayer originates from a movement of lipids from the upper leaflet to the lower leaflet, in order to increase the proportion of hydrophilic lipid heads in close proximity to the substrate [107]. Such a net movement of lipids would cause the upper leaflet to become stretched due to lipid depletion, thus lowering the overall bilayer thickness. In addition to explaining the thickness reduction caused by hydrophilicity, this mechanism can also explain our observation that the reduction is coverage dependent. Since bilayer edges are sites where the two leaflets are connected, they provide a path for lipids to move from the upper to lower leaflet, and thus would be needed to establish the thickness difference. The only alternative, direct movement of lipids through the bilayer interior ('flip-flop'), is an extremely slow process due to the penalties associated with moving hydrophilic heads through the hydrophobic

core of the bilayer.

While these theoretical studies predicting that the support would reduce bilayer thickness have been present in the literature for over ten years, this is to our knowledge the first time such an effect has been experimentally demonstrated. Rendering the surface hydrophilic is an important step in SLB preparation in order to promote association of the hydrophilic lipid headgroups with the support. This is true not only in spin coating [56, 111], but also in Langmuir-Blodgett [22] and SUV rupture techniques [32, 112], which are the most widely used methods for producing SLBs. Thus, our finding that the degree of hydrophilicity can cause reductions in the thickness of the SLB (albeit in a coverage dependent manner) has important implications for any experiments on SLBs where the bilayer thickness is a parameter of interest. Future experiments might try to more precisely map the relationship between thickness and hydrophilicity, and could investigate the hydrophilicity effect on other commonly used SLB substrate materials such as mica, or on bilayers with different compositions, such as those formed from charged lipids.

An additional factor that we found affected the thickness difference is the choice of fluorophore. Since qDIC is a label-free technique, we could compare the behaviour of SLBs prepared with fluorophores and without. Compared to those bilayers labelled with ATTO488-DOPE (where the thickness difference was 0.44 ± 0.04 nm), it was found that the thickness difference between first and second bilayers in the unlabelled samples was significantly lower, at 0.32 ± 0.04 nm, indicating that the inclusion of the ATTO488-DOPE fluorophore somehow enhances the effect of the substrate hydrophilicity on the bilayer thickness. In contrast, it was found that using the tail-labelled fluorophore TopFluorPC at the same concentration as ATTO488-DOPE actually reduced the thickness difference compared to the unlabelled case, to just 0.24 ± 0.03 nm, at a confidence level of 1.5σ.

This is an important result for a number of reasons. Aside from being a further influence on the thickness reduction, the fact that the incorporation of such a low concentration of fluorophore can have a significant influence on bilayer thickness is important considering the widespread use of fluorophores for experiments not only on supported bilayers, but other on model systems as well. In contrast to the usual assumption that fluorophore concentrations below a few mol% have a negligible effect on bilayer properties, our data suggest that the concentrations typically used in experiments on membrane model systems can significantly influence the bilayer behaviour, in this case by somehow modulating the influence of the support on the first bilayer thickness.

Exactly how the fluorophore is influencing the bilayer is unclear. While it is known that fluorophores can alter the properties of the bilayer by promoting the oxidation of surrounding lipid molecules, such effects cannot be the cause of the observed effect, for two reasons. Firstly, fluorophore-induced oxidation would effect both the first and second bilayer equally, assuming an equal proportion of fluorophore between bilayers. Secondly, this would not explain why the two different fluorophores had opposite effects on the thickness difference. It is unlikely that the fluorophore interactions with the support are the cause of the effect either, as while the headgroup of ATTO488-DOPE would have significantly different interactions with the support than the surrounding DOPC molecules, the same is not true for TopFluorPC, since TopFluorPC has a phosphocholine headgroup identical to that of DOPC, and so should exhibit the same response to the substrate.

The explanation we propose in Sec. 3.4 is that the fluorophores are altering the

area elastic modulus of the upper leaflet, changing the amount of stretching that it can endure due to the trans-leaflet lipid movement, and that this is the means by which the fluorophores modulate the substrate-bilayer interaction. This hypothesis is admittedly somewhat speculative, but a role for the area elasticity in modulating the thickness difference is an intuitive consequence of the upper leaflet stretching being the cause of the first bilayer thickness reduction. Separate experiments designed to explicitly measure changes in the area elastic modulus of the lipid bilayer caused by the incorporation of fluorophore could be carried out in the future to properly test this hypothesis.

These findings are all based on the direct comparison of the first bilayer thickness with the thicknesses of other bilayers within the same sample, and thus demonstrate the advantages of qDIC over other available techniques for measuring bilayer thickness. For example, X-ray and neutron scattering techniques rely on averages over many hundreds of lipid bilayers, and so would not be able to detect any difference between the first bilayer and those bilayers formed on top. The contribution of the first bilayer to the average thickness would be negligible, and so any thickness changes in the first bilayer caused by varying the substrate properties would be invisible using this technique. Additionally, the necessity for complete stacks of many bilayers would make it incapable of exploring the effect of coverage on the thickness of a single bilayer as we do with qDIC.

Atomic force microscopy is probably the most widely used technique for measuring the thickness of single bilayers, and so can compare bilayers within a multilamellar stack as we do with qDIC. However, the fact that AFM always measures both the bilayer and hydration layer thickness together means that any meaningful difference in the thickness between bilayers may be obscured by the uncertainty in the thickness of the hydration layer. In contrast, in qDIC, the hydration layer does not affect the steps at all, as there is no phase gradient caused between a thin water layer under the bilayer, and an equally thick water layer outside the bilayer. An additional concern regarding thickness measurements taken with AFM is that the degree to which the AFM tips indent into the bilayer is also uncertain, and so complicates the interpretation of the bilayer thickness measurements yet further [70]. To our knowledge, no experiments reporting a thickness difference between the first and other bilayers in a multilamellar film have been reported with AFM.

In terms of speed of acquisition, our qDIC measurements are faster than AFM. In measurements of SLBs, AFM can measure approximately 33,000 points per second [142], while with our camera, qDIC has double this speed. Even faster qDIC measurements may be possible, but would result in reduced signal-to-noise unless a camera with a higher full well capacity was used. In terms of the size of the fields of view that can be measured, ease of use, and compatibility with other optical microscopy techniques such as fluorescence, qDIC has clear benefits over AFM for imaging SLBs. However, since the resolution of qDIC is diffraction limited, AFM has a higher lateral resolution than qDIC. Additionally, AFM also allows force spectroscopy measurements which provide information on the bilayer mechanical properties, which are unobtainable from SLBs using optical methods[1]. Whether qDIC or AFM is more appropriate for a given application will thus depend on the specific question to be addressed.

One technique which could measure the same thickness difference that we observe

[1]Such measurements can however be taken optically on other model systems such as GUVs by looking at positional fluctuations of the bilayer. This may be a future application of qDIC.

is ellipsometry. Like AFM and qDIC, ellipsometry is also capable of measuring the thicknesses of single lipid bilayers with sub-nanometre precision. Indeed, a thickness difference between the first and second bilayers in a multilamellar spin coated film has been reported from ellipsometry data [111]. Unlike qDIC where the phase information can be interpreted directly, data from ellipsometry experiments must be interpreted using a theoretical model of the optical properties of the sample and the substrate [143]. Image acquisition in ellipsometry requires approximately 20 seconds for a field of view several hundred microns in width and height [143]. This is comparable to the acquisition speed of our qDIC system, which requires around 100 acquisitions at each polarisation, though ellipsometry can be significantly faster when taking measurements only from a single point.

Many ellipsometry measurements on SLBs use only a single wavelength for illumination, and so are constrained by the same limitation as qDIC, that the refractive index must be already known in order to obtain the bilayer thickness (or vice versa) [143]. In contrast, in spectroscopic ellipsometry, the refractive index and thickness of the bilayer can both be determined from the data by using multiple different laser wavelengths [101], which is a considerable advantage over the single-wavelength qDIC technique described here, where our investigations into changes to the bilayer thickness caused by the properties of the substrate rely on an assumption of a constant refractive index. However, the use of multiple wavelengths to extract the refractive index could in future also be applied to qDIC, by using different filters to take DIC images at different illumination wavelengths, and then applying a refractive index dispersion model to the data to extract the refractive index.

Much like AFM, in ellipsometry there is a contribution to the measurements from the hydration layer, which must be disentangled from the bilayer data in order to obtain accurate measurements of the bilayer thickness. This can be done by including the hydration layer in the theoretical model used to fit the data; however, in simple models of the bilayer thickness, the contribution to the thickness from the hydration layer is ignored [143], which would reduce the accuracy of the thickness measurement. This then leads to the same problem inherent to the AFM thickness measurements, where differences in the first bilayer thickness can be dismissed due to uncertainties in properties of the hydration layer. This was in fact the case for the reported thickness difference; an increase in the apparent thickness of the first bilayer relative to other bilayers detected using ellipsometry was considered to be the result of a sharp increase in the hydration layer refractive index (to match the refractive index of the bilayer) and ignored [111].

Other quantitative phase techniques could also be used to measure the thickness difference between bilayers. Interferometric reflectometry for instance could detect the thickness difference, and, because it measures two variables (the amplitude and phase of the field reflected from the sample), it could theoretically measure both the thickness and the refractive index of the bilayer using only a single wavelength of illumination. The measured phase would contain a contribution from the hydration layer which can be accounted for either by using a suitable model, or by combining the interferometric reflectometry phase measurements with the qDIC phase measurements, which contain a contribution from the bilayer only. The latter approach would, in principle, allow the thickness of the hydration layer to be measured along with the refractive index and thickness of the bilayer, assuming a known refractive index of the hydration layer. Development of this technique is ongoing.

Another influence on bilayer thickness that we found was the ionic strength of

the medium. We found that the thickness of bilayers formed in distilled water was approximately 20% larger than those formed in PBS solution, which has a nominal osmolality of around 300 mOsm/kg. Changes in the bilayer thickness due to ionic strength of the medium can be detected using other techniques, and have been widely reported in the literature. However, most of these reports suggest that the bilayer should be thicker in media with higher ionic strength, in contrast to our observation. The reasons for this discrepancy between our measurements and the majority of the literature reports remain unclear.

Having applied qDIC to simple, fluid phase SLBs in Chapter 3, in Chapter 4 we moved on to bilayer systems with more complex behaviour. One such system was the mixture of DOPC, sphingomyelin, and cholesterol, which phase separates at room temperature into coexisting L_d and L_o phase domains. The L_o domains formed by mixtures such as this are a popular model for cell membrane rafts, and so an interesting candidate for study using qDIC. In the qDIC phase images, the L_o domains were clearly visible as round regions of increased optical thickness within the bilayer. This interpretation was verified using corresponding fluorescence images, where the L_o domains were visible as dark patches within the lighter L_d phase bilayer, due to their exclusion of the ATTO488-DOPE fluorophore.

Just as for the single component bilayers, extracting the absolute thickness of the L_o domains using qDIC, requires a value for the refractive index of the L_o phase. This is more complicated to estimate than for the pure DOPC bilayers, because a wide variety of different L_o domain compositions are used in the literature, which each have different thicknesses and refractive indices. Ultimately, the refractive index of a porcine brain sphingomyelin bilayer was chosen as a model for the L_o phase refractive index in our system, which is compositionally similar to the chicken egg sphingomyelin mixture we used in our sample preparation, though with generally slightly longer hydrocarbon chains. An additional complication was the lack of edges over which to directly measure the thickness of the L_o phase. To overcome this, the directly measured L_d phase thickness was used with the refractive indices to calculate the thickness of the L_o phase from the difference in optical thickness between the two domains.

For bilayers containing 0.1 mol% of the ATTO488-DOPE fluorophore, the thickness of the L_o domains was found to be 5.19 ± 0.06 nm ($n = 48$), when formed on a fully hydrophilic surface ($\theta = (3.4 \pm 0.1)°$) and hydrated in PBS. As in the case of the pure L_d-phase DOPC SLBs, it was found that the thickness of the L_o domains was affected by the hydrophilicity of the glass surface, with domains in the first bilayer formed on lower hydrophilicity surfaces ($\theta = (11.3 \pm 1.0)°$) showing an increased thickness of 5.56 ± 0.06 nm ($n = 91$). The magnitude of this result is somewhat surprising, as although sphingomyelin has the same headgroup as DOPC, and so should experience the same attraction to the substrate, the increased rigidity of the L_o phase might have been expected to limit the stretching of the upper leaflet and thus reduce or eliminate the hydrophilicity-induced thickness reduction. In contrast, the 7.9° increase in the contact angle causes a roughly 7% increase in the L_o phase thickness, almost double the approximately 3% increase measured in pure L_d phase bilayers. The cause of this is unclear.

Additionally, our qDIC measurements of the L_o domains found that the thickness difference between L_o and L_d domains changed depending on whether or not a fluorescent label was incorporated into the sample. In the labelled samples, the L_o phase was 1.29 ± 0.08 nm thicker than the surrounding L_d phase, while in

the samples without fluorescent labels, the L_o phase was 1.06 ± 0.06 nm thicker, a separation of 2.3σ. The difference in these values can be attributed to the ATTO488-DOPE fluorophore enhancing the hydrophilicity induced thickness reduction in the L_d phase, as previously found in the pure L_d phase DOPC samples. The thickness of the L_o phase, which excludes the fluorophore, would be the same in both samples. This conclusion is supported by the observation that there is no change in the thickness difference between phases in the second bilayer regardless of whether the fluorophore is present or not.

As previously mentioned, the exact value of the thickness of L_o domains is highly dependent on the exact composition used, which makes comparison of our measurements with literature values difficult. However, the thickness difference we find between L_d and L_o phases in unlabelled samples is in good agreement with AFM experiments on lipid monolayers, which find that the thickness difference is approximately 0.5 nm for monolayers formed from DOPC, brain sphingomyelin and cholesterol [144], a system which is close to ours in terms of composition. Our value for unlabelled bilayers is double this monolayer value, as expected, suggesting that our measurements of the thickness difference between coexisting liquid phases qDIC are accurate.

Compared to fluorescence, qDIC provides significant advantages for studying L_o domains. The first and most obvious point is that concerns relating to fluorophores altering the phase behaviour (either due to their own effect, or because of fluorophore mediated photodamage to the bilayer) are eliminated. However, there also are inherent advantages to using phase-based measurements of domains, since in the phase images, ordered domains have a distinct signal, unlike in fluorescence where they can only be inferred by the absence of signal. Combining phase and fluorescence measurements therefore allows regions that would otherwise have the same fluorescence intensity, such as L_o domains and holes, or single bilayer regions and stacks of L_o and L_d domains, to be distinguished without the need for additional labels for the L_o phase.

For thickness measurements of L_o domains, qDIC has advantages over other techniques such as AFM. In AFM, only the topography of the upper surface of the bilayer is measured. Any protrusion of the L_o phase below the lower surface of the bilayer is not detectable, and so AFM studies on lipid bilayers may only be measuring half the thickness change [111]. In contrast, qDIC is sensitive to the optical thickness of the whole bilayer and so detects the full change over the domain boundary. However, qDIC is limited by the fact that the refractive index is much harder to know with certainty in the L_o domains, because of the wide variety of different compositions used in the literature, and the uncertain distribution of lipid components between the two phases. This concern is also true of ellipsometry measurements where the refractive index is not measured. Each of these spatially resolved techniques for measuring L_o domain thickness therefore suffers from accuracy limitations.

Having imaged L_o domains, we next applied the qDIC technique to the main L_d-S_o phase transition, which is generally studied using AFM for laterally resolved measurements. For this we used an SLB formed from $DC_{15}PC$, which has a nominal main phase transition temperature, T_m, of 33.7 °C [36]. This is a much more challenging system to study than the L_o domains, because while the L_o domains are static over the period of experimental observation, the phase boundary in a sample transitioning from the L_d to S_o phases is constantly moving, and so tests the ability

of qDIC to image dynamic bilayer events.

Because DIC is a label-free technique, we were able to use it to study the influence of the fluorophore on the phase transition. We found that the incorporation of ATTO488-DOPE fluorophore into the bilayer artificially extends the L_d-S_o phase transition, with the temperature range of L_d-S_o phase coexistence increasing from 0.6 °C when no fluorophore was included in the bilayer, to 2.7 °C for a fluorophore concentration of 1.00 mol%. This effect we determine to be the result of the accumulation of the low T_m lipids carrying the fluorophores in the L_d domains, rather than some action of the fluorescent labels themselves, as unlabelled DOPE incorporated into the bilayer at the same concentration as the fluorophore causes the same extension of the phase transition.

Unlike the L_o domains which are clearly visible in the qDIC phase reconstructions, the L_d-S_o phase boundary appears very weak, barely resolvable above the noise level, making it difficult to see the structure of the expanding S_o domains during cooling of the sample. Measurements of the thickness difference over the phase boundary were taken, but this required the use of the corresponding fluorescence images as a reference to assist in the identification of domain boundaries in the qDIC phase image. Nevertheless, we obtained values for the step between L_d and S_o phases which were in reasonable agreement with values in the literature, assuming a constant refractive index over the phase transition. We were also able to directly measure step heights for both phases by taking measurements over bilayer edges; the difference between the two phase thicknesses agreed well with the height of the boundary that we measured.

At present, as a method of studying the dynamic behaviour of the individual S_o domains as they form during cooling, qDIC as demonstrated here is currently somewhat limited compared to methods like AFM, where the structural changes in the S_o domains during cooling can be followed (albeit often in a smaller field of view) with high precision and good temporal resolution. Because the static L_o domains (which have a thickness difference relative to the L_d phase comparable to that of the S_o domains), can be clearly seen with qDIC, the difficulties encountered in imaging the dynamic L_d and S_o phases during the phase transition are not necessarily due to the limitations of the qDIC technique itself, but rather the speed of the camera being used.

Any reduction in the approximately 20 s time required to take qDIC measurements should reduce blurring of the L_d-S_o phase boundary during the transition, and thus making it more visible in the qDIC phase image. Considerably faster cameras, with higher full well capacity than the Hamamatsu Orca 285 used here, are available, and could be used to achieve such a reduction in acquisition time without increasing the image noise. For example, a more recently purchased Adimec Q-2HFW CMOS camera has the same number of photoelectrons in a single frame as 100 frames of the Hamamatsu camera, and is capable of 550 frames per second at full resolution. While the acquisition speed would still be limited by the speed of the servo used to change the polariser angle between positive and negative angles, this should nevertheless be sufficient to produce clear images of the L_d-S_o phase boundary.

In addition to measuring planar bilayer structures, we also applied qDIC to study tubular membrane structures that formed on the surface in some samples. Utilising our measurements of the optical thickness of planar bilayers to measure the radius of membrane tubes, we found that the tubes in fluid phase bilayers had a typical

radius in the range from 100 to 300 nm, consistent with theoretical predictions and similar to the thicknesses of membrane tubes studied in the literature. We were able to monitor changes in the tube radius during the main phase transition, finding that tube radius actually decreased when cooled to the S_o phase, in contrast to what would be expected based on bending rigidity alone.

While our average qDIC thickness measurements have a high degree of precision, the high level of noise limits the accuracy of individual measurements, which in turn limits our ability to investigate certain properties of the bilayer. For example while we can obtain reasonably accurate measurements of the average thickness of L_o domains, the high error on the thickness measurements of individual L_o domains made it impossible for us to establish whether there was a relationship between the size and the thickness difference of individual domains, which might be expected based on literature measurements that find size and thickness mismatch between phases are correlated.

Image noise seems to also be an issue when attempting to measure the birefringence in bilayer tubes, as our measurements of the birefringence induced phase mismatch across the tubes find no discernible correlation between the radius of the tube and the extent of the mismatch. This should not be the case since thicker tubes should have a greater effect on the phase reconstruction, and so lead to a greater phase mismatch. This therefore is likely to be another example of image noise obscuring subtle effects in individual measurements.

Considering then the importance of the image noise in the application of qDIC to supported bilayers, the origin of this noise, and possible means to suppress it were investigated. Increasing the number of averages by a factor of ten results in marginal improvement in the background noise level, and reduces the error in the average bilayer thickness measurements. However the tenfold increase in image acquisition time makes such an approach clearly impractical for imaging fast events like the L_d-S_o phase transition, and increases the risk of sample changes between positive and negative polariser images. Investigations into the precise nature of the image noise revealed that the major contribution to the noise in the bilayer phase step measurements in qDIC was not the camera noise, but rather the roughness of the underlying glass substrate.

In theory, the roughness of the glass could be removed from a qDIC image by taking a second qDIC image of the same region after removal of the bilayer, so that the second image showed just the underlying glass roughness. Taking the difference between these two images would thus produce a clear image of the bilayer with no contribution from the surface. However, this proved impractical in simulated tests, which showed that the requirements for achieving real reductions in background noise using this technique would be unachievable under normal experimental conditions, possibly due to limitations in the image registration. Alternatives to reduce the contribution from glass noise might include using a smoother substrate for the SLB, such as mica, or by using a substrate with a refractive index closer to the water (which would lower the phase gradient caused by glass roughness).

In summary then, qDIC has been shown to be capable of accurately measuring the average thickness of supported lipid bilayers with sub-nanometre resolution, and compares favourably with other tools for measuring bilayer thicknesses. Using qDIC, we have provided the first experimental evidence showing that the hydrophilicity of the substrate can induce major changes in the thickness of supported lipid bilayers, and that this effect is modulated by the choice of fluorophore, and the extent of lipid

coverage at the surface. The reconstructed qDIC phase maps of supported bilayer samples show the lateral structure of the sample in large fields of view, with an acquisition speed which is comparable to, or faster than, other techniques.

The detection of different membrane phases without the need for fluorescent labels has allowed us to explore how the inclusion of fluorophore affects the bilayer phase behaviour, however noise limitations caused by the acquisition speed and the roughness present limits to the information that was obtained. Paths to improving the speed and suppression the noise from the data shown in this work have been given, and should provide two orders of magnitude speed (the aforementioned CMOS camera with over 500 fps and 2Me full well capacity) and one order of magnitude noise improvements (different substrate closer to water index, or flatter substrate).

Appendix A

Lipid Species and Nomenclature

As previously mentioned, the amphiphilic lipids that are the major constituents of cell membranes are formed from two hydrophobic hydrocarbon tails attached to a hydrophilic headgroup. The wide variety of different headgroups and possible hydrocarbon tails therefore allows for a huge variety of possible combinations, each with distinct properties. It is therefore necessary to be able to distinguish between these different species.

To this end, several different systems of nomenclature for phospholipids are used in the literature. Generally, the hydrocarbon chains are listed first, followed by the headgroup. This stems from the fact that phospholipids are built around a phosphate backbone, with the hydrocarbon tails attached at the first and second carbon atoms, while the headgroup is attached to the third.

The hydrocarbon tails are described by their length and degree of saturation. For example, myristic acid, which has a hydrocarbon chain that is fully saturated and 14 carbons long, might be written as 14:0, where the first number represents the hydrocarbon chain length, while the second gives the number of unsaturated bonds along the chain. In this system, a lipid that has two such chains attached to a phosphocholine (PC) headgroup would be described as 14:0 PC. This system is simple and easy to interpret, but becomes increasingly unwieldy as more complex lipids are described.

When there are unsaturated bonds in the hydrocarbon chain, it is necessary to describe not just the number of these bonds, but also their position and the cis-trans configuration of the bond. For a phosphocholine lipid with two oleic acid chains, which are 18 carbons long, each with a single unsaturated bond in the middle of the chain, the name under this system would be 18:1 (Δ9-cis) PC. If a phosphocholine lipid had different chains, for example one 14:0 chain and one 18:1 (Δ9-cis) chain, its name under this system would be 14:0-18:1 (Δ9-cis) PC. While this system efficiently conveys the relevant structural information, its length and the lack of any simple means of abbreviating it renders it impractical.

The most widely used system is the stereospecific numbering system recommended by the International Union of Pure and Applied Chemistry (IUPAC) [145]. In this system, lipid names are composed of three parts; the names of the fatty acids which form the tails, the glycerol linker molecule, and the name of the headgroup. The trivial name of the 14:0 fatty acid is myristic acid, so in this system the 14:0 PC discussed in the previous paragraphs would be 1,2-dimyristoyl-*sn*-glycero-3-phosphocholine. The *sn* stands for 'stereospecifically numbered', and indicates that the numbers describe the specific positions of the groups added along the length of

Fatty acid tail	Proportion
16:0	86%
18:0	6%
22:0	3%
24:1	3%
Unknown	2%

Table A.1: Table fatty acid distribution of chicken egg sphingomyelin according to the manufacturer.

the glycerol backbone. This lipid name would be abbreviated DMPC, and this abbreviation is the name by which the lipid is most commonly known in the literature.

In cases where there are different hydrocarbon chains, this is reflected in the name. A lipid with one myristic acid chain and one oleic acid chain would then be either MOPC or OMPC depending on the relative positions of the chains. The system is complicated somewhat by the fact that there are multiple fatty acids beginning with the same letter; pentadecanoic acid (15:0) and palmitic acid (16:0) might both be abbreviated as 'DPPC' for example, though in practise that abbreviation is almost exclusively reserved for the latter.

Adding further confusion, some fatty acids have both a trivial and a systematic name, while for others there is only a systematic name. For instance, palmitic acid is sometimes referred to by its systematic name, hexadecanoic acid, and so, rarely, 16:0 PC might be written in the literature as DHPC. In this work, the most common abbreviations will be used. In the case of the pentadecanoic acid example, a phosphocholine lipid with such chains will be referred to as $DC_{15}PC$, where the C_{15} refers to the length of the hydrocarbon chains. A description of the various lipids mentioned in this work is provided in Table A.2.

Unlike phospholipids which are built around a glycerol backbone, sphingomyelins are built around a sphingosine backbone. One additional fatty acid is added to sphingosine (shown in Fig. 1.2a) at the amine group, and like phospholipids, this can be one of a wide array of different fatty acids. Sphingomyelin has a phosphocholine headgroup attached at the end hydroxy group, though other sphingolipids can have different headgroups. As such, specific sphingomyelins are identified by the additional fatty acid. For example, when the fatty acid attached to the sphingosine backbone is palmitic acid, the molecule would be referred to as palmitoyl sphingomyelin.

Natural lipid extracts contain mixtures of many different types of lipid, and this mixture varies according to the species and tissue from which the lipids were derived. While mixtures have less well defined properties than pure lipids, they are more representative of the biological membranes, as well as less costly. We use a sphingomyelin mixture extracted from chicken eggs, which has a fatty acid tail distribution (according to the manufacturer's specifications) shown in Table A.1.

Abbreviation	Shorthand notation	Full name	T_m (°C)	Refractive index
DLPC	12:0 PC	1,2-dilauroyl-*sn*-glycero-3-phosphocholine	3.5 [36]	
DMPC	14:0 PC	1,2-dimyristoyl-*sn*-glycero-3-phosphocholine	23.6 [36]	1.443 (at 26 °C) [65]
$DC_{15}PC$	15:0 PC	1,2-dipentadecanoyl-*sn*-glycero-3-phosphocholine	33.7 [36]	
DPPC	16:0 PC	1,2-dipalmitoyl-*sn*-glycero-3-phosphocholine	41 [101], 41.3 [36]	1.438 [120]
DOPC	18:1 (Δ9-cis) PC	1,2-dioleoyl-*sn*-glycero-3-phosphocholine	-17 [101], -18.3 [36]	1.445 [29]
POPC	16:0-18:1 (Δ9-cis) PC	1-palmitoyl-2-oleoyl-*sn*-glycero-3-phosphocholine	-2.5 [36]	
DOPE	18:1 (Δ9-cis) PE	1,2-dioleoyl-*sn*-glycero-3-phosphoethanolamine	-7.34 [146]	

Table A.2: Descriptions of the various phospholipid species mentioned in this work, including the fatty acid tails, the main S_o to L_d phase transition temperatures (T_m) and reported values of the refractive indices.

Appendix B

Development of Spin Coating Protocols

Compared to other SLB preparation techniques, spin coating is relatively new. In the original paper which proposed forming SLBs by spin coating in 2002, many different solvents were tested including pure chloroform, trifluoroethanol and 2-propanol [55]. Later work established that spin coating could be done using an abundance of different solvents including hexane, methanol, carbon tetrachloride, toluene, methylene chloride, and hexafluoro-2-propanol [56, 147], with specific combinations of solvents recommended for particular lipids [147].

The most important factor regarding the choice of solvent is the quality of the SLBs it produces, however there are also considerations regarding the cost and safety of the solvents. Some of the above listed solvents are extremely toxic [147], and so ideally the least dangerous solvent mixture which produces good quality SLBs would be used. Many solvent mixtures recommended for spin coating are based around mixing a non-polar solvent (often chloroform) with a polar solvent [147] to adjust the effective polarity of the solvent mixture. The polar component serves to help dissolve the hydrophilic lipid heads, while the hydrophobic tails are dissolved by the non-polar solvent. This was used as the starting point for our solvent development process, and we selected a combination of chloroform and acetonitrile at a ratio of 95:5 (v/v). Acetonitrile is a small polar molecule, which has been shown to be capable of dissolving lipid bilayers [148], and so was considered a suitable choice for the polar component of the mixture.

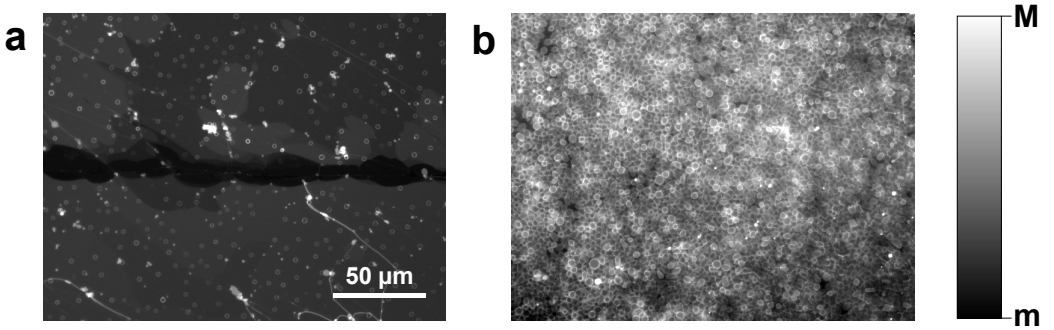

Figure B.1: Fluorescence images of spin-coated DOPC/ATTO488-DOPE(99.9/0.1) samples after hydration in a) PBS solution (m = 500 pe to M = 4095 pe), and b) distilled water (m = 1600 pe to M = 2620 pe).

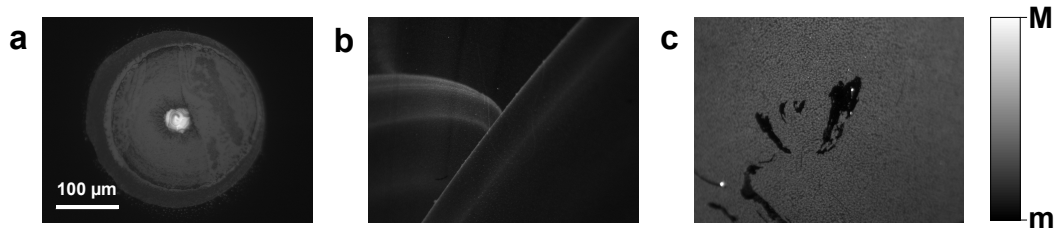

Figure B.2: Fluorescence images of dry spin-coated $DC_{15}PC$ lipid films formed using a concentration of a) 1 mg/ml in chloroform:acetonitrile (m = 180 pe to M = 3000 pe, γ= 0.5), b) 5 mg/ml in chloroform:acetonitrile (m = 280 pe to M = 850 pe), and c) 1 mg/ml in 2-propanol (m = 450 pe to M = 4095 pe).

This solvent proved effective during initial testing, as can be seen in Fig. B.1, which shows spin coated DOPC/ATTO488-DOPE (99.9:0.1) lipid films prepared from 10 mg/ml in chloroform:acetonitrile (95:5). The other parameter of interest during early testing was the hydration medium. While using PBS to hydrate the spin coated film would result in an environment closer to that experienced by cellular membranes (due to its higher ionic strength), a distilled water medium would provide a more straightforward system with fewer variables acting on the bilayer. As such the effect of directly hydrating the spin coated lipid film in PBS and distilled water was tested. The images in Fig. B.1 show the spin coated film after hydration in PBS, which results in a stack of bilayers as expected, and distilled water, which results in an adhered layer of vesicles covering the sample. It was therefore decided to use PBS as a hydration medium.

Having developed a minimal working spin-coating procedure for a DOPC SLB which is in the L_d phase at room temperature, next came development of the procedure for $DC_{15}PC$ samples which form an S_o phase at room temperature. Having established that the 95:5 chloroform:acetonitrile solvent mixture was effective for the DOPC samples, this was used as the basis for initial efforts for producing $DC_{15}PC$ bilayers. The results of this are shown in Fig. B.2a and Fig. B.2b.

As can be seen, there was next to no lipid on the surface when using this mixture. To verify that lipid was not being lost somehow during the hydration process, the sample was imaged dry, immediately after spin-coating. It was found that the majority of the coverslip was completely devoid of lipid, with only a few highly multilamellar regions showing any lipid attachment to the surface, thus proving the problem was due to the lipid not interacting with the substrate, rather than some stability issue with the $DC_{15}PC$ mixture during hydration. Increasing the concentration by a factor of five resulted in an increase in coverage, but the expected lamellar arrangement still did not form.

It was therefore decided to test different solvents. The next solvent to be tested was dichloromethane (CH_2Cl_2), which is chemically similar to chloroform ($CHCl_3$). This however proved ineffective due to the significantly reduced ability to dissolve the lipid mixture; the lipids would come out of solution within a short period of time after preparation of the mixture in dichloromethane and would not return to solution. After this 2-propanol was tested, which was listed as a viable solvent for spin-coating DMPC (a structurally similar lipid to $DC_{15}PC$) SLBs in the literature [55]. This proved to be more effective at getting lipid to interact with the glass, as can be seen in Fig. B.2c, which shows near total coverage of the surface by lipid.

However, the lipid still did not have the desired SLB arrangement after hydration

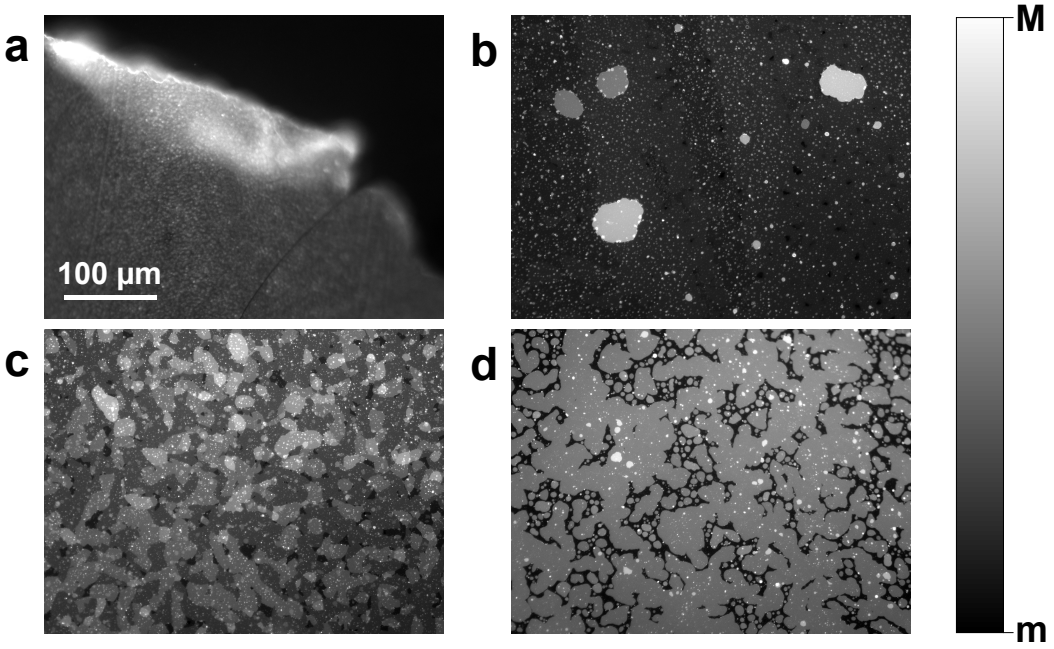

Figure B.3: Fluorescence images of spin-coated $DC_{15}PC$ lipid films after hydration formed using a) 1 mg/ml in 2-propanol handled at room temperature (m = 260 pe to M = 1230 pe), b) 5 mg/ml in 2-propanol with 30 minute heating to 37 °C applied after hydration (m = 400 pe to M = 2570 pe), c) 2 mg/ml in 2-propanol with a room temperature pre-hydration step (m = 300 pe to M = 770 pe), and d) 1 mg/ml in 2-propanol with a 37 °C pre-hydration step (m = 510 pe to M = 1430 pe). Image a) is at room temperature. All others are at 37 °C.

at room temperature, instead forming a coarse film which peeled off the glass surface, as can be seen in Fig. B.3a. In order to improve the sample, it was decided to test heating the sample above T_m to see if the lipids would adopt the expected lamellar arrangement when heated. This proved successful as shown in Fig. B.3b, as following heating the lipids formed a multilamellar film, albeit one with considerable variation in lamellarity and large numbers of adhered vesicles. Such vesicles are problematic for the qDIC analysis.

In order to refine the technique and reduce the number of vesicles forming, a room temperature pre-hydration step was introduced. This involved placing the coverslip inside a 50 ml centrifuge tube, which contained a small piece of wet tissue positioned at the base. As previously touched upon in Sec. 2.3, it was reasoned that this would allow the bilayer to absorb moisture before full hydration, reducing the hydration gradient over the bilayer, and thereby reduce vesicle formation (as well as the lipid detachment seen in Fig. B.3a). To prevent peroxidation of the lipids, the centrifuge tube was filled with nitrogen and sealed. The tube was stored horizontally such that the tissue and the coverslip were not in direct contact. This pre-hydration step was somewhat successful, as can be seen in Fig. B.3c, but while the size of the vesicles was reduced, many remained.

To further improve on this process, it was decided to attempt the pre-hydration at 37 °C, above T_m for $DC_{15}PC$. This resulted in a good quality bilayer as can be seen in Fig. B.3d, which shows mostly flat bilayers with relatively few vesicles adhered to the surface. As such, this pre-hydration step was incorporated into all sample

preparation going forward. This step had the additional benefit of allowing the use of distilled water as a hydration medium for DOPC samples, as it was found that the elimination of the hydration gradient by this pre-hydration step prevented the formation of the vesicular layer shown in Fig. B.1b. Although using distilled water was possible, bilayers were generally of poorer quality than those formed in PBS, so PBS was retained as the default hydration medium.

Finally came the development of protocols for SLBs exhibiting liquid-liquid phase separation at room temperature. Two different lipid mixtures were tested. The first was DOPC/DPPC/Chol/ATTO488-DOPE (39.9/40.0/20.0/0.1), which attempted to use the saturated chain phospholipid DPPC for the L_o phase, while the second was DOPC/ESM/Chol/ATTO488-DOPE (54.9/25.0/20.0/0.1), which attempted to form a more physiologically relevant ESM-based L_o phase[1]. For both mixtures, the lipid ratios were chosen to target a miscibility temperature in the range 30 - 35 °C. This range was chosen to be comfortably above room temperature, but also below the 37 °C temperature of the available ovens. Given the mixtures were both formed from a high proportion of DOPC, it was decided to first attempt to form SLBs using the chloroform:acetonitrile (95:5) solvent mixture since this had proven to be effective for the DOPC/ATTO488-DOPE (99.9/0.1) SLBs. Images of SLB formed from these mixtures are shown in Fig. B.4.

In both cases, using the chloroform:acetonitrile (95:5) solvent mixture led to extremely poor bilayer coverage of the sample, with virtually no lipid across the coverslip. In the DPPC-based mixture, there were a few large multilamellar patches, an example of which can be seen in Fig. B.4a. In the case of the ESM-based mixture, there was only a single region where several very small multilamellar bilayer patches had formed. No domains were visible when imaged immediately after full hydration in either sample. Given that 2-propanol had been shown to be an effective solvent for the spin-coated $DC_{15}PC$ bilayers, it was decided to test this on the ESM-based lipid mixture. This proved to be an effective mixture for the multi-component lipid mixtures also, producing bilayers with the expected lamellar arrangement and good coverage of the coverslip. While no domains were present in the test sample immediately after hydration, when the sample was re-imaged seven days later it was found that macroscopic domains had formed.

Given that the ESM-based mixture represented the more 'ideal' mixture for the production of L_o domains due to its closer compositional similarity to biological lipid rafts, it was deemed unnecessary to attempt to perfect the DPPC-based mixture by testing with the 2-propanol solvent, and the ESM-based mixture was used for all experiments where L_o domains were needed.

[1] While pure palmitoyl sphingomyelin would have a more well defined behaviour, the egg sphingomyelin mixture was chosen for cost reasons.

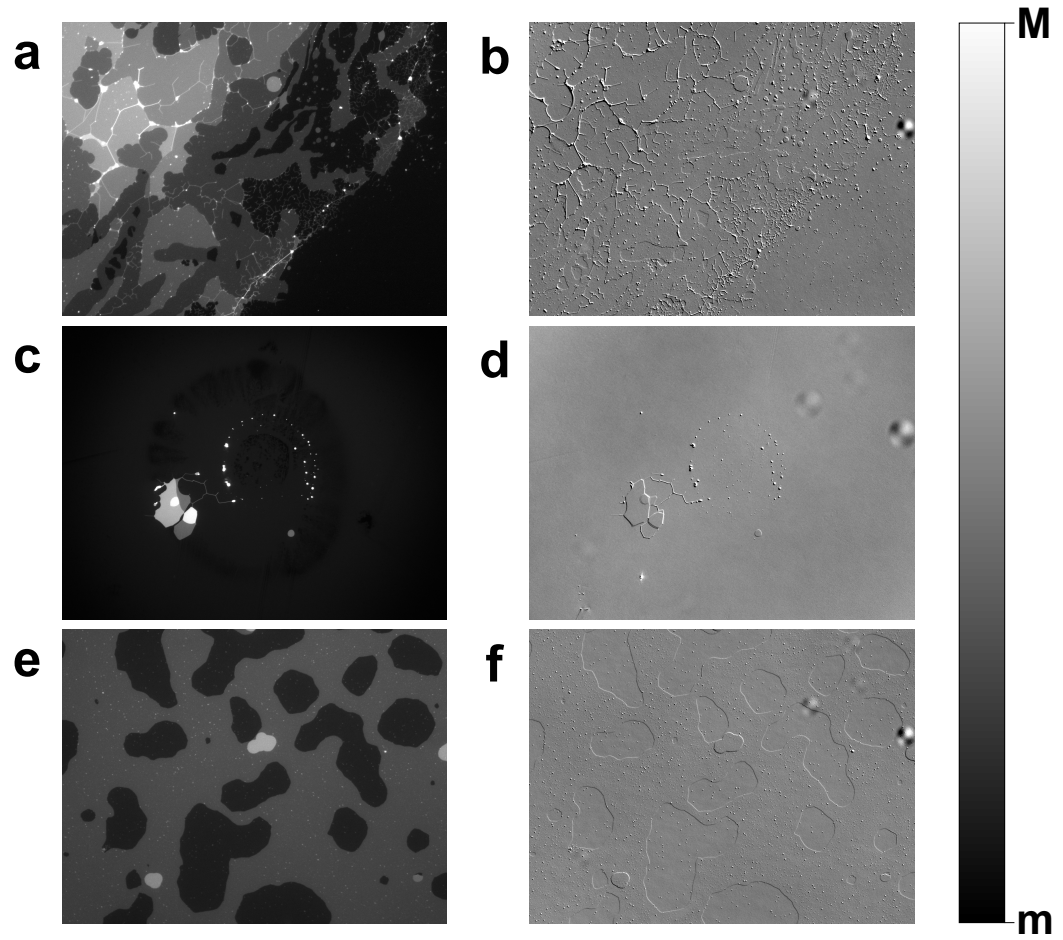

Figure B.4: Images of SLB test samples made from a) the DPPC-based mixture in chloroform:acetonitrile solvent, shown in fluorescence (scaled from $m = 220$ pe to $M = 560$ pe) and b) the same region of the same sample in DIC (scaled from $m = -0.0040$ to $M = 0.0045$). The SM-based mixture dissolved in chloroform:acetonitrile is shown in panels c) in fluorescence (scaled from $m = 210$ pe to $M = 1120$ pe) and d) in DIC (scaled from $m = -0.0044$ to $M = 0.0036$). The ESM-based mixture dissolved in 2-propanol is shown in panels e) in fluorescence (scaled from $m = 210$ pe to $M = 700$ pe) and f) in DIC (scaled from $m = -0.0045$ to $M = 0.0044$). Panels a), b), e) and f) show a 290.6×221.4 µm^2 region, while panels c) and d) show a 434.0×330.6 µm^2 field of view.

Appendix C

Miscellaneous Additional Data

C.1 Line Cut Examples

As mentioned throughout Chapters 3 and 4, for both the qDIC and fluorescence analysis, line profiles are taken over the edges of the individual lipid bilayers comprising the SLB stacks within the images. An example of this is shown in Fig. C.1. The example shown is the full field of view in a qDIC phase image of a DOPC/ATTO488-DOPE (99.9/0.1) sample, comparable to the one shown in Fig. 3.1, prepared from the old lipid stock and formed on a fully hydrophilic ($\theta = 3.5°$) piranha etched surface.

The upper left region is mostly unilamellar with gaps, while the lower right corner is mostly bare glass with a few small unilamellar patches. Both of these regions are ideal for analysis because of the large number of first bilayer edges running perpendicular to the shear direction. In the middle is a large bilamellar region, which has smaller regions of greater lamellarity. In this field of view, 50 measurements of the first bilayer phase step were taken, along with 8 measurements of the second bilayer phase step and 12 measurements of the combined first and second bilayer phase step.

Two artefacts caused by dirt on the camera are present in the upper right portion of the image which appear as alternating light and dark streaks running parallel to the shear. These artefacts are present in the same position in every image taken with this setup, and are always avoided when carrying out the analysis. Additionally, a region of higher intensity is visible in the upper left corner which does not correlate with any structure on the sample. This may be caused by the presence of dirt on the underside of the coverslip, which appears in the focal plane as a defocussed blob. Such dirt is removed as much as possible before imaging by wiping the coverslip with acetone soaked cleanroom paper after the sample preparation is completed, and again immediately before the sample is mounted on the microscope stage.

In Fig. 4.20, twelve different line cuts were taken, each of a different tube, split over two fields of view. While the structure of four individual example tubes as a function of temperature is shown in Fig. 4.20b, the positions of the individual cuts is not indicated. The location of the line cuts taken over these four example tubes is shown in Fig. C.2. The images show the first temperature point at which the tube shown could be measured, which is different for each of the four examples. In Fig. C.2a the sample is at 32.6 °C, in Fig. C.2b it is at 31.7 °C, in Fig. C.2c it is at 32.3 °C, and in Fig. C.2d it is at 32.0 °C.

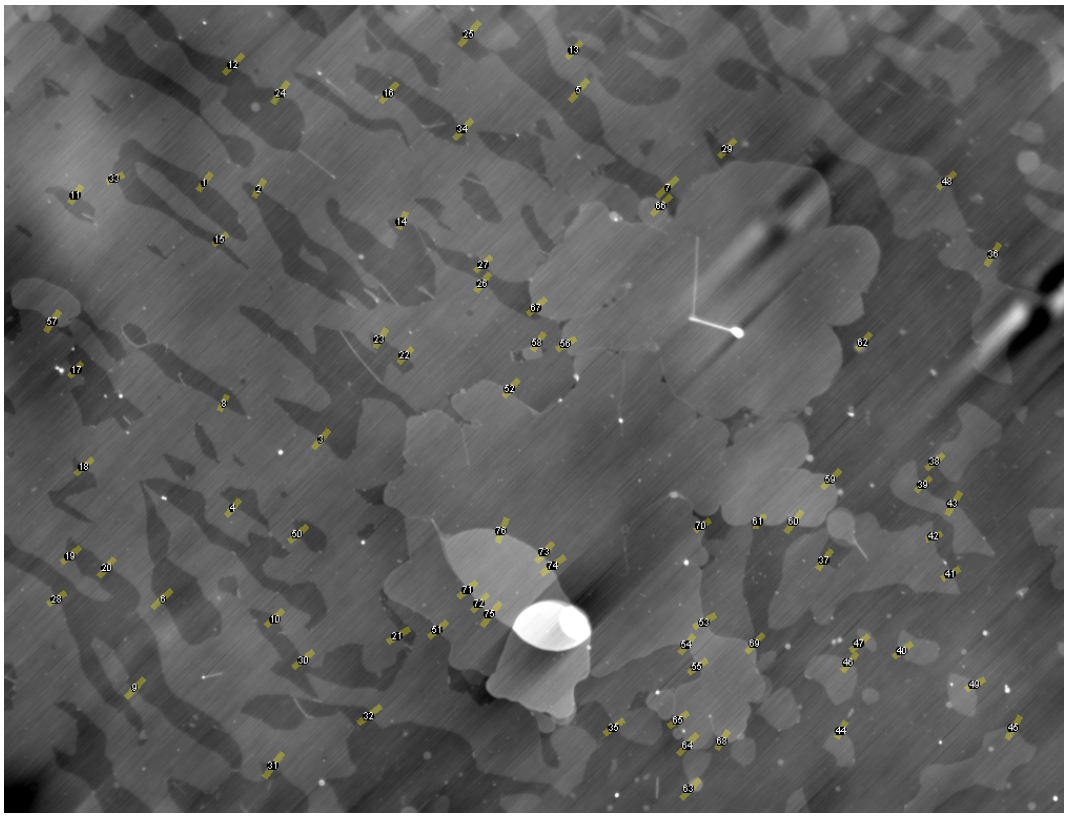

Figure C.1: An example of a qDIC phase image with the positions of the individual line cuts indicated. Image is scaled from -0.0338 to 0.0165 mrad, and shows an area of 290.4 × 221.3 µm.

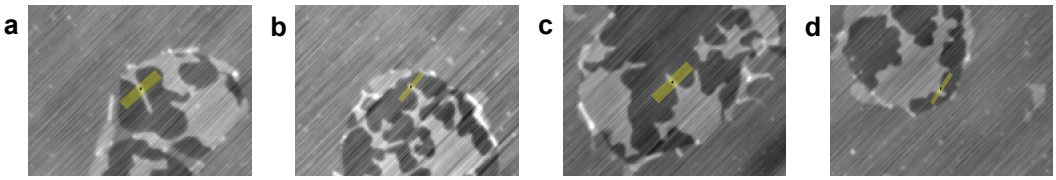

Figure C.2: The positions of the line cuts used in Fig. 4.20. The panels show a) tube 1 (m = -0.04807 rad to M = -0.01345 rad), b) tube 5 (m = -0.04546 rad to M = -0.2218 rad), c) tube 7 (m = -0.05741 rad to M = -0.02651 rad) and d) tube 10 (m = -0.05969 rad to M = -0.02890 rad). Images show a 36.3 × 27.7 µm^2.

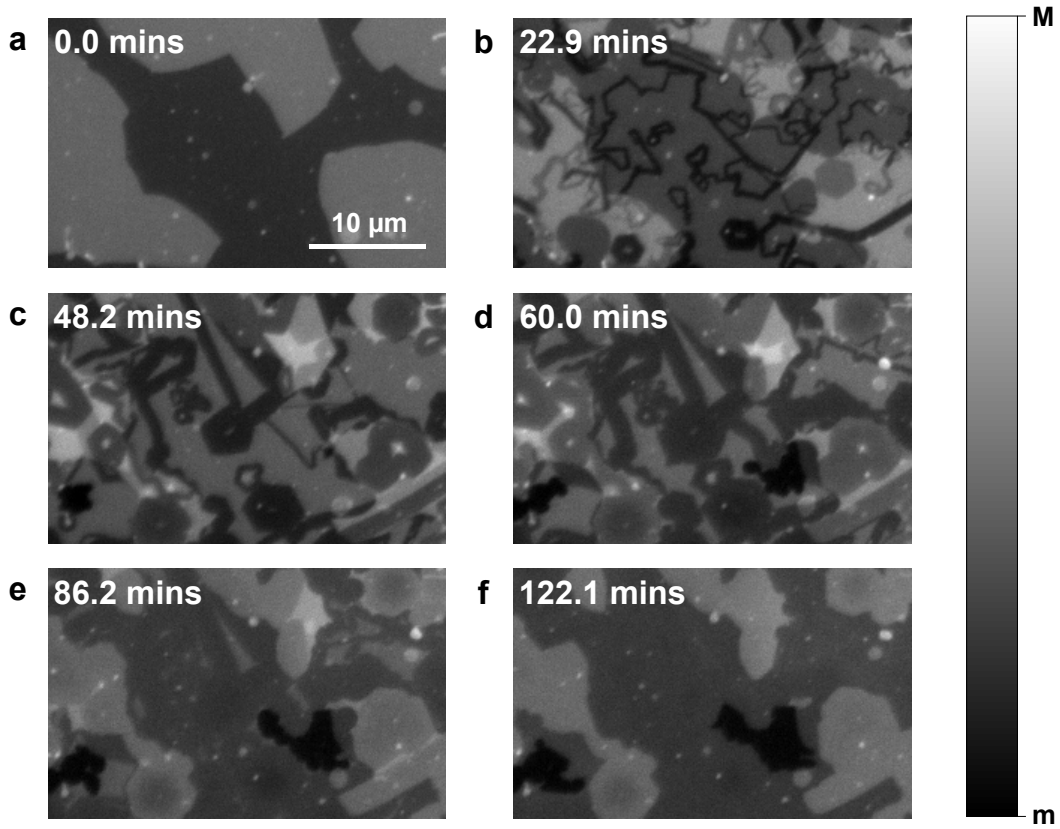

Figure C.3: A $DC_{15}PC$ bilayer labelled with 1 mol% ATTO488-DOPE undergoing a phase transition during cooling. The images show the region at set temperatures of a) 33.9°C, b) 33.3°C, c) 32.7°C, d) 32.4°C, e) 31.8°C, f) 30.9°C. The time elapsed from the acquisition of image a) is shown in the images. The fluorescence intensity is scaled from m = 324 to M= 1513 pe.

C.2 Additional Fluorescence Images

In this section, fluorescence data corresponding to regions either not shown, or only shown as qDIC contrast phase images will be presented. Image acquisition parameters, including the objective and tube lens used, as well as the exposure time, are given in Appendix D for all images shown.

A composite image of a $DC_{15}PC$ bilayer being cooled to below T_m is shown in Fig. 4.4 in Sec. 4.2, with the fluorescence signal shown as an overlay in the green colour channel. In order that the fluorescence in this field of view can be more clearly seen, Fig. C.3 directly shows the fluorescent intensity. Just as for the overlay in Fig. 4.4, the fluorescence images in Fig. C.3 have been corrected for photobleaching using the procedure described in Sec. 4.2. The fluorescent intensity scale in Fig. C.3 has been adjusted slightly compared to Fig. 4.4.

Fluorescence images corresponding to the regions shown in Fig. 4.15 and Fig. 4.16 not presented in Sec. 4.5 are shown in Fig. C.4 and Fig. C.5. The fluorescence images in Fig. C.4 are scaled so the internal structure of the vesicle can be seen. The fluorescence images in Fig. C.5 are not photobleach corrected, resulting in a progressive loss of intensity. This is because the usual assumptions used (constant fluorescence within the field of view) are not valid because of the large amount of lipid lost from the surface during imaging.

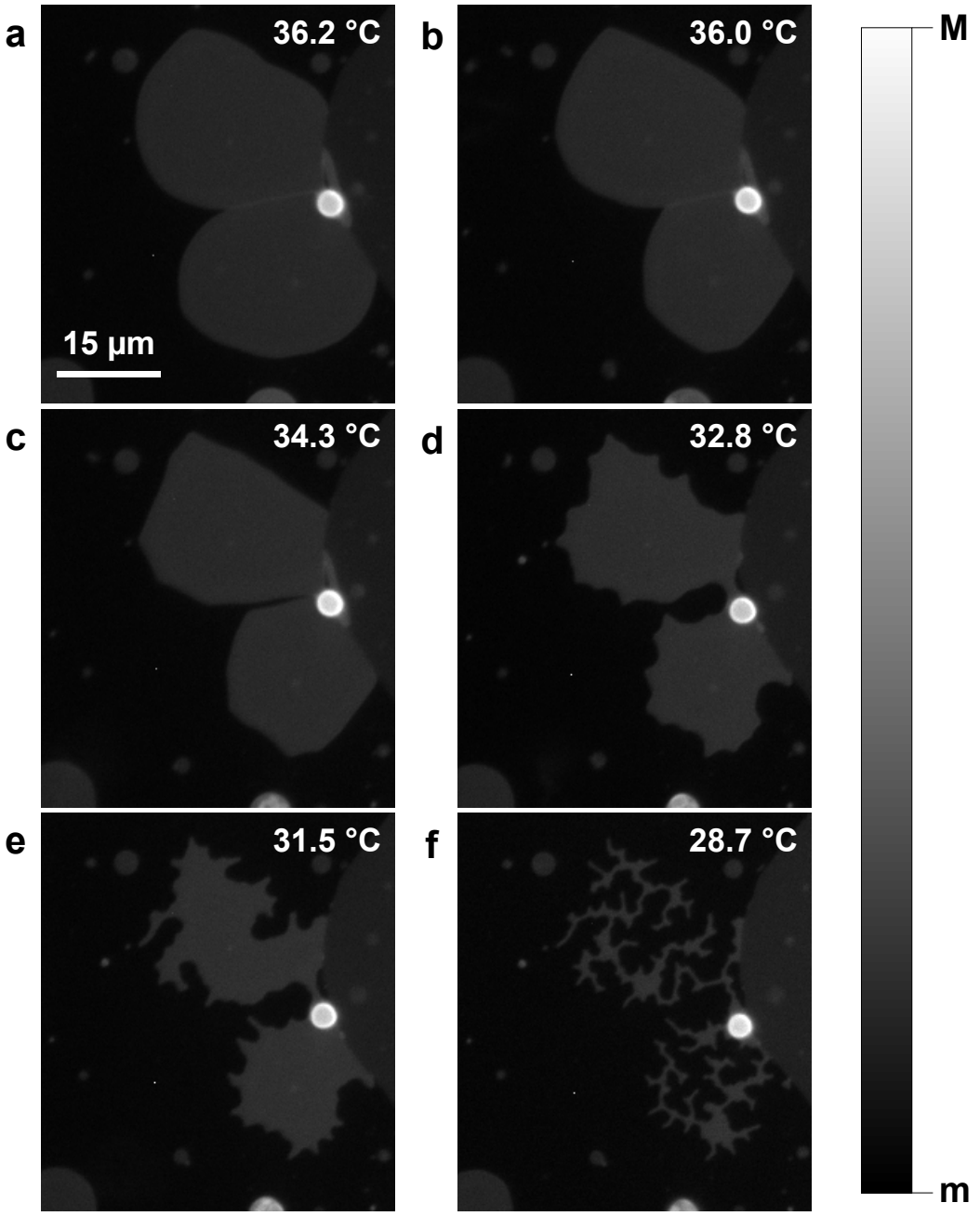

Figure C.4: Fluorescence images of a double bilayer region of a $DC_{15}PC$/ATTO488-DOPE (99.9/0.1) lipid film undergoing a shape change into a network of lipid tubes during cooling of the sample. A single-bilayer region is present to the right. Temperatures given are the measured temperature at the sample. Temperatures given are the measured temperature at the sample. Images are scaled from $m = 25$ pe to $M = 750$ pe.

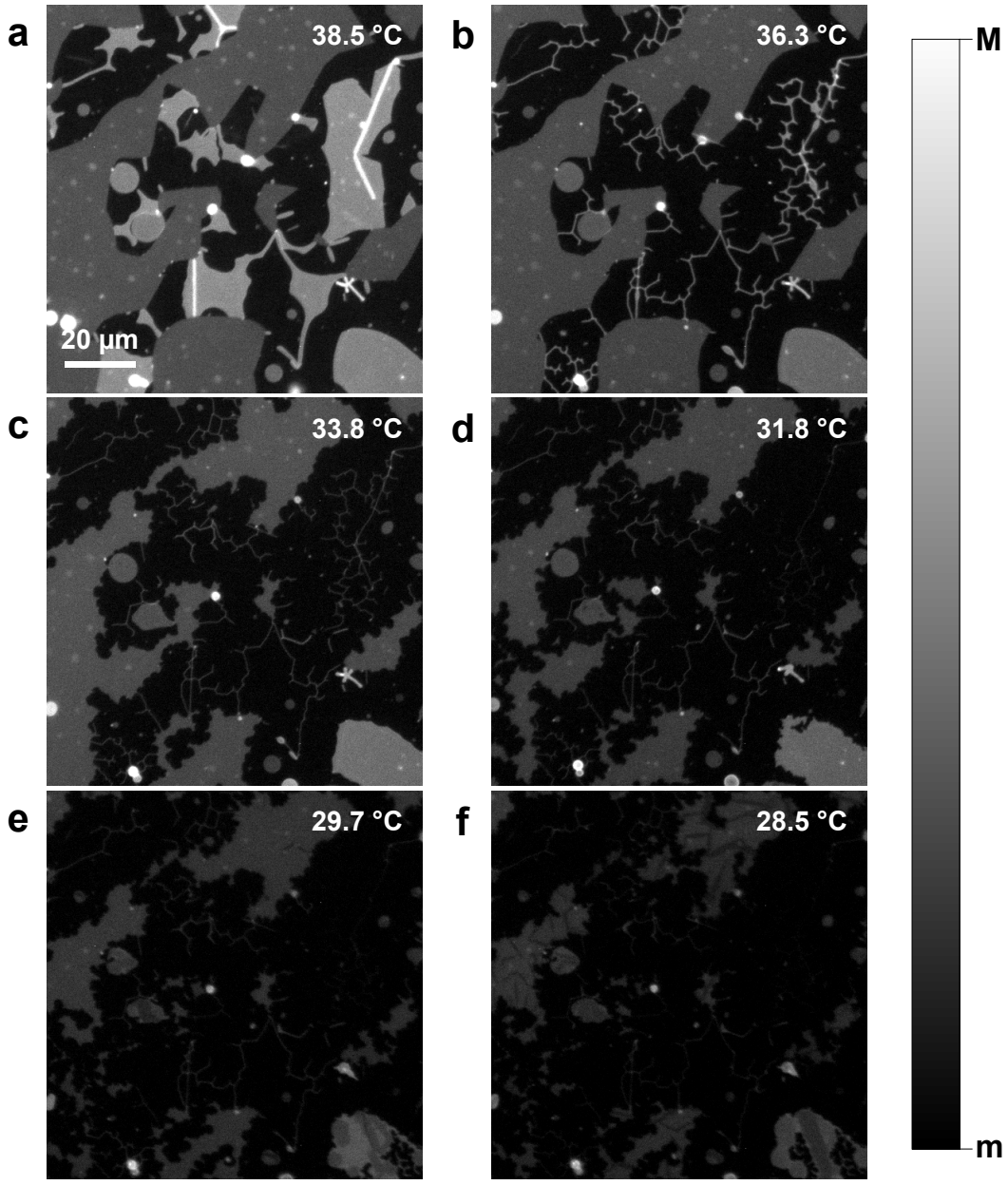

Figure C.5: Fluorescence images of a mixed lamellarity region of a $DC_{15}PC$/ATTO488-DOPE (99.9/0.1) lipid film during cooling of the sample. After double bilayer regions connected to the single bilayer regions have fully reorganised into tubes, the single bilayer regions and free-standing double bilayer regions begin to lose area. Temperatures given are the measured temperature at the sample. Images are scaled from $m = 30$ pe to $M = 180$ pe.

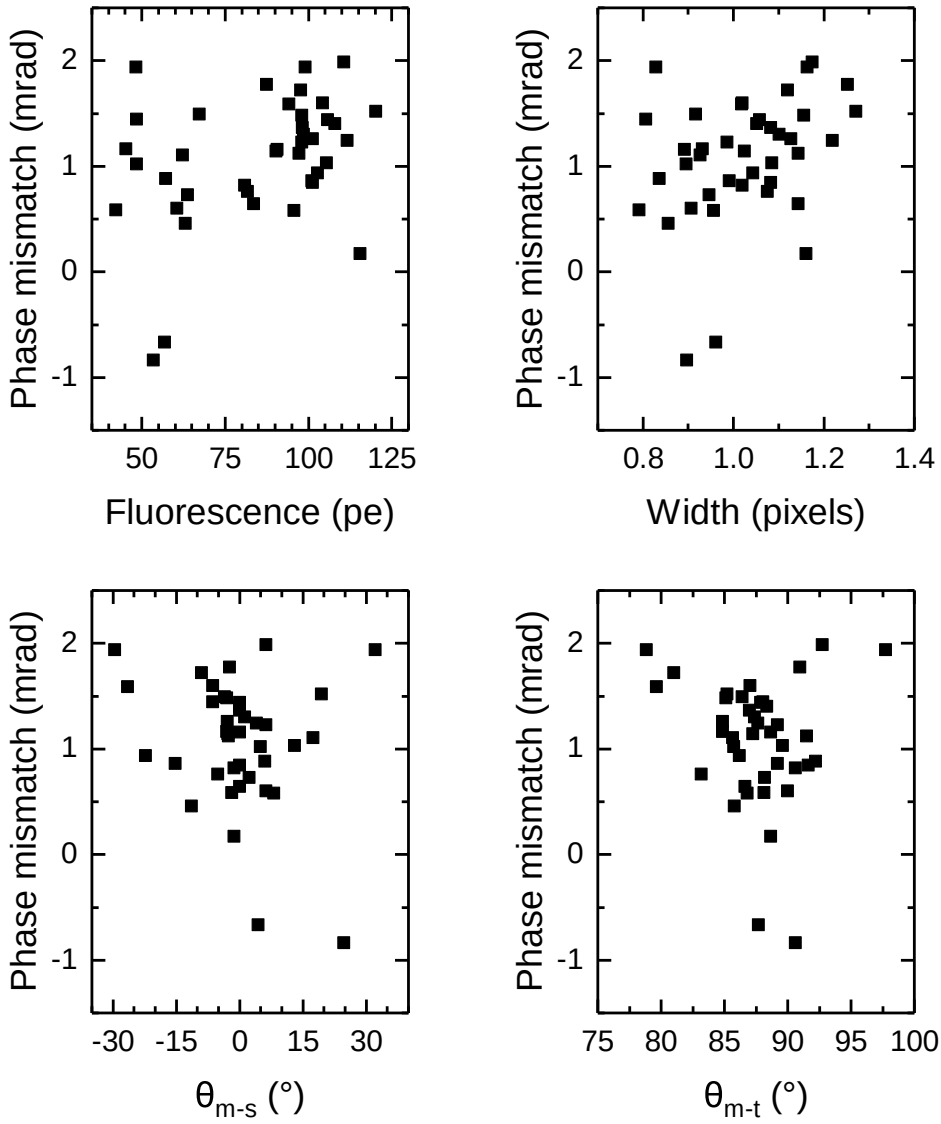

Figure C.6: The relationship between the phase mismatch over the birefringent tubes, and the tube fluorescent intensity, tube width, the angle of the line profile relative to the shear (θ_{m-s}), or the angle of the line profile relative to the tube (θ_{m-t}).

C.3 Tube Birefringence

In Sec. 4.4, the lack of correlation between the phase mismatch over the birefringent tubes, and the fluorescent intensity of the tube, the width of the tube, the angle of the line profile relative to the shear, or the angle of the line profile relative to the tube. For completeness, we show the relationship between the phase mismatch and these parameters in this section, in Fig. C.6.

Appendix D

Image Acquisition Parameters

This section gives the image acquisition and analysis parameters for all the images shown within the main text and the appendices. In Table D.1, this includes exposure time (Exp.), objective, tube lens (T.L.), polariser angle ψ, number of averages (Avs.), qDIC signal-to-noise ratio (κ) and the minimisation (Minim.). For those qDIC images which have been processed with the energy minimisation, the parameters are given in Table D.2. The acquisition parameters for fluorescence images are given in Table D.3.

Figure	Exp. (ms)	Objective	T.L.	ψ (°)	Avs.	κ	Minim.
3.1	100	60×, 1.27 NA	1.0×	12.9	100	1000	No
3.2b	100	60×, 1.27 NA	1.0×	12.9	100	1000	No
3.2d	100	20×, 0.75 NA	1.5×	12.9	100	4000	No
3.3	100	60×, 1.27 NA	1.5×	12.9	64	1000	No
3.4	100	60×, 1.27 NA	1.5×	12.9	64	4000	No
3.6	100	60×, 1.27 NA	1.0×	12.9	100	Given	No
3.12	100	20×, 0.75 NA	1.5×	15.0	100	4000	No
3.19	100	20×, 0.75 NA	1.5×	12.9	100	4000	No
3.22	100	20×, 0.75 NA	1.5×	12.9	Given	4000	No
3.27	100	20×, 0.75 NA	1.5×	12.9	100	4000	No
3.28	100	20×, 0.75 NA	1.5×	12.9	100	4000	No
4.2	100	20×, 0.75 NA	1.5×	15.0	100	4000	No
4.4	100	20×, 0.75 NA	1.5×	12.9	100	4000	No
4.6	100	20×, 0.75 NA	1.5×	12.9	100	4000	No
4.7	100	20×, 0.75 NA	1.5×	12.9	100	4000	Yes
4.11	100	20×, 0.75 NA	1.5×	15.0	100	4000	No
4.15	100	20×, 0.75 NA	1.5×	12.9	100	4000	No
4.16	100	20×, 0.75 NA	1.5×	12.9	100	4000	Yes
4.20	100	20×, 0.75 NA	1.5×	15.0	100	4000	No
B.4b	100	20×, 0.75 NA	1.5×	12.9	100	4000	No
B.4d	100	20×, 0.75 NA	1.0×	12.9	100	4000	No
B.4f	100	20×, 0.75 NA	1.5×	12.9	100	4000	No

Table D.1: Image acquisition parameters for qDIC phase and contrast images.

Figure	Smoothness power α	Smoothness weight λ	# Iterations
4.7	0.5	1×10^{-6}	10051
4.16	0.5	1×10^{-6}	20000

Table D.2: Parameters used in the qDIC global minimisation for each figure.

Figure	Exp. (ms)	Objective	T.L.	Filters
3.1	1000	60×, 1.27 NA	1.0×	-
3.12	1000	20×, 0.75 NA	1.5×	None
3.19	1000	20×, 0.75 NA	1.5×	-
4.1	1000	20×, 0.75 NA	1.5×	-
4.2	1000	20×, 0.75 NA	1.5×	ND8
4.4	1000	20×, 0.75 NA	1.5×	-
4.6	1000	20×, 0.75 NA	1.5×	-
4.7	1000	20×, 0.75 NA	1.5×	-
4.18	1000	20×, 0.75 NA	1.5×	None
B.1	500	10×, 0.45 NA	1.0×	-
B.2a	100	20×, 0.75 NA	1.0×	-
B.2b	1000	20×, 0.75 NA	1.0×	-
B.2c	1000	20×, 0.75 NA	1.0×	-
B.3a	100	20×, 0.75 NA	1.0×	-
B.3b	100	20×, 0.75 NA	1.0×	ND4
B.3c	100	20×, 0.75 NA	1.0×	ND4
B.3d	1000	20×, 0.75 NA	1.0×	ND4
B.4a	1000	20×, 0.75 NA	1.0×	-
B.4c	1000	20×, 0.75 NA	1.0×	-
B.4e	1000	20×, 0.75 NA	1.5×	-
C.4	2000	20×, 0.75 NA	1.5×	-
C.5	1000	20×, 0.75 NA	1.5×	-

Table D.3: Image acquisition parameters for fluorescence images.

Publications

Publications relating to the work presented in this thesis are listed below.

Articles

Published

1. Wolfgang Langbein, **David Regan**, Iestyn Pope and Paola Borri. Invited Article: Heterodyne dual-polarization epi-detected CARS microscopy for chemical and topographic imaging of interfaces. *APL Photonics 3*. 2018.

2. **David Regan**, Joseph Williams, Francesco Masia, Paola Borri and Wolfgang Langbein. Measuring sub-nanometre thickness changes during phase transitions of supported lipid bilayers with quantitative differential interference contrast microscopy. *Proceedings of SPIE*. 2019.

3. **David Regan**, Joseph Williams, Paola Borri and Wolfgang Langbein. Lipid bilayer thickness measured by quantitative DIC reveals phase transitions and effects of substrate hydrophilicity. *Langmuir*. 2019.

In Preparation

1. Joseph Williams, **David Regan**, Robin Islam, Francesco Masia, Paola Borri and Wolfgang Langbein. High sensitivity quantitative analysis of differential interference contrast images. *In preparation*. 2020.

Conferences

1. **David Regan**, Joseph Williams, George Zoriniants, Paola Borri and Wolfgang Langbein. Measuring the thickness of supported lipid bilayers with quantitative differential interference contrast microscopy. *Poster presentation*, Bio-Nano Photonics symposium, Cardiff University, U.K. (2017).

2. Alexander Nahmad-Rohen, George Zoriniants, **David Regan**, Paola Borri and Wolfgang Langbein. Simultaneous measurement of thickness and refractive index by interferometric reflectometry. *Poster presentation*, Bio-Nano Photonics symposium, Cardiff University, U.K. (2017).

3. Joseph Williams, **David Regan**, George Zoriniants, Paola Borri and Wolfgang Langbein. qDIC - Extracting quantitative information from Differential Interference Contrast (DIC) images. *Poster presentation*, Bio-Nano Photonics symposium, Cardiff University, U.K. (2017).

4. **David Regan**, Joseph Williams, Paola Borri and Wolfgang Langbein. Measuring sub-nanometre thickness changes in supported lipid bilayers with quantitative DIC microscopy. *Oral presentation*, Photon 18, Aston University, U.K. (2018).

5. Joseph Williams, Francesco Masia, **David Regan**, George Zoriniants, Paola Borri and Wolfgang Langbein. qDIC - Extracting quantitative information from Differential Interference Contrast (DIC) images. *Oral presentation*, Photon 18, Aston University, U.K. (2018).

6. **David Regan**, Joseph Williams, Paola Borri and Wolfgang Langbein. Measuring sub-nanometre thickness changes in supported lipid bilayers with quantitative DIC microscopy. *Oral presentation*, Photonics West 2019, San Francisco, U.S.A. (2019).

7. Alexander Nahmad-Rohen, **David Regan**, Paola Borri and Wolfgang Langbein. Simultaneous measurement of thickness and refractive index by interferometric reflectometry. *Poster presentation*, Focus on Microscopy 2019, London, U.K. (2019).

8. **David Regan**, Joseph Williams, Paola Borri and Wolfgang Langbein. Measuring sub-nanometre thickness changes in supported lipid bilayers with quantitative DIC microscopy. *Oral presentation*, Microscience Microscopy Congress 2019, Manchester, U.K. (2019).

9. **David Regan**, Joseph Williams, George Zoriniants, Paola Borri and Wolfgang Langbein. Measuring the thickness of supported lipid bilayers with quantitative differential interference contrast microscopy. *Poster presentation*, Microscience Microscopy Congress 2019, Manchester, U.K. (2019).

Bibliography

[1] Todd P. Silverstein. The real reason why oil and water don't mix. *Journal of Chemical Education*, 75(1):116, Jan 1998.

[2] Marc Eeman and Magali Deleu. From biological membranes to biomimetic model membranes. *Biotechnology, Agronomy, Society and Environment*, 14(4):720–736, 2010.

[3] Justyna Widomska, Marija Raguz, and Witold K. Subczynski. Oxygen permeability of the lipid bilayer membrane made of calf lens lipids. *Biochimica et Biophysica Acta (BBA) - Biomembranes*, 1768(10), 2007.

[4] Lei Kai and Ralf Kaldenhoff. A refined model of water and CO2 membrane diffusion: Effects and contribution of sterols and proteins. *Scientific Reports*, 4:6665 EP –, Oct 2014. Article.

[5] Joost C.M. Holthuis and Anant K. Menon. Lipid landscapes and pipelines in membrane homeostasis. *Nature*, 510:48–58, 2014.

[6] Gerrit van Meer and Anton I. P. M. de Kroon. Lipid map of the mammalian cell. *Journal of Cell Science*, 124(1):5–8, 2011.

[7] Oswald Quehenberger, Aaron M. Armando, Alex H. Brown, Stephen B. Milne, David S. Myers, Alfred H. Merrill, Sibali Bandyopadhyay, Kristin N. Jones, Samuel Kelly, Rebecca L. Shaner, Cameron M. Sullards, Elaine Wang, Robert C. Murphy, Robert M. Barkley, Thomas J. Leiker, Christian R. H. Raetz, Ziqiang Guan, Gregory M. Laird, David A. Six, David W. Russell, Jeffrey G. McDonald, Shankar Subramaniam, Eoin Fahy, and Edward A. Dennis. Lipidomics reveals a remarkable diversity of lipids in human plasma. *Journal of Lipid Research*, 51(11):3299–3305, Nov 2010. jlr.M009449[PII].

[8] Jonas Henriksen, Amy C. Rowat, and John H. Ipsen. Vesicle fluctuation analysis of the effects of sterols on membrane bending rigidity. *European Biophysics Journal*, 33(8):732–741, 2004.

[9] Jonathan Lombard. Once upon a time the cell membranes: 175 years of cell boundary research. *Biology Direct*, 9:32–32, Dec 2014.

[10] Evert Gorter and François Grendel. On bimolecular layers of lipoids on the chromocytes of the blood. *Journal of Experimental Medicine*, 41(4):439–443, Mar 1925.

[11] Michael Edidin. Lipids on the frontier: a century of cell-membrane bilayers. *Nature Reviews Molecular Cell Biology*, 4(1):414–418, 2003.

[12] Yosuke Senju, Maria Kalimeri, Essi V. Koskela, Pentti Somerharju, Hongxia Zhao, Ilpo Vattulainen, and Pekka Lappalainen. Mechanistic principles underlying regulation of the actin cytoskeleton by phosphoinositides. *Proceedings of the National Academy of Sciences*, 114(43):E8977–E8986, 2017.

[13] Kecheng Zhou, Andrea Dichlberger, Hector Martinez-Seara, Thomas K. M. Nyholm, Shiqian Li, Young Ah Kim, Ilpo Vattulainen, Elina Ikonen, and Tomas Blom. A ceramide-regulated element in the late endosomal protein LAPTM4B controls amino acid transporter interaction. *ACS Central Science*, 4(5):548–558, 2018.

[14] J. E. Kyle, K. E. Burnum-Johnson, J. P. Wendler, A. J. Eisfeld, Peter J. Halfmann, Tokiko Watanabe, Foday Sahr, R. D. Smith, Y. Kawaoka, K. M. Waters, and T. O. Metz. Plasma lipidome reveals critical illness and recovery from human ebola virus disease. *Proceedings of the National Academy of Sciences*, 116(9):3919–3928, 2019.

[15] Marios G. Krokidis, Maria Louka, Eleni K. Efthimiadou, Sevasti-Kiriaki Zervou, Kyriakos Papadopoulos, Anastasia Hiskia, Carla Ferreri, and Chryssostomos Chatgilialoglu. Membrane lipidome reorganization and accumulation of tissue DNA lesions in tumor-bearing mice: An exploratory study. *Cancers*, 11(4):480, Apr 2019.

[16] Qianhui Yu, Zhisong He, Dmitry Zubkov, Shuyun Huang, Ilia Kurochkin, Xiaode Yang, Tobias Halene, Lothar Willmitzer, Patrick Giavalisco, Schahram Akbarian, and Philipp Khaitovich. Lipidome alterations in human prefrontal cortex during development, aging, and cognitive disorders. *Molecular Psychiatry*, 2018.

[17] S. J. Singer and Garth L. Nicolson. The fluid mosaic model of the structure of cell membranes. *Science*, 175(4023):720–731, 1972.

[18] Morris J. Karnovsky, Alan M. Kleinfeld, Richard L. Hoover, and Richard D Klausner. The concept of lipid domains in membranes. *The Journal of Cell Biology*, 94(1):1–6, 1982.

[19] Linda J. Pike. Rafts defined: a report on the Keystone symposium on lipid rafts and cell function. *Journal of Lipid Research*, 47(7):1597–1598, 2006.

[20] H.M. Seeger, G. Marino, A. Alessandrini, and P. Facci. Effect of physical parameters on the main phase transition of supported lipid bilayers. *Biophysical Journal*, 97(4):1067 – 1076, 2009.

[21] Erdinc Sezgin, Ilya Levental, Satyajit Mayor, and Christian Eggeling. The mystery of membrane organization: composition, regulation and roles of lipid rafts. *Nature Reviews Molecular Cell Biology*, 18:361 EP –, Mar 2017.

[22] Sung-Tae Yang, Volker Kiessling, and Lukas K. Tamm. Line tension at lipid phase boundaries as driving force for HIV fusion peptide-mediated fusion. *Nature Communications*, 7(11401):1–9, 2016.

[23] Katharina Gaus, Elena Chklovskaia, Barbara Fazekas de St Groth, Wendy Jessup, and Thomas Harder. Condensation of the plasma membrane at the

site of T lymphocyte activation. *Journal of Cell Biology*, 171(1):121–131, Oct 2005.

[24] Jun Fan, Maria Sammalkorpi, and Mikko Haataja. Formation and regulation of lipid microdomains in cell membranes: Theory, modeling, and speculation. *FEBS Letters*, 584(9):1678–1684, 2010.

[25] Matthew B. Stone, Sarah A. Shelby, and Sarah L. Veatch. Super-resolution microscopy: Shedding light on the cellular plasma membrane. *Chemical Reviews*, 117(11):7457–7477, Jun 2017.

[26] Walther Stoeckenius and Donald M. Engelman. Current models for the structure of biological membranes. *The Journal of Cell Biology*, 42(3):613–646, 1969.

[27] Sean Munro. Lipid rafts: Elusive or illusive? *Cell*, 115(4):377 – 388, 2003.

[28] Linda J. Pike. Lipid rafts: heterogeneity on the high seas. *The Biochemical journal*, 378(Pt 2):281–292, Mar 2004.

[29] Savitha Devanathan, Zdzislaw Salamon, Göran Lindblom, Gerhard Gröbner, and Gordon Tollin. Effects of sphingomyelin, cholesterol and zinc ions on the binding, insertion and aggregation of the amyloid Aβ1-40 peptide in solid-supported lipid bilayers. *FEBS Journal*, 273(7):1389–1402, 2006.

[30] Christina G. Siontorou, Georgia-Paraskevi Nikoleli, Dimitrios P. Nikolelis, and Stefanos K. Karapetis. Artificial lipid membranes: Past, present, and future. *Membranes (Basel)*, 7(3):38, Jul 2017.

[31] Georgia-Paraskevi Nikoleli, Dimitrios Nikolelis, Christina Siontorou, Marianna-Thalia Nikolelis, and Steve Karapetis. The application of lipid membranes in biosensing. *Membranes*, 8:108, Nov 2018.

[32] Poul M. Bendix, S. Nader S. Reihani, and Lene B. Oddershede. Direct measurements of heating by electromagnetically trapped gold nanoparticles on supported lipid bilayers. *ACS Nano*, 4(4):2256–2262, 2010. PMID: 20369898.

[33] Julien Massiot, Véronique Rosilio, and Ali Makky. Photo-triggerable liposomal drug delivery systems: from simple porphyrin insertion in the lipid bilayer towards supramolecular assemblies of lipid-porphyrin conjugates. *Journal of Materials Chemistry B*, 7(11):1805–1823, 2019.

[34] Evgenyi Y. Shalaev and Peter L. Steponkus. Phase diagram of 1,2-dioleoylphosphatidylethanolamine (DOPE):water system at subzero temperatures and at low water contents. *Biochimica et Biophysica Acta (BBA) - Biomembranes*, 1419(2):229 – 247, 1999.

[35] Shalene Sankhagowit, Ernest Y. Lee, Gerard C. L. Wong, and Noah Malmstadt. Oxidation of membrane curvature-regulating phosphatidylethanolamine lipid results in formation of bilayer and cubic structures. *Langmuir*, 32(10):2450–2457, 2016.

[36] Rumiana Koynova and Martin Caffrey. Phases and phase transitions of the phosphatidylcholines. *Biochimica et Biophysica Acta (BBA) - Reviews on Biomembranes*, 1376(1):91 – 145, 1998.

[37] Andrea Alessandrini and Paolo Facci. Phase transitions in supported lipid bilayers studied by AFM. *Soft Matter*, 10:7145–7164, 2014.

[38] Laura Picas, Felix Rico, and Simon Scheuring. Direct measurement of the mechanical properties of lipid phases in supported bilayers. *Biophysical journal*, 102(1):L01–L3, Jan 2012.

[39] J. F. Nagle and S. Tristram-Nagle. Structure of lipid bilayers. *Biochimica et Biophysica Acta*, 1469(3):159–195, Nov 2000.

[40] Jian Dai, Mohammad Alwarawrah, and Juyang Huang. Instability of cholesterol clusters in lipid bilayers and the cholesterol's umbrella effect. *The Journal of Physical Chemistry. B*, 114(2):840–848, Jan 2010.

[41] J. Peter Slotte. The importance of hydrogen bonding in sphingomyelin's membrane interactions with co-lipids. *Biochimica et Biophysica Acta (BBA) - Biomembranes*, 1858(2):304 – 310, 2016.

[42] Joan V. Bleecker, Phillip A. Cox, Rami N. Foster, Jonathan P. Litz, Matthew C. Blosser, David G. Castner, and Sarah L. Keller. Thickness mismatch of coexisting liquid phases in noncanonical lipid bilayers. *J. Phys. Chem. B*, 120(10):2761–2770, 2016. PMID: 26890258.

[43] Mathias Winterhalter. Black lipid membranes. *Current Opinion in Colloid & Interface Science*, 5(3):250 – 255, 2000.

[44] Hannah Stein, Susann Spindler, Navid Bonakdar, Chun Wang, and Vahid Sandoghdar. Production of isolated giant unilamellar vesicles under high salt concentrations. *Frontiers in Physiology*, 8:63–63, Feb 2017.

[45] Craig I. McPhee, George Zoriniants, Wolfgang Langbein, and Paola Borri. Measuring the lamellarity of giant lipid vesicles with differential interference contrast microscopy. *Biophysical Journal*, 105(6):1414 – 1420, 2013.

[46] Margarita Staykova, Douglas P. Holmes, Clarke Read, and Howard A. Stone. Mechanics of surface area regulation in cells examined with confined lipid membranes. *Proceedings of the National Academy of Sciences*, 108(22):9084–9088, 2011.

[47] Ross S. Gunderson and Aurelia R. Honerkamp-Smith. Liquid-liquid phase transition temperatures increase when lipid bilayers are supported on glass. *Biochimica et Biophysica Acta (BBA) - Biomembranes*, 2018.

[48] Lukas K. Tamm and Harden M. McConnell. Supported phospholipid bilayers. *Biophysical Journal*, 47(1):105 – 113, 1985.

[49] Ryugo Tero. Substrate effects on the formation process, structure and physicochemical properties of supported lipid bilayers. *Materials*, 5(12):2658–2680, 2012.

[50] Toshinori Motegi, Kenji Yamazaki, Toshio Ogino, and Ryugo Tero. Substrate-induced structure and molecular dynamics in a lipid bilayer membrane. *Langmuir*, 33(51):14748–14755, 2017. PMID: 29236511.

[51] Ryugo Tero, Gen Sazaki, Toru Ujihara, and Tsuneo Urisu. Anomalous diffusion in supported lipid bilayers induced by oxide surface nanostructures. *Langmuir*, 27(16):9662–9665, 2011.

[52] Jakob Andersson and Ingo Köper. Tethered and polymer supported bilayer lipid membranes: Structure and function. *Membranes*, 6(2):30, May 2016.

[53] Johannes Schmitt, Birgit Danner, and Thomas M. Bayerl. Polymer cushions in supported phospholipid bilayers reduce significantly the frictional drag between bilayer and solid surface. *Langmuir*, 17(1):244–246, 2001.

[54] Raghuveer Parthasarathy, Cheng-han Yu, and Jay T. Groves. Curvature-modulated phase separation in lipid bilayer membranes. *Langmuir*, 22(11):5095–5099, May 2006.

[55] Ulrike Mennicke and Tim Salditt. Preparation of solid-supported lipid bilayers by spin-coating. *Langmuir*, 18(21):8172–8177, 2002.

[56] Adam Cohen Simonsen and Luis A. Bagatolli. Structure of spin-coated lipid films and domain formation in supported membranes formed by hydration. *Langmuir*, 20(22):9720–9728, 2004. PMID: 15491207.

[57] Artem G. Ayuyan and Fredric S. Cohen. Lipid peroxides promote large rafts: Effects of excitation of probes in fluorescence microscopy and electrochemical reactions during vesicle formation. *Biophysical Journal*, 91(6):2172 – 2183, 2006.

[58] Tobias Baumgart, Geoff Hunt, Elaine R. Farkas, Watt W. Webb, and Gerald W. Feigenson. Fluorescence probe partitioning between L_o/L_d phases in lipid membranes. *Biochimica et Biophysica Acta (BBA) - Biomembranes*, 1768(9):2182 – 2194, 2007.

[59] Alexander P. Demchenko, Yves Mély, Guy Duportail, and Andrey S. Klymchenko. Monitoring biophysical properties of lipid membranes by environment-sensitive fluorescent probes. *Biophysical Journal*, 96(9):3461 – 3470, 2009.

[60] Michael Heinrich, Aiwei Tian, Cinzia Esposito, and Tobias Baumgart. Dynamic sorting of lipids and proteins in membrane tubes with a moving phase boundary. *Proceedings of the National Academy of Sciences*, 107(16):7208–7213, 2010.

[61] Xiangxu Kong, Eyal Nir, Kambiz Hamadani, and Shimon Weiss. Photobleaching pathways in single-molecule FRET experiments. *Journal of the American Chemical Society*, 129(15):4643–4654, 2007.

[62] Roland Faller. Molecular modeling of lipid probes and their influence on the membrane. *Biochimica et Biophysica Acta (BBA) - Biomembranes*, 1858(10):2353 – 2361, 2016. Biosimulations of lipid membranes coupled to experiments.

[63] Kathleen F. Wang, Ramanathan Nagarajan, Charlene M. Mello, and Terri A. Camesano. Characterization of supported lipid bilayer disruption by chrysophsin-3 using QCM-D. *The Journal of Physical Chemistry B*, 115(51):15228–15235, 2011. PMID: 22085290.

[64] Tiago N. Figueira, João M. Freire, Catarina Cunha-Santos, Montserrat Heras, João Gonçalves, Anne Moscona, Matteo Porotto, Ana Salomé Veiga, and Miguel A. R. B. Castanho. Quantitative analysis of molecular partition towards lipid membranes using surface plasmon resonance. *Scientific Reports*, 7, Mar 2017.

[65] R. Horváth, G. Fricsovszky, and E. Papp. Application of the optical waveguide lightmode spectroscopy to monitor lipid bilayer phase transition. *Biosensors and Bioelectronics*, 18(4):415 – 428, 2003.

[66] Victor J. Hruby and Gordon Tollin. Plasmon-waveguide resonance (PWR) spectroscopy for directly viewing rates of GPCR/G-protein interactions and quantifying affinities. *Current Opinion in Pharmacology*, 7(5):507–514, Oct 2007.

[67] Norbert Kučerka, John F. Nagle, Jonathan N. Sachs, Scott E. Feller, Jeremy Pencer, Andrew Jackson, and John Katsaras. Lipid bilayer structure determined by the simultaneous analysis of neutron and X-ray scattering data. *Biophysical Journal*, 95(5):2356 – 2367, 2008.

[68] Norbert Kučerka, Mu-Ping Nieh, and John Katsaras. Fluid phase lipid areas and bilayer thicknesses of commonly used phosphatidylcholines as a function of temperature. *Biochimica et Biophysica Acta, Biomembranes*, 1808(11):2761 – 2771, 2011.

[69] Norbert Kučerka, Jeremy Pencer, Jonathan N. Sachs, John F. Nagle, and John Katsaras. Curvature effect on the structure of phospholipid bilayers. *Langmuir*, 23(3):1292–1299, 2007.

[70] M. Beckmann, P. Nollert, and H.-A. Kolb. Manipulation and molecular resolution of a phosphatidylcholine-supported planar bilayer by atomic force microscopy. *The Journal of Membrane Biology*, 161(3):227–233, Feb 1998.

[71] Z.V. Leonenko, E. Finot, H. Ma, T.E. S. Dahms, and D.T. Cramb. Investigation of temperature-induced phase transitions in DOPC and DPPC phospholipid bilayers using temperature-controlled scanning force microscopy. *Biophysical Journal*, 86(6):3783 – 3793, 2004.

[72] YongKeun Park, Christian Depeursinge, and Gabriel Popescu. Quantitative phase imaging in biomedicine. *Nature Photonics*, 12(10):578–589, 2018.

[73] Alan Lasslet. Principles and applications of differential interference contrast light microscopy. *Microscopy and Analysis*, 2006(5):9 – 11, 2006.

[74] Ahmad Darudi Lobat Tayebi Vahideh Farzamrad, Ali-Reza Moradi. Digital holographic microscopy of phase separation in multicomponent lipid membranes. *Journal of Biomedical Optics*, 21:21 – 21 – 6, 2016.

[75] Isabelle L. Di Maio, Daniel Carl, Patrik Langehanenberg, Stella M. Valenzuela, Andrew R. Battle, Sabah Al Khazaaly, Murray Killingsworth, Bjorn Kemper, Gert von Bally, and Donald K. Martin. Structural properties of liposomes from digital holographic microscopy. *SPIE Conference Proceedings*, 6036, 2006.

[76] Christophe Minetti, Victoria Vitkova, Frank Dubois, and Isak Bivas. New optical method for measuring the bending elasticity of lipid bilayers. *Journal of Physics: Conference Series*, 682(1):012031, 2016.

[77] YongKeun Park, Catherine A. Best-Popescu, Ramachandra R. Dasari, and Gabriel Popescu. Light scattering of human red blood cells during metabolic remodeling of the membrane. *Journal of Biomedical Optics*, 16:16 – 16 – 7, 2011.

[78] Chang-Soo Park Dug Young Kim Seungrag Lee, Ji Yong Lee. Detrended fluctuation analysis of membrane flickering in discocyte and spherocyte red blood cells using quantitative phase microscopy. *Journal of Biomedical Optics*, 16:16 – 16 – 7, 2011.

[79] Seungeun Oh, Christopher Fang-Yen, Wonshik Choi, Zahid Yaqoob, Dan Fu, YongKeun Park, Ramachandra R. Dassari, and Michael S. Feld. Label-free imaging of membrane potential using membrane electromotility. *Biophysical Journal*, 103(1):11 – 18, 2012.

[80] Gabriel Popescu, Takahiro Ikeda, Keisuke Goda, Catherine A. Best-Popescu, Michael Laposata, Suliana Manley, Ramachandra R. Dasari, Kamran Badizadegan, and Michael S. Feld. Optical measurement of cell membrane tension. *Physics Review Letters*, 97:218101, Nov 2006.

[81] Michael Shribak, James LaFountain, David Biggs, and Shinya Inouè. Orientation-independent differential interference contrast microscopy and its combination with an orientation-independent polarization system. *Journal of Biomedical Optics*, 13(1):014011–014011, 2008.

[82] Rafael Piestun Carol J. Cogswell Chrysanthe Preza Sharon V. King, Ariel R. Libertun. Quantitative phase microscopy through differential interference imaging. *Journal of Biomedical Optics*, 13(2):1 – 10 – 10, 2008.

[83] Xiquan Cui, Matthew Lew, and Changhuei Yang. Quantitative differential interference contrast microscopy based on structured-aperture interference. *Applied Physics Letters*, 93(9):091113, 2008.

[84] Juan Campos, Leonid P. Yaroslavsky, A. Moreno, and Maria J. Yzuel. Integration in the fourier domain for restoration of a function from its slope: comparison of four methods. *Optics Letters*, 27(22):1986–1988, Nov 2002.

[85] Norbert Wiener. *Extrapolation, Interpolation, and Smoothing of Stationary Time Series*. Wiley, 1949.

[86] Erik B. van Munster, E.K. Winter, and Jacob A. Aten. Measurement-based evaluation of optical pathlength distributions reconstructed from simulated differential interference contrast images. *Journal of Microscopy*, 191(2):170–176, 1998.

[87] Hiroshi Ishiwata, Masahide Itoh, and Toyohiko Yatagai. A new method of three-dimensional measurement by differential interference contrast microscope. *Optics Communications*, 260(1):117 – 126, 2006.

[88] Joseph B. Williams. High sensitivity quantitative analysis of differential interference contrast images. *In Preparation*, 2020.

[89] Krisztian Koos, József Molnár, Lóránd Kelemen, Gábor Tamás, and Peter Horvath. DIC image reconstruction using an energy minimization framework to visualize optical path length distribution. *Scientific Reports*, 6:30420, July 2016.

[90] Christine D. Keating, Terrence G. D'Onofrio, Anat Hatzor, Amy S. Whelpley, Michael J. Natan, and Paul S. Weiss. Manipulation of lipid bilayer membranes in solution using laser tweezers and microsphere handles. *SPIE Proceedings*, 3924, 2000.

[91] Chris Edwards, Amir Arbabi, Basanta Bhaduri, Xiaozhen Wang, Raman Ganti, Peter J. Yunker, Arjun G. Yodh, Gabriel Popescu, and Lynford L. Goddard. Measuring the nonuniform evaporation dynamics of sprayed sessile microdroplets with quantitative phase imaging. *Langmuir*, 31(40):11020–11032, 2015.

[92] Jaideep Chatterjee. Limiting conditions for applying the spherical section assumption in contact angle estimation. *Journal of Colloid Interface Science*, 259(1):139 – 147, 2003.

[93] Philippe Méléard, Luis A. Bagatolli, and Tanja Pott. *Methods in Enzymology*, volume 465, chapter Chapter 9 - Giant Unilamellar Vesicle Electroformation: From Lipid Mixtures to Native Membranes Under Physiological Conditions, pages 161–176. Academic Press, 2009.

[94] Joshua A. Jackman, Jae-Hyeok Choi, Vladimir P. Zhdanov, and Nam-Joon Cho. Influence of osmotic pressure on adhesion of lipid vesicles to solid supports. *Langmuir*, 29(36):11375–11384, Sep 2013.

[95] M. Autiero, L. Celentano, R. Cozzolino, P. Laccetti, M. Marotta, G. Mettivier, M. C. Montesi, P. Riccio, G. Roberti, and P. Russo. Hematoporphyrin mediated laser induced fluorescence in vivo imaging of tumor and organs structure in small animals. In *IEEE Symposium Conference Record Nuclear Science 2004.*, volume 6, pages 3743–3747 Vol. 6, 2004.

[96] George Zoriniants, Francesco Masia, Naya Giannakopoulou, Wolfgang Langbein, and Paola Borri. Background-free 3D nanometric localization and sub-nm asymmetry detection of single plasmonic nanoparticles by four-wave mixing interferometry with optical vortices. *Physical Review X*, 7(4):041022, Oct 2017.

[97] Anne S. Ulrich, Malkit Sami, and Anthony Watts. Hydration of DOPC bilayers by differential scanning calorimetry. *Biochimica et Biophysica Acta (BBA) - Biomembranes*, 1191(1):225 – 230, 1994.

[98] Rafael L. Schoch, Larisa E. Kapinos, and Roderick Y. H. Lim. Nuclear transport receptor binding avidity triggers a self-healing collapse transition in FG-nucleoporin molecular brushes. *Proceedings of the National Academy of Sciences of the U. S. A.*, 109(42):16911–16916, 2012.

[99] Jianjun Pan, Stephanie Tristram-Nagle, Norbert Kučerka, and John F. Nagle. Temperature dependence of structure, bending rigidity, and bilayer interactions of dioleoylphosphatidylcholine bilayers. *Biophysical Journal*, 94(1):117 – 124, 2008.

[100] Jana Gallová, Daniela Uhríková, Akhmed Islamov, Alexander Kuklin, and Pavol Balgavý. Effect of cholesterol on the bilayer thickness in unilamellar extruded DLPC and DOPC liposomes: SANS contrast variation study. *General Physiology Biophysics*, 23(2):113 – 128, 2004.

[101] Sagar Kamble, Snehal Patil, Mandar Kulkarni, and Appala Venkata Ramana Murthy. Spectroscopic ellipsometry of fluid and gel phase lipid bilayers in hydrated conditions. *Colloids and Surfaces B: Biointerfaces*, 176:55 – 61, 2019.

[102] Piotr Jurkiewicz, Agnieszka Olżyńska, Lukasz Cwiklik, Elena Conte, Pavel Jungwirth, Francesco M. Megli, and Martin Hof. Biophysics of lipid bilayers containing oxidatively modified phospholipids: Insights from fluorescence and EPR experiments and from MD simulations. *Biochimica et Biophysica Acta - Biomembranes*, 1818(10):2388 – 2402, 2012.

[103] Kalani J. Seu, Anjan P. Pandey, Farzin Haque, Elizabeth A. Proctor, Alexander E. Ribbe, and Jennifer S. Hovis. Effect of surface treatment on diffusion and domain formation in supported lipid bilayers. *Biophysical Journal*, 92(7):2445 – 2450, 2007.

[104] Liam Stubbington, Marino Arroyo, and Margarita Staykova. Sticking and sliding of lipid bilayers on deformable substrates. *Soft Matter*, 13:181–186, 2017.

[105] Lance D. Eske and David W. Galipeau. Characterization of SiO_2 surface treatments using AFM, contact angles and a novel dewpoint technique. *Colloids and Surfaces A: Physicochemical and Engineering Aspects*, 154(1):33 – 51, 1999.

[106] Akira Nakajima, Kazuhito Hashimoto, and Toshiya Watanabe. *Molecular Materials and Functional Polymers*, chapter Recent Studies on Super-Hydrophobic Films, pages 31–41. Springer Vienna, Vienna, 2001.

[107] Asma Poursoroush, Maria Maddalena Sperotto, and Mohamed Laradji. Phase behavior of supported lipid bilayers: A systematic study by coarse-grained molecular dynamics simulations. *Journal of Chemical Physics*, 146(15):154902, 2017.

[108] Zun-Jing Wang and Daan Frenkel. Pore nucleation in mechanically stretched bilayer membranes. *Journal of Chemical Physics*, 123(15):154701, 2005.

[109] Gary Ayton, Alexander M. Smondyrev, Scott G. Bardenhagen, Patrick McMurtry, and Gregory A. Voth. Calculating the bulk modulus for a lipid bilayer with nonequilibrium molecular dynamics simulation. *Biophysical Journal*, 82(3):1226 – 1238, 2002.

[110] Matthew I. Hoopes, Markus Deserno, Margie L. Longo, and Roland Faller. Coarse-grained modeling of interactions of lipid bilayers with supports. *The Journal of Chemical Physics*, 129(17):175102, 2008.

[111] Mette Marie Bruun Nielsen and Adam Cohen Simonsen. Imaging ellipsometry of spin-coated membranes: Mapping of multilamellar films, hydrated membranes, and fluid domains. *Langmuir*, 29(5):1525–1532, 2013. PMID: 23281595.

[112] Hanna P. Wacklin. Composition and asymmetry in supported membranes formed by vesicle fusion. *Langmuir*, 27(12):7698–7707, 2011. PMID: 21612246.

[113] Zdzislaw Salamon and Gordon Tollin. Optical anisotropy in lipid bilayer membranes: Coupled plasmon-waveguide resonance measurements of molecular orientation, polarizability, and shape. *Biophysical Journal*, 80(3):1557 – 1567, 2001.

[114] Frédéric F. Harb and Bernard Tinland. Effect of ionic strength on dynamics of supported phosphatidylcholine lipid bilayer revealed by FRAPP and Langmuir—Blodgett transfer ratios. *Langmuir*, 29(18):5540–5546, 2013. PMID: 23581462.

[115] Takeshi Fukuma, Michael J. Higgins, and Suzanne P. Jarvis. Direct imaging of lipid-ion network formation under physiological conditions by frequency modulation atomic force microscopy. *Physics Review Letters*, 98:106101, Mar 2007.

[116] Georg Pabst, Aden Hodzic, Janez Štrancar, Sabine Danner, Michael Rappolt, and Peter Laggner. Rigidification of neutral lipid bilayers in the presence of salts. *Biophysical Journal*, 93(8):2688 – 2696, 2007.

[117] Daniela Uhríková, Norbert Kučerka, José Teixeira, Valentin Gordeliy, and Pavol Balgavý. Structural changes in dipalmitoylphosphatidylcholine bilayer promoted by Ca2+ ions: a small-angle neutron scattering study. *Chemistry and Physics of Lipids*, 155(2):80 – 89, 2008.

[118] Alireza Mashaghi, Marcus Swann, Jonathan Popplewell, Marcus Textor, and Erik Reimhult. Optical anisotropy of supported lipid structures probed by waveguide spectroscopy and its application to study of supported lipid bilayer formation kinetics. *Analytical Chemistry*, 80(10):3666–3676, 2008. PMID: 18422336.

[119] Sarah L. Veatch and Sarah L. Keller. Miscibility phase diagrams of giant vesicles containing sphingomyelin. *Phys. Rev. Lett.*, 94:148101, Apr 2005.

[120] Chao Liu, Min Wang, Junxue An, Esben Thormann, and Andra Dėdinaitė. Hyaluronan and phospholipids in boundary lubrication. *Soft Matter*, 8:10241–10244, 2012.

[121] A. Charrier and F. Thibaudau. Main phase transitions in supported lipid single-bilayer. *Biophysical journal*, 89(2):1094–1101, Aug 2005.

[122] Stephanie Tristram-Nagle, Yufeng Liu, Justin Legleiter, and John F. Nagle. Structure of gel phase DMPC determined by X-ray diffraction. *Biophysical Journal*, 83(6):3324–3335, Dec 2002.

[123] S. Knippenberg, G. Fabre, S. Osella, F. Di Meo, M. Paloncýová, M. Ameloot, and P. Trouillas. Atomistic picture of fluorescent probes with hydrocarbon tails in lipid bilayer membranes: An investigation of selective affinities and fluorescent anisotropies in different environmental phases. *Langmuir*, 34(30):9072–9084, Jul 2018.

[124] Andrey S. Klymchenko and Rémy Kreder. Fluorescent probes for lipid rafts: From model membranes to living cells. *Chemistry & Biology*, 21(1):97 – 113, 2014.

[125] Sarah L. Veatch and Sarah L. Keller. Separation of liquid phases in giant vesicles of ternary mixtures of phospholipids and cholesterol. *Biophysical journal*, 85(5):3074–3083, Nov 2003.

[126] Jun Ando, Masanao Kinoshita, Jin Cui, Hiroyuki Yamakoshi, Kosuke Dodo, Katsumasa Fujita, Michio Murata, and Mikiko Sodeoka. Sphingomyelin distribution in lipid rafts of artificial monolayer membranes visualized by Raman microscopy. *Proceedings of the National Academy of Sciences*, 112(15):4558–4563, 2015.

[127] Li Li, Haifeng Wang, and Ji-Xin Cheng. Quantitative coherent anti-Stokes Raman scattering imaging of lipid distribution in coexisting domains. *Biophysical Journal*, 89(5):3480 – 3490, 2005.

[128] Frederick A. Heberle, Robin S. Petruzielo, Jianjun Pan, Paul Drazba, Norbert Kučerka, Robert F. Standaert, Gerald W. Feigenson, and John Katsaras. Bilayer thickness mismatch controls domain size in model membranes. *Journal of the American Chemical Society*, 135(18):6853–6859, May 2013.

[129] Wolfgang Helfrich. Elastic properties of lipid bilayers: Theory and possible experiments. *Zeitschrift fur Naturforschung. Teil C: Biochemie, Biophysik, Biologie, Virologie*, 28, 12 1973.

[130] Thomas Portet and Rumiana Dimova. A new method for measuring edge tensions and stability of lipid bilayers: Effect of membrane composition. *Biophysical Journal*, 99(10):3264 – 3273, 2010.

[131] Travers H. Anderson, Younjin Min, Kim L. Weirich, Hongbo Zeng, Deborah Fygenson, and Jacob N. Israelachvili. Formation of supported bilayers on silica substrates. *Langmuir*, 25(12):6997–7005, Jun 2009.

[132] Hélène Bouvrais. *Advances in Planar Lipid Bilayers and Liposomes*, volume 15, chapter Chapter one - Bending Rigidities of Lipid Bilayers: Their Determination and Main Inputs in Biophysical Studies, pages 1–75. Academic Press, 2012.

[133] Russell E. McConnell, James N. Higginbotham, David A. Shifrin, David L. Tabb, Robert J. Coffey, and Matthew J. Tyska. The enterocyte microvillus is a vesicle-generating organelle. *The Journal of Cell Biology*, 185(7):1285–1298, 2009.

[134] John C. Fiala and Kristen M. Harris. *Dendrites*, chapter 1 - Dendrite Structure, pages 1–5. Oxford University Press, 1999.

[135] Aurélien Roux, Giovanni Cappello, Jean Cartaud, Jacques Prost, Bruno Goud, and Patricia Bassereau. A minimal system allowing tubulation with molecular motors pulling on giant liposomes. *Proceedings of the National Academy of Sciences of the United States of America*, 99(8):5394–5399, Apr 2002.

[136] Mohammad Rahimi, David Regan, Marino Arroyo, Anand Bala Subramaniam, Howard A. Stone, and Margarita Staykova. Shape transformations of lipid bilayers following rapid cholesterol uptake. *Biophysical Journal*, 111(12):2651 – 2657, 2016.

[137] Hélène Bouvrais, Tanja Pott, Luis A. Bagatolli, John H. Ipsen, and Philippe Méléard. Impact of membrane-anchored fluorescent probes on the mechanical properties of lipid bilayers. *Biochimica et Biophysica Acta (BBA) - Biomembranes*, 1798(7):1333–1337, 2010.

[138] Aiwei Tian, Benjamin R. Capraro, Cinzia Esposito, and Tobias Baumgart. Bending stiffness depends on curvature of ternary lipid mixture tubular membranes. *Biophysical Journal*, 97(6):1636 – 1646, 2009.

[139] Mijo Simunovic, Coline Prévost, Andrew Callan-Jones, and Patricia Bassereau. Physical basis of some membrane shaping mechanisms. *Philosophical Transactions of the Royal Society A: Mathematical, Physical and Engineering Sciences*, 374(2072):20160034, 2016.

[140] S. Svetina, B. Žekš, R. E. Waugh, and R. M. Raphael. Theoretical analysis of the effect of the transbilayer movement of phospholipid molecules on the dynamic behavior of a microtube pulled out of an aspirated vesicle. *European Biophysics Journal*, 27(3):197–209, Apr 1998.

[141] Oumaima Et-Thakafy, Nicolas Delorme, Cédric Gaillard, Cristelle Mériadec, Franck Artzner, Christelle Lopez, and Fanny Guyomarc'h. Mechanical properties of membranes composed of gel-phase or fluid-phase phospholipids probed on liposomes by atomic force spectroscopy. *Langmuir*, 33(21):5117–5126, 2017.

[142] Pranav R. Adhyapak, Suresh V. Panchal, and Appala Venkata Ramana Murthy. Cholesterol induced asymmetry in DOPC bilayers probed by AFM force spectroscopy. *Biochimica et Biophysica Acta (BBA) - Biomembranes*, 1860(5):953–959, 2018.

[143] Michael C. Howland, Alan W. Szmodis, Babak Sanii, and Atul N. Parikh. Characterization of physical properties of supported phospholipid membranes using imaging ellipsometry at optical wavelengths. *Biophysical Journal*, 92(4):1306–1317, Feb 2007.

[144] Jared C. Lawrence, David E. Saslowsky, J. Michael Edwardson, and Robert M. Henderson. Real-time analysis of the effects of cholesterol on lipid raft behavior using atomic force microscopy. *Biophysical Journal*, 84(3):1827–1832, Mar 2003.

[145] Edward H. Ahrens. The nomenclature of lipids*. *Journal of Lipid Research*, 8(5):523–528, 1967.

[146] Rumiana Koynova and Martin Caffrey. Phases and phase transitions of the hydrated phosphatidylethanolamines. *Chemistry and Physics of Lipids*, 69(1):1 – 34, 1994.

[147] Stephanie A. Tristram-Nagle. Preparation of oriented, fully hydrated lipid samples for structure determination using x-ray scattering. *Methods in Molecular Biology*, 400:63–75, 2007.

[148] Kazunari Yoshida, Keitaro Horii, Yasuhiro Fujii, and Izumi Nishio. Real-time observation of liposome bursting induced by acetonitrile. *ChemPhysChem*, 15(14):2909–2912, Oct 2014.